ATOMIC STRUCTURE AND NON-ELECTRONIC PROPERTIES OF SEMICONDUCTORS

Low-temperature relaxation of a solid solution of iron in gallium phosphide

E. S. Demidov, V. V. Karzanov, A. B. Gromoglasova, and O. N. Morozkin

Nizhniĭ Novgorod State University, 603600 Nizhniĭ Novgorod, Russia
(Submitted August 3, 1998; accepted for publication September 22, 1998)
Fiz. Tekh. Poluprovodn. **33**, 385–388 (April 1999)

Electron spin resonance (ESR) and the Hall effect are used to investigate low-temperature relaxation of solid solutions of iron in gallium phosphide, as well as the distribution profiles for paramagnetic iron centers in GaP located at *A*-site ($g=2.02$) and *B*-site ($g=2.133$). The data obtained are consistent with the idea that the *A*-site corresponds to an iron atom in a substitutional position, i.e., Fe_s^{3+}(Ga) ($3d^5$), whereas the *B*-site corresponds to an interstitial neutral iron atom, i.e., Fe_i^0 ($3d^8$). As a solid solution of GaP : Fe undergoes low-temperature relaxation, the *A*-centers are observed to be stable against annealing in the temperature range 293–800 K. In contrast, the intensity of the ESR spectrum from the *B*-center has complicated kinetics that qualitatively resembles the annealing kinetics of paramagnetic Fe_i^0-centers in silicon. © *1999 American Institute of Physics.* [S1063-7826(99)00104-0]

INTRODUCTION

Semiconductors doped with *d*- and *f*-transition metal impurities have excited new interest recently as investigators uncover new nanoelectronics uses for the multicharged deep levels these impurities generate in quantum-well structures. Since the distances over which defects can move by diffusion are small at room temperature, the long-term stability of the operating characteristics of semiconductor devices that incorporate solid solutions of transition elements is determined by the low-temperature relaxation of these solutions. Hence, it is critical to understand this relaxation when the device applications involve operation at room temperature. Low-temperature solid-solution relaxation has been rather thoroughly studied for solutions of $3d$-impurities from the iron group in silicon. In these systems, the preferred mode of solution in Si is to occupy interstitial positions, i.e., Me_i, which have especially high diffusive mobility even at room temperature. For chromium or iron impurities in Si, for example, it is known[1–4] that after samples of single-crystal silicon are quenched from the high temperatures used in diffusion doping the most rapid relaxation processes involve combining with vacancies. Once these have occurred, some of the remaining impurities form complexes with shallow acceptors. The time constant for this latter process is given by the expression $\tau=\tau_0\exp(Q/kT)$, where $\tau_0\approx 10^{-9}$ s and $Q\approx 0.85$ eV. Conversely, above the first inflection point Q at $T_1\approx 400$ K these complexes dissociate, and at temperatures higher than the second inflection point Q $T_2\approx(450-490)$ K the solid solution of $3d$ impurities decays as a whole. Both of these processes – complex formation and solid-solution decay in the bulk of the crystal – can be controlled by bombarding the silicon surface with argon ions at energies of $\sim$40 keV (Refs. 5–7) (the effect of long-range ion implantation Q).

For III–V compounds it has been known since the pioneering work of Ludwig and Woodbury in the 1960 (Ref. 1) that $3d$ elements substitutionally occupy the position of the *A* component in these crystals, i.e., Me_s(A). Later investigations revealed that the activation energies for diffusion of these impurities were quite high, i.e., $Q\approx$ 2–3 eV.[8] However, evidence was also found (for the examples of Mn in GaAs (Ref. 9) and Fe in GaP (Refs. 10 and 11) that some of these impurities could also be interstitials, i.e., Me_i, and that the fraction of them was comparable to that of the Me_s(A). In view of this circumstance, transition-element solutions in III–V compounds should exhibit significant low-temperature relaxation. This is indirectly confirmed by the observation[4,12] of long-range Q effects, analogous to those mentioned above in Si : Fe and Si : Cr, when semi-insulating samples of gallium arsenide and indium phosphide compensated by $3d$ transition elements are bombarded by argon ions.

In this paper we report the first results of experimental studies of low-temperature solid-solution relaxation in III–V compounds for the example of GaP : Fe crystals using the techniques of electron spin resonance (ESR). In these crystals, which are convenient to use because it is easy to observe ESR in them at 77 K, two signals are observed: an *A*-center spectrum with a *g*-factor of 2.02, which corresponds to Fe_s^{3+}(Ga) ions with the configuration $3d^5(^6S_{5/2})$, and a *B*-center spectrum with $g=2.133$ (Refs. 13 and 14). Based on their observations of hyperfine splitting of the *B*-site ESR spectral lines, it was concluded[10] that these centers correspond to interstitial Fe_i^0 ions with the configuration $3d^8(^3S_1)$, analogous to such centers in silicon. Further confirmation of this assignment of the *B*-spectrum was obtained by one of us in Ref. 11, based on the considerably larger diffusion length for *B*-centers than for *A*-centers and analysis of the balance of concentrations of *B*-centers and conduction-band electrons, which is inconsistent with the claim made in

 © 1999 American Institute of Physics

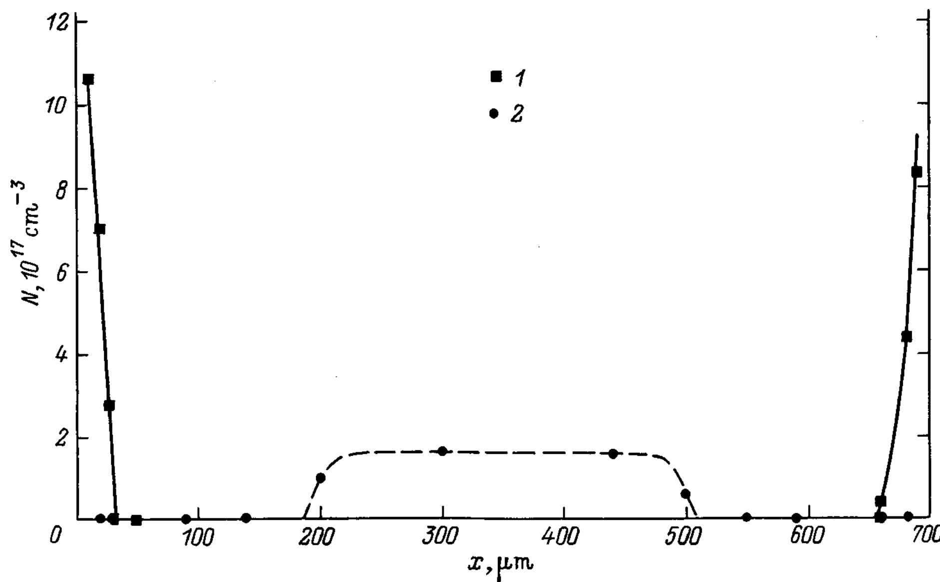

FIG. 1. Distributions of iron at *A*- and *B*-centers in a crystal of gallium phosphide, plotted versus depth. 1—*A*-center $[Fe_s^{3+}(Ga)]$, 2—*B*-center $[Fe_i^0]$.

Ref. 3 that these defects are $Fe_s^+(Ga)$ with the configuration $3d^7(^4S_{3/2})$.

EXPERIMENT

The GaP single crystals we investigated were 600 μm wide, with an initial shallow-donor concentration of $2\times10^{17}\,\mathrm{cm}^{-3}$. These crystals were diffusion-doped with iron by placing them in evacuated quartz cells along with a charge of Fe_2O_3 as an iron source, a charge of red phosphorus to stabilize the GaP surface, and a charge of metallic aluminum as a getter of uncontrolled impurities.[4] The cells were heated for 5 hours at 1250 °C, then removed from the furnace and rapidly cooled in air. In order to study low-temperature solid-solution relaxation at temperatures in the range 293–800 K, these crystals were held in air at these temperatures, and then their ESR spectra were measured along with their electrical conductivities and Hall effect, using a special apparatus which was developed by one of us (see Ref. 4) and which automatically held the temperature at nearly zero.

RESULTS AND DISCUSSION

Figure 1 shows the distributions of paramagnetic *A*- and *B*-centers versus depth *x* in one of the GaP crystals. It is clear from the figure that the iron that substitutionally replaces gallium is concentrated in the skin layer with thickness $\sim 50\mu$m. In these layers, the maximum concentration $N \simeq 1.5\times10^{18}\,\mathrm{cm}^{-3}$ (taking into account the $5\times10^{17}\,\mathrm{cm}^{-3}$ background of shallow donors for the original crystals), which is close to the maximum solubility of iron in GaAs and GaP.[8] The falloff in the concentration of *A*-centers corresponds to a diffusion $D\approx2\times10^{-9}\,\mathrm{cm}^2/\mathrm{s}$, in good agreement with the data of Ref. 15: $D=2.5\times10^{-9}\,\mathrm{cm}^2/\mathrm{s}$ at 1250 °C.

According to Fig. 1, the *B*-centers are concentrated in a layer of thickness 300 μm at the center of the crystal. Their maximum concentration N is $\simeq 1.5\times10^{17}\,\mathrm{cm}^{-3}$ if the spectrum corresponds to Fe_i^0 centers with $3d^8$ occupation of the *d*-shell and spin $S = 1$, or $8\times10^{16}\,\mathrm{cm}^{-3}$ if it corresponds to $Fe_s^+(Ga)$ ions substituting for gallium with $3d^7$ occupation of the *d*-shell and spin $S = 3/2$. However, calculations based on classical diffusion in a crystal of finite thickness[16] show that for $D=2\times10^{-9}\,\mathrm{cm}^2/\mathrm{s}$, i.e., iron substituting for gallium, the concentration at the center of the crystal should be two orders of magnitude smaller than that shown in Fig. 1. This fact provides additional confirmation that the *B*-centers are occupied by the fast-diffusing interstitial iron component Fe_i. A result of considerable interest is the high solubility we deduce for interstitial iron in these crystals, which exceeds by an order of magnitude the value $\sim 10^{16}\,\mathrm{cm}^{-3}$ for the maximum solubility of interstitial iron in silicon .[2,4]

Electrical measurements show that after the iron diffusion a conducting layer of *n*-type material forms at the surface of the crystal, extending ~ 5 μm inward, with a Fermi level at approximately E_c–0.15 eV. At the depth where the *B*-centers are located (~ 200 μm) a very-high-resistance region, made up of semi-insulating GaP, with a resistivity greater than $10^{10}\Omega\cdot$cm, is formed. In the 300-μm-thick layer of *B*-centers, we see an *n*-type conductivity, with a Fermi level at E_c–0.34 eV if it is assumed that the effective density-of-states mass of conduction-band electrons is 20% larger than the mass of a free electron, as is the case for heavy electrons in GaAs. If we argue by analogy with Fe_i^0 in silicon that a similar center is present in gallium phosphide, then the analogous energy level is below E_c–0.34 eV. The position of the Fermi level in this layer is thus controlled by centers other than interstitial iron. Based on the behavior of charge-transfer levels deduced in Ref. 17, we expect the first donor level of Fe_i^0 to be located near E_v+1 eV, i.e., almost 1 eV lower than the Fermi level in the *B*-layer. This level is somewhat higher than the first acceptor level 2+/3+ with charge-transfer energy $E_v+0.7$ eV for $Fe_s(Ga)$ in GaP .[4,18] Figure 1 shows that at distances between ~ 50 and ~ 200 μm from the crystal surface there are no *A*- or *B*-centers; in this region the Fermi level probably lies between $E_v+0.7$ eV and E_v+1 eV. A more detailed investigation of the electrical properties of crystals with a nonuniform distribution of iron

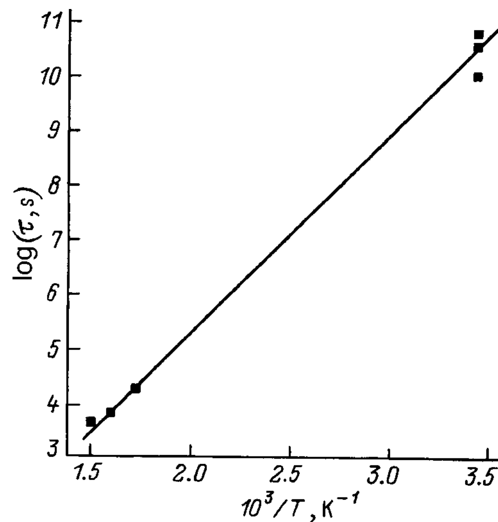

FIG. 2. Temperature dependence of the time constant for low-temperature relaxation of a solid solution of *B*-centers of iron in a gallium phosphide crystal.

such as those shown in Fig. 1 will probably confirm this assumption eventually.

ESR studies of low-temperature solid-solution relaxation in a number of GaP : Fe crystals held at room temperature for 12 years showed that the intensity of the *B*-spectrum had decreased by 10–50 %. With increasing temperature, the intensity of the *B*-spectrum decreases more rapidly. At 723 K the process slows; at 773 K an increase in the amplitude of the *B*-spectrum is observed, and then at higher temperatures the intensity decreases again, as in the region $T < 723$ K. The amplitude of the *A*-spectrum remains nearly constant, consistent with the expected thermal stability of the Fe_s^{3+}(Ga) state. Figure 2 shows the temperature dependence of the time constant associated with the decrease in the number of *B*-centers in the approximation that the decay of the *B*-center concentration is exponential in the low-temperature portion of the relaxation process. It is given by the expression $\tau = \tau_0 \exp(Q/kT)$ with parameters $\tau_0 \approx 3 \times 10^{-2}$ s and an activation energy $Q = 0.66$ eV.

Thus, we have obtained further confirmation that the *B*-centers should be associated with the state Fe_i^0. The solubility of Fe_i^0 in GaP is an order of magnitude higher than it is in Si. Moreover, Fe_i^0 forms complexes with unknown *X*- defects in GaP, as it does in silicon (Fe_i^0 plus a shallow acceptor). The inverse process of complex dissociation is also observed, again as in silicon.[2,4] The higher value of the inflection-point Q temperature can be taken as evidence that the binding energy for the complex is larger than it is in silicon (0.65 eV). The activation energy for diffusion – 0.66 eV from Fig. 2 – is smaller than in silicon ($Q = 0.85$ eV), which suggests low potential barriers between neighboring interstitial locations. The stronger shift of low-temperature solid-solution relaxation towards higher temperatures, which is associated with the small value of τ_0, is caused not by a low concentration of *X* partners (in Si, the concentration of partners is of the same order of magnitude as that of Fe_i^0), but rather by the more limited possibilities for hopping to neighboring interstitial sites, and for the most part by the smaller vibrational lattice contribution to the entropy factor for τ_0.

We are grateful to Professor Rembeza and his colleagues, with whom we had fruitful discussions about the physics of 3*d*-centers that stimulated this work.

[1] G. W. Ludwig and H. H. Woodbury, Solid State Physics **13**, 223 (1962). ''Electron Spin Resonance in Semiconductors,'' Mir, Moscow, 1964.
[2] L. S. Kimmerling and J. L. Benton, Physica **116B**, 297 (1983).
[3] S. I. Rembeza, *Paramagnetic Resonance in Semiconductors* [in Russian], Metallurgiya, Moscow, 1988.
[4] E. S. Demidov, Doctoral Dissertation [in Russian], Nizh. Novgorod, 1994.
[5] P. V. Pavlov, E. S. Demidov, and G. V. Zorina, Fiz. Tekh. Poluprovodn. **21**, 984 (1987) [Sov. Phys. Semicond. **21**, 603 (1921)].
[6] E. S. Demidov, V. V. Karzanov, and P. V. Pavlov, Fiz. Tekh. Poluprovodn. **23**, 548 (1989) [Sov. Phys. Semicond. **23**, 342 (1989)].
[7] V. V. Karzanov, P. V. Pavlov, and E. S. Demidov, Fiz. Tekh. Poluprovodn. **23**, 2064 (1989) [Sov. Phys. Semicond. **23**, 1276 (1989)].
[8] D. T. Dzhafarov, in *Physics and Material Science of Semiconductors with Deep Levels* [in Russian], Metallurgiya, Moscow, 1987, p. 95.
[9] S. J. C. H. M. Gisbergen, A. A. Ezhevskii, N. T. Son, T. Gregokievich, and C. A. J. Ammerlaan, Phys. Rev. B **49**, 10 999 (1993).
[10] V. F. Masterov, S. I. Markov, L. P. Pasechnik, and V. K. Sobolevskiĭ, Fiz. Tekh. Poluprovodn. **17**, 1130 (1983) [Sov. Phys. Semicond. **17**, 711 (1983)].
[11] E. S. Demidov and A. A. Ezhevskiĭ, Fiz. Tekh. Poluprovodn. **19**, 1629 (1985) [Sov. Phys. Semicond. **19**, 1003 (1985)].
[12] P. V. Pavlov, E. S. Demidov, and V. V. Karzanov, Fiz. Tekh. Poluprovodn. **26**, 1118 (1992) [Sov. Phys. Semicond. **26**, 855 (1992)].
[13] K. Suto and J. Nishisawa, J. Phys. Soc. Jpn. **26**, 1556 (1969).
[14] K. Suto and J. Nishisawa, J. Appl. Phys. **43**, 2247 (1972).
[15] F. S. Shishiyanu and V. G. Gheorgiu, Fiz. Tekh. Poluprovodn. **10**, 2188 (1976) [Sov. Phys. Semicond. **10**, 1301 (1976)].
[16] B. I. Boltaks, *Diffusion in Semiconductors* [in Russian], Moscow, 1961.
[17] E. S. Demidov, Fiz. Tverd. Tela (Leningrad) **34**, 37 (1992) [Sov. Phys. Solid State **34**, 18 (1992)].
[18] E. M. Omel'yanovskiĭ and V. I. Fistul', *Transition-Metal Impurities in Semiconductors* [in Russian], Metallurgiya, Moscow, 1983.

Translated by Frank J. Crowne

Modeling Si nanoprecipitate formation in SiO_2 layers with excess Si atoms

A. F. Leĭer, L. N. Safronov, and G. A. Kachurin

Institute of Semiconductor Physics, Russian Academy of Sciences, Siberian Branch, 530090 Novosibirsk, Russia

(Submitted March 23, 1998; accepted for publication October 8, 1998)
Fiz. Tekh. Poluprovodn. **33**, 389–394 (April 1999)

Computer simulations based on the Monte Carlo method are used to analyze processes leading to the formation of luminescence centers in SiO_2 implanted with Si ions. The simulations, which take place in a two-dimensional space, mimic the growth of silicon nanoprecipitates in layers containing several at. % of excess silicon. It is assumed that percolation clusters made up of neighboring Si atoms form first. As the annealing temperature increases, these clusters grow and compactify into nano-sized inclusions of a well-defined phase. It is shown that a dose dependence arises from an abrupt enhancement of the probability of forming direct Si–Si bonds when the concentration of silicon exceeds ~1 at. %. Under these conditions, percolation chains and clusters form even before annealing begins. The effect of the temperature of subsequent anneals up to 900 °C is modeled via the well-known temperature dependence of Si diffusion in SiO_2. It is assumed that annealing at moderate temperatures increases the mobility of Si atoms, thereby facilitating percolation and development of clusters due to an increase in the interaction radius. Intrinsic diffusion processes that occur at high temperatures transform branching clusters into nanoprecipitates with well-defined phase boundaries. The dose and temperature intervals for the formation of precipitates obtained from these simulations are in agreement with the experimental intervals of dose and temperatures corresponding to the appearance of and changes in luminescence. © *1999 American Institute of Physics.*
[S1063-7826(99)00204-5]

INTRODUCTION

The recently observed ability of silicon nanostructures to emit intense visible luminescence has generated considerable interest in these systems. There is particular interest in identifying the mechanisms that lead to the appearance of silicon nanostructures and the nature of the centers for visible light. Among the various ways used to generate these nanostructures, one that has shown considerable promise is implantation of Si ions into a layer of SiO_2, because it is easy to monitor, because it is highly controllable, and because it is compatible with contemporary semiconductor technology.[1–13] However, despite successes in implementing this technique experimentally, the nature of the resulting centers of visible luminescence and the mechanisms that generate them still remain subjects for discussion. We can state with reasonable confidence that the intense emission band in the wavelength range $\lambda \simeq 700–850$ nm, which appears only after annealing at temperatures $T_a > 1000\,°C$, is connected with the formation of Si crystallites in the implanted SiO_2, whose dimensions are 3–5 nm.[2–6,9] The visible light is attributable to the widening of the band gap in the Si nanocrystallites due to the quantum-well effect. However, despite the fact that Si nanocrystallites do not form in the implanted SiO_2 layers when $T_a < 900\,°C$, the layers yield a wide spectrum of visible luminescence with peaks in the blue and orange regions even after low-temperature processing.[1–12] This emission is observed when sufficiently large doses of Si ions ($\geqslant 10^{16}\,cm^{-2}$) are incorporated, and low-temperature annealing can either enhance or attenuate the luminescence.[1,4,8–12] As the annealing temperatures approach, $T_a \simeq 900\,°C$, quenching of the luminescence is observed.[4,6,11,12] These effects are undoubtedly associated with distinct stages in the decay of the supersaturated solid solution of Si in implanted SiO_2 layers; however, in order to understand their evolution and effect on the illumination, additional analysis is required.

Kachurin *et al.*[5,6] proposed the following scheme for generating light-emitting nanoprecipitates during the annealing of Si layers implanted by SiO_2 ions. At doses $D > 10^{16}\,cm^{-2}$ the probability for direct interaction of Si atoms among themselves increases abruptly with the formation of Si–Si bonds. A Si–Si bond in SiO_2 is equivalent to a neutral oxygen vacancy, which absorbs photons with energy 5 eV and emits photons with energy 2.7 eV. The blue light is thus a consequence of the formation of complexes and chains of Si atoms in SiO_2 (Refs. 8, 10, 12, and 13). This process occurs at temperatures where the computed diffusion length of Si in SiO_2 is much smaller than the interatomic distance, and hence it should be viewed not as diffusion-controlled growth of the precipitate but rather as percolation along sites where silicon atoms are close to one another. An increase in T_a enhances the segregation of Si, which not only anneals out structural damage but also causes the luminescence intensity to increase. Large-scale percolation clusters are capable of emitting light in the orange portion of the spectrum.[10] However, starting with $T_a \simeq 700\,°C$ another process comes into play—the conversion of chains with no

 © 1999 American Institute of Physics

phase boundaries and percolation clusters into nano-sized inclusions of the amorphous phase of Si. The presence of dangling bonds and other centers of nonradiative recombination in these precipitates suppresses their luminescence, which accounts for the disappearance of the emission as T_a approaches the interval 800–900 °C. At $T_a > 1000$ °C, the diffusion of Si in SiO_2 is already large enough for diffusion-controlled growth of these precipitates, and they reach sizes that ensure the stability of the crystal lattice (>2 nm). At this stage the strong red emission and near-infrared emission, which are attributable to the quantum-well effects in the silicon nanocrystallites, appear.

This scheme agrees qualitatively with the currently obtained data on the generation of light-emitting silicon precipitates. It is therefore important to quantitatively analyze whether these processes can actually occur for a given dose of Si ions and anneal temperature. In this paper we do this by computer simulation, using the smallest possible number of numerical parameters. Our basic interest centers on temperatures below 900 °C, because at these temperatures T_a, the nuclei of future nanocrystallites, which give strong red-infrared emission, form homogeneously; however, these same nuclei are also capable of emitting at shorter wavelengths.

COMPUTATIONAL MODEL

Both processes – generation of percolation clusters and compacting them into nano-inclusions of a well-defined phase – were simulated by the Monte Carlo method in a two-dimensional space. In the first case, Si atoms, which can have up to three bonds at angles of 120°, arrive at random points on a plane, where they form bonds and occupy the vertices of a hexagonal lattice. The distance at which capture is first possible is assumed to be the ordinary bond length between silicon atoms, $L_0 = 0.234$ nm. Since SiO_2 is itself made up of one-third Si atoms, which can participate in clustering, we did two simulations – one without allowance for and one allowing for the ''stoichiometric'' Si. In the former case, the initial condition was that 33% of the sites on the plane were occupied by equidistant immovable Si ions. These ''host'' atoms do not interact among themselves, so that cluster growth is fed only by the arriving atoms, which bond with the host atoms and each other as they find sites of the hexagonal lattice. A particle's membership in a cluster is established using a geometric criterion.

It is assumed that the growth of percolation clusters and their compactification into phase inclusions are affected by temperature, because the mobility of the silicon atoms increases with temperature. This effect is taken into account quantitatively through the diffusion equation for Si in SiO_2 from Ref. 14, despite the fact that only the compactification process is intrinsically diffusion-driven, while percolation that occurs via isolated atomic translations is made easier because the capture length L increases with time:

$$L = L_0 + 2\sqrt{\mathscr{D}t},$$

where $\mathscr{D}$ is the diffusion coefficient, and t is the time.

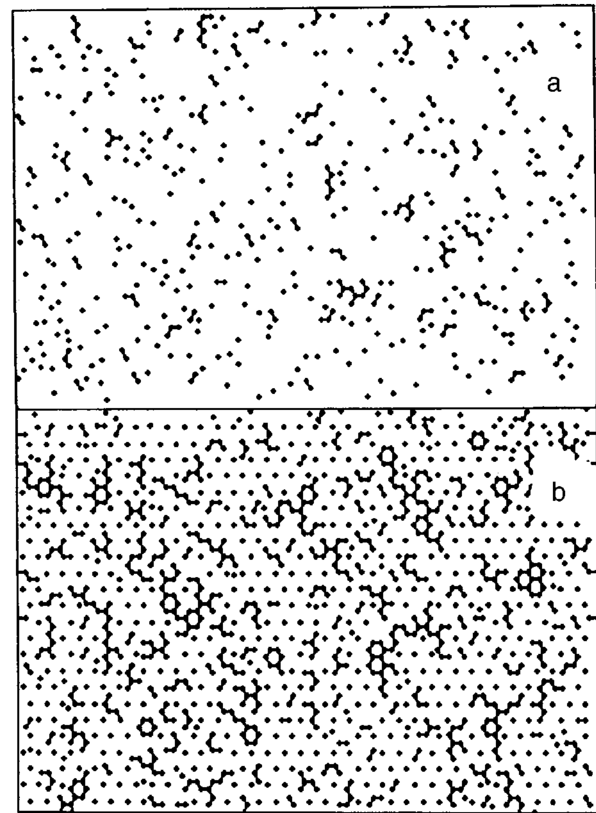

FIG. 1. Generation of silicon clusters in SiO_2 without additional heating at excess silicon concentrations of 10 at. %. a—without including the Si contained in SiO_2, b— including it.

The clusters are compacted as the Si atoms approach each other randomly due to interatomic interaction. Compaction is described by introducing elastic bonds which act in the direction of the nearest-neighbor atoms. The angles between the covalent bonds are elastically fixed by taking into account interactions with atoms in the second coordination sphere. The elasticity constants of the bonds are calculated from the values of the compression and shear moduli of crystalline silicon. In our Monte Carlo simulation of diffusion-driven compaction, each atom is randomly displaced after one cycle by an amount whose mean-square value is proportional to the diffusion length at the given temperature in accordance with the diffusion equation from Ref. 14. The tendency for this system to migrate to an energy minimum forces the branching (fractal) clusters to change into compact dense inclusions with well-defined phase boundaries.

SIMULATION RESULTS

Figure 1 shows the results of two simulations of cluster formation after incorporation of a Si dose corresponding to 10 at. %, one including and one not including the Si atoms that enter into the composition of SiO_2. It is clear that when the Si in the substrate is not included, only very limited numbers of simple clusters can form. However, if we include the Si in SiO_2, then for each arriving Si atom the probability of forming simple clusters is large at the outset: a dose of 10 at. % leads to the formation of chains containing ten or more Si atoms. Figure 2 shows the quantitative dependences of the

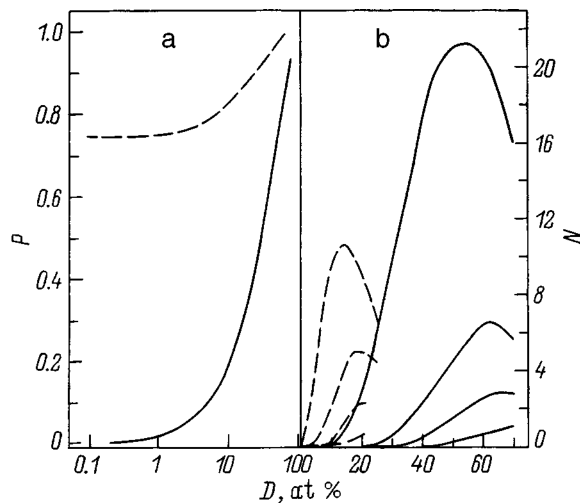

FIG. 2. Dependence of the probability of forming Si–Si bonds (P) (a) and the number of clusters of a given size N (b) on the dose of Si ions. The solid curves are the results without allowance for the Si contained in SiO_2; the dashed curves are the results which include it. The curves from top to bottom correspond to clusters containing 5, 10, 15, and 25 Si atoms.

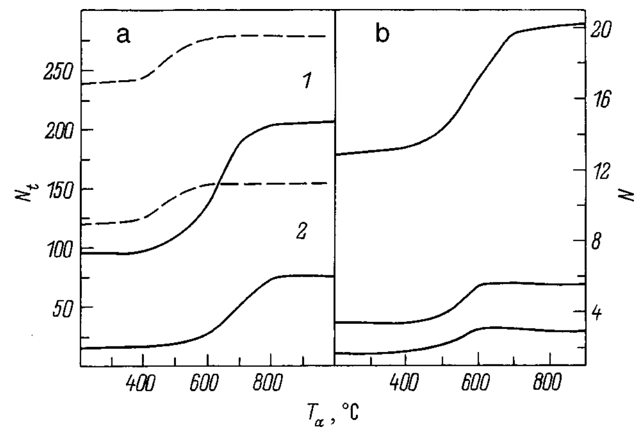

FIG. 3. Dependence of cluster formation on the temperature T_a of 30-min isochronous anneals. a—Total number of clusters N_t for Si doses of 13 (*1*) and 5 (*2*) at. % without allowance for (solid curves) and allowing for (dashed curves) the Si contained in SiO_2. b—plots the number of clusters (from top to bottom) that contain 5, 8, and 10 Si atoms for a dose of 13 at. %.

probability of forming Si–Si bonds (P) and the number of clusters (N) of a preset size on the dose of implanted ions (D). When SiO_2 is not included, the rate of formation of Si–Si bonds increases rapidly once the dose increases above ~1 at. %. When the Si in the substrate is included, for doses >1 at. % an increase is observed in the probability of forming Si–Si bonds, although in this case it is large at the outset. This is easily seen from Fig. 2a. Note also that the simplest clusters remain in the majority even when the Si in the substrate is taken into account. The presence of Si in SiO_2 causes a very sizable shift toward the low-dose end at the start of formation of large-scale clusters, but the number of these clusters in this case is limited by absorption of Si by simpler clusters. It also follows from Fig. 2b that as the dose increases, the number of clusters of a specific size increases, reaches a maximum, and then falls off. This occurs because of attachment of arriving atoms to clusters that already exist, and because small precipitates merge into large ones. The simulation shows that when ~10 at. % of Si is implanted into SiO_2, the largest individual silicon clusters can contain as many as 100 atoms per two-dimensional grid, even before thermal processing.

The influence of post-implantation heating on cluster formation is shown in Fig. 3. The increase of the capture radius with temperature leads to an increase in the total number of clusters (N_t). This process is most noticeable when the anneal temperature T_a is above 400 °C. By the time we reach 800 °C, the process is complete, since all the excess mobile Si atoms are attached to clusters. The presence of Si atoms in SiO_2 leads not only to an increase in the number of clusters, but also to their formation at lower temperatures (Fig. 3a). The total number of clusters increases with anneal temperature primarily due to the creation of new clusters and an increase in the absolute number of the smallest precipitates, although the relative numerical increase is larger for larger clusters (Fig. 3b). It should also be noted that when the Si in the substrate is taken into account, the relative number of very simple complexes decreases due to the formation of larger clusters.

Along with segregating silicon clusters from SiO_2, the interatomic interaction also causes them to compactify into dense inclusions. Figure 4 shows a time history (in Monte Carlo steps) of this compactification up to a certain time $t=t_1$ for two clusters whose densities are initially ($t=0$) different. It is clear that as time passes, the more dense cluster is converted into a single formation with a well-defined phase boundary. When the cluster is loose, the probability of its breakup into two or more parts is high during compactification. We used simulation to investigate how cluster compactification depends on temperature, density, and cluster size (Fig. 5). The quantitative measure of the degree of compactification was taken to be the number of Si atoms attached to three nearest neighbors (Si*). From Fig. 5a it is clear that

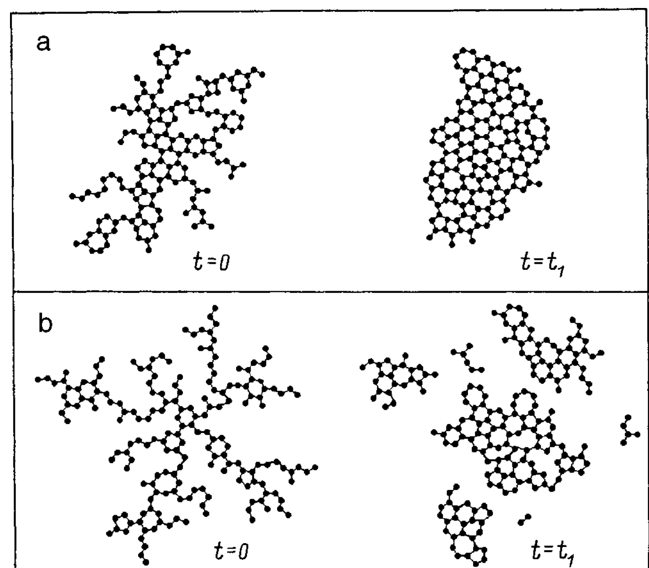

FIG. 4. Compactification versus time t for two clusters with different masses and large (a) and small (b) initial densities.

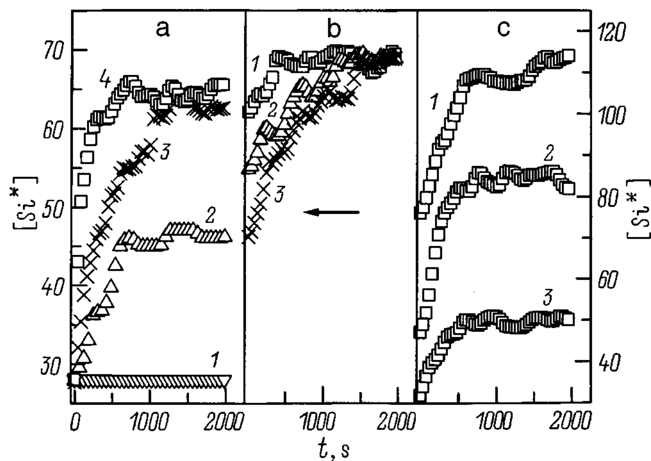

FIG. 5. Increase in the number of triply coordinated Si atoms Si* (compactification of clusters) with time. a—anneal temperatures T_a= 600 (*1*), 700 (*2*), 750 (*3*), and 850 °C (*4*). b—clusters with large (*1*), medium (*2*), and small (*3*) densities; T_a=800 °C. c—large (*1*), medium (*2*), and small (*3*) size clusters (radius of gyration); T_a=800 °C.

after the usual experimental anneal time (~30 min) at 600 °C, transformation of the clusters practically ceases. Increasing the annealing temperature by only 100 °C greatly activates the process, and at 850 °C the transformation of a non-phase inclusion into a phase inclusion takes place in roughly 500 sec. Figure 5b shows how the rate of transformation of clusters at 800 °C depends on the initial density. A higher initial density corresponds to a larger number of triply coordinated Si atoms at $t=0$. The looser the initial cluster is, the more rapidly it is transformed into a phase inclusion. The transformation rate also depends on the cluster size. Our measure of cluster size was the radius of gyration, which characterizes the average departure of each of the atoms in the cluster from the others. Equal density was ensured by a suitable selection of cluster masses and radii of gyration. Figure 5c shows that the compactification of large-sized precipitates (or high mass if the density is fixed) requires a considerably longer time at a fixed temperature.

DISCUSSION OF RESULTS

The range of medium-energy Si ions in SiO_2 characteristically lies in the interval 0.1–0.3 μm, and their straggle is about 0.03–0.1 μm. Hence, delivering a dose of $D \simeq 10^{16}\,\mathrm{cm}^{-2}$ implies a doping level on the order of $10^{21}\,\mathrm{cm}^{-3}$ (~2 at. %) and an average distance between excess Si atoms of roughly 1 nm. For such doses the most closely spaced impurity atoms are able to interact directly with each other, since the distance between them becomes comparable to the Si–Si bond length. The significant enhancement of cluster formation revealed by simulation, and the increased number of new luminescence centers observed in real experiments at doses greated than $10^{16}\,\mathrm{cm}^{-2}$ (Refs. 7 and 8), indicate that the appearance of these centers is a consequence of direct interaction of silicon atoms among themselves. As is clear from these results, this does not require intrinsic diffusion.

Although the presence of ''stoichiometric'' Si in SiO_2 turns out to be a significant factor, it does not alter the numerical dominance of small clusters over large ones. This dominance is preserved even under annealing; however, there is no indication that it occurs in real experiments. In our model we made no provision for the simplest clusters to decay under heating, whereas it is known from experiments that at certain stages of the annealing the short-wavelength emission disappears.[10] It is important to note that simulations of temperature dependences based on diffusion constants predict a rapid increase in cluster formation above $T_a \simeq 400$ °C, where the computed diffusion shift is much smaller than the interatomic distance. This matches the experimentally observed sensitivity of the short-wavelength luminescence to even small amounts of heating. The agreement is explained by the fact that both diffusion and enhancement of percolation are caused by an increase in the mobility of atoms as the temperature increases.

Another important fact, which was revealed by our simulation and which agrees with the experimental data, is that percolative formation of clusters of fractal type ''outstrips'' compactification into nano-sized inclusions with well-defined phase boundaries. Because the latter process is diffusive in nature, it occurs at higher temperatures (>700 °C). Since compactification depends on the size and looseness of the percolating cluster, we can identify conditions where percolation will dominate—low doses and temperatures, and short anneal times. The last implies, in particular, that large-radius percolation clusters can be formed by very short pulsed anneals up to the point where they compactify into phase inclusions. Moreover, by changing the implantation dose and using combinations of anneals at different temperatures and durations, we can control the formation and final sizes of the nanostructures. Our recent experimental results on pulsed annealing and combinations of pulsed annealing with annealing in a furnace confirm what we have said. In addition, the simulation data correlate with such well-known facts as the dominant role of nucleus formation over growth for highly supercooled solid solutions[15] or the need to reach certain temperatures and saturation levels of impurity in order to form nano-sized phase inclusions.[14,16] We also argue that the results of our work are immediately relevant to the problem of uniform nucleus formation as a supersaturated solid solution decays. It is normally assumed that nuclei that form uniformly out of fluctuations correspond to the smallest phase volumes that can grow by attaching excess atoms from the surrounding medium.[17–19] The experimental data show that the phase inclusions interfere with the non-phase inclusions, depending on saturation and heating regime, which in turn affects the specific behavior and further growth of the phase precipitates.

CONCLUSIONS

Our simulation results show that when the concentration of excess Si in SiO_2 reaches values on the order of $10^{21}\,\mathrm{cm}^{-3}$, cluster formation is abruptly enhanced. When implantation doses of Si ions in real experiments reach this

level of doping, they give rise to an intense band of blue luminescence which is attributable to the formation of Si–Si bonds in SiO_2 (oxygen vacancies). At doping levels used to create light-emitting silicon nanostructures (<20 at.%), small clusters are predicted to predominate over large clusters numerically, even when Si atoms contained in SiO_2 are included in the simulation. Despite this fact, incorporating Si atoms from the host does lead to enlargement of the precipitates. Heating increases the size of the clusters even more, which can be understood in terms of the increase in the interaction radii of Si atoms proportional to $\sqrt{\mathscr{D}t}$. Although we have included temperature effects through diffusion constants, the creation of new bonds actually takes place because of isolated atomic displacements rather than due to random walks. The system's tendency to minimize its energy forces compactification of branching clusters into dense precipitates with well-defined phase boundaries. This process, which was simulated using the same diffusion characteristics of Si in SiO_2, is manifestly temperature-dependent in the interval 600–900 °C. In experiments, quenching of the luminescence is observed at these temperatures, which is interpreted as the conversion of non-phase inclusions of Si into precipitates of the amorphous phase that contain centers of nonradiative recombination, in particular, dangling bonds. The time it takes to compactify a cluster increases as its size increases and its density decreases; for large and loose clusters the probability of breakup into several parts increases. Since cluster growth is possible at smaller values of $\sqrt{\mathscr{D}t}$ than compactification, the use of pulsed and combination annealings allows us in principle to control the precipitates. The fact that both calculated temperature dependences can be made to agree with experiment using only the single parameter $\sqrt{\mathscr{D}t}$ indicates that cluster growth and compactification are determined (as in ordinary diffusion) by the mobility of Si atoms in SiO_2, i.e., the probability of their translation to a neighboring position per unit time. However, only compactification, which occurs at higher temperatures, is intrinsically diffusive in character.

We wish to thank Professor L. S. Smirnov for a useful discussion of this work.

[1] H. A. Atwater, K. V. Shcheglov, S. S. Wong, K. J. Vahala, R. S. Flagan, M. I. Brongersma, and A. Polman, Mater. Res. Soc. Symp. Proc. **321**, 363 (1994).

[2] T. Shimizu-Iwayama, S. Nakao, and K. Saitoh, Appl. Phys. Lett. **65**, 1814 (1994).

[3] P. Mutti, G. Ghislotti, S. Bertoni, J. Bonoldi, G. F. Cerofolini, J. Meda, E. Grilli, and M. Guzzi, Appl. Phys. Lett. **66**, 851 (1995).

[4] T. Shimizu-Iwayama, Y. Terao, A. Kamiya, M. Takeda, S. Nakao, and K. Saitoh, Nucl. Instrum. Methods Phys. Res. B **112**, 214 (1996).

[5] G. A. Kachurin, I. E. Tyschenko, K. S. Zhuravlev, N. A. Pazdnikov, V. A. Volodin, A. K. Gutakovsky, A. F. Leier, W. Skorupa, and R. A. Yankov, Nucl. Instrum. Methods Phys. Res. B **112**, 571 (1997).

[6] G. A. Kachurin, K. S. Zhuravlev, N. A. Pazdnikov, A. F. Leier, I. E. Tyschenko, V. A. Volodin, W. Skorupa, and R. A. Yankov, Nucl. Instrum. Methods Phys. Res. B **127/128**, 583 (1997).

[7] W. Skorupa, R. A. Yankov, I. E. Tyschenko, H. Frob, T. Bohme, and K. Leo, Appl. Phys. Lett. **68**, 2410 (1996).

[8] W. Skorupa, R. A. Yankov, L. Rebohle, H. Frob, T. Bohme, K. Leo, I. E. Tyschenko, and G. A. Kachurin, Nucl. Instrum. Methods Phys. Res. B **119**, 106 (1996).

[9] G. A. Kachurin, I. E. Tyschenko, W. Skorupa, R. A. Yankov, K. S. Zhuravlev, N. A. Pazdnikov, V. A. Volodin, A. K. Gutakovskiĭ, and A. F. Leĭer, Fiz. Tekh. Poluprovodn. **31**, 730 (1997) [Semiconductors **31**, 626 (1997)].

[10] I. E. Tyschenko, G. A. Kachurin, K. S. Zhuravlev, N. A. Pazdnikov, V. A. Volodin, A. K. Gutakovsky, A. F. Leier, H. Frob, K. Leo, T. Bohme, L. Rebohle, R. A. Yankov, and W. Skorupa, Mater. Res. Soc. Symp. Proceedings **438**, 453 (1997).

[11] G. Ghislotti, B. Nielsen, P. Asoka-Kumar, K. G. Lynn, A. Gumbhir, L. F. Di Mauro, and C. E. Bottani, J. Appl. Phys. **79**, 8660 (1996).

[12] L.-S. Liao, X.-M. Bao, N.-S. Li, X.-Q. Zheng, and N.-B. Min, J. Lumin. **68**, 199 (1996).

[13] G. A. Kachurin, L. Rebohle, I. Skorupa, R. A. Yankov, I. E. Tyschenko, H. Frob, T. Bohme, and L. Leo, Fiz. Tekh. Poluprovodn. **32**, 439 (1998) [Semiconductors **32**, 395 (1998)].

[14] L. A. Nesbit, Appl. Phys. Lett. **46**, 38 (1985).

[15] J. Maeda, Phys. Rev. B **51**, 1658 (1995).

[16] A. Hartstein, J. C. Tsang, D. J. Di Maria, and D. W. Dong, Appl. Phys. Lett. **36**, 836 (1980).

[17] F. S. Ham, J. Appl. Phys. **30**, 1518 (1959).

[18] I. M. Lifshits and V. V. Slezov, Zh. Éksp. Teor. Fiz. **35**, 479 (1958) [Sov. Phys. JETP **8**, 331 (1958)].

[19] A. B. Pevtsov, V. Ju. Davydov, N. A. Feoktistov, and V. G. Karpov, Phys. Rev. B **52**, 955 (1995).

Translated by Frank J. Crowne

ELECTRONIC AND OPTICAL PROPERTIES OF SEMICONDUCTORS

Optical spectra and electronic structure of indium nitride

V. V. Sobolev and M. A. Zlobina

Udmurt State University, 426034 Izhevsk, Russia

(Submitted March 16, 1998; accepted for publication September 29, 1998)
Fiz. Tekh. Poluprovodn. **33**, 395–401 (April 1999)

A complete set of fundamental optical functions is calculated for hexagonal indium nitride (w-InN) in the energy range 0–130 eV based on knowledge of the reflection spectrum. The integrated spectrum of the dielectric permittivity is resolved into elementary components. Three fundamental parameters are determined for each component (the maximum energy, the width, and the oscillator strength). A possible origin of these components of the dielectric constant is proposed on the basis of known theoretical calculations of the indium nitride band structure. © *1999 American Institute of Physics.* [S1063-7826(99)00304-X]

INTRODUCTION

Indium nitride usually crystallizes as a hexagonal wurtzite lattice (w-InN).[1,2] Thin films are obtained by cathode sputtering or microwave gas-phase epitaxy from metallorganic compounds on various substrates (substrates of hexagonal sapphire Al_2O_3 give the best results known to date).

The long-wavelength absorption edge of InN has been discussed in many papers.[1–7] As a rule, samples of InN contain a high concentration of free carriers (up to $10^{20}\,\mathrm{cm}^{-3}$ or higher) and every possible lattice defect. This prevents us from studying free excitons and the fine structure of the threefold-degenerate top of the valence band, as is done in GaN.[1] Analysis of the data in these papers gives a width of the band gap corresponding to direct allowed transitions in the range $E_g=1.7$–2.0 eV. Refractive indices of strongly doped polycrystalline films measured over the band of photon energies where they are transparent are found to vary from 2.90 at a photon energy $E=1.4$ eV down to 1.63 at $E=0.78$ eV (Ref. 4).

Both pure InN and its solid solutions with GaN and AlN are promising materials for making optoelectronic and solar-cell elements. Before their device parameters can be quantitatively determined, however, it is necessary to know their absorption spectra, i.e., their dielectric permittivities in the region of intrinsic absorption. InN is also theoretically interesting as a model semiconducting elemental nitride crystal.

Although the electronic structure of w-InN has been investigated theoretically in many papers,[1] there is little experimental data available.[1,2] Maxima are observed in the reflection spectra of InN films[8] at 5.0, 5.5, 5.8, 7.3, and 8.8 eV. Sullivan *et al.*[6] studied the dielectric permittivity spectrum in the range 2.5–5.5 eV. It consists of a single band with a maximum at 5 eV. There is therefore an urgent need for experimental and theoretical studies of the optical spectra and electronic structure of w-InN over a wide range of energies for fundamental absorption. Such a study became possible after publication[9,10] of the reflection spectrum of single-crystal films of w-InN in the energy range $E=2$–130 eV.

The problem of identifying the electronic structure of a solid in a wide range of fundamental absorption energies can be addressed in three stages. First, the spectrum of at least one optical function must be measured; secondly, this spectrum must be used to calculate optical spectra for all the remaining functions. Finally, the structures of at least some of these functions must be identified and compared with known theoretical data on energy levels and transition spectra. As a rule, all three of these stages reduce to discussing theoretical results based on only a single reflection spectrum.

It is well known that the best way to obtain extensive amounts of revealing information about the parameters and distinctive features of a material's electronic structure is to derive a complete set of spectra of the fundamental optical functions in the energy range for intrinsic absorption. These functions are: the reflection coefficient (R); the absorption coefficient (μ); the refraction index (n) and absorption index (k); the real (ε_1) and imaginary (ε_2) parts of the dielectric permittivity (ε); the function $E^2\varepsilon_2$, which is proportional to the combined density of states in the approximation of a constant transition probability; the number of valence electrons $n_{\mathrm{eff}}(E)$ that participate in transitions up to a given energy E, in fractions of the total number of valence electrons per unit cell; the characteristic bulk ($-\mathrm{Im}\varepsilon^{-1}$) and surface [$-\mathrm{Im}(1+\varepsilon)^{-1}$] electron loss functions; and the electro-optic functions α and β used for quantitative analysis of modulated optical spectra, etc.[11]

Guo *et al.*[9,10] used the reflection spectrum, but did not calculate a full set of functions. Specifically, they did not resolve the spectrum of ε_2 into its components; instead, they gave a comparison with theory for only the six maxima of ε_2 in the range $E=4$–12 eV based on one of many theoretical papers. Their calculated values for the refractive index n turned out to be smaller than unity for energies $E>10$ eV; moreover, the calculated value of ε_2 at 2 eV reported in Ref. 9 is ~ 2 instead of zero, i.e., it is greatly overestimated. These physically meaningless results are probably an indica-

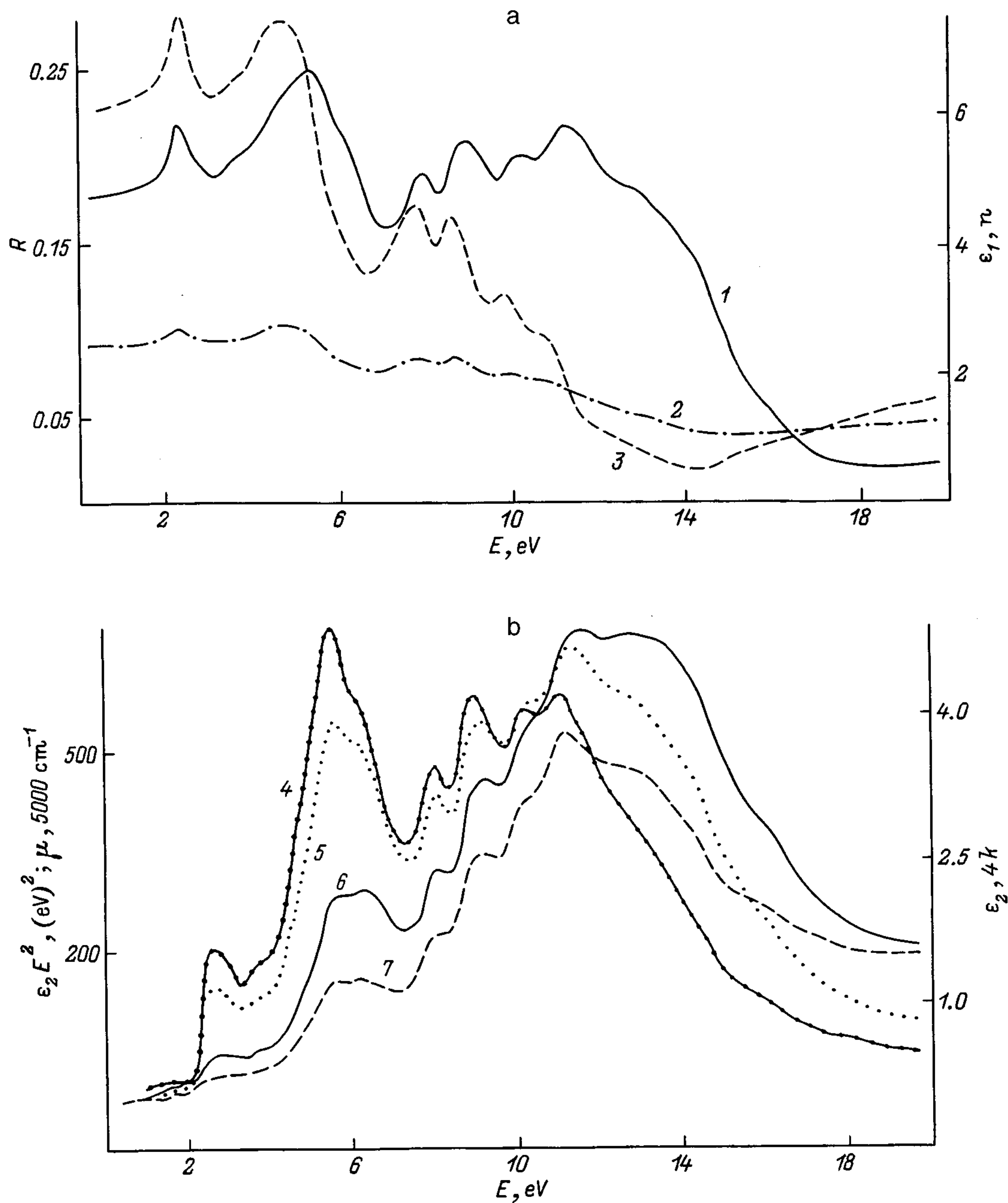

FIG. 1. Experimental reflection spectrum R of indium nitride based on data from Ref. 9 (a,1) and computed spectra. a: 2 — n, 3 — ε_1; b: 4 — ε_2, 5 — k, 6 — μ, 7 — $E^2\varepsilon_2$; c: 8 — n_{eff}, 9 — $[-\text{Im}\,\varepsilon^{-1}]$, 10 — $[-\text{Im}\,(\varepsilon+1)^{-1}]$; d: 11 — α, 12 — β.

tion that the calculations of the authors are insufficiently accurate. This deficiency will in turn make the calculations of the other optical functions erroneous as well.

The goal of this report is to derive a full set of optical functions for w-InN in the range $E=2$–130 eV, to resolve the overall spectra of ε_2 and ε_1 into components, to determine three parameters for each component, and to compare the results obtained with the data from theoretical calculations of the bands and ε_2 (Figs. 1 and 2, and Table I).

METHOD OF CALCULATIONS

The method we used to derive the set of optical functions and resolve the total dielectric permittivity curve into elementary components has been used many times and described in detail in Ref. 11. Let us briefly consider its fundamental features. Usually the input data to such calculations are known experimental reflection spectra in a wide range of intrinsic absorption energies from E_g up to 10 or 100 eV, as well as in the transparent range. The missing portion of the spectrum at high energies is traditionally modeled by adding terms like E^{-p}, where p is a fitting parameter between 2 and 4. As a rule, $R \ll 0.1$ in the energy range $E > 10$ eV, which is also true for our case, i.e., InN. Therefore, the method used to extrapolate the reflection coefficient to spectral region where it does not change will to high accuracy have no effect on the computed values of the other functions. The integrated Kramers-Kronig relations with respect to the reflection spectrum are then used to compute the phase of the

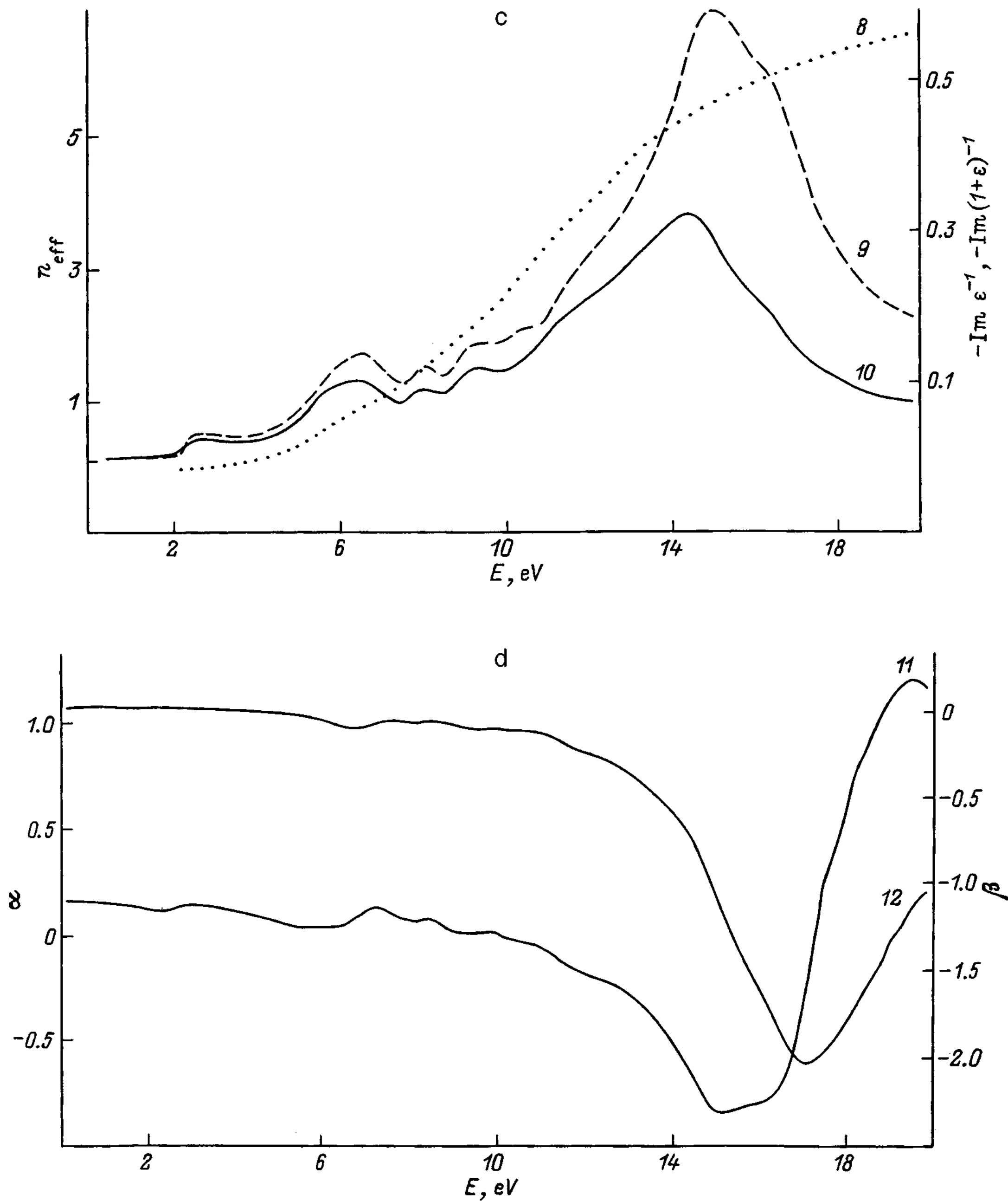

(Continuation of Fig. 1)

reflected wave. All the remaining optical functions except for n_{eff} and the effective dielectric permittivity $\varepsilon_{\mathrm{eff}}$ (see Ref. 11) can easily be determined from simple analytic expressions; and n_{eff} and $\varepsilon_{\mathrm{eff}}$ can be determined from simple integrals over the functions $E\varepsilon_2$ and $E^{-1}\varepsilon_2$.

The experimental reflection curve and other optical functions calculated from it are the result of summing over contributions from all transitions from occupied states to free states over the entire volume of the Brillouin zone. Because of the large half-width of the transition bands and their strong overlap, some of these bands do not give rise to maxima in the integrated spectrum of R or ε_2; moreover, the energy positions of maxima of the total spectra of R or ε_2 can differ significantly from the true energies at which the individual transition bands have peaks. Very often the total spectra of R or ε_2 are modeled as N symmetric Lorentzian oscillators with a large number of fitting parameters (from 12 for $N=4$ to 30(!) for $N=10$ or higher). This model requires three parameters for each oscillator: the energy of the maximum E_i, its half-width H_i, and the oscillator strength f_i.

In this paper we use the method of combined Argand diagrams, which is based on the idea that for a symmetric Lorentzian oscillator the function $\varepsilon_2=f(\varepsilon_1)$ has the form of an almost perfect circle, whose center coordinates and radius directly determine the three oscillator parameters (E_i, H_i, f_i). We first construct an overall Argand diagram based on the total spectra of ε_2 and ε_1 of the crystal. Analysis of this diagram allows us to unambiguously resolve the total spectrum of ε_2 into its elementary components without any fitting parameters, and to determine its parameters.

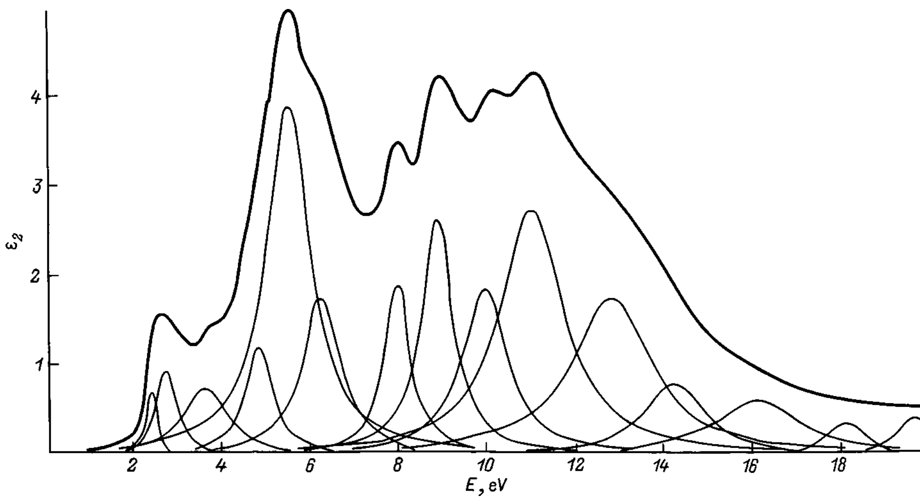

FIG. 2. Integrated spectrum of ε_2 for w-InN (upper curve) and its resolution into components.

DISCUSSION OF RESULTS

The experimental spectrum of w-InN given in Ref. 9 in the range E=2–20 eV contains maxima at ~2.3, 5.3, 7.95, 8.90, 10.25, 11.2 eV (Fig. 1a). All of these maxima are located in a region of intense intrinsic absorption. The reflection coefficient in the energy range $E>$ 15 eV is very small: ~ 0.02 and 0.002, respectively, at 20 and 100 eV (Ref. 10). We will therefore discuss our results only in the range 2–20 eV.

The resolved maxima in the spectra of n and ε_2 are almost the same (Fig. 1a). With increasing energy, these spectra shift toward lower energies relative to such reflection maxima; this shift increases from zero at E=2.3 eV to 0.3–0.5 eV at subsequent maxima. The refractive index is a maximum (n=2.78) at 4.80 eV, and is greater than unity over the entire energy range. The real part of the dielectric permittivity ε_1 attains its largest values of 7.56 and 7.42 at 2.30 and 4.45 eV, respectively, and is positive in the entire region, i.e., $n>k$ in the range E=2–20 eV.

The spectra of four other functions (ε_2, k, μ, and $E^2\varepsilon_2$) are similar in the entire wide range of energies E=2–20 eV (Fig. 1b). Their largest values are as follows: ε_2=4.93 (at 5.55 eV), k=0.99 (at 5.65 eV), $\mu=1.14\times10^6$ cm^{-1} (at 11.60 eV), and $E^2\varepsilon_2$= 528.7 (eV)^2 (at 11.2 eV). The shift of

TABLE I. Parameters E_i, H_i, f_i, and $S_i/S_{\max}$ of InN oscillators (O_i), and the nature and energy (in eV) of components of ε_2 based on theory from Refs. 12 and 14–16.

O_i	Our data				12	14	15	16
	E_i, eV	H_i, eV	f_i	$S_i/S_{\max}$	EPP	MPP	OLCAO	SETB
O_1	2.46	0.2	0.59	0.04	···	···	···	···
O_2	2.79	0.5	0.90	0.10	···	···	···	···
O_3	3.7	1.1	0.75	0.17	Δ 4	Δ 3.4	···	Γ*A* 4.4
O_4	4.85	0.7	0.39	0.18	···	Σ 4.8, Δ 4.4	···	···
O_5	5.55	1.2	1.27	1.0	Σ 5.5	*M* 5.2	*LA* 5.6	···
O_6	6.3	1.0	0.33	0.37	···	Σ 6.4, *M* 5.8	Σ 6.2	Σ 6.7
O_7	7.0	0.9	0.13	0.17	*M* 7.2	Σ 7.2	Σ 7.0	Σ 6.7
O_8	7.5	0.7	0.07	0.09	Σ 7.6	Σ 7.4, 7.8	Σ 7.7	*L* 7.3
O_9	8.0	0.7	0.19	0.28	Γ 7.9, *K* 8.1	*M* 8	Σ 8.3, 8.0	Σ 8.3, Γ*A* 8.3
O_{10}	8.9	0.85	0.27	0.48	Δ 9	Σ 8.8	*LA* 8.6, 9.0	Σ 9.2, Γ 9
O_{11}	9.3	0.5	0.04	0.08	*K* 8.6	Σ 9.2, 9.5, 9.6	Σ 9.3	Σ 9.2, Γ 9
O_{12}	10.0	1.2	0.22	0.48	*M* 8.6	Σ 10.2	Σ 10.1	*L* 11
O_{13}	11.1	1.7	0.40	0.99	*K*, *M* 11.3	Σ 10.6, 10.8	Σ 10.7, 11.1 *LA* 10.7	*L* 11
O_{14}	11.8	1.4	0.08	0.22	*M* 11.7 Γ 11.7, Δ 12	*M* 11.6, 12 Σ 12, 12.2	Σ 11.5 *LA*,12	Σ 12
O_{15}	12.85	2.1	0.27	0.78	Σ 14.5	Σ 14	Σ 13, 12.8	Γ 14
O_{16}	14.25	1.6	0.09	0.27	···	···	Σ 14, 14.6 *LA* 14	···
O_{17}	16.15	2.2	0.09	0.29	Σ 16.2 *H* 16.7	 ···	*LA* 15.6, 16 Σ 16.5	 ···
O_{18}	18.15	0.9	0.02	0.07	*H* 17.5	···	Σ 17.5	···
O_{19}	19.65	0.87	0.03	0.08	···	···	Σ 20.5 *LA* 21, 19	···

Note: EPP—method of empirical pseudopotentials; MPP—method of model pseudopotentials; OLCAO—method of orthogonalized linear combination of atomic orbitals in the local-density approximation; and SETB—semi-empirical tight-binding method.

the maxima of μ and k relative to the maxima of ε_2 at high energies increases rapidly with decreasing wavelength. The position of many maxima of the spectra of R and ε_2 are almost the same.

The spectra of characteristic bulk and surface losses for electrons are also similar (Fig. 1c). Their maxima are shifted toward high energies relative to maxima of ε_2 by ~0.1–0.4 eV. This shift determines the energy of longitudinal-transverse splitting of the transitions.

With decreasing wavelength, the effective number of valence electrons participating in the transitions increases, first slowly (for $E<5$ eV), and then very rapidly and almost linearly with increasing energy in the region $E=8-14$ eV. After $E\approx 14$ eV we observe a transition to saturation with $n_{\text{eff}}\approx$ 6.5 (at $E=20$ eV). The maxima of the two most intense and broadest bands of the excitation spectra (bulk and surface plasmons) of *w*-InN are located at 15.05 and 14.45 eV and, accordingly, the effective number of valence electrons n_{eff} increases within the half-width of the band of bulk plasmons from 4.5 to 6.25. Since a single formula unit of InN contributes five valence electrons, the increased value of n_{eff} in the band of bulk plasmons shows that electrons from deeper levels participate to a considerable degree in the excitation of bulk plasmons, in addition to the five uppermost valence electrons.

The electro-optic function β is negative in the range $E=0-19$ eV, while the function $\alpha>0$ in the intervals $E=0-10$ eV and 17.5–20 eV (Fig. 1d). In the range $E=0-4$ eV we have $|\beta|\ll\alpha$; i.e., in this region—where modulation spectra are currently most often encountered—we can disregard the contribution from changes in the imaginary part of the dielectric permittivity.

In the energy range $E=60-130$ eV the measured reflection is very weak: $R\leqslant 0.003$ (Ref. 10). The computed values of other functions lie in the following ranges: $\varepsilon_1=1.15-1.24$, $n=1.08-1.11$, $\varepsilon_2=0.04-0.1$, and $k=0.02-0.05$. The number of valence electrons n_{eff} increases with increasing energy linearly from 10 at 60 eV to 14 at 113 eV, and then undergoes a rather small jump to 15.7 at 128 eV.

Thus, we have obtained a complete set of optical functions for *w*–InN in the range $E=0-130$ eV. Comparison of our results with data from calculations of n, k, ε_2, given in Refs. 9 and 10, reveals errors in these papers: a physically meaningless values $n<1$ in the range $E=10-50$ eV, overestimation of μ, ε_2, k in the range $E=2-4$ eV, overestimation of μ in the range $E=8-13$ eV, etc.

Of all the optical functions, theoretical calculations are available only for ε_2 (in relative units) in the range $E=1.15-16$ eV (Ref. 12). This spectrum of ε_2 contains maxima in the neighborhood of the maxima of our spectra; i.e., it would seem that the theoretical data for ε_2 is in good agreement with our results. However, the theoretical spectrum differs from our experimental-calculated spectrum of ε_2 by the absence of a very long-wavelength maximum and an expected strong decrease in intensity of ε_2 with increasing energy. The latter effect is characteristic of theoretical calculations of ε_2 and R for many crystals. The nature of this discrepancy has yet to be been explained.[11]

Using the method of Argand diagrams,[11,13] we resolved the total ε_2 curve for *w*-InN into components in the range $E=2-130$ eV (in Fig. 2 and in Table I we show only results for the range $E=2-20$ eV). Often the oscillator strength f_i is averaged with respect to the total number of valence electrons. In this case f_i is proportional to the area of the band S_i in the spectrum $\varepsilon_2(E)$. However, in the presence of $n_{\text{eff}}(E)$ it is more correct to take $n_{\text{eff}}(E)$ into account in computing f_i. Both methods of calculating the band intensities are represented in Table I by values of f_i and S_i/S_{max}. In resolving the spectrum of the dielectric permittivity, in addition to the six bands that coincide with maxima of the overall curve ε_2 we identified another twelve bands which are not observed structurally in the total spectra of the optical functions. The distribution of bands with respect to intensity can be analyzed using the standard method: according to their area S_i.

Our model for resolving the total spectrum of ε_2 into components is the widely used theoretical representation of the dielectric permittivity as a sum of contributions from symmetric Lorentzian oscillators. The set we used for *w*-InN was the smallest possible. Each component sums up transitions that are close in energy, but not necessarily of similar nature.

Of all the optical functions, we obtain only the reflection spectrum experimentally over the wide range of energies for intrinsic absorption. The energies at which it peaks are used to determined several of the fitting parameters of the theory. Accordingly, we introduce errors into the theoretical calculations, and sometimes very large ones, since the transition energies correspond to maxima of ε_2 (or μ,k), but not maxima of R. It is important to note that theoretical calculations of the bands and spectra of optical functions could not be verified with only the previously used reflection spectrum available. This clearly shows how much new and detailed information we gain by using a complete set of optical functions and by resolving the total spectrum of ε_2 into its components, information that can be the basis for new theoretical calculations of the electronic structure and determination of parameters for phenomena in *w*-InN.

It is difficult to determine unambiguously what specific material property the components of the ε_2 spectrum represent. At this time, there is no theory of optical properties that can combine the direct-interband-gap model with the metastable- exciton model.[11] One widely used qualitative guideline says that the most intense interband, and accordingly excitonic, transitions must be observed betweeen pairs of bands—a valence band and a conduction band—that are parallel. Let us accordingly discuss the specific nature of components of ε_2 on the basis of one of the two models mentioned above. We must take into account corrections for the binding energy of metastable excitons, which can reach values of 0.5 eV or larger. Although the maxima in the spectrum of ε_2 can be explained much easier on the basis of an excitonic model than in the approximation of interband transitions, calculations for metastable excitons are unknown. Therefore, the nature of optical spectra is usually discussed in a band model.

In the range $E=30-130$ eV, reflection and absorption are very weak. In the total curves for R, ε_2, k, and μ, how-

ever, the maxima are barely noticeable at ~33.70 eV and ~120 eV. The resolved spectrum of ε_2 in this range contains more than twelve bands. Our data on the spectra of optical functions and their components and the parameters of the bands involved in transitions will be presented in more detail in another paper.

The band structure of *w*-InN has been calculated by various methods: empirical[12] and model-based[14] pseudopotentials, orthogonalized linear combinations of atomic orbitals in the local-density approximation,[15] and the semi-empirical tight-binding method.[16] We have searched for pairs of almost parallel bands based on data from these theoretical papers, viewing them as the most likely candidates for interband transitions. Their energies and natures are listed in Table I. In cases where there is no enumeration of the bands we give only points (Γ, L) or directions (Σ, M, LA) in the Brillouin zone. The theoretical results for energies and the specific nature of the transitions E_i which we have identified sometimes differ from one paper to another, and this is natural. Since the reflection spectrum of *w*-InN was unknown to theorists, the model we have adopted, using the energies of maxima in the reflection, could not be applied. Consequently, we cannot give preference to any one theoretical paper (see Refs. 12 and 14–16) at this time. Our identifications of the transition bands, which we list in Table I, constitute a first attempt to compare theory and experiment for the electronic structure of *w*-InN in the fundamental-absorption energy range.

CONCLUSIONS

We have derived the first complete set of fundamental optical functions for *w*-InN in the energy range $E=2-20$ eV, and have resolved the total spectrum of the dielectric permittivity into 19 transition bands without fitting parameters. We have also identified their nature on the basis of known band calculations, thereby providing a new data base for more precise calculations and understanding of the electronic structure of *w*-InN.

This work was supported by the Center for Fundamental Natural Science at St. Petersburg State University.

[1] V. V. Sobolev, *Optical Fundamental Spectra of Group A^3-B^5 Compounds* [in Russian], ShTIINTsA, Kishinev, 1979.

[2] S. Strite and H. Morcoç, J. Vac. Sci. Technol. B **10**, 1237 (1992).

[3] K. Osamura, K. Nakajima, Y. Murakami, P. H. Shingu, and A. Ohtsuki, Solid State Commun. **11**, 617 (1972).

[4] V. A. Tyagaĭ, A. M. Evstigneev, A. N. Krasiko, A. F. Andreev, and V. Ya. Malakhov, Fiz. Tekh. Poluprovodn. **11**, 2142 (1977) [Sov. Phys. Semicond. **11**, 1257 (1977)].

[5] T. L. Tansley and C. P. Foley, J. Appl. Phys. **59**, 3241 (1986).

[6] B. T. Sullivan, R. R. Parsons, K. L. Westra, and M. Y. Brett, J. Appl. Phys. **64**, 4144 (1988).

[7] D. W. Yenkins and Y. D. Dow, Phys. Rev. B **39**, 3317 (1989).

[8] V. V. Sobolev, S. G. Kroitoru, A. F. Andreeva, and V. Ya. Malakhov, Fiz. Tekh. Poluprovodn. **13**, 823 (1979) [Sov. Phys. Semicond. **13**, 485 (1979)].

[9] Q. Guo, O. Kato, M. Fujisawa, and A. Yoshida, Solid State Commun. **83**, 721 (1992).

[10] Q. Guo, H. Ogawa, and A. Yoshida, J. Electron Spectrosc. Relat. Phenom. **79**, 9 (1996).

[11] V. V. Sobolev and V. V. Nemoshkalenko, *Methods of Computational Physics in Solid State Theory. Electronic Structure of Semiconductors* [in Russian], Kiev, Naukova Dumka, 1988.

[12] C. P. Foley and T. L. Tansley, Phys. Rev. B **33**, 1430 (1986).

[13] V. V. Sobolev and V. Val. Sobolev, Fiz. Tverd. Tela (St. Petersburg) **36**, 2560 (1994) [Phys. Solid State **36**, 1393 (1994)].

[14] S. N. Grinyaev, V. Ya. Malakhov, and V. A. Chaldyshev, Izv. vuzov. Fizika **29**, 69 (1986).

[15] Y.-N. Xu and W. Y. Ching, Phys. Rev. B **48**, 4335 (1993).

[16] T. Yang, S. Nakajima, and Sh. Sakai, Jpn. J. Appl. Phys. **34**, 5912 (1995).

Translated by Frank J. Crowne

Electrostatic model of the energy gap between Hubbard bands for boron atoms in silicon

N. A. Poklonskiĭ and A. I. Syaglo

Belorussian State University, 220050 Minsk, Belarus
(Submitted June 5, 1998; accepted for publication August 25, 1998)
Fiz. Tekh. Poluprovodn. **33**, 402–404 (April 1999)

Electrostatics is used to model the narrowing of the energy gap ε_2 between Hubbard bands (the A^0- and A^+-bands) in a *p*-doped semiconductor with increasing acceptor concentration $N=N_0+N_{-1}+N_{+1}$ and with increasing degree of compensation K by donors for $N_{-1}\approx KN$. The screening of impurity ions by holes hopping from acceptor to acceptor is taken into account. It is shown that this effect leads to a shift of the A^0-band towards the valence band and the A^+-band towards the conduction band. The concentration of holes hopping in the A^+-band $N_{+1}N_0/N$ is determined by the energy of their thermal generation ε_2 from the A^0-band. The values of ε_2 calculated for Si:B are in agreement with experimental data. © *1999 American Institute of Physics.* [S1063-7826(99)00404-4]

1. It is known[1] that strongly doped, weakly compensated Si:B crystals support not only A^0-centers, i.e., boron atoms in charge states (-1) and (0), but also coexisting A^+-centers, i.e., boron atoms in charge state $(+1)$. Because states of holes bound to neutral acceptors have a statistical scatter in energy, they form the A^+-band (the upper Hubbard band), which is closer to the top of the valence band than the A^0-band (the lower Hubbard band).

In the model of Ref. 2 (see also Ref. 3), the authors solved the Schrödinger equation in order to find the splitting of symmetric and antisymmetric terms of a positively charged molecule consisting of two acceptors in charge states (0) and $(+1)$. It was shown that the exchange interaction for these molecules causes the activation energy ε_x for the transition of a hole from the A^+-band to the valence band to increase with increasing acceptor concentration N as the temperature $T\rightarrow 0$ K. According to Refs. 2 and 4, the energy gap ε_2 between Hubbard bands is

$$\varepsilon_2=I_a-I_d-4\pi a_0^3NV_0\left[1+\frac{16(4+\alpha)}{(2+\alpha)^3}\right]=I_a-\varepsilon_x, \quad (1)$$

where I_a and I_d are transition energies for a hole from an isolated neutral acceptor (a) and positively charged acceptor (d) to the valence band (the v-band); ε_x is the energy gap between the A^+- and v-bands, and $V_0=e^2/8\pi\varepsilon a_0$; $\varepsilon=\varepsilon_r\varepsilon_0$ is the static dielectric permittivity of the undoped crystal ($\varepsilon_r=11.47$ for Si; see Ref. 5); $a_0=\hbar/\sqrt{2mI_a}$ is the Bohr radius for localization of a hole at a neutral acceptor; $\alpha=a_0/a_{+1}$ is the ratio of a_0 to the localization length of a hole at a positively charged acceptor $a_{+1}=\hbar/\sqrt{2mI_d}$; and $m=0.153m_0$ is the effective mass of a light hole in Si.[1,6] For boron atoms in silicon we have $I_a\approx$ 44.4 meV (Ref. 7), $I_d\approx$ 2 meV (Ref. 1); and $\alpha=a_0/a_{+1}\approx 0.212$.

However, the shift of the A^0-band toward the v-band, which strongly affects the probability of thermal ejection of a hole from the A^0- to the A^+-band, was disregarded in Refs. 2 and 3. In addition, those authors did not determine the dependence of ε_x on temperature T and degree of compensation K of the acceptors by donors. (The experiments of Ref. 1 showed that ε_x increases with increasing K and T.)

In Ref. 8 the energy ε_x required to transport one of the two holes bound to a A^+-center to infinity was calculated with allowance for the screening of the Coulomb interaction between charges of the A^+-center by the degenerate gas of v-band holes. However, the conclusion of Ref. 8 that ε_x decreases with increasing hole concentration in the v-band has found no support in the experiments of Ref. 4, where ε_x was inferred from studies of the thermal ejection of holes from the A^+-band to the v-band for various values of N (see also Ref. 1).

In this study our goal was to describe the variation of ε_2 with increasing acceptor concentration and the degree of compensation for holes in the A^+- and A^0- bands that move by hopping transport and screen the impurity ions.

2. The equation of electrical neutrality for a semiconductor with A^+- and A^0-bands has the form

$$N_{+1}+KN=N_{-1}, \quad (2)$$

where $N=N_0+N_{+1}+N_{-1}$ is the total concentration of acceptors in charge states (0), $(+1)$, and (-1), respectively, and KN is the concentration of acceptors compensated by donors.

The concentration of neutral N_0, negatively charged N_{-1} acceptors, and positively charged N_{+1} acceptors averaged over the crystal, taking into account that their energy levels $E_d=E_{-1}-E_0$ and $E_a=E_0-E_{+1}$ are distributed with densities g_a and g_d, is[9,10]

$$N_t=N\int\int f_t g_a g_d dE_a dE_d, \quad (3)$$

where

$$f_t^{-1}=\sum_{s=-1}^{+1}\gamma_s\gamma_t^{-1}\exp[-[(s-t)E_F-E_t+E_s]/k_BT].$$

 © 1999 American Institute of Physics

Here f_t is the probability that an acceptor with energy E_t and number of quantum states γ_t is found in one of the three possible charge states $t=-1,0,+1$; $E_F>0$ is the Fermi level; and k_BT is the thermal energy. We choose to measure energies from the top of the v-band of undoped Si. If the excited states of holes localized at a boron atom are ignored, we have:[1,10] $\gamma_a=\gamma_0/\gamma_{-1}=4$, $\gamma_d=\gamma_0/\gamma_{+1}=1/4$.

The transition of an acceptor from a neutral (0) to a negatively charged (-1) state with thermal emission of a hole from the A^0- to the v-band is accompanied by absorption of an energy $E_a=E_{-1}-E_0>0$. The transition of an acceptor from a positively charged $(+1)$ state to a neutral (0) state is accompanied by absorption of an energy $E_d=E_0-E_{+1}$ (emission of a hole from the A^+-band to the v-band). When two neutral acceptors ''decay'' into negatively and positively charged ions, an energy $E_a-E_d=E_{-1}+E_{+1}-2E_0$ is absorbed.

Let us assume that the acceptor levels E_a and E_d are normally distributed with densities centered around $\overline{E_a}$ and $\overline{E_d}$, corresponding to the centers of the A^0- and A^+-bands:[9]

$$g_{a(d)}=\frac{1}{\sqrt{2\pi}W_{a(d)}}\exp\left[-\frac{1}{2}\left(\frac{E_{a(d)}-\overline{E_{a(d)}}}{W_{a(d)}}\right)^2\right]. \tag{4}$$

If we postulate a pure Coulomb interaction between neighboring ions, $W_{a(d)}$ is given by the expression[11]

$$W_a=W_d=W\approx 1.64\frac{e^2}{4\pi\varepsilon}\left(\frac{8\pi}{3}N_{-1}\right)^{1/3}. \tag{5}$$

The total concentration of ionized impurities is $N_{-1}+N_{+1}+KN=2N_{-1}$.

As the authors of Refs. 11 and 12 showed, screening of ions by holes hopping from motionless acceptor to motionless acceptor causes the level $\overline{E_a}$ to shift toward the v-band and the level $\overline{E_d}$ to shift away from the v-band. These shifts of the A^0- and A^+-bands in opposite directions are explained by the decrease in the energies E_{-1} and E_{+1} of the negative and positive acceptor charge states due to their screening by holes hopping from acceptor to acceptor:[12]

$$\overline{E_a}=I_a-\frac{3e^2}{16\pi\varepsilon(\lambda+l)},\quad \overline{E_d}=I_d+\frac{3e^2}{16\pi\varepsilon(\lambda+l)}, \tag{6}$$

where $I_a=I_{-1}-I_0$; $I_d=I_0-I_{+1}$; $l=0.554[(1+K)N]^{-1/3}$ is the average distance between the closest impurity atoms; and λ is the screening length for the electrostatic field:[9]

$$\lambda^{-2}=\frac{e^2N}{2\varepsilon k_BT}\sum_{t=-1}^{+1}\sum_{s=-1}^{+1}(t-s)^2\int\int f_tf_sg_ag_d\,dE_a\,dE_d. \tag{7}$$

Note that if we take Eqs. (7) and (5) into account, Eq. (6) implies that the transition energy of a hole from the A^+-band to the v-band ($\overline{E_d}$) increases with increasing N, in agreement with the experimental data reported in Ref. 1.

3. According to Ref. 13, the electrical conductivity due to hopping of holes from acceptor to acceptor is made up of the electrical conductivity of the A^0-band $\sigma_{h1}=eN_{h1}M_{0,-1}$ and the electrical conductivity of the A^+-band $\sigma_{h2}=eN_{h2}M_{+1,0}$, where $N_{h1}=N_0N_{-1}/N$ is the concentration and $M_{0,-1}$ is the mobility of holes that hop in the A^0-band, while $N_{h2}=N_{+1}N_0/N$ is the concentration and $M_{+1,0}$ is the mobility of holes that hop in the A^+-band. The concentrations of holes hopping in the A^0- and A^+- bands for $N_{+1}=N_{-1}\gg KN$ has a maximum value $N_{h1}=N_{h2}=N/8$.

According to the estimates of Refs. 1, 4, 14, and 15, the hopping mobility of holes in the A^+-band ($M_{+1,0}$) is much larger than in the A^0-band ($M_{0,-1}$). Consequently, for the ranges of temperatures, compensation degrees, and acceptor concentrations where $\sigma_{h2}\gg\sigma_{h1}$, the temperature dependence of the hopping conductivity is[13]

$$\sigma_{h1}+\sigma_{h2}\approx\sigma_{h2}\propto\exp\left(-\frac{\varepsilon_2}{k_BT}\right), \tag{8}$$

where ε_2 is the energy of thermal generation of holes from A^0- to A^+-bands.

The temperature dependence of σ_{h2} is determined by the change in the concentration of holes $N_{h2}=N_{+1}N_0/N$ that hop in the A^+-band, while the dependence of $M_{+1,0}$ on T gives the activation energy for transport of a hole in the A^+-band, whose value is smaller or at most equal to W. For $\varepsilon_2\gg W$ we then have the following expression from Eq. (8):

$$\varepsilon_2=-k_B\frac{d\ln\sigma_{h2}}{d(1/T)}\approx-k_B\frac{d\ln N_{h2}}{d(1/T)}=-k_B\left[N_0^{-1}\frac{dN_0}{d(1/T)}+N_{+1}^{-1}\frac{dN_{+1}}{d(1/T)}\right], \tag{9}$$

where the derivatives with respect to temperature are determined from the equation of electrical neutrality (2) with allowance for Eq. (3); the dependence of W and λ on T can be ignored.

For $N_{+1}\ll N_{-1}\approx KN\ll N$, in accordance with Eq. (7), the primary contribution to the screening comes from the holes of the A^0-band, because $N_{h1}\gg N_{h2}$. For $k_BT\gg W$, using Eqs. (2)–(7), from Eq. (9) we can then write for ε_2

$$\varepsilon_2\approx I_a-I_d-\frac{3e^2}{8\pi\varepsilon(\lambda+l)}-2\frac{W^2}{k_BT}. \tag{10}$$

As the concentration of acceptors N increases, the conditions for applicability of Eq. (10) at low temperatures and low degrees of compensation are satisfied as long as the Fermi level is closer to the A^0- than to the A^+-band, i.e., $E_F>(\overline{E_d}+\overline{E_a})/2$. As the occupation of the A^+-band by holes increases, the condition $N_{+1}\ll N_{-1}\approx KN$ is violated, and the A^+- and A^0-bands rapidly broaden and shift apart from one another. For $\overline{E_d}-\overline{E_a}\approx W$ the activated character of the hopping conductivity arises not only from the temperature dependence of the occupation of the A^+-band by holes from the A^0-band, but is also determined by the activation energies for transport of holes from acceptor to acceptor in the A^+- and A^0-bands. Therefore, when $N_{+1}\gg KN$, Eqs. (9) and (10) for ε_2 cannot be used.

4. Figure 1 shows activation energies ε_2 for hopping electrical conductivity stimulated by thermal ejection of holes from the A^0-band to the A^+-band for the example of Si : B as a function of boron concentration; these are experimental data[13,14] and calculations based on Eq. (9) and on the

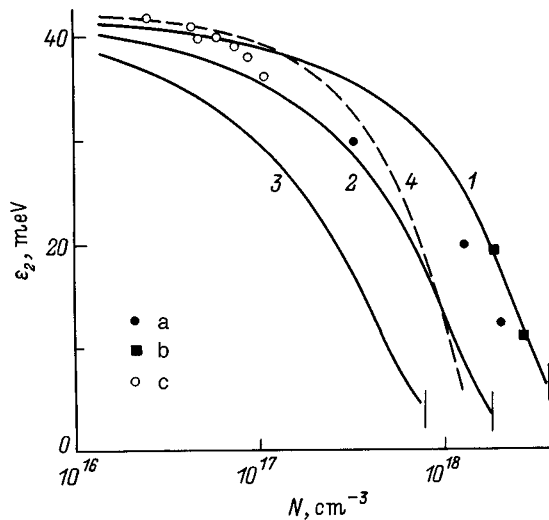

FIG. 1. Dependence of the thermal activation energy for transitions of holes from the A^0- to the A^+-band on the concentration of boron atoms in Si. Calculations using Eq. (9) at $T=$ 20 K for the following degrees of compensation K: *1* — 3×10^{-4}, *2* — 10^{-3}, *3* — 3×10^{-3}; *4* — calculation (see Ref. 2) based on Eq. (1). Experimental values: a—results of Ref. 14, b—data from Ref. 15, c—calculated using the expression $\varepsilon_2=I_a+I_d-\varepsilon_x$ and data for ε_x from Ref. 4.

model of Ref. 2. In the calculations we assume $T=20$ K, because in the neighborhood of this temperature thermally activated conductivity is observed in the A^+-band.[14] For these calculations three values of compensation were chosen ($K=3\times10^{-4}$, 10^{-3}, and 3×10^{-3}), which are close to experimental data.[14,15] For large N the value of K is smaller. It is clear that in accordance with experiment[1,4] the energy ε_2 decreases with increasing compensation. The calculated curves 1–3 at T = 20 K are bounded by the same values of N as long as $N_{+1}\ll N_{-1}\approx KN$; the limiting values of N are denoted by vertical lines. According to the data of Refs. 14 and 16,* the activation energy for hopping conductivity in the A^0-band of Si : B $\varepsilon_2\approx$ 5 meV for $N\approx10^{17}-10^{18}\,\text{cm}^{-3}$, $K<10^{-2}$, and $T<10\,$K.

In Ref. 4 the activation energy ε_x for electrical conductivity in the v-band was measured by photoexciting holes from the A^0-band to the A^+-band, which were subsequently emitted thermally into the v-band. These experiments were done at acceptor concentrations $N<10^{17}\,\text{cm}^{-3}$, at which there is no hopping conductivity from acceptor to acceptor in the A^+-band without illumination. In this case the activation energy ε_x corresponds to the average energy $\overline{E_d}$ for a hole to go from the A^+-band to the v-band (see Ref. 12). In order to compare ε_x from Ref. 4 with our calculations of ε_2, we must take into account that at low acceptor concentrations $\varepsilon_2\approx\overline{E_a}-\overline{E_d}$ and $\varepsilon_x\approx\overline{E_d}$. From Eq. (6) it follows that in this case the value of $\overline{E_d}$ increases with increasing N by as much as the quantity $\overline{E_a}$ decreases (i.e., $\overline{E_d}-I_d=I_a-\overline{E_a}$). Then the energy for thermal activation of the transition of a hole from A^0- to A^+-band is $\varepsilon_2\approx I_a+I_d-2\varepsilon_x$. In Fig. 1 we plot values of ε_2 versus N, based on data for ε_x taken from Ref. 4 (open circles).

5. In summary, we have derived an electrostatic model for the narrowing of the energy gap ε_2 between Hubbard bands in a p-type doped semiconductor with increasing acceptor concentration $N=N_0+N_{-1}+N_{+1}$ and degree of compensation K by donors when $N_{-1}=N_{+1}+KN\approx KN$, and applied it to the case of boron atoms in Si. In this model we take into account screening of the impurity ions by holes that hop from acceptor to acceptor in the A^0- and A^+-bands. We start by writing the hopping conductivity in the A^+-band as the concentration of hopping holes $N_{+1}N_0/N$ times the hole mobility and charge, and eventually obtain an expression for ε_2. For the example of Si : B we have shown that the computed values of ε_2 agree with experimental data.[4,14,15] Note that our electrostatic model for calculating ε_2 agrees qualitatively with the model of Refs. 2 and 3, but does not support the conclusion of Ref. 8 regarding the shift of the A^+-band toward the v-band with increasing acceptor concentration.

*Ref. 16 is cited in the Russian original, but is not listed in reference section.

1. E. M. Gershenzon, A. P. Mel'nikov, R. I. Rabinovich, and N. A. Serebryakova, Usp. Fiz. Nauk **132**, 353 (1980) [Sov. Phys. Usp. **132**, 153 (1980)].
2. H. Nushimura, Phys. Rev. **138**, A815 (1965).
3. L. P. Ginzburg, Fiz. Tekh. Poluprovodn. **12**, 564 (1978) [Sov. Phys. Semicond. **12**, 326 (1978)].
4. E. M. Gershenzon, F. M. Ismagilova, and L. B. Litvak-Gorskaya, Fiz. Tekh. Poluprovodn. **28**, 671 (1994) [Semiconductors **28**, 401 (1994)].
5. J. Bethin, T. G. Castner, and N. K. Lee, Solid State Commun. **14**, 1321 (1974).
6. *Semiconductors: Group IV Elements and III–V Compounds*, edited by O. Madelung (Springer-Verlag, Berlin–Heidelberg, 1991), p. 164.
7. T. M. Lifshits, Instrum. Exp. Tech., No. 1 10 (1993).
8. D. E. Phelps and K. K. Bajaj, Phys. Rev. B **26**, 912 (1982).
9. N. A. Poklonski, V. F. Stelmakh, V. D. Tkachev, and S. V. Voitikov, Phys. Status Solidi B **88**, K165 (1978).
10. V. S. Bonch-Bruevich and S. G. Kalashnikov, *Semiconductor Physics* [in Russian], Nauka, Moscow (1990), ch. 5, p. 189.
11. N. A. Poklonskiĭ and A. I. Syaglo Fiz. Tverd. Tela (St. Petersburg) **40**, 147 (1998) [Phys. Solid State **40**, 51 (1998)].
12. N. A. Poklonskiĭ and A. I. Syaglo, *Abstracts of the Proceedings 3rd All-Russia Conf. in Semiconductor Physics* [in Russian], FIAN, Moscow (1997), p. 117.
13. N. A. Poklonski and V. F. Stelmakh, Phys. Status Solidi B **117**, 93 (1983).
14. F. M. Ismagilova, L. B. Litvak-Gorskaya, G. Ya. Lugovaya, and I. E. Trofimov, Fiz. Tekh. Poluprovodn. **25**, 225 (1991) [Sov. Phys. Semicond. **25**, 132 (1991)].
15. E. M. Gershenzon, Yu. A. Gurvich, A. P. Mel'nikov, L. N. Shestakov, Fiz. Tekh. Poluprovodn. **25**, 160 (1991) [Sov. Phys. Semicond. **25**, 95 (1991)].

Translated by Frank J. Crowne

The influence of defect clusters on redistribution of doping impurities in *n*- and *p*-type $Si_{0.7}Ge_{0.3}$ irradiated by reactor neutrons

A. P. Dolgolenko

Institute for Nuclear Reasearch, Academy of Sciences of Ukraine, 252028 Kiev, Ukraine
(Submitted April 15, 1998; accepted for publication September 7, 1998)
Fiz. Tekh. Poluprovodn. **33**, 405–409 (April 1999)

Samples of a silicon-germanium solid solution with *n*- and *p*-type conductivities and resistivities of $1-2\times10^{-3}\,\Omega\cdot$cm doped with a natural mixture of phosphorus and boron isotopes were studied while being irradiated in the reactor core of the VVR-M reactor at temperatures in the range 200–500 °C. By using effective-medium theory it is possible to calculate the dose dependence of the resistivity and thermoelectric power of these samples in detail under conditions where clusters can act as effective nuclei for condensation of the doping impurities. Volumes are determined within which clusters can trap doping boron and phosphorus impurities during irradiation, and mean-statistical radii are calculated for the defect clusters and cross sections for their incorporation. It is shown that precipitation of phosphorus primarily decreases the concentration of carriers in a conducting host of the sample during irradiation, while trapping of boron changes the concentration of carriers in the clusters. © *1999 American Institute of Physics.* [S1063-7826(99)00504-9]

INTRODUCTION

The search for heat-resistant radiation-hard thermoelectric materials has sparked much interest in the behavior of high-temperature materials based on solid solutions of silicon and germanium irradiated by reactor neutrons.[1–3] However, the literature contains very little conclusive data on the behavior of boron and phosphorus in a cubic lattice as part of an overall picture of accumulation and annealing of radiation defects caused by reactor neutrons.

Nevertheless, the authors of Ref. 4 have established that at doping levels of the order of $10^{19}\,cm^{-3}$ phosphorus remains in the silicon lattice at substitutional positions up to temperatures of 200 °C, both during annealing and during irradiation by neutrons, while boron (up to 95%) enters into complexes with defects but can be reactivated at 400 °C. After high-temperature irradiation of a semiconductor, the primary defects that remain are clusters surrounded by space-charge regions. In these regions, where electric field intensities can reach values of 10^6 V/cm, any 10 Å-size mobile defect can obtain an energy of the order of 0.1 eV from the electric field.[5,6]

The electric and strain fields that surround clusters are not only capable of confining defects,[7] but also of interacting vigorously with impurities they capture.[3,6] In their studies of the influence of internal fields in neutron-irradiated silicon, the authors of Ref. 6 showed that positively charged atoms of lithium that enter the capture volume of a cluster decrease its negative charge. The loss of lithium from the conducting volume is proportional to the density of defects introduced. Therefore, the question of how these clusters react with boron and phosphorus during neutron irradiation is a relevant issue not only for the application of neutron doping, but also for radiation stability of highly doped semiconducting thermoelectric materials.

EXPERIMENT

The objects of our studies were samples of silicon-germanium solid solution with *n*- and *p*-type conductivities and resistivities of $1-2\times10^{-3}\,\Omega\cdot$cm obtained by high-temperature sintering and naturally doped with mixtures of phosphorus and boron isotopes. These samples were irradiated in the reactor core of the VVR-M reactor at temperatures in the range 200–500 °C in a mixed neutron field. Measurements were made of the resistivity and thermoelectric power in the course of the irradiation, and the information obtained was accumulated in a computer for subsequent processing and analysis. Figures 1 and 2 show the experimentally determined data on resistivity and absolute thermoelectric power for samples of *n*- and *p*-type $Si_{0.7}Ge_{0.3}$ with

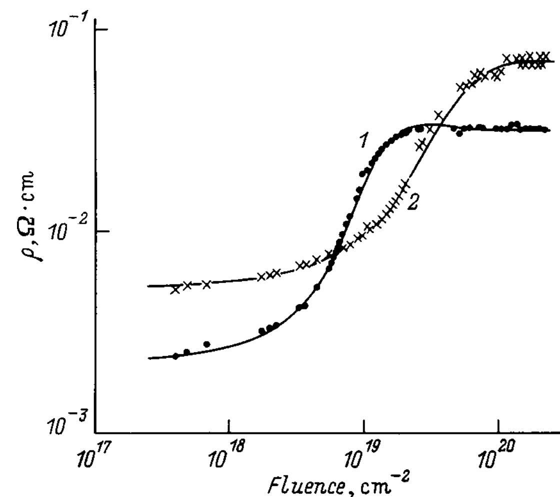

FIG. 1. Dependence of the resistivity ρ of the alloy $Si_{0.7}Ge_{0.3}$ on the fast-neutron flux (irradiation temperature 420 °C): *1*—*p*-type sample, *2*—*n*-type sample; solid curves are calculations.

 © 1999 American Institute of Physics

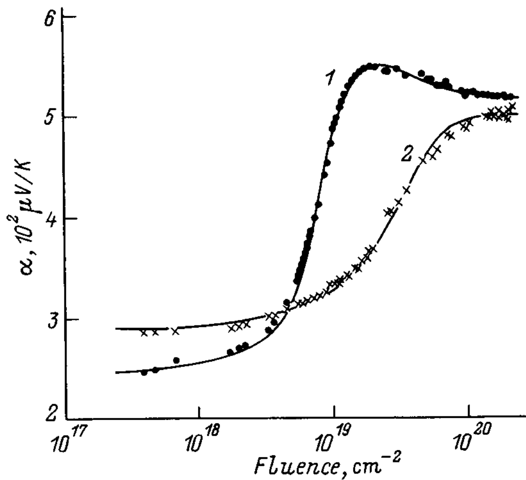

FIG. 2. Dependence of the thermoelectric power α of the alloy $Si_{0.7}Ge_{0.3}$ on fast-neutron flux. Conductivity type of sample and irradiation temperature: *1*—p-type, 430 °C (see Ref. 2), *2*—n-type, 450 °C.

starting carrier concentrations $n_0 = 1.24\times10^{20}\,\mathrm{cm}^{-3}$ and $p_0 \equiv 1.08\times10^{20}\,\mathrm{cm}^{-3}$ after their irradiation with various doses of fast neutrons. Usually, the changes in resistivity and thermoelectric power recorded as a function of the fast neutron flux can be described in the framework of effective-medium theory as a transition from the initial conductivity to a conductivity determined by regions with the introduced defects.[8]

THEORY

In Ref. 9 it was shown that neutrons with energies above 36 keV are capable of creating clusters of defects in silicon. The probability per unit length of fast neutrons creating these clusters, which is the same in n- and p-type $Si_{0.7}Ge_{0.3}$, is $\Sigma = 0.15\,\mathrm{cm}^{-1}$ if we assume that each scattered neutron creates a cluster of defects independently of the irradiation temperature. This assumption is based on the idea that if increased irradiation temperature leads to annealing of the small-size clusters, then heavy doping of samples of Si–Ge solid solution can lead to a spatial separation of primary-generated subcascades. Walker and Thompson[10] used the Monte Carlo method to calculate the dimensions of cascades created by first-generation knocked-out atoms in silicon, from bismuth to nitrogen, and showed that with decreasing mass of these first-generation atoms the size of an average cascade increases along with the possibility of generating isolated subcascades. Because p-type samples were doped naturally with a mixture of boron isotopes, thermal neutrons can react with ^{10}B according to the reaction $^{10}\mathrm{B}(n,\alpha)^7\mathrm{Li}$. As a result, α-particles and Li nuclei, whose total energies amount to 2.66 MeV, are formed. Allowance for cluster formation during scattering of α-particles ($E_\alpha = 1.69$ MeV) leads to a change in the cross section for cluster formation by fast neutrons of only 2%. An increased concentration of defects forms at the end of the α-particle range. These defects, however, cannot form clusters or at least nuclei, as a result of aggregation, for subsequent vacancy formation, which then could be converted into defect aggregates.

Let us estimate how efficiently neutrons can form defect clusters, with allowance for scattering of ^{7}Li nuclei with most probable energies on the order of 1 MeV by silicon or germanium atoms. We assume that the capture of each thermal neutron by a ^{10}B nucleus results in the creation of one defect cluster on the average. Then the cross section for creating defect clusters that lead to a fast-neutron flux (Σ) is

$$\Sigma = \gamma_a p\,\eta R + \Sigma_1, \tag{1}$$

where γ_a is the cross section for capture of thermal neutrons by ^{10}B ($\gamma_a = 3838$ barn); p and η are the doping impurity concentration and fraction of ^{10}B atoms; R is the ratio of flux densities for thermal and fast neutrons; and Σ_1 is the macroscopic cross section for formation of defect clusters caused by the scattering of fast neutrons. The number of defect clusters created (N_k) will then be

$$N_k = \Sigma\Phi, \tag{2}$$

where Φ is the flux of fast neutrons with energies $E_n \geqslant 36$ keV.

As shown in Ref. 7, allowance for the strain-electrostatic fields of defects when regions of disorder are created significantly increases the concentration of divacancies in the damaged region. In Ref. 3 it was proposed that even after the formation of a defect cluster the presence of strain and electrostatic fields around the damaged region can serve as a nucleus for the condensation of copper in p-Cu_2Se. Once it has precipitated out in the capture volume of the cluster, this copper is found to be electrically inert, whereas the concentration of holes in the conducting copper selenide host increases.

It is natural to assume that defect clusters can also be sinks for doping impurities with a small diffusion coefficient when a sample is irradiated at sufficiently high temperatures, conditions that exist in a reactor. Therefore, in order to describe the dose dependence of the resistivity and thermoelectric power of the n-type $Si_{0.7}Ge_{0.3}$ samples in more detail, we will assume that when they are irradiated in a reactor at a temperature of about 420 °C, the doping phosphorus impurities they contain will lose their electrical activity, both by virtue of natural precipitation onto intrinsic defects in the presence of irradiation and after subsequent deposition at clusters. Usually, $\leqslant$40% of an initial phosphorus doping level ($n_0 = 1.24\times10^{20}\,\mathrm{cm}^{-3}$) precipitates out before irradiation. Because the irradiation temperature of the samples of n,p-type $Si_{0.7}Ge_{0.3}$ exceed 400 °C, not only do the phosphorus atoms remain electrically active during the irradiation process (unless they turn out to be trapped by defect clusters or intrinsic defects), but the boron atoms retain their electrical activity as well, both in the conducting host of the samples and when they are captured in clusters. The change in carrier concentration of the conducting n-$Si_{0.7}Ge_{0.3}$ host, and in the defect clusters created in p-$Si_{0.7}Ge_{0.3}$ by nuclear radiation from the reactor, is then directly proportional to the fraction of capture volume of the clusters:

$$\Delta P = P_\infty[1 - \exp(-\Sigma V_a \Phi)]. \tag{3}$$

Here P_∞ is the maximum boron or phosphorus concentration precipitated out into the capture volume of the clusters, or

TABLE I.

Parameter	Material type	n_0^*, 10^{20} cm^{-3}	P_1, 10^{18} cm^{-3}	P_∞, 10^{19} cm^{-3}	r_1, 10^{-8} cm	r_a, 10^{-8} cm	y
α, μV/K	p	1.08	1.0	0.35	47	26.5	1.7
α, μV K	n	0.73	6.3	−2.0	41	47.0	0.88
ρ, $\Omega\cdot$cm	p	1.08	1.0	0.35	42	33.0	1.7
ρ, $\Omega\cdot$cm	n	0.73	6.3	−2.0	38	47.0	0.88

lost from the conducting host (for p- and n-type $Si_{0.7}Ge_{0.3}$ sample, respectively); and $V\equiv(4/3)\pi r_a^3$ is the capture volume of a defect with radius r_a. Consequently, the conductivity of the n-type $Si_{0.7}Ge_{0.3}$ host is

$$\sigma_0^n = qn\mu_n, \tag{4}$$

where q is the electron charge, μ_n is the mobility of electrons in n-type $Si_{0.7}Ge_{0.3}$ before irradiation, and $n=n_0^*-\Delta p$ is the concentration of carriers in the conducting host. The conductivity per unit volume of cluster created in p-$Si_{0.7}Ge_{0.3}$ can be written as

$$\sigma_1^p \equiv qp\mu_p, \tag{5}$$

where μ_p is the mobility of holes in the cluster volume for p-type samples, and $p=p_1+\Delta p$ is the concentration of carriers in the clusters.

According to effective-medium theory, the conductivity of a medium containing high-resistivity clusters of defects with conductivity σ_1 embedded in a host consisting of a material with conductivity σ_0 (Ref. 8) is given by the expressions

$$\sigma_{\rm eff} = f\sigma_0, \quad f = a + \left(a^2 + \frac{x}{2}\right)^{1/2},$$

$$a = \frac{1}{2}\left[\left(\frac{3}{2}C - \frac{1}{2}\right)(1-x) + \frac{x}{2}\right], \quad x = \sigma_1/\sigma_0, \tag{6}$$

where $\sigma_{\rm eff}$ is the conductivity of the medium with incorporated defect clusters, and C is the fraction of conducting volume.

Using the standard expression for the fraction of nonconducting volume occupied by defect clusters, we can show that

$$C = \exp(-\Sigma V\Phi), \tag{7}$$

where $V\equiv(4/3)\pi r_1^3$ is the volume of a cluster with radius r_1.

The combined solution of Eqs. (6) under conditions (1) and (7) allows us to compute the average radius of defect clusters created by neutron irradiation in samples of n-, p-type $Si_{0.7}Ge_{0.3}$ at temperatures of about 700 K (Ref. 3). In order to describe the experimental dependence of the resistivity on irradiation dose (fast-neutron flux) in more detail, we took into account the change in carrier concentration according to Eqs. (3)–(5) in solving Eq. (6). The results of these calculations are shown in Table I, where n_0^* is the carrier concentration after an hour of irradiation in the reactor.

We can determine the defect concentration (N_d) in clusters created by neutrons when the latter overlap fully by measuring the concentration of carriers in the sample before and after irradiation:

$$N_d = N_0 - N_\Phi, \tag{8}$$

where N_0 and N_Φ are the carrier concentrations before and after irradiation. Using the relation between the conductivity, the Hall constant, and the Hall mobility for charge carriers, we can use the following expressions to describe the change in the thermoelectric power as a result of neutron bombardment (Φ):[8]

$$R = hR_0, \quad \mu = g\mu_0,$$

$$h = g/f, \quad y = \mu_1/\mu_0,$$

$$g = f^{-1}\left[1 - \frac{(2f+1)^2(1-C)(1-xy)}{(2f+1)^2(1-C)+(2f+x)^2 C}\right], \tag{9}$$

where R_0 and R are the Hall constants before and after neutron bombardment, μ_0 and μ are the charge-carrier mobilities before and after irradiation, and μ_1 is the charge-carrier mobility for overlapping clusters.

While the sample was being irradiated in the channel of the reactor, we measured the differential thermoelectric power which allowed us to calculate the absolute thermoelectric power. If we assume that a simple parabolic band is sufficient to describe the silicon-germanium solid solution, and that the scattering factor ($r=1$) does not change during irradiation in the reactor core at temperatures in the range 200–500 °C, we can find not only the carrier concentration from the experimental values of the thermoelectric power (α), but also use Eqs. (6) and (9) from effective-medium theory to calculate the thermoelectric power:

$$\alpha(\mathrm{F}_{1/2}) = \mathrm{cspline}[P_0 h^{-1} N_v^{-1}], \tag{10}$$

where $\mathrm{F}_{1/2}$ is the Fermi integral of degree 1/2, N_v is the density of states in the conduction band, and P_0 is the carrier concentration in the conducting host of the sample.

The matrix for the procedure CSPLINE is calculated from the known dependence of the thermoelectric power on the reduced Fermi level for a parabolic band when the scattering factor $r=1$.

RESULTS

Using Eqs. (6) and (9) from effective-medium theory and taking into account redistribution of doping boron and phosphorus impurities according to Eqs. (3)–(5), we can de-

scribe the experimental data for dose dependence of the resistivity and thermoelectric power in Si–Ge samples.

Our analysis of the experimental thermoelectric-power data in the framework of effective-medium theory revealed that the charge-carrier mobility increases in *p*-type samples and decreases in *n*-type samples of $Si_{0.7}Ge_{0.3}$ alloys (before irradiation these mobilities are $\mu_n \approx 50\,\mathrm{cm}^2/(\mathrm{V}\cdot\mathrm{s})$ and $\mu_p \approx 40\,\mathrm{cm}^2/(\mathrm{V}\cdot\mathrm{s})$ for electrons and holes at room temperature). However, the computed changes in carrier mobility (y) for these materials do not correspond to their values measured after irradiation (the mobility of carriers in *n*-type $Si_{0.7}Ge_{0.3}$ decreases by roughly a factor of 10, while in *p*-type $Si_{0.7}Ge_{0.3}$ it increases by only roughly a factor of 1.4). In our view, this behavior is attributable to the presence of potential and strain fields that surround the defect clusters, which disappear when the clusters overlap fully at high irradiation fluxes.

Table I shows clearly how much the carrier concentration in the conducting host and in the defect clusters changes during irradiation. The concentration of electrically active phosphorus in the conducting host of an *n*-type $Si_{0.7}Ge_{0.3}$ sample, for example, decreases by 30% in the course of neutron irradiation due to precipitation at clusters, while for *p*- $Si_{0.7}Ge_{0.3}$ samples the concentration of holes in clusters increases by roughly a factor of 3 from its initial value. The calculations show that the radius of the capture volume of a cluster is smaller for boron than for phosphorus. In our view, this result is attributable to the fact that boron, in preserving its electric (negative) charge, is confined by the electric field of the cluster, whereas phosphorus probably is confined by the cluster's strain field.

As it does for the dose dependence of the resistivity, allowance for the redistribution of doping impurities in *n*-*p*-$Si_{0.7}Ge_{0.3}$ samples via Eqs. (3)–(5) leads to a more detailed description of the experimental thermoelectric-power data as a function of fast-neutron flux. We were able to describe, for example, the dependence of the hole thermoelectric power in *p*-$Si_{0.7}Ge_{0.3}$ (Fig. 2) on the neutron flux well enough to predict not only its maximum value at a flux of about $10^{19}\,\mathrm{cm}^2$, but also its falloff to values close to that of the electron thermoelectric power at a flux on the order of $2\times10^{20}\,\mathrm{cm}^2$ in *n*-type $Si_{0.7}Ge_{0.3}$. The parameters used in calculating values of the thermoelectric power in the effective-medium theory are given in Table I.

When we take into account the redistribution of doping impurities during irradiation along with the consumption of ^{10}B in *p*-type $Si_{0.7}Ge_{0.3}$ and the precipitation of phosphorus in *n*-$Si_{0.7}Ge_{0.3}$ at intrinsic defects, we find that the defect concentration in clusters created in *n*-type samples turns out to be $9.8\times10^{19}\,\mathrm{cm}^{-3}$, while in *p*-type samples it is $9.6\times10^{19}\,\mathrm{cm}^{-3}$, In this case we assume that when clusters form near precipitation sites, the phosphorus atoms recover their electrical activity.

CONCLUSIONS

We have shown that irradiation of highly doped materials by reactor neutrons, in particular materials based on silicon-germanium solid solutions, at elevated temperatures of about 700°K leads to spatial redistribution of the doping impurities in the samples. During the irradiation, the impurities interact with the electrical and strain fields of the defect clusters created by neutrons from the reactor. Phosphorous loses its electrical activity during irradiation, not only because of precipitation at intrinsic defects but also at the newly introduced defect clusters, which are nuclei for its deposition. At these irradiation temperatures, boron does not lose its electrical activity in the samples, even if it is drawn by an electric field into a damaged cluster region. The model we have developed for defect formation allows us to describe in detail the changes in kinetic coefficients as a function of fast-neutron flux. Our model gives more precise values not only of the sizes of the defect clusters but also the concentrations of defects within them.

[1] A. P. Dolgolenko and N. D. Marchuk, in *Proceedings of the XII International Conference on Thermoelectrics* (Yokohama, Japan, 1993) p. 66.
[2] A. P. Dolgolenko and N. D. Marchuk, Bull. Belarus Acad. Sci., Ser. Phys.-Mater. Sci. **3**, 35 (1991).
[3] N. D. Marchuk, A. P. Dolgolenko, and N. N. Kolychev, in *Proceedings of the International Conference on Radiation Materials Science*, Alushta, May 22–25, 1990 (Kharkov, Ukraine, 1991), v. 9, p. 113.
[4] V. D. Akhmetov and V. V. Bolotov, Fiz. Tekh. Poluprovodn. **22**, 1556 (1988) [Sov. Phys. Semicond. **22**, 984 (1988)].
[5] L. C. Kimerling and P. D. Drevinsky, IEEE Trans. Nucl. Sci. **NS-18**, 60 (1971).
[6] L. C. Kimerling, *Defects and Radiation Effects in Semiconductors*, Ser. 46 (Bristol–London, 1979), ch. 1, p. 56.
[7] V. A. Artem'ev, V. V. Mikhnovich, and S. G. Titarenko, Fiz. Tekh. Poluprovodn. **22**, 750 (1988) [Sov. Phys. Semicond. **22**, 468 (1988)].
[8] M. H. Cohen and J. Jortner, Phys. Rev. Lett. **30**, 15, 696 (1973).
[9] A. P. Dolgolenko, *Radiation Effects in Silicon*, Preprint KIYaI-76-23 [in Russian], Kiev, (1976), p. 12.
[10] R. S. Walker and D. A. Thompson, Radiat. Eff. **37**, 113 (1978).

Translated by Frank J. Crowne

Acoustostimulated activation of bound defects in CdHgTe alloys

A. I. Vlasenko, Ya. M. Olikh, and R. K. Savkina

Institute of Semiconductor Physics, National Academy of Sciences of Ukraine, 252028 Kiev, Ukraine

(Submitted June 29, 1998; accepted for publication September 7, 1998)
Fiz. Tekh. Poluprovodn. **33**, 410–414 (April 1999)

This paper describes the results of acoustodynamic studies of the electrical parameters (effective electron concentration $n=1/eR_H$ and Hall mobility $\mu_H=R_H/\rho$) of n-$Cd_xHg_{1-x}Te$ crystals ($x\approx 0.22$). It is shown that ultrasonic loading (with intensities up to 0.5×10^4 W/m^2) leads to an increase in the values of n and μ_H in the impurity-conductivity temperature range ($T\approx 100$ K). The authors explain the effects observed by invoking acoustostimulated liberation (activation) of donor-like bound defects, leading to a corresponding decrease in the scattering potential of alloy nonuniformities. Characteristic parameters of the acoustoelectric interaction are evaluated in the framework of an assumed dislocation model. © *1999 American Institute of Physics.* [S1063-7826(99)00604-3]

1. INTRODUCTION

A well-known characteristic of $Cd_xHg_{1-x}Te$ crystals is the presence of impurities and intrinsic point defects bound to extended structural imperfections (dislocations, inclusions of a second phase, small-angle boundaries, etc.). It is highly likely that external perturbations can cause these defects to become electrically active and give an additional contribution to the conductivity. One such perturbation is temperature; another is intense high-frequency ultrasonic loading of the crystal. Previous studies of the effect of ultrasonic loading on the electrical and photoelectric parameters of $Cd_xHg_{1-x}Te$ crystals, which focused primarily on residual effects (after ultrasonic processing),[1,2] established that the nature of the acoustostimulated effects in II–VI semiconductors is determined by acoustodislocation interactions and effective conversion of the absorbed ultrasonic energy into internal vibrational states of the crystal.[3] When this ultrasonic energy is absorbed in a $Cd_xHg_{1-x}Te$ sample, it intensifies the diffusion-driven redistribution of point nonequilibrium defects between the bulk ''subblock'' and extended defects.[4–6] However, dynamic ultrasonic loading at below-threshold intensities in samples with quasi-equilibrium states of their defect structure gives rise to completely different ac processes which manifest themselves by reversible changes in the electrical and acoustic parameters[5,6] which require a special study.

In order to clarify the mechanism of ac defect transformation we have studied the temperature and amplitude dependences (from the intensity of the ultrasound) of the electrical parameters (the concentration $n=1/eR_H$ and Hall mobility $\mu_H=R_H/\rho$) of n-$Cd_xHg_{1-x}Te$ crystals ($x\approx 0.22$).

2. EXPERIMENTAL METHOD

In order to bring about a regime of dynamic ultrasonic loading, we added acoustic elements to the setup for a standard Hall experiment (including a 0.45-T dc magnetic field).[7] Longitudinal ultrasonic vibrations (with frequency 5–7 MHz and intensity $W_{US}\leqslant 0.5\times 10^4$ W/m^2) were generated by a lithium niobate (35°*Y*-cut) transducer, and fed to the sample through a quartz buffer, which was used for electrical isolation and acoustic matching. In order to prevent irreversible ultrasonic effects, the intensity W_{US} did not exceed 0.5×10^4 W/m^2; high values of W_{US} were used only at low temperatures $T<200$ K. Particular attention was paid to monitoring the temperature, due to the possibility of additional ultrasonic heating. We were able to keep the temperature constant to within at least 0.2 K, while making the ultrasonic measurements. The scheme for ultrasonically loading the sample is shown in the inset in Fig. 1.

3. EXPERIMENTAL RESULTS

Figure 1 shows temperature dependences of the concentration n that are typical of the n-$Cd_xHg_{1-x}Te$ samples we investigated, measured both without (curve *1*) and with ultrasonic loading (curve *2*) in the temperature range $T=77$–200 K. The method of preparing the samples for measurement was described in Refs. 1, 2, and 9. When $T<110$ K, the function $n(T)$ was observed to saturate, i.e., the conductivity was impurity-like in character. Figure 1 also shows the functions $\mu_H(T)$ and data on the mobility of a structurally perfect sample (curve *4*).[8] It is clear that at low temperatures ($T<120$ K) the values of μ_H for our samples are smaller than those of a structurally perfect crystal, which is evidence for the nonuniformity of the samples under study.[9,10] It is noteworthy that thermodynamic disorder at a level of 2–3% is a general characteristic of this material, due to the particular features of the phase diagram; for the most part, this determines the physical properties of the material as a whole.[8,11]

For all the samples we investigated (see Table I), the effect of ultrasonic loading on the electrical parameters in the impurity-conductivity temperature range ($T<120$ K) manifests itself as a decrease in the quantity R_H and an increase in μ_H. It noteworthy that switching on and switching off the ultrasonic loading led to reversible relaxation of the electrical parameters, and the values of n and μ_H returned to their

 © 1999 American Institute of Physics

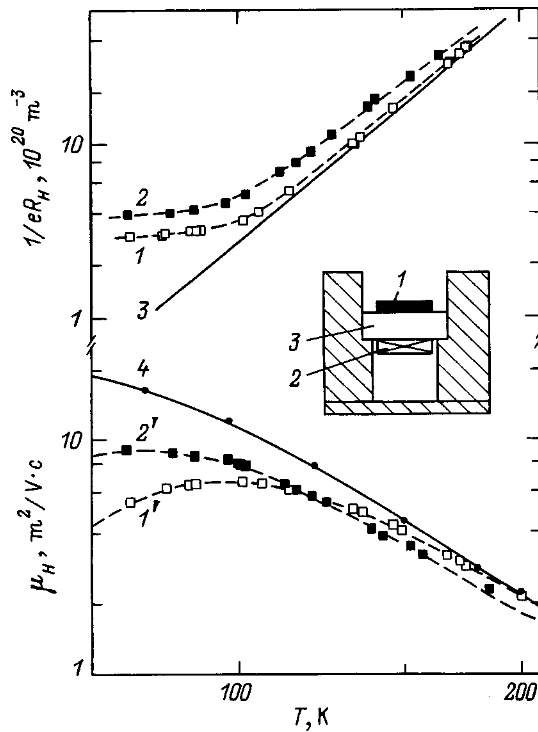

FIG. 1. n-$Cd_{0.21}Hg_{0.79}Te$ (sample 3). Temperature dependences of the concentration $n = 1/eR_H$ (*1–3*) and Hall mobility $\mu_H = R_H/\rho$ (*1′*, *2′*, *4*) for sample 3 of n-$Cd_{0.21}Hg_{0.79}Te$. *1* and *1′* are without ultrasonic loading, *2* and *2′* are with ultrasonic loading ($\sigma_{US} \approx 4\times10^5$ Pa), *3*—theoretical dependence of intrinsic concentration for $x \approx 0.21$, *4*—mobility of a structurally perfect crystal (see Ref. 8) The inset shows the scheme for ultrasonically loading the sample: *1*—sample, *2*—piezoelectric transducer, *3*— buffer. The magnetic field is directed perpendicular to the plane of the piezoelectric transducer.

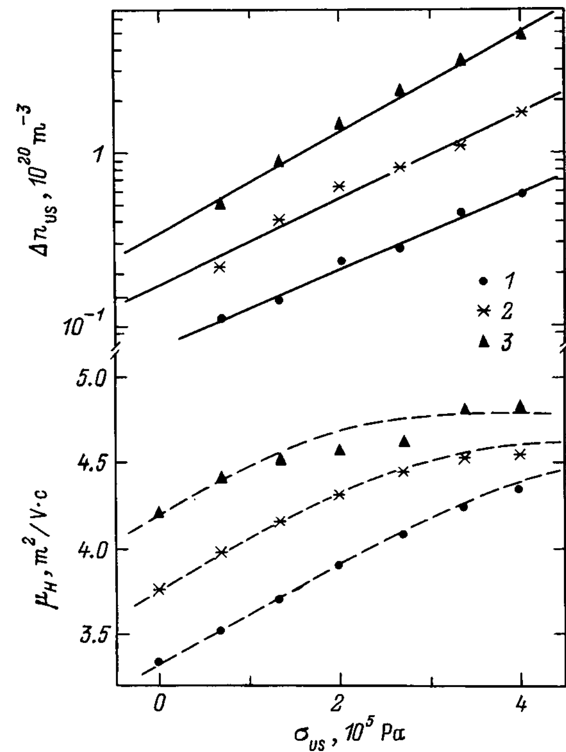

FIG. 2. Plots of the change in concentration $\Delta n_{US} = n(T_i, \sigma_{US}) - n(T_i, 0)$ (upper curves) and mobility μ_H (lower curves) versus the stress of the ultrasonic vibrations σ_{US}, measured at temperatures T_i, K: *1* — 87, *2* — 93, *3* — 103, for sample 2 of n-$Cd_{0.22}Hg_{0.78}Te$.

original values. The time for this relaxation oscillated between a few seconds and hundreds of seconds, depending on the sample, the ultrasound intensity, and the temperature.

The dependences of n and μ_H on the effective ultrasonic stress amplitude σ_{US}, i.e., $n(\sigma_{US})$ and $\mu_H(\sigma_{US})$, are plotted in Fig. 2 for one of the samples. The magnitude of σ_{US} is determined by

$$\sigma_{US} = (2\rho v_{US} W_{US})^{1/2},$$

where ρ is the density, and v_{US} is the velocity of ultrasound in the crystal; for $Cd_xHg_{1-x}Te$ we have $\rho \approx 7.6$ kg/m^3, and $v_{US} \approx 3.4\times10^3$ m/s. It is clear that increasing the ultrasonic loading leads to an exponential growth in n, where the slope of the function $\log n = f(\sigma_{US})$ increases somewhat with temperature. Every plot we made of the amplitude dependence $\mu_H(\sigma_{US})$ exhibited an initial range of linear growth in μ_H with subsequent saturation. However, in contrast to the function $n(\sigma_{US})$, the slope of the linear portion of $\mu_H(\sigma_{US})$ did not change appreciably with increasing temperature, while its threshold for saturation shifted towards lower values of σ_{US}.

4. DISCUSSION OF RESULTS

In analyzing the experimental data it is natural to start from the fact that the behavior of the electrical characteristics at low temperatures $T < 120$ K is determined by the defect state of the structure, while the dynamic changes of n and μ_H

TABLE I. Values of the Hall parameters and computed acoustoelectric interaction parameters for the samples of n-$Cd_xHg_{1-x}Te$ under study ($x \approx 0.21-0.22$).

Sample No.	T, K	$1/(eR_H^0)$, 10^{20} m^{-3}	μ_H^0, m^2/(V·s)	σ_{US}, 10^5 Pa	$1/(eR_H^{US})$, 10^{20} m^{-3}	μ_H^{US}, m^2/(V·s)	γ_n, 10^{-27} m^3	$\gamma_\mu/\Delta E$, 10^{-26} m^3/eV	ΔE, eV
1*	77	9.3	4.0	5.3	14.7	7.0	6.1	14	0.05
2	87	3.1	5.5	3.7	4.4	9.1	6.2	6.6	0.09
2	93	3.2	6.7	3.7	4.5	8.4	7.4	6.6	0.11
2	103	3.9	6.8	3.7	5.4	7.6	9.7	6.6	0.14
3	77	3.0	5.3	3.3	4.0	9.0	···	···	···
4	77	2.8	14	3.7	3.4	16	···	···	···

**Note:* The label "0" indicates a parameter obtained in the absence of ultrasonic loading; the label "US" indicates the presence of ultrasonic loading. The values of ΔE are estimated assuming that $\gamma_\mu = \gamma_n$.

in the ultrasonic field are a consequence of nonequilibrium short-time processes driven by the ac current (ac processes) that transforms this defect state. It is noteworthy that previously investigated mechanisms for residual ac-induced changes in the electrical parameters of n-$Cd_xHg_{1-x}Te$ samples (internal ac annealing,[2,4] decay of HgTe inclusions,[11] etc.) are not controlling factors for ultrasonic loading in the dynamic regime. In fact, when the current flow is uniform throughout the entire volume of the subblock, the diffusive processes listed above require the presence of sources (or sinks) of point defects (dislocations, low-angle boundaries, inclusions of a second phase, etc.[12]), and also rather high diffusion coefficients and processing times. The relaxation times we observed, combined with the approximation of using known high-temperature chemical diffusion coefficients,[13] indicate that at low temperatures ($T<150$ K) the estimated diffusion length does not exceed a few lattice constants even for the most mobile component of the solid solution, i.e., interstitial Hg_i atoms. This allows us to assume that ac processes in $Cd_xHg_{1-x}Te$ crystals are nonequilibrium in character. Primary evidence for this conclusion is their reversibility and the absence of residual phenomena.

The decisive factor that creates these AC processes is the presence of an atmosphere of impurities and intrinsic defects ''bound'' at dislocations and other imperfections. These impurities can exist in the neutral and in the ionized states; in the latter case they form space-charge regions. During ultrasonic loading, some of these bound defects can be detached and enter their electrically active state via thermal activation with subsequent ionization, thereby becoming the same as the previously ionized defects.

4.1. THE EFFECT OF ULTRASOUND ON THE ELECTRON CONCENTRATION

Let us denote the contributions of ''free'' donors N_d^0 and ''free'' acceptors N_a^0 to the total carrier concentration in the absence of ultrasonic loading by $n_0=N_d^0-N_a^0$, and the contribution from bound defects by $n_b=N_d^b-N_a^b$. It is important to note that for our $Cd_xHg_{1-x}Te$ crystals ($x\approx0.21-0.23$) all the donor impurity levels practically coincide with the bottom of the conduction band and are ionized even at liquid-helium temperatures, while for the intrinsic concentration we have $n_i<n_b\ll n_0$ when $T\leqslant 100$ K. Taking this circumstance into account, but disregarding the possibility of multiple ionization of various impurity levels, we can write the carrier concentration in the form

$$n=n_0+n_b=(N_d^0-N_a^0)+(N_d^b-N_a^b). \quad (1)$$

For each group, the thermal activation of bound defects is described by a corresponding expression:[13]

$$N_{d,a}^b(T)=N_0^b\exp(-U_0/kT), \quad (2)$$

where $N_{d,a}^b$ is the concentration of donor- or acceptor-type defects, which as a result of thermal activation enter an electrically active state; N_0^b is the total concentration of bound defects; and U_0 is their binding (activation) energy. Disregarding thermoacoustic activation (and/or gettering) of acceptor-type defects N_a^b (compared to N_d^b) for n-type crystals, we can write from Eqs. (1) and (2) the expression

$$n(T)-n_0=n_b(T)=N_0^b\exp(-U_0/kT). \quad (3)$$

Thermal activation of bound defects should manifest itself as a weak temperature dependence of the concentration in the impurity-conductivity temperature range. It is clear that when $n_b\ll n_0$, it is very difficult to discern any such dependence in $n(T)$. However, a careful analysis of our data, together with experimental data from the literature, shows that certain $Cd_xHg_{1-x}Te$ samples exhibit a weak increase in n (in the range $80<T<150$ K). We should emphasize one more time that the increase in concentration in this temperature range cannot be connected with ionization of impurities or with the contribution of intrinsic carriers ($n_i<n_b\ll n_0$). Using the fact that $n_0\approx n$ (77 K) and the experimental data on the function $n(T)$ measured in the absence of ultrasound, we derive the following estimates from Eq. (3): $U_0=(0.05\pm0.02)$ eV and $N_0^b=(2\pm1)\times10^{22}\,\mathrm{m}^{-3}$. The importance of these parameters for clarifying the specific nature of the bound defects is beyond question; however, because of the comparatively narrow temperature range in which our investigations were carried out (up to 78 K), the accuracy of determining N_0^b and U_0 is rather low.

The effect of ultrasonic loading on the electrical parameters will be discussed in the framework of dislocation mechanisms,[3,4] i.e., we identify U_0, on the one hand, as the energy for binding an impurity to a dislocation and, on the other, as the energy of vibrational motion of a dislocation. Let us consider the case of reversible effects, i.e., below-threshold values of the intensity W_{US}, for which we can ignore the stepwise motion of the dislocation. From theory it is known that external mechanical loading decreases the binding energy of a dislocation to a defect according to an approximately linear law.[14,15] Assuming in the case of ultrasonic loading that $U_{US}=U_0-\gamma_n\sigma_{US}$ (Ref. 3), we rewrite Eq. (2) in the form

$$N_d^b(T,\sigma_{US})=N_0^b\exp[-(U_0-\gamma_n\sigma_{US})/kT], \quad (4)$$

where γ_n is the effective interaction of an ultrasonic wave with a crystal defect. Since the quantity $\sigma_{US}\equiv\sigma_0\cos(2\pi ft)$ enters into the exponent in Eq. (4), the average value of the change in concentration over a period of the sound wave $\Delta n_{US}=n(T_i,\sigma_{US})-n(T_i,0)$ will not equal zero for $(\gamma_n\sigma_{US}/kT_i)\geqslant1$, where T_i is a fixed temperature at which the amplitude measurements were made. This implies that during the expansion of a certain microvolume of crystal the increase in concentration of ionized defects in this microvolume will not be compensated for in the next half-period of compression.[3]

In the theory of dislocations the quantity $\gamma=abl$ has the sense of an activation volume, where a and l are the amplitude of displacement and length of the vibrating segment of dislocation, respectively; and b is the Burgers vector.[14] Note that in our analysis of the vibrational ac motion of a dislocation in a $Cd_xHg_{1-x}Te$ crystal we assume a thermally activated character for its motion, which is determined at tem-

peratures $T<300\,^\circ\mathrm{C}$ by the impurity atmosphere.[17] Therefore, using Eq. (4), we can analyze the amplitude dependence $n(\sigma_{US})$ by writing:

$$n_b(\sigma_{US})=n(T_i,\sigma_{US})-n_0(T_i,0)$$
$$=N_0^b\,\exp[-(U_0-\gamma_n\sigma_{US})/kT_i]. \quad (5)$$

The values of γ_n can be calculated according to Eq. (5) from the slope of the experimental curves $\log[n_b(\sigma_{US})]=f(\sigma_{US})$ at fixed values of the temperature T_i (see Fig. 2) (the data are listed in Table I). The observed increase in γ_n, as the temperature increases, confirms the thermally activated character of dislocation vibrations in II–VI crystals.[15]

4.2. EFFECT OF ULTRASOUND ON ELECTRON MOBILITY

We now turn to analysis of the influence of ultrasound on the function $\mu_H(T)$. Recall that for $Cd_xHg_{1-x}Te$ crystals in the temperature range $T\approx 100$ K, we should consider scattering by alloy nonuniformities and by lattice vibrations in determining μ_H. [1,10,16] It is clear that the process of ultrasonic activation of bound donors described above is not uniform over the entire volume of the crystal, but rather is more effective in regions of maximum absorption of ultrasonic energy, i.e., in regions with structural imperfections (nonuniformities). Consequently, a local ac increase in the number of ionized donors leads to ''smoothing out'' of fluctuations in the nonuniformities of the potential (a change in the space-charge region), which in turn must lead to a decrease in the scattering of the carriers. For a charge carrier relaxation time determined primarily by scattering by nonuniformities, the following expression is known:[16]

$$\tau=A/(m_0^{3/2}\Delta E^2),$$

where m_0 is the effective mass, ΔE is the scattering potential associated with nonuniformities of the solid solution, and A is a coefficient that depends on the band parameters of the crystal and composition of the solid solution.[16] Assuming that ultrasonic loading decreases ΔE according to a linear law

$$\Delta E_{US}=\Delta E-\gamma_\mu\sigma_{US},$$

and ignoring the influence of ultrasound on other parameters entering into Eq. (6), we obtain an expression for the change in the quantity μ_H in an ultrasonic field:

$$\Delta\mu_{US}=(\mu_{US}-\mu_0)=(e/m)(\tau_{US}\tau_0)$$
$$=\mu_0(2\sigma_{US}\gamma_\mu/\Delta E). \quad (6)$$

If we assume that at $T=100$ K the dominant mechanism for scattering in our samples is an alloy mechanism, then using Eq. (7) and the experimental data of Fig. 2 we can estimate the quantity $\gamma\mu/\Delta E$. The data are presented in Table I. It is interesting to estimate the value of ΔE. Assuming that $\gamma_\mu\approx\gamma_n$, we find that $\Delta E\approx 0.1$ eV. For comparison, we note that the ''zero-order'' approximation in the theory of alloy scattering makes use of the difference in band-gap widths of the alloy components.[16]

Since μ_H is determined by several electron scattering mechanisms in $Cd_xHg_{1-x}Te$, an ac decrease in the contribution of scattering by nonuniformities should lead to an increased role for other scattering mechanisms, which might depend only weakly on the ultrasound (or perhaps not—compare curves *1'* and *2'* for $T>150$ K in Fig. 1). It is likely that the observed saturation of the function $\mu_H(\sigma_{US})$ is connected with this circumstance. The latter conclusion is also confirmed by the fact that the more perfect a crystal of $Cd_xHg_{1-x}Te$ is, i.e., the closer $\mu_H(T)$ is to curve *4* (Fig. 1), the smaller the ultrasonic effect of increasing mobility is in the impurity-conductivity range (see Table I, sample 4).

5. CONCLUSIONS

In this paper we report the first results of an experimental study the electrical parameters of crystals of $Cd_xHg_{1-x}Te$, using the Hall effect in the presence of dynamic ultrasonic loading. We have shown that ultrasonic loading at an intensity $W_{US}\leqslant 0.5\times 10^4$ W/m^2 leads to an increase in the effective concentration of electrons and in their mobility. The observed effects are explained in the framework of a dislocation model for acoustostimulated, thermally activated liberation of bound defects of donor type and a corresponding decrease in the scattering potential at alloy nonuniformities. Comparing the experimental data with theoretical calculations on the basis of the model proposed here, we can estimate the characteristic parameters of the acoustoelectric interaction, whose values can be used for preliminary estimates of the structural quality of the original semiconductor samples of $Cd_xHg_{1-x}Te$.

In summary, by activating some of the bound defects high-intensity sound can cause some appreciable transient changes in the electrical parameters of the material, and for $Cd_xHg_{1-x}Te$ crystals it is actually ''active.''[18]

[1] L. A. Karachevtseva, A. V. Lyubchenko, K. A. Myslivets, and Ya. M. Olikh, Ukr. Fiz. Zh. **35**, 468 (1990).
[2] K. A. Myslivets and Ya. M. Olikh, Fiz. Tverd. Tela (Leningrad) **32**, 682 (1990) [Sov. Phys. Solid State **32**, 250 (1990)].
[3] I. V. Ostrovskiĭ, *Acoustoluminescence and Defects in Crystals* (Higher School, Kiev, 1995), part 4, ch. 6.
[4] Ya. M. Olikh and Yu. I. Shavlyuk, Fiz. Tverd. Tela (St. Petersburg) **38**, 468 (1996) [Phys. Solid State **38**, 235 (1996)].
[5] A. V. Lyubchenko and Ya. M. Olikh Fiz. Tverd. Tela (Leningrad) **27**, 2505 (1985) [Sov. Phys. Solid State **27**, 1500 (1985)].
[6] V. A. Kalitenko, Ya. M. Olikh, and V. M. Perga, Ukr. Fiz. Zh. **33**, 788 (1988).
[7] Ya. M. Olikh and R. K. Savkina, Ukr. Fiz. Zh. **42**, 1385 (1997).
[8] G. Nimtz, G. Bauer, and R. Dornhaus, Phys. Rev. B **10**, 3302 (1974).
[9] A. I. Vlasenko, A. V. Lyubchenko, and E. A. Sal'kov, Ukr. Fiz. Zh. **25**, 1318 (1980).
[10] H. R. Vydynat, J. Electrochem. Soc. **128**, 2609 (1981).
[11] P. I. Baranskiĭ, A. E. Belyaev, S. M. Komirenko, and N. V. Shevchenko, Fiz. Tverd. Tela (Leningrad) **32**, 2159 (1990) [Sov. Phys. Solid State **32**, 1257 (1990)].
[12] A. I. Vlasenko, A. V. Lyubchenko, and V. G. Chalaya, Fiz. Tekh. Poluprovodn. **30**, 377 (1996) [Sov. Phys. Semicond. **30**, 209 (1996)].
[13] F. A. Zaitov, F. K. Isaev, and A. V. Gorshkov, *Defect-Formation and Diffusion Processes in Certain Semiconducting Solid Solutions* [in Russian], Azerneshr, Baku (1984), p. 81.
[14] J. P. Hirth and J. Lothe, *Theory of Dislocations* (McGraw-Hill, New York, 1967) [Russ. transl. Atomizdat, Moscow, 1972), ch. 16.
[15] Yu. A. Osip'yan and V. F. Petrenko, in *Physics of II–VI Compounds* [in Russian], Nauka, Moscow (1986), p. 35.
[16] D. Chattopadhyay and B. R. Nag, Phys. Rev. **12**, 5676 (1975).
[17] B. P. Koman, Ukr. Fiz. Zh. **32**, 908 (1987).
[18] Ya. M. Olikh, *Abstracts from the Proceedings 12th All- Union Conf. on the Physics of Semiconductors*, Kiev, 1990 [in Russian], Naukova Dumka, Kiev (1990), part 2, p. 87.

Translated by Frank J. Crowne

A model of how the thermal ionization energy of impurities in semiconductors depends on their concentration and compensation

N. A. Poklonskiĭ and A. I. Syaglo

Belorussian State University, 220050 Minsk, Republic of Belarus

G. Biskupski

University of Science and Technology, 59655 Lille, France
(Submitted April 1, 1998; accepted for publication October 5, 1998)
Fiz. Tekh. Poluprovodn. **33**, 415–419 (April 1999)

An electrostatic model is derived for the dependence of the thermal ionization energy of hydrogenic impurities E_1 on their concentration N and degree of compensation K, with allowance for the screening of ions by electrons (holes) that hop from impurity to impurity. It is shown that the change in E_1 with increasing N and K is connected with broadening of the impurity band and its shift toward the valence (v) band for acceptors and toward the conduction band (c) for donors. The shift in the impurity band is explained by a decrease in the affinity energy of an ionized acceptor for a hole (or a donor for an electron) due to screening of the ions. The impurity ion distribution density over the crystal is assumed to be Poisson-like, while its energy distribution is normal. The electron densities of states in the v- and c-bands are assumed to be those of the undoped crystal for the temperature interval in which E_1 is determined. The values of $E_1(N,K)$ calculated using the expressions given here coincide with known experimental data for transmutation- doped Ge crystals. A description is given of the dependence on N and K of the thermal ionization energy of Zn atoms in p-type Ge as they change from a charge state (-1) to (-2). © *1999 American Institute of Physics.* [S1063-7826(99)00704-8]

1. For definiteness let us assume the crystalline semiconductor is p-type, which contains $p=N_{-1}-KN$ holes per unit volume, $N=N_0+N_{-1}$ acceptors in charge states (-1) and (0), and KN donors. Here and in what follows N denotes the concentration of majority-carrier doping impurities, and K is their degree of compensation.

The thermal ionization energy E_{1a} equals the energy required to detach a hole from a hydrogenic acceptor due to thermal fluctuations at the given temperature. Ordinarily, the value of E_{1a} is determined by analyzing the temperature dependence of the Hall concentration of holes p_H as they are ejected into the valence (v) band from the acceptors. In this case it is assumed that in a strong magnetic field the following proportionality relations are correct for a three-dimensional hole gas:[1]

$$pT^{-3/2}\propto p_H T^{-3/2}\propto \exp\left(-\frac{E_{1a}}{k_BT}\right).$$

In this case the thermal (Hall) ionization energy of the acceptors is

$$E_{1a}=-k_Bd\ \ln(pT^{-3/2})/d(1/T)>k_BT, \tag{1}$$

where

$$p=2\left(\frac{2\pi m_{pd}k_BT}{(2\pi\hbar)^2}\right)^{3/2}\exp\left(-\frac{E_F}{k_BT}\right)\ll K(1-K)N;$$

k_BT is the thermal energy, $E_F>0$ is the Fermi level measured from the top of the v-band of an undoped crystal, m_{pd} is the effective mass of the hole density of states, and h is Planck's constant.

Here we note that for a nondegenerate semiconductor at low temperatures the average thermal wavelength of the hole in the v-band, $\pi\hbar/\sqrt{3m_{pd}k_BT}$, is much larger than the average radius of the region assigned to a single point charged particle $(3/8\pi N_{-1})^{1/3}$. The hole, in fact, does not "feel" the potential well of the "immobile" ionized impurities,[2] so that the tail of the density of states of the v-band can be ignored, and the expression for p is applicable.

In order to describe the dependence of E_{1a} on N and K, we developed the methods of Refs. 3–7, which allow a comparison with experimental data,[8] when the width of the impurity band is much larger[3] or much smaller[4] than the thermal energy.

The goal of this paper is to derive an electrostatic model for the dependence of the thermal ionization energy of an impurity on its concentration and compensation for arbitrary relations between the width of the impurity band and the thermal energy in crystalline semiconductors.

2. The Fermi level E_F and also dE_F/dT are required in order to calculate the ionization energy E_{1a} according to Eq. (1). These quantities are found from the equation of electrical neutrality (we disregard the excited states of neutral and ionized acceptors):

$$N_{-1}=N\int_{-\infty}^{+\infty}g_af_{-1}d(E_a-\bar{E}_a)=p+KN, \tag{2}$$

 © 1999 American Institute of Physics

where $g_a=(\sqrt{2\pi}W_a)^{-1}\exp(-(E_a-\bar{E}_a)^2/2W_a^2)$ is the normal density of the distribution of acceptor energy levels; $f_{-1}=1-f_0=(1+\beta\exp((E_a-E_F)/k_BT))^{-1}$ is the probability that an acceptor with energy level $E_a>0$ relative to the top of the v-band is ionized; β is a degeneracy factor (β=4 for atoms of Ga in Ge); W_a is the effective width of the acceptor-band; and $\bar{E}_a>0$ is the difference of acceptor energies in charge states (-1) and (0) averaged over the crystal.

Let us compute the dependence of the acceptor band parameters W_a and $\bar{E}_a$ on the concentration of doping impurities and degree of compensation.

The mean-square fluctuation W_z of the potential energy of an ion with charge ze, taking into account a pure Coulomb interaction only with the nearest point defect $z'e$ is[9,10]

$$W_z^2=\sum_{z'}\int_0^\infty P_{z'}u_{zz'}^2dr, \tag{3}$$

where

$$P_{z'}dr=4\pi r^2C_{z'}\exp\left[-(4\pi/3)r^2\sum_{z'\neq 0}C_{z'}\right]dr$$

is the Poisson probability that the point charge $z'e$ located at a distance from r to $r+dr$ is the closest charge to ion c with charge ze, $\Sigma_{z'\neq 0}C_{z'}$ is the concentration of all the charged particles, $u_{zz'}(r)=zz'e^2/4\pi\varepsilon r$ is the Coulomb energy of interaction of two nearest charges, and $\varepsilon=\varepsilon_r\varepsilon_0$ is the dielectric constant of the crystal lattice. The potential energy of an ion with charge ze averaged over the crystal is

$$\bar{U}_z=\sum_{z'}\int_0^\infty P_{z'}u_{zz'}dr=0.$$

From Eq. (3) we find the mean-square fluctuation of acceptor energy levels

$$W_a=\sqrt{W_0^2+W_{-1}^2}=W_{-1}\approx 1.64\frac{e^2}{4\pi\varepsilon}\left(\frac{8\pi}{3}N_{-1}\right)^{1/3}. \tag{4}$$

In the framework of linear screening theory,[11–14] we assume that the shift of the middle of the acceptor-band $\bar{E}_a$ toward the v-band is caused by the correlation interaction between negatively charged, mobile states of the immobile acceptors, i.e., holes migrating by hopping from acceptor to acceptor, and positively charged donors and holes in the v-band.

Each negatively charged acceptor is surrounded by a cloud (spherically symmetric on the average) of charges that screen it, so that the total electrical potential is $\varphi_s(r)=-[e/4\pi\varepsilon r(1+l/\lambda)]\exp[-(r-l)/\lambda]$, where for $p\ll K(1-K)N$ the quantity $l\approx 0.554(N(1+K))^{-1/3}$ determines the minimum approach between ionized impurities (taking into account hopping of holes from acceptor to acceptor); and λ is the screening length[14]

$$\lambda^{-2}=\frac{e^2}{\varepsilon}\left(\frac{\partial N_{-1}}{\partial E_F}-\frac{\partial p}{\partial E_F}\right)\approx\frac{e^2}{\varepsilon}\frac{\partial N_{-1}}{\partial E_F}. \tag{5}$$

The energy of interaction of an acceptor in charge state (-1) with the cloud screening it equals $-e^2/4\pi\varepsilon(\lambda+l)$; the interaction energy of charges in the cloud (with bulk density $-e\varphi_s(r)/\lambda^2$ and total charge $+e$) among themselves is $e^2/16\pi\varepsilon(\lambda+l)$. The total electrostatic energy of the system (ion plus screening cloud)[13] is $3e^2/16\pi\varepsilon(\lambda+l)$. According to the data of Refs. 9 and 10, the difference between the average energy of an ionized acceptor (with the charge cloud that screens it) $\bar{E}_{-1}=I_{-1}-3e^2/16\pi\varepsilon(\lambda+l)$ and the energy of a neutral acceptor $\bar{E}_0\approx I_0$ determines the position of the center of the acceptor band relative to the top of the v-band:

$$\bar{E}_a=\bar{E}_{-1}-\bar{E}_0=I_a-\frac{3e^3}{16\pi\varepsilon(\lambda+l)}, \tag{6}$$

where $I_a=I_{-1}-I_0>0$ is the energy level of an isolated acceptor.

In calculating the shift of the center of the acceptor band $\bar{E}_a$ toward the v-band based on Eq. (6), we assume that the change in the energy of a charged acceptor due to interaction with its surroundings is much larger than the change in energy of the neutral acceptor. In fact, based on estimates from Refs. 15 and 16, the polarization shift of the energy level of the ground state of a neutral acceptor, when it is screened by a degenerate gas of holes from the v-band (when $l\ll\lambda$) is $I_0-\bar{E}_0\approx 1.2(a_H/\lambda)^4I_a$, where $a_H=e^2/8\pi\varepsilon I_a$ is the Bohr radius for localizing a hole at an isolated acceptor. Since for a nondegenerate semiconductor $\lambda\gg a_H$, we have $I_0-\bar{E}_0\ll I_{-1}-\bar{E}_{-1}$.

Here we note that, according to Eq. (6), the quantity $I_a-\bar{E}_a$ is the decrease in the affinity energy of holes in the v-band for a negatively charged acceptor due to its screening by other charges. In thermodynamic equilibrium the affinity energy of a hole for a negatively charged acceptor averaged over the crystal equals the ionization energy of the neutral acceptor.

Let us show for the example of nondegenerate Ge : Ga that in the temperature range where E_{1a} is determined a negatively charged Ga atom, prior to capturing a hole from the v-band, surrounds itself by a cloud of screening charge.

From experimental data for Ge : Ga (Refs. 17 and 18) we can determine the temperature T_h at which the electrical conductivity by holes in the v-band σ_p equals the conductivity σ_h for hopping between Ga atoms. For $2\times 10^{14}<N<2\times 10^{16}\,\text{cm}^{-3}$, when $K\approx 0.35$, the following approximations are valid: $T_h=5.3\times 10^{-4}N^{0.27}$, where T_h is in K, N is in cm^{-3}, and the width of the acceptor band $W_a\geq 4k_BT_h$. In a sample with $N=2.3\times 10^{15}\,\text{cm}^{-3}$ for $K=0.35$ at a temperature $T_h=7.45\,\text{K}$, when the electrical conductivity is $\sigma_p+\sigma_h=2\sigma_p\approx 2\times 10^{-6}\,\Omega^{-1}\cdot\text{cm}^{-1}$ (Ref. 17), the Maxwell relaxation time $\tau_s=\varepsilon/(\sigma_p+\sigma_h)\approx 7\times 10^{-7}\,\text{s}$ ($\varepsilon_r=15.4$ for undoped Ge; see Ref. 19). The lifetime of an acceptor in a negatively charged state $\tau_{-1}=1/pSv$ is determined by the concentration of holes p in the v-band, their capture cross section S, and the average thermal velocity $v=(8k_BT/\pi m_{pc})^{1/2}$, where $m_{pc}=0.29m_0$ is the effective mass for electrical conductivity. At $T_h=7.45\,\text{K}$ the capture cross section of a hole from the v-band by a negatively charged Ga atom in germanium $S\approx 7\times 10^{-13}\,\text{cm}^{-2}$ (Ref. 20). For $N=2.3\times 10^{15}\,\text{cm}^{-3}$ the experimental value of the Hall constant $(R_v\sigma_p^2+R_a\sigma_h^2)/(\sigma_p+\sigma_h)^2\approx R_v/4\approx 7\times 10^8\,\text{cm}^3/\text{Cl}$, where

for $\sigma_p=\sigma_h$ the Hall constant for holes that hop from acceptor to acceptor satisfies the condition $R_a \ll R_v$. At $T=T_h$ the concentration of holes in the v-band is $p(T_h)=1/eR_v \approx 2.2 \times 10^9\,\text{cm}^{-3}$. We then have $\tau_{-1}\approx 2\times 10^{-4}$ s, which is considerably larger than the time for setting up the screening τ_s. It is clear that the relation $\tau_{-1}\gg \tau_s$ is also preserved for other N when $K=$ const, since $\tau_s \propto \tau_{-1}\propto 1/p$.

Using (2) and (6), we obtain from Eq. (1) the thermal ionization energy of an acceptor (disregarding the fluctuations or the shift of the top of the v-band) in the form

$$E_{1a}=-k_B\frac{d\ \ln(pT^{-3/2})}{d(1/T)}=\bar{E}_a+\Gamma_a=I_a-\frac{3e^2}{16\pi\varepsilon(\lambda+l)}+\Gamma_a, \tag{7}$$

where

$$\Gamma_a=\frac{\int_{-\infty}^{+\infty}(E_a-\bar{E}_a)g_a f_{-1}f_0 d(E_a-\bar{E}_a)}{\int_{-\infty}^{+\infty}g_a f_{-1}f_0 d(E_a-\bar{E}_a)};$$

$$W_a=1.64\frac{e^2}{4\pi\varepsilon}\left(\frac{8\pi}{3}KN\right)^{1/3};$$

$$\lambda^{-2}=\frac{e^2}{\varepsilon k_B T}N\int_{-\infty}^{+\infty}g_a f_{-1}f_0 d(E_a-\bar{E}_a);$$

$$l=0.554[(1+K)N]^{-1/3}.$$

At low temperatures ($W_a\gg k_BT$) it follows from Eq. (7) that

$$E_{1a}=\bar{E}_a+\Gamma_a=E_F-k_BT\ \ln\ \beta, \tag{8}$$

where the screening length and Fermi level are determined from the relations

$$\lambda^{-2}=\frac{e^2}{\varepsilon}\frac{N}{\sqrt{2\pi}W_a}\exp\left(-\frac{(E_F-\bar{E}_a-k_BT\ \ln\ \beta)^2}{2W_a^2}\right);$$

$$2K=1+\text{erf}\left(\frac{E_F-\bar{E}_a-k_BT\ \ln\ \beta}{\sqrt{2}W_a}\right)=1+\text{erf}\left(\frac{\Gamma_a}{\sqrt{2}W_a}\right).$$

We note that $\Gamma_a=E_F-\bar{E}_a$ in the limit $T\to 0$ K.

Since $W_a\propto(KN)^{1/3}$, we have from Eq. (8) the relation

$$I_a-E_{1a}=\frac{e^2N^{1/3}}{4\pi\varepsilon}F_0(K), \tag{9}$$

where $F_0(K)\to 0$ as $K\to 0$. In the model of Ref. 3 $F_0(K)$ is represented in the form of a table determined by equating the threshold energy for charge flow (mobility) of holes in the v-band and the Fermi level E_F.

At high temperatures ($k_BT\gg W_a$) we find from Eq. (7) that $\Gamma_a\ll k_BT$, and the thermal ionization energy of an acceptor E_{1a} coincides with the average energy level of an acceptor $\bar{E}_a$ (the energy distance between the top of the v-band and the center of the acceptor band):

$$E_{1a}=\bar{E}_a=I_a-\frac{3e^2}{16\pi\varepsilon(\lambda+l)}, \tag{10}$$

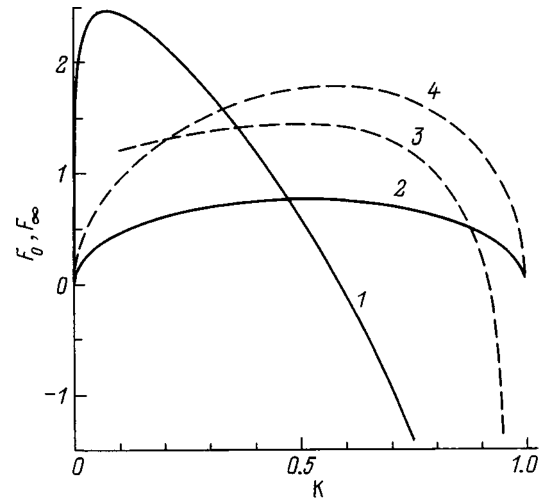

FIG. 1. Dependence of the dimensionless functions F_0 and F_∞ on the degree of compensation of the majority-carrier doping impurity; *1* and *2* are calculations of F_0 and F_∞ based on Eqs. (9) and (11); *3* is F_0 from the model of Ref. 3; *4* is F_∞ from Ref. 4.

where

$$\lambda^{-2}=\frac{e^2K(1-K)N}{\varepsilon k_BT}.$$

For $\lambda\gg l$ we have from Eq. (10)

$$I_a-E_{1a}=\frac{e^3N^{1/2}}{8\pi\varepsilon^{3/2}(k_BT)^{1/2}}F_\infty(K), \tag{11}$$

where $F_\infty(K)=1.5\sqrt{K(1-K)}$. The model of Ref. 4 gives $F_\infty(K)=(K+3)\sqrt{K(1-K)}$.

3. Figure 1 shows the dependences of F_0 and F_∞ on the degree of compensation, calculated using Eqs. (7)–(11), which are compared with the electrostatic models of Refs. 3 and 4.

Figure 2 shows the change in thermal ionization energy (I_a-E_{1a}) of Ga atoms as their concentration N increases as a result of neutron transmutation (Ga) doping of crystals with a natural component of isotopes. The experimental values of the degree of compensation were $K=$ 0.31, 0.35 (Ref. 17); $K\approx$ 0.4 (Ref. 18); and $K\approx$ 0.27, 0.36, and 0.43 (Ref. 21). Since $W_a\geq 4k_BT_h$ (see the discussion above), I_a-E_{1a} was calculated using Eq. (8) and setting $I_a=$ 11.32 meV (Refs. 22 and 23) and $K=$ 0.35. For $W_a\gg k_BT$ when $K=$ 0.35 we have from Eq. (8) that $I_a-E_{1a}\approx 1.47e^2N^{1/3}/4\pi\varepsilon$, in reasonably good agreement with the value calculated according to the model of Ref. 3.

Figure 3 shows the dependence of the thermal ionization energy of As atoms on the dose Φ of thermal neutrons irradiating a crystal of n-type Ge enriched with the isotope ^{74}Ge (Ref. 24). The equation of electrical neutrality has the form $n+KN=N_{+1}$, where $N=N_0+N_{+1}$ and $K\approx$ 0.8. Following Ref. 25, we assume that for a dose $\Phi\approx 10^{18}\,\text{cm}^{-2}$ the concentration of electrons in the c-band is $n=(1-K)N\approx 8\times 10^{15}\,\text{cm}^{-3}$ at $T=$ 300 K. The energy level of an isolated As atom in germanium is $I_d=$ 14.18 meV (Refs. 22 and 23). The thermal ionization energy calculated according to Eq.

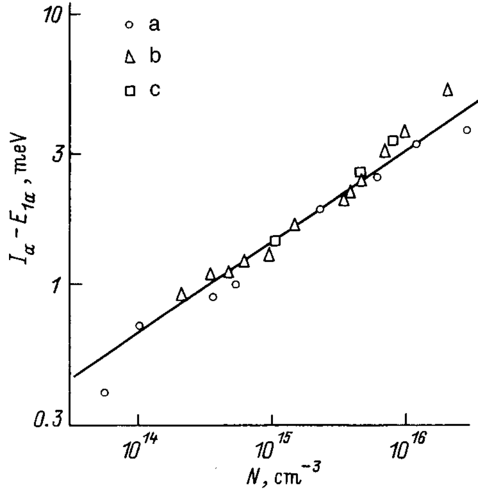

FIG. 2. Calculation based on Eq. (8) of the change in the thermal ionization energy $I_a - E_{1a}$ of Ga atoms in Ge versus their concentration N for a degree of compensation $K=0.35$ when $W_a \gg k_B T$. Experimental data: a—$K=0.31$, 0.35 (Ref. 17); b—$K=0.4$ (Ref. 18); c—$K=0.27$, 0.36, 0.43 (Ref. 21). The energy level of an isolated gallium atom is $I_a = 11.32$ meV (see Refs. 22 and 23).

(7) for donors is $E_{1d} = -k_B d \ln(nT^{-3/2})/d(1/T) = \bar{E}_d + \Gamma_d$ when $n \ll K(1-K)N$ and $W_d = W_{+1} \gg k_B T$, which is larger than the experimental values[24] (curve *1*).

It seems that when the degree of compensation is high and $W_d \gg k_B T$, the measured electrical conductivity $(\sigma_n + \sigma_h)$ and Hall constant $(R_c \sigma_n^2 + R_d \sigma_h)^2/(\sigma_n + \sigma_h)^2$ are determined[26] by thermally excited electrons at the center of the donor band (σ_h, R_d) and by electrons in the c-band (σ_n, R_c). In this case, when $n \ll K(1-K)N$ and $W_d \gg K_b T$, the thermal (Hall) ionization energy of As corresponds to Γ_d (the difference between the energy of the center of the donor band and the Fermi level as $T \to 0$ K) (Fig. 3, curve *2*). According to Eq. (8), the quantity $\Gamma_d = -(\bar{E}_d + E_F + k_B T \ln 2)$ is determined from the equation of electrical neutrality $2K = 1 + \mathrm{erf}(\Gamma_d/\sqrt{2}W_d)$, where $\bar{E}_d > 0$ and $E_F < 0$ are measured from the bottom of the c-band:

$$\bar{E}_d = I_d - \frac{3e^2}{16\pi\varepsilon(\lambda + l)};$$

$$\lambda^{-2} \approx -\frac{e^2}{\varepsilon}\frac{\partial N_{+1}}{\partial E_F}$$

$$= -\frac{e^2 N}{\varepsilon}\frac{\partial}{\partial E_F}\int_{-\infty}^{+\infty}\frac{g_d d(E_d - \bar{E}_d)}{1 + 2\exp[(E_d + E_F)/k_B T]}.$$

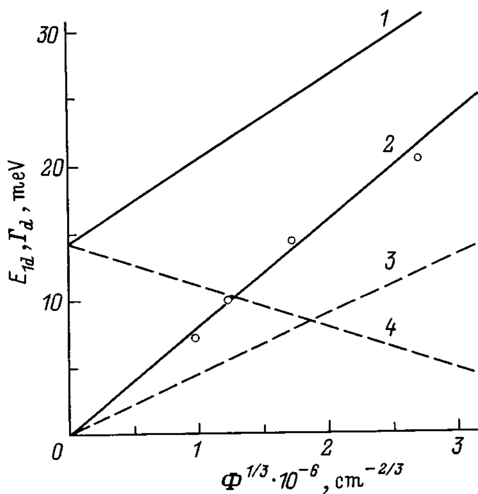

FIG. 3. Experimental dependence (see Ref. 24) of the thermal ionization energy E_{1d} of an As atom on the dose of thermal neutrons for samples of n-type Ge with varying isotopic compositions and the degree of compensation $K=0.79$. *1,2*—calculation of E_{1d} and Γ_d based on our model; *3,4*—calculation of E_{1d} and $|E_F + \bar{E}_d|$ based on the model of Ref. 3. The energy level for an isolated As atom in germanium is $I_d = 14.18$ meV (see Refs. 22 and 23).

For comparison, Fig. 3 shows values of the thermal ionization energy E_{1d} calculated using the model of Ref. 3 for $K = 0.79$ (the difference between the threshold energy for transport and E_F; curve *3*) and $|E_F + \bar{E}_d|$ (curve *4*).

4. Let us consider the dependence of the thermal ionization energy of Zn atoms in p-type Ge, where the hole concentration p in the v-band is determined by transitions of Zn from charge state (-1) to charge state (-2) through the capture of an electron from the v-band.[27] Let the concentration of Zn atoms equal $N = N_{-1} + N_{-2}$; the concentration of singly ionized positive donors is KN, where $1 < K < 2$. The the equation of electrical neutrality $p^+ + KN = N_{-1} + 2N_{-2} = N + N_{-2}$ then has the form

$$N_{-2} = N\int_{-\infty}^{+\infty} g_t f_{-2} d(E_t - \bar{E}_t) = p + (K-1)N, \tag{12}$$

where $g_t = (\sqrt{2\pi}W_t)^{-1}\exp(-(E_t - \bar{E}_t)^2/2W_t^2)$; the probability that a Zn atom is in the charge state (-2) is $f_{-2} = 1 - f_{-1} = [1 + 4\exp((E_t - E_F)/k_B T)]^{-1}$; and the zinc energy levels $E_t > 0$ and $E_F > 0$ are measured from the top of the v-band.

According to Eq. (3), the variance of fluctuations in the energy level of a Zn atom when it makes transitions from charge states (-1) to (-2) for $p \ll KN$ is

$$W_t = \sqrt{W_{-2}^2 + W_{-1}^2} = \sqrt{5}W_{-1}$$

$$\approx 3.67\frac{e^2}{4\pi\varepsilon}\left(\frac{4\pi}{3}N(1+K)\right)^{1/3}\left(\frac{4K-2}{1+K}\right)^{1/2}. \tag{13}$$

The average value of the energy level, i.e., the difference between energies of Zn atoms in charge states (-1) and (-2), is [compare Eq. (6)]

$$\bar{E}_t = \bar{E}_{-2} - \bar{E}_{-1} = I_t - \frac{9e^2}{16\pi\varepsilon(\lambda + l)}, \tag{14}$$

when $\bar{E}_{-2} = I_{-2} - 12e^2/16\pi\varepsilon(\lambda + l)$, $\bar{E}_{-1} = I_{-1} - 3e^2/16\pi\varepsilon \times (\lambda + l)$, $I_t = I_{-2} - I_{-1} \approx 86.5$ meV is the energy level of an isolated Zn atom in charge state (-1) in p-type Ge (Ref. 23), $l = 0.554[N(1+K)]^{-1/3}$, and the screening length[11] is

$$\lambda^{-2} \approx \frac{e^2}{\varepsilon}\frac{\partial N_{-2}}{\partial E_F} = \frac{e^2 N}{\varepsilon k_B T}\int_{-\infty}^{+\infty} g_t f_{-2} f_{-1} d(E_t - \bar{E}_t). \tag{15}$$

Note that $I_{-2}-\bar{E}_{-2}$ is the decrease in affinity energy of a hole for a Zn atom in charge state (-2) due to its screening by the distributed charge $(+2e)$.

Upon determining E_F and dE_F/dT, from Eq. (12) based on Eq. (1), when $p \ll (2-K)(K-1)N$, we find the thermal ionization energy of a negatively charged Zn ions in p-type Ge:

$$E_{1t}=-k_B\frac{d\ \ln(pT^{-3/2})}{d(1/T)}=\bar{E}_t+\Gamma_t, \tag{16}$$

where

$$\Gamma_t=\frac{\int_{-\infty}^{+\infty}(E_t-\bar{E}_t)g_t f_{-1} f_{-2}d(E_t-\bar{E}_t)}{\int_{-\infty}^{+\infty}g_t f_{-1} f_{-2}d(E_t-\bar{E}_t)}.$$

A calculation based on Eq. (16), with allowance for Eqs. (12)–(15), for $5\times10^{14}<N<5\times10^{16}\,\mathrm{cm}^{-3}$, $K\approx 1.3$, and $T \approx 100$ K, gives $E_{1t}<I_t$, which agrees with experiment.[27] For example, when $N=3\times10^{16}\,\mathrm{cm}^{-3}$, the thermal ionization energy $E_{1t}\approx 65$ meV. For $K\approx 1.5$ and $T\approx 150$ K, the measured quantity $E_{1t}\approx I_t$ is nearly independent of the concentration of Zn atoms. This is also understandable in view of Eq. (16): when $K\approx 1.5$, the decrease (shift towards the v-band) of $\bar{E}_t$ as N increases compensates for the increase in Γ_t (due to the shift of E_F into the depth of the band gap).

Here we note that the measurement of E_{1t} in Ref. 27 was made in the temperature interval where $W_t\approx k_BT$, and the limiting expressions for F_0 and E_∞ obtained in Refs. 3 and 4 cannot be used.

5. In summary, we have developed a model for the dependence of the thermal ionization energy of an impurity E_1 on its concentration N and degree of compensation K. We have calculated the width of the impurity band W, taking into account the Coulomb interaction between nearest-neighbor charges only. We also have taken into account the screening of ions by holes (or electrons) that hop from impurity to impurity in the temperature range in which E_1 was determined. Tails in the densities of states of the v- and c- bands were disregarded. At extremely low ($W \gg k_BT$) and extremely high ($W \ll k_BT$) temperatures, we obtained analytic expressions (9) and (11) for the thermal ionization energy, which were compared with other theoretical models. For the example of crystalline germanium doped with the hydrogenic impurities Ga and As, and also the multicharged acceptor Zn, we showed that the calculated values of E_1 agree with experimental data for various degrees of compensation and temperature.

The authors express their heartfelt gratitude to A. G. Zabrodskiĭ for useful discussions of this work.

This work was supported by a Grant from INTAS (94-4435).

[1] A. Ya. Shik, Fiz. Tekh. Poluprovodn. **17**, 2220 (1983) [Sov. Phys. Semicond. **17**, 1422 (1983)].
[2] J. M. Ziman, *Models of Disorder* [London–New York–Melbourne, Cambridge University Press (1979), ch. 13, p. 574; Mir, Moscow, 1982].
[3] N. V. Lien and B. I. Shklovskiĭ, Fiz. Tekh. Poluprovodn. **13**, 1763 (1979) [Sov. Phys. Semicond. **13**, 1025 (1979)].
[4] A. A. Uzakov and A. L. Efros, Fiz. Tekh. Poluprovodn. **21**, 922 (1987) [Sov. Phys. Semicond. **21**, 562 (1987)].
[5] J. Monecke, W. Siegel, E. Ziegler, and G. Kuhnel, Phys. Status Solidi B **103**, 269 (1981).
[6] V. L. Bonch-Bruevich, Izv. vuzov. Fizika **28**, 98 (1985).
[7] D. Schechter, J. Appl. Phys. **61**, 591 (1987).
[8] A. G. Zabrodskiĭ and M. P. Timofeev, Fiz. Tekh. Poluprovodn. **21**, 2217 (1987) [Sov. Phys. Semicond. **21**, 1344 (1987)].
[9] N. A. Poklonskiĭ and A. I. Syaglo, Zh. Prikl. Spektrosk. **64**, 367 (1997).
[10] N. A. Poklonskiĭ, A. I. Syaglo, and F. N. Borovik, Fiz. Tekh. Poluprovodn. **30**, 1767 (1996) [Semiconductors **30**, 924 (1996)].
[11] N. A. Poklonski, V. F. Stelmakh, V. D. Tkachev, and S. V. Voitikov, Phys. Status Solidi B **88**, K165 (1978).
[12] S. A. Maĭorov, A. N. Tkachev, and S. I. Yakovlenko, Izv. vuzov. Fizika **35**, 10 (1992).
[13] D. ter Haar, in *Problems in Thermodynamics and Statistical Physics*, edited by P. T. Landsberg [London, Pion (1971); Mir, Moscow (1974), 380 pp.].
[14] N. A. Poklonskiĭ, Izv. vuzov. Fizika **27**, 41 (1984).
[15] M. I. Chibisov, Zh. Éksp. Teor. Fiz. **93**, 1671 (1987) [Sov. Phys. JETP **66**, 954 (1987)].
[16] V. S. Marchenko, Zh. Éksp. Teor. Fiz. **94**, 46 (1988) [Sov. Phys. JETP **67**, 1111 (1988)].
[17] A. G. Andreev, V. V. Voronkov, G. I. Voronkova, A. G. Zabrodskiĭ, and E. A. Petrova, Fiz. Tekh. Poluprovodn. **29**, 2218 (1995) [Semiconductors **29**, 1157 (1995)].
[18] L. V. Govor, V. P. Dobrego, and N. A. Poklonskiĭı, Fiz. Tekh. Poluprovodn. **18**, 2075 (1984) [Sov. Phys. Semicond. **18**, 1292 (1984)].
[19] T. G. Castnerr, N. K. Lee, H. S. Tan, L. Moberly, and O. Symko, J. Low Temp. Phys. **38**, 447 (1980).
[20] V. N. Abakumov, V. I. Perel', and I. N. Yassievich, Fiz. Tekh. Poluprovodn. **12**, 3 (1978) [Sov. Phys. Semicond. **12**, 1 (1978)].
[21] A. G. Beda, F. M. Vorobkalo, V. V. Vaĭnberg, L. I. Zarubin, I. M. Libeznik, and V. V. Ovcharov, Fiz. Tekh. Poluprovodn. **22**, 2065 (1988) [Sov. Phys. Semicond. **22**, 1308 (1988)].
[22] T. M. Lifshits, Instrum. Exp. Tech. **1**, 10 (1993).
[23] *Semiconductors: Group IV Elements and III–V Compounds,* edited by O. Madelung (Springer-Verlag, Berlin–Heidelberg, 1991).
[24] A. N. Ionov, M. N. Matveev, I. S. Shlimak, F. M. Vorobkalo, L. I. Zarubin, and I. Yu. Nemish, Fiz. Tekh. Poluprovodn. **25**, 413 (1991) [Sov. Phys. Semicond. **25**, 251 (1991)].
[25] A. N. Ionov, M. N. Matveev, and D. V. Shmikk, Zh. Tekh. Fiz. **59**, 169 (1989) [Sov. Phys. Tech. Phys. **34**, 351 (1989)].
[26] E. M. Gershenzon, L. B. Litvak-Gorskaya, and G. Ya. Lugovaya, Fiz. Tekh. Poluprovodn. **15**, 1284 (1981) [Sov. Phys. Semicond. **15**, 742 (1981)].
[27] T. M. Burbaev, V. A. Kurbatov, and N. A. Penin, Fiz. Tekh. Poluprovodn. **15**, 1486 (1981) [Sov. Phys. Semicond. **15**, 861 (1981)].

Translated by Frank J. Crowne

Low-temperature photoluminescence in holmium-doped silicon

B. A. Andreev

Microstructure Physics Institute, Russian Academy of Sciences, 603600 N. Novgorod, Russia

N. A. Sobolev and Yu. A. Nikolaev

A. F. Ioffe Physicotechnical Institute, 194021 St. Petersburg, Russia

D. I. Kuritsin

High Purity Material Chemistry Institute, Russian Academy of Sciences, 603600 N. Novgorod, Russia

M. I. Makovijchuk and E. O. Parshin

Institute of Microelectronics, Russian Academy of Sciences, 150007 Yaroslavl', Russia
(Submitted December 28, 1998; accepted for publication December 29, 1998)
Fiz. Tekh. Poluprovodn. **33**, 420–422 (April 1999)

In this paper the photoluminescence (PL) of holmium-doped silicon is discussed. The silicon was first implanted with holmium ions at energies of 1–2 MeV and doses of $1\times10^{13}-3\times10^{14}\,\mathrm{cm}^{-2}$, and then annealed at temperatures of 620–900 °C for 0.5–1 h. In order to increase the concentration of electrically and optically active centers, the silicon was implanted a second time with oxygen ions at energies of 0.14–0.29 MeV and doses of $1\times10^{14}-3\times10^{15}\,\mathrm{cm}^{-2}$. Several photoluminescence lines, which are attributable to the transitions of electrons from the first excited state of the Ho^{3+} ion ($^5I_7$) to the ground state ($^5I_8$), were observed. The amplitudes of the most intense lines, which correspond to transitions at frequencies 5119 and 5103 cm^{-1}, decreased by more than an order of magnitude in the temperature range 4.2–78 K. The PL intensity of the holmium ions increased with increasing concentrations of the implanted rare-earth ions and oxygen. © *1999 American Institute of Physics.*
[S1063-7826(99)00804-2]

Silicon doped with rare-earth elements has continued to attract interest as a promising material for optoelectronics. Its fundamental advantage derives from the fact that electronic transitions of the internal *f*-shell of the rare-earth element are accompanied by light emission with a temperature-independent emission frequency and very small spectral line width.[1] Conferences at which the properties of semiconductors doped with rare-earth ions are discussed are held almost yearly.[2–4] Most current interest centers on erbium impurities, because the emission of this particular rare-earth atom at a wavelength of 1.54 μm can be used in fiber-optic communication lines. At this time, the motivation for doping silicon with other rare-earth elements is primarily to identify patterns of behavior in the rare-earth incorporation process, which can lead either to structural defects or electrically active centers. Aleksandrov *et al.*,[5] for example, were the first to report that inclusion of Ho and Dy impurities leads to the formation of donor centers, and that the concentration of these centers increases with increasing oxygen content either in the original material or one implanted later. They found that implantation of the rare-earth elements Ho, Dy, Er, and Yb followed by annealing leads to formation of oxygen-containing thermal donors and donor centers in the band gap of silicon, which incorporate the rare-earth elements,[6] and that: a) the concentration of oxygen-containing shallow thermal donors, whose ionization energies are distributed in the range $E_c-(20–40)$ meV, does not depend on the type of rare-earth element and is proportional to the implantation dose; b) each rare-earth element enters into the composition of two donor centers with discrete ionization energies near $\sim E_c-$ 70 meV and $\sim E_c-$ 140 meV; in this case the ionization energy of the donors increases with increasing atomic-number position of the rare-earth element in the (Mendeleev's) periodic table. The properties of the structural defects and the distinctive features of the so-called dislocation luminescence associated with their presence are also insensitive to whether Ho, Dy, or Er is incorporated into the silicon.[7,8] This weak dependence of the structural and electrical properties of silicon on the type of rare-earth element introduced is a consequence of the almost identical geometric sizes of these elements and electronic structures of their outer *s*- and *p*-shells. The fundamental difference between rare-earth elements is in the structure of their 4*f*-shells, which also determines the optical and magnetic properties of the material. As far as we know, there have been to date no investigations of these properties in silicon doped with holmium (Si : Ho). Our goal in this study was to investigate the optical properties of Si : Ho obtained by ion implantation.

Ions of holmium were implanted into samples of Czochralski-grown silicon, i.e., *Cz*-Si ⟨100⟩, with *n*- and *p*-type conductivities, at energies $E_{\mathrm{Ho}}=$ 1.0, 1.6, and 2.0 MeV and doses $D_{\mathrm{Ho}}=1\times10^{13}$, 1×10^{14}, and $3\times10^{14}\,\mathrm{cm}^{-2}$. Some samples were implanted a second time with oxygen at energies E_{O} chosen in such a way that the projected ranges

 © 1999 American Institute of Physics

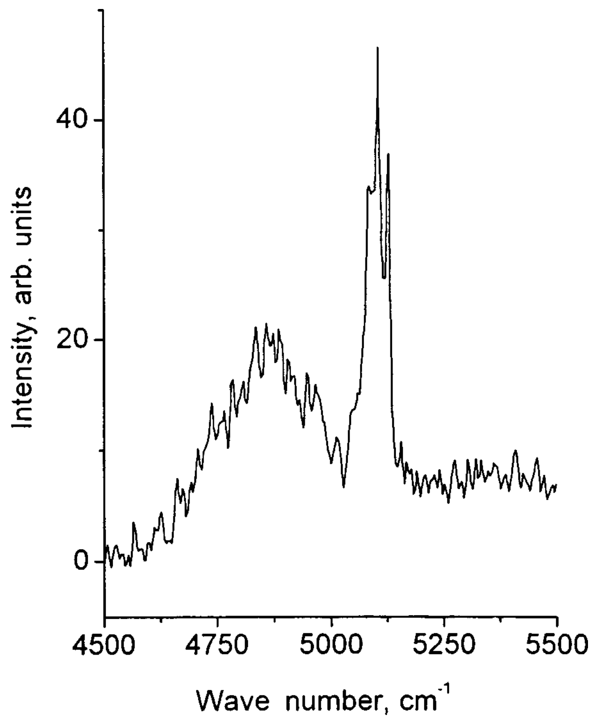

FIG. 1. PL spectrum of Si : Ho : O at 4.2 K after implantation of holmium and oxygen with energies $E_{\mathrm{Ho}}=$ 1 MeV and $E_{\mathrm{O}}=$ 0.14 MeV at doses $D_{\mathrm{Ho}}=1\times10^{13}\,\mathrm{cm}^{-2}$ and $D_{\mathrm{O}}=1\times10^{14}\,\mathrm{cm}^{-2}$, respectively. The resolution of the spectrum was 10 cm^{-1}.

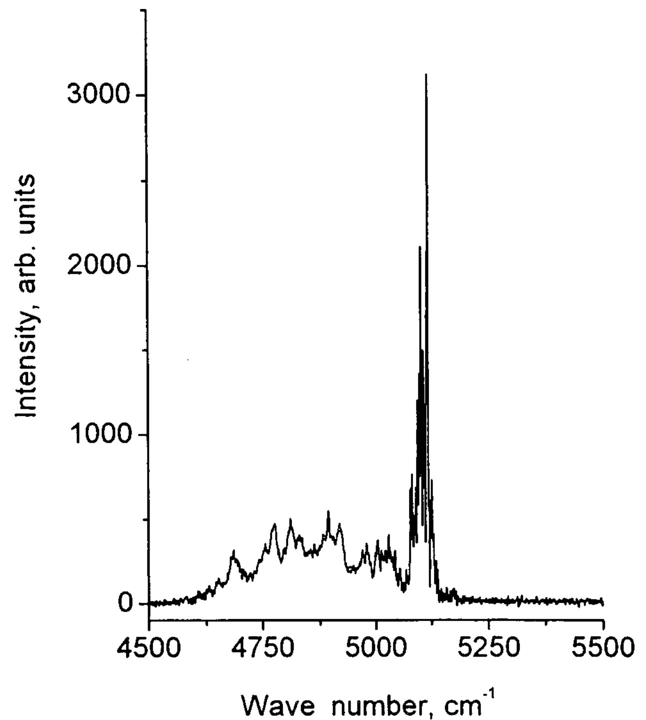

FIG. 2. PL spectrum of Si : Ho : O at 4.2 K after implantation of holmium and oxygen with energies $E_{\mathrm{Ho}}=$ 1 MeV and $E_{\mathrm{O}}=$ 0.14 MeV at doses $D_{\mathrm{Ho}}=1\times10^{14}\,\mathrm{cm}^{-2}$ and $D_{\mathrm{O}}=1\times10^{15}\,\mathrm{cm}^{-2}$, respectively. The resolution of the spectrum was 1 cm^{-1}.

of ions of both types were the same, and at doses (D_{O}) an order of magnitude higher than the holmium dose. Samples implanted with non-amorphizing doses of holmium ($D_{\mathrm{Ho}}=1\times10^{13}\,\mathrm{cm}^{-2}$) were annealed at a temperature of 900 °C for half an hour. Amorphized layers ($D_{\mathrm{Ho}}\geqslant1\times10^{14}\,\mathrm{cm}^{-2}$) were annealed twice, one at 620 °C for 1 hour, the other at 900 °C for 0.5 hour. The first anneal leads to crystallization of the amorphous layer via the mechanism of solid-phase epitaxy, while the second anneal creates the optically and electrically active centers that contain the rare-earth elements.[9]

In order to photoexcite the silicon we used cw emission from a krypton laser (with wavelength $\lambda=$ 647 nm) at power levels of up to 300 mW. The excitation light (whose power level at the input to the cryostat was usually 50–80 mW) is transmitted through an opening in a mirror that focuses the secondary illumination normal to the surface from the implanted side of the layer. The optical power was monitored using a IMO-4C photoelectric power detector. The relative change in power did not exceed 10% at the time the spectrum was recorded (<15 min). The samples were placed in a liquid-helium bath of an optical cryostat with quartz windows in order to input and output the light. The reflected and scattered light at $\lambda=$ 647 nm was attenuated by an optical filter at the input to the spectrometer. The photoluminescence (PL) spectra were recorded with a resolution of up to 0.5 cm^{-1} by a "Bomem- DA3" vacuum Fourier spectrometer in the range 3000–12 000 cm^{-1} with a quartz beam divider in the interferometer and an InSb detector (with a detectivity no less than $4\times10^{11}\,\mathrm{cm}\cdot\mathrm{Hz}^{1/2}\times\mathrm{W}^{-1}$ at an operating temperature of 78 K and a cold filter).

After implantation of a dose $D_{\mathrm{Ho}}=1\times10^{13}\,\mathrm{cm}^{-2}$ of holmiun atoms followed by annealing, no PL lines associated with $4f$-transitions of electrons in the rare-earth element were observed. However, in samples subjected to a second implant with oxygen the PL signal of the Ho^{3+} ion appeared at liquid-helium temperatures (Fig. 1). The most intense lines were observed at frequencies of 5119 and 5103 cm^{-1}. This pair of lines is due to splitting of the holmium terms $^5I_7$ and $^5I_8$ in the crystal field of the silicon host. Clearly, oxygen ions are capable of forming optically active holmium-containing centers, and may enter into the composition of these centers. Note that these lines, which are the dominant lines of the transitions $^5I_7\rightarrow{}^5I_8$ of Ho^{3+} ions, are shifted towards shorter wavelengths in the semiconductor material compared to the position of the dominant lines in insulators.[10]

Increasing the implantation dose of holmium and oxygen by an order of magnitude leads to the appearance of additional lines and a considerable increase in the PL intensity of Ho^{3+} ions at 4.2 K (Fig. 2). However, the 5119 and 5103-cm^{-1} lines continue to dominate the spectrum. Further increasing the implantation doses to $D_{\mathrm{Ho}}=3\times10^{14}\,\mathrm{cm}^{-2}$ and $D_{\mathrm{O}}=3\times10^{15}\,\mathrm{cm}^{-2}$ decreases the intensity of the Ho^{3+} PL somewhat, which probably is attributable to the appearance of additional nonradiative recombination channels.

In the PL spectrum at 4.2 K, in addition to the holmium lines, we see lines of excitons bound at the centers doped by boron and phosphorus impurities. The intensity of these bound exciton lines is roughly an order of magnitude smaller than the intensity of the lines from the Ho^{3+} ions. When the temperature is increased from 4.2 to 78 K, a considerable

decrease is observed (by more than an order of magnitude) in the intensity of the luminescence with no change in the positions of the most intense lines at 5119 and 5103 cm^{-1}. The observed temperature quenching of PL from Ho^{3+} in the spectral range near 5100 cm^{-1} upon raising the temperature is accompanied by the disappearance of the exciton lines bound at the silicon impurities and by the appearance of the dominant free-exciton peak.

In summary, we have observed PL in silicon associated with transitions of electrons from the first excited state to the ground state of Ho^{3+} ions, i.e., ${}^5I_7 \rightarrow {}^5I_8$. Increasing the concentration of implanted holmium ions and oxygen leads to an increase in the PL intensity. In the range of temperatures 4.2–78 K we observed rather strong temperature quenching of the holmium PL intensity.

We wish to thank A. M. Emel'yanov for useful discussions of several results from this work.

The work was supported in part by the Russian Fund for Fundamental Research (Grants 96-02-17901 and 96-03-32581).

[1] N. A. Sobolev, Fiz. Tekh. Poluprovodn. **29**, 1153 (1995) [Semiconductors **29**, 595 (1995)].
[2] MRS Symp. Proceedings **422** (1996).
[3] MRS Symp. Proceedings **486** (1998).
[4] J. Luminesc (1999) [*Proceedings European MRS Spring Meeting* (Strasbourg, 1998)].
[5] O. V. Aleksandrov, A. O. Zakhar'in, N. A. Sobolev, E. I. Shek, M. I. Makoviĭchuk, and E. O. Parshin, Fiz. Tekh. Poluprovodn. **32**, 1029 (1998) [Semiconductors **32** , 921 (1998)].
[6] V. V. Emtsev, V. V. Emtsev Jr., D. S. Poloskin, E. I. Shek, and N. A. Sobolev, J. Luminesc. (1999) (in press).
[7] V. I. Vdovin, T. G. Yugova, N. A. Sobolev, E. I. Shek, M. I. Makovijchuk, and E. O. Parshin, Nucl. Instrum. Methods Phys. Res. B **147**, 116 (1999).
[8] N. A. Sobolev, E. I. Shek, A. M. Emel'yanov, V. I. Vdovin, and T. G. Yugova, Fiz. Tekh. Poluprovodn. **33** (1999) [Semiconductors **33** (1999)] (in press).
[9] N. A. Sobolev, A. M. Emel'yanov, and K. F. Shtel'makh, Appl. Phys. Lett. **71**, 1930 (1997).
[10] *Laser Handbook*, edited by A. M. Prokhorov (Sov. Radio, Moscow, 1978) Vol. 1, part II, Chaps. 11–13.

Translated by Frank J. Crowne

SEMICONDUCTOR STRUCTURES, INTERFACES AND SURFACES

Generation-recombination instabilities in thin-film structures

V. V. Kolobaev

Moscow Power Engineering Institute, 111250 Moscow, Russia
(Submitted June 6, 1998; accepted for publication July 28, 1998)
Fiz. Tekh. Poluprovodn. **33**, 423–424 (April 1999)

The possibility of negative differential resistance, which appears in symmetric thin-film metal-semiconductor-metal structures, is discussed. A model, which can explain to first approximation why generation-recombination processes that take place in the bulk of this sample during bipolar injection should lead to bistability, is proposed. It is shown that the design and use of these negative differential resistance structures could lead to promising new devices for detecting and processing information. © *1999 American Institute of Physics.*
[S1063-7826(99)00904-7]

The symmetric thin-film metal-semiconductor-metal structures (with film thicknesses <1 μm) exhibit a region of negative differential conductivity.[1] Since the thickness of such films is comparable to the diffusion length of injected carriers, it is reasonable to assume that their effective carrier concentrations could be controlled by recombination processes.[2,3]

The goal of our study was to evaluate this possibility. Figure 1 shows a sketch of the structure under consideration, which will be used in subsequent calculations. In this sketch we include only two types of transitions: generation transitions Y_1, Y_2 (which stimulate the instability) and recombination transitions T_{r1}, T_{r2} (which ensure that dynamic equilibrium is established).

Our problem is to determine whether it is possible for bistability to appear, and to estimate the dependence of the threshold voltage (corresponding to the breakdown point) on the generation-recombination parameters of the structure. To address it, we make several simplifying assumptions. Let us assume that the conductivity of the film is close to intrinsic, and that its thickness is less than the Debye screening length and the diffusion length for charge carriers (we ignore the diffusion processes). We also assume that at high electric fields double injection takes place and multiplication of both electrons and holes is possible.

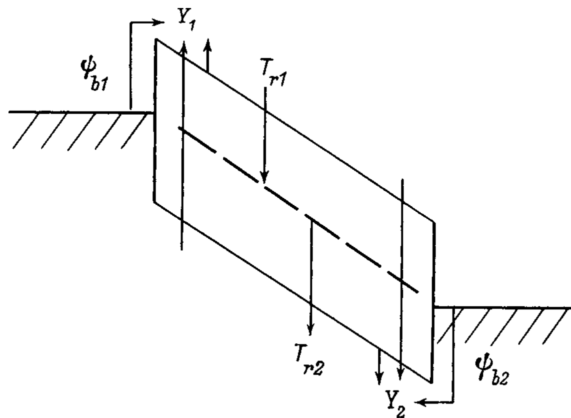

FIG. 1. Schematic diagram used to simulate the appearance of bistability. Y_1 and Y_2 are generation rates of electrons and holes in the semiconductor, T_{r1} and T_{r2} are capture coefficients for electrons and holes by trapping levels, and ϕ_{b1} and ϕ_{b2} are the heights of the contact barriers.

Disregarding the concentration of intrinsic charge carriers compared to the injected charge, we can write the following equations for the structure as a whole:

$$n' = Y_1 n + Y_2 p - T_{r1} n (N_t - n_t),$$

$$p' = Y_1 n + Y_2 p - T_{r2} p n_t,$$

$$n_t' = p' - n', \tag{1}$$

where n, n_t, and p are concentrations of electrons in the conduction band, electrons at trapping levels, and holes in the valence band, respectively; n', p', and n_t' are their derivatives with respect to time, Y_1 and Y_2 are voltage-dependent parameters that characterize the multiplication of injected charge carriers, T_{r1} and T_{r2} are parameters that characterize the interaction of recombination levels with the conduction and valence bands, respectively; and N_t is the concentration of trapping centers. The condition for electrical neutrality is $n_t + n - p = 0$.

Using Eq. (1) with $n_t' = 0$, we find the following relation between the steady-state concentrations of trapped and free carriers:

$$n_t = \frac{T_{r1} N_t n}{T_{r1} n + T_{r2} p}. \tag{2}$$

Using Eq. (2) and the first two equations from (1), we obtain

$$p = \frac{an \pm \sqrt{a^2 - 4 Y_1 Y_2 T_{r1} T_{r2}}}{2 T_{r1} T_{r2}}, \tag{3}$$

where $a = T_{r1} T_{r2} N_t - 4 Y_1 Y_2 T_{r1} T_{r2}$.

Equation (1) and the condition for electrical neutrality of the sample can then be used to find the concentrations of free charge carriers and trapped electrons.

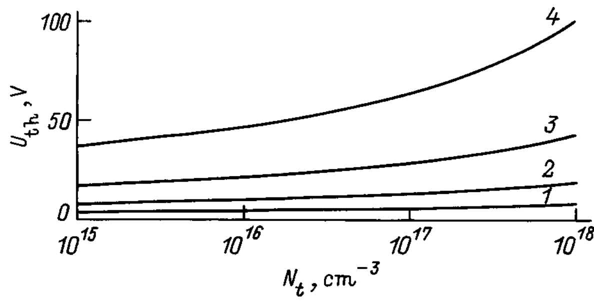

FIG. 2. Dependence of the threshold voltage U_{th} on the concentration of trapping centers N_t for the following film thicknesses d, μm: *1* — 0.5; *2* — 1; *3* — 2; *4* — 4. $E_0 = 5\times10^5$ V/cm, $T_{r1} = T_{r2} = 10^{-8}$ cm^3/s.

The system has a stable high-resistance state at zero charge carrier concentration. From Eq. (3) it is clear that the threshold condition for a transition from an unstable to a stable state occurs when

$$a^2 - 4Y_1Y_2T_{r1}T_{r2} = 0. \tag{4}$$

Let us assume that $T_{r2} = T_{r1} = T_r$ and $Y_2 = Y_1 = Y$. Then Eq. (4) implies that the condition for breakdown of a structure with area S and thickness d can be written

$$T_rN_tdS = 4Y. \tag{5}$$

Taking into account injection from the contacts and ignoring the intrinsic concentrations, we can write the following expression for the generation of carriers in the sample:

$$Y = \frac{4S\pi m^*(kT)^2}{h^3}\, e^{-\phi_b/kT} e^{-E_0/E} \tag{6}$$

(where ϕ_b is the height of the contact barrier). From Eqs. (5) and (6) we can determine the threshold value for the breakdown voltage:

$$U_{th} = \frac{E_0 d}{\ln[4\pi m^*(kT)^2/h^3T_rN_td] - \phi_b/kT}. \tag{7}$$

Figure 2 shows the dependence of the threshold voltage U_{th} on the concentration of trapping centers for various film thicknesses d. It is clear that the threshold voltage increases smoothly with increasing concentration of trapping centers; however, this dependence is weak.

This discussion allows us to conclude that when carrier multiplication is possible, bipolar injection into thin semiconductor layers can lead to a dynamic phase transition,[4] in which the threshold voltage is controlled by generation-recombination parameters of the film. For small thicknesses this voltage is comparable to the value of the operating voltage of semiconductor devices, which makes it possible to use structures of this type as devices for recording and processing information. The response time is determined by the time for accumulation of charge at the trapping centers; for devices with sizes of about 0.1 μm we estimate this time to be about 10^{-9} s, which makes thin-film structures with negative differential resistance of the generation-recombination type promising.

[1] E. N. Voronkov and V. V. Kolobaev, *Current Instability in Thin Films of Cadmium Telluride. Noise and Degradation Processes in Semiconductor Devices* [in Russian], Publ. of the A. S. Popov MNTORES, Moscow (1997), p. 206.

[2] V. I. Stafeev, Fiz. Tverd. Tela (Leningrad) **1**, 841 (1959) [Sov. Phys. Solid State **1**, 763 (1959)].

[3] M. Lampert and P. Mark, *Current Injection in Solids* [Academic Press, New York, 1970; Mir, Moscow, 1973].

[4] E. Sholl, *Self-Organization in Semiconductors. Nonequilibrium Phase Transitions in Semiconductors Caused by Generation-Recombination Processes* (Mir, Moscow, 1991).

Translated by Frank J. Crowne

Oscillations in the induced photopleochroism of In(Au)/Si thin-film structures

V. M. Botnaryuk

University of Moldova, MD 20009 Kishinev, Moldova

Yu. V. Zhilyaev and Yu. V. Rud'

Physicotechnical Institute, Russian Academy of Sciences, 194021 St. Petersburg, Russia

V. Yu. Rud'

St. Petersburg State Technical University, 195251 St. Petersburg, Russia

(Submitted 25 July, 1998; accepted for publication 28 July, 1998)
Fiz. Tekh. Poluprovodn. **33**, 425–428 (April 1999)

The fabrication of photosensitive In(Au)/Si barrier-contact structures is described and the photoelectric behavior of these structures upon exposure to linearly polarized light incident obliquely on the barrier-contact side is investigated. Oscillations are observed in the spectral dependences of the photoconversion quantum efficiency and induced photopleochroism. The oscillations are explained by interference of the linearly polarized light in the thin silicon films. © *1999 American Institute of Physics.* [S1063-7826(99)01004-2]

It is known that the induced photopleochroism P_I of surface-barrier structures based on cubic semiconductors remains practically unchanged over the entire photosensitivity range, and that its value is controlled by the refractive index of the semiconductor and the angle of incidence Θ on the receiving plane of these structures.[1–3] It was recently established that interference conditions for linearly polarized light at the input window of a heterojunction between porous and crystalline phases of Si can lead to oscillations in the induced photopleochroism.[4] In this paper we report a first attempt to observe these oscillations in the spectral dependence of photopleochroism for surface-barrier structures created by depositing metals on thin single-crystal films of silicon.

1. Single-crystal films of Si with thickness $d=0.6-0.8$ μm were deposited on sapphire plates by a gas-phase method. Under transillumination, the layers of Si were a uniform dark-yellow color and adhered strongly to the substrates we used. The spectra of optical transmission and photoconductivity i_{pc} of these Si layers usually contained clearly marked oscillations in the spectral range 1.2 –2.5 eV, caused by interference of the incident light (Fig. 1). The obvious interference pattern attests to the high quality of the film. Estimating its thickness from the position of successive photoconductivity maxima using the known index of refraction of silicon[5] gives film thicknesses corresponding to measured values.

2. The surface-barrier structures were made by vacuum thermal sputtering of layers of Au and In with thicknesses of 0.5–1 μm on the surface of the Si films, which were only degreased between growth and deposition of the metals. The areas of the prepared In(Au)/Si structures were ~ 1 cm^2.

The resulting structures were excellent rectifiers, with the forward-bias direction corresponding to positive polarity of the external bias on the barrier contact. The residual resistance of these structures was in the range $R_0=10^9-10^{11}\,\Omega$. Illumination of the In/Si and Au/Si structures produced a photovoltaic effect, for which the barrier contacts were charged positive relative to the substrate, which correlates with the forward bias direction. For the best structures the voltage photosensitivity reached 20–30 V/W at $T=300$ K and dominated when the structures were illuminated on the barrier-contact side.

Spectral dependences of the relative photoconversion quantum efficiency η in natural light for typical In/Si and Au/Si structures are shown in Fig. 2. In these structures the long-wavelength edge for η is determined by absorption in silicon; extrapolating the product of the short-circuit photocurrent and the photon energy $(i\hbar\omega)^{1/2}$ as $\hbar\omega\rightarrow 0$, gives the cutoff energy $E_0=1.08$ eV (Fig. 2, curve $2'$), which agrees

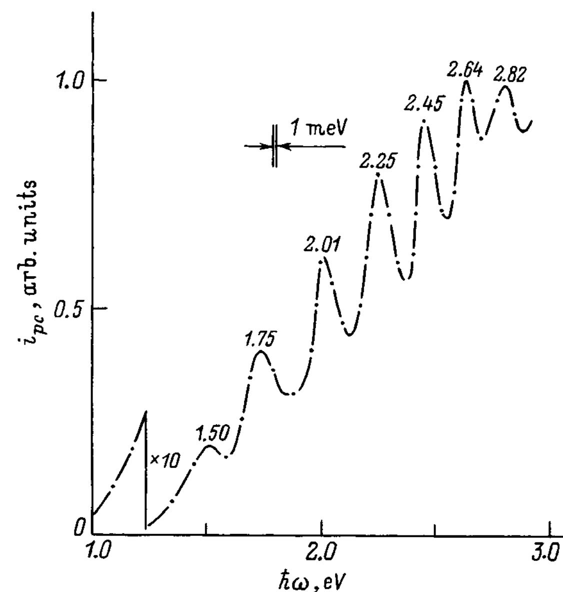

FIG. 1. Spectral dependence of the steady-state photoconductivity of Si films at $T=300$ K in natural light.

 © 1999 American Institute of Physics

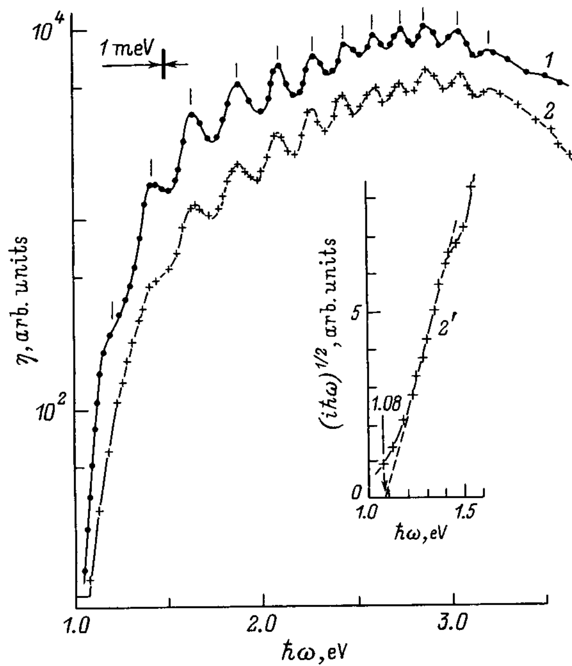

FIG. 2. Spectral dependence of the relative photoconversion quantum efficiency of an In/Si structure (*1*) and an Au/Si structure (*2,2'*) at $T=$ 300 K in natural light (illumination along the normal from the barrier side).

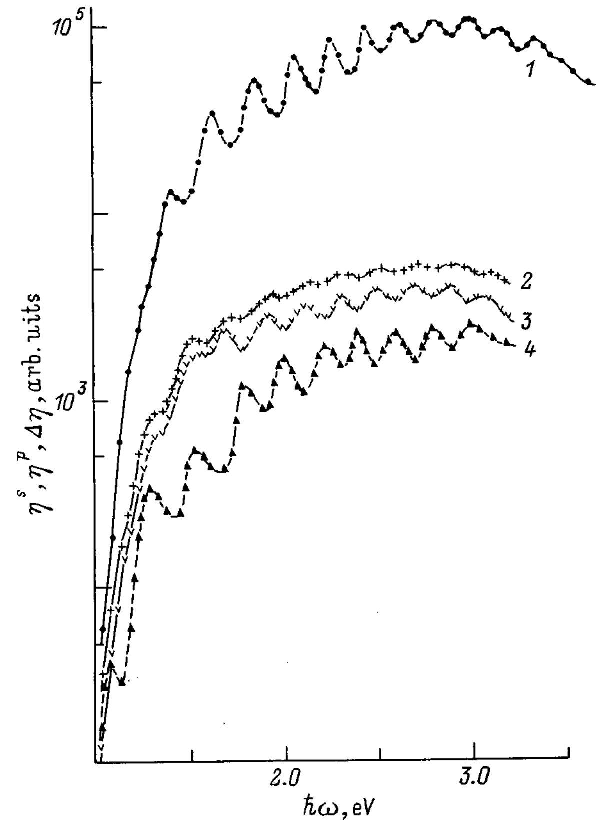

FIG. 3. Spectral dependence of the relative quantum efficiency (*1–3*) and polarization difference (*4*) of the photoconversion quantum efficiency in an Au/Si structure at $T=$ 300 K illuminated by linearly polarized light (*1*—$\Theta=0°$; *2*—$\Theta=50°$).

with the known band gap of crystalline silicon.[6] It is clear from Fig. 2 that in both types of structures an increase in η takes place as the photon energy increases and penetrates deeper into the region of fundamental absorption of the Si film, and that the photosensitivity falls off appreciably only above 3 eV. The spectral dependence of η for our structures attests to their rather high quality with regard to suppression of recombination of nonequilibrium electron-hole pairs at the semiconductor surface. It is characteristic that the photosensitivity spectra η clearly exhibit 12 maxima, independent of the nature of the barrier metal (In or Au), which corresponds to the photoconductivity spectrum of the Si film (Fig. 1) on which these structures were made. From this result it follows that the oscillations in the photosensitivity spectra for these surface-barrier structures are due to interference of the incident light in the semiconductor film itself.

3. When the surface-barrier In(Au)/Si structures were illuminated by linearly polarized light along the normal to the plane of the barrier contact ($\Theta=0°$), the photosensitivity did not depend on the position of the electrical vector **E** of the light wave relative to the crystal axes in the Si crystal. Figure 3 (curve *1*) shows the spectral dependence of the photosensitivity for one of the structures illuminated by linearly polarized light with two mutually orthogonal polarizations. It is clear that for $\Theta=0°$ the spectrum of η in linearly polarized light corresponds to the spectrum obtained for natural light. This derives from the fact that the photoconductivity in a silicon crystal is isotropic. As $\Theta>0°$ increases, the photosensitivity spectrum η^p for polarization parallel to the plane of incidence (**E**$\|$PI) begins to deviate from the spectrum of η^s for **E**$\perp$PI. Figure 3 shows a typical example of the spectra of η^p and η^s when $\Theta=50°$. From this figure it is clear that each polarization of the linearly polarized light has its own spectral dependence of the photosensitivity, and that the relative displacement of these functions along the ordinate increases with increasing Θ. The induced photopleochroism is usually used to characteristize the effect of polarization on the photosensitivity of structures:[7]

$$P_I=\left(\frac{\eta^p-\eta^s}{\eta^p+\eta^s}\right)100\%, \tag{1}$$

where the polarization difference $\Delta\eta=\eta^p-\eta^s$ gives exactly the displacement of the photosensitivity curves as the optical polarization changes. Figure 3 shows the spectral function $\Delta\eta(\hbar\omega)$ at $\Theta=50°$ (curve *4*). It is clear that the curve $\Delta\eta(\hbar\omega)$ also exhibits oscillations. In this case the minima of $\Delta\eta$ are located in regions where η is a maximum, which is associated with the maximal efficiency of transillumination; conversely, the maxima of $\Delta\eta$ occur in the region where η is a minimum, indicating a maximum loss of light to reflection. In comparing curves *2* and *3* (Fig. 3), we should also note the fact that the modulation depth of the spectral photosensitivity curves is larger as a rule for *P*-polarization, and that the maximum approach $\eta^s\rightarrow\eta^p$ corresponds to a minimum of $\Delta\eta$ and conversely. From Eq. (1) it is clear that the nature of the extremum of the induced photopleochroism (minimum or maximum) is directly connected with the character of the extremum in $\Delta\eta$.

Figure 4 shows angular dependences of the induced photopleochroism that are typical of the structures we investi-

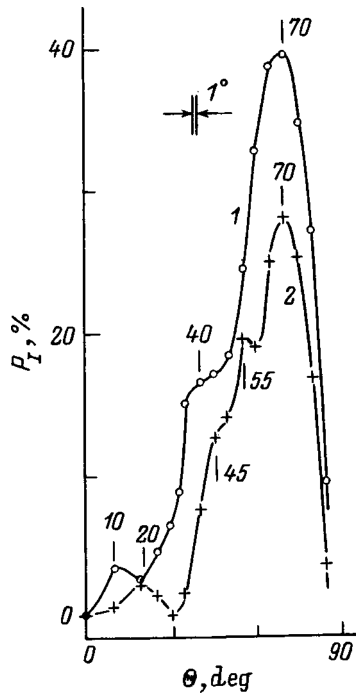

FIG. 4. Angular dependence of the induced photopleochroism for an In/Si structure at $T=$ 300 K ($\hbar\omega$, eV: *1*—1.96; *2*—1.84).

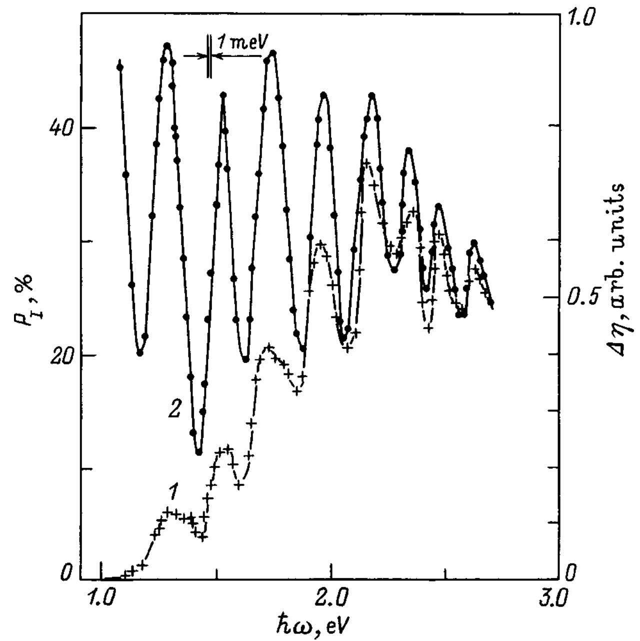

FIG. 5. Spectral dependence of the photoconversion quantum efficiency polarization difference (*1*) and induced photopleochroism (*2*) for an In/Si structure at $T=$ 300 K.

gated in the neighborhood of the adjacent extrema of $\Delta\eta$. It is clear that as the angle of incidence increases, the induced photopleochroism varies nonmonotonically in heterojunctions made of porous Si/Si (Ref. 4), although the primary tendency of these variations reduces to an increase in P_I with increasing Θ with a close to quadratic dependence, $P_I \sim \Theta^2$. The nonmonotonicity of the experimental function $P_I(\Theta)$ arises from interference effects, which are sensitive to the effective thickness of the absorbing layer. From Fig. 4 it is also clear that the character of the angular functions P_I is preserved as the wavelength changes, and that the latter change simply causes a transition from the maximum to the nearest minimum in P_I. We should emphasize here that a decrease in the photopleochroism (Fig. 4) and, accordingly, the polarization difference of the photosensitivity accompanies the decrease in losses to reflection.

On the basis of our investigations, we also found that in the neighborhood of maxima of the spectra $\Delta\eta$ (Fig. 3, curve *4*) the angular dependences of the quantum efficiencies $\eta^p(\Theta)$ and $\eta^s(\Theta)$ correspond to what was expected from the Fresnel relations, which describe the passage of linearly polarized light through the boundaries of two media.[8,9] In fact, for a *P*-wave the quantum efficiency initially increases with increasing Θ, passes through a maximum, and then decreases, whereas for an *S*-wave η increases monotonically with increasing Θ. The angular dependences of η^p and η^s are comparable in the neighborhood of minima of the spectra $\Delta\eta$ (Fig. 3, curve *4*), at which losses to reflection are minimized, and initially an increase is observed in the quantum efficiency, which reaches a maximum and then decreases for both polarizations. Thus there are grounds for associating the decrease in P_I with the effect of transillumination.

Figure 5 shows the spectral dependence of the induced photopleochroism for a typical structure compared with $\Delta\eta(\hbar\omega)$ at a fixed angle of incidence. In agreement with the relation $P_I \sim \Delta\eta$ implied by Eq. (1), in-phase oscillations are clearly present in the spectrum of the polarization difference of quantum efficiencies and in spectra of P_I as a result of interference of the linearly polarized light in the Si film. The period of oscillation of the photopleochroism is the same as that of the photoconductivity (Fig. 1), since the interference of linearly polarized light is also determined in the silicon film. Maximum values of the induced photopleochroism $P_I^{\max}$ at $\Theta=70°$ reach values of 48–50%, which, based on Ref. 10, gives a value $n=$ 3.5 for the refractive index, which is close to the known value for Si.[5] The minima in the spectrum of the coefficient of induced photopleochroism $P_I^{\min}=10$–18% (Fig. 5, curve *2*) are due to interference transillumination and therefore cannot be used to estimate n since in Ref. 10 the interference was disregarded.

Thus, the interference of linearly polarized light in the active regions of photosensitive structures (for the example of In/Si and Au/Si structures) is accompanied by the appearance of oscillations in the spectrum of the induced photopleochroism. This effect may find applications in polarization photoelectronics as a way to create selective photoanalyzers of linearly polarized light.

[1] S. G. Konnikov, D. Melebaev, V. Yu. Rud', and M. Serginov, Pis'ma Zh. Tekh. Fiz. **18**, 39 (1992) [Sov. Tech. Phys. Lett. **18**, 382 (1992)].
[2] S. G. Konnikov, V. Yu. Rud', Yu. V. Rud', D. Melebaev, A. Berkeliev, M. Serginov, and S. Tilevov, Jpn. J. Appl. Phys. **32**, 515 (1993).
[3] V. Yu. Rud', Doctoral Dissertation (A. F. Ioffe Physicotekh. Inst., Russ. Acad. Sci., St. Petersburg, 1995).
[4] V. Yu. Rud' and Yu. V. Rud', Fiz. Tverd. Tela (St. Petersburg) **31**, 245 (1997) [Phys. Solid State **31**, 152 (1997)].
[5] E. M. Voronkova, V. N. Grechushnikov, G. I. Distler, and I. P. Petrov, *Optical Materials for Infrared Engineeering* [in Russian], Nauka, Moscow, 1965 .

[6]Yu. I. Ukhanov, *Optical Properties of Semiconductors* [in Russian], Nauka, Moscow, 1977.
[7]Yu. V. Rud', Izv. vuzov. Fizika, 8, p. 68 (1968).
[8]G. S. Landsberg, *Optics* [in Russian], Nauka, Moscow, 1976.
[9]R. Azzam and M. Bashara, *Ellipsometry and Polarized Light*, Mir, Moscow, 1981.
[10]G. A. Medvedkin and Yu. V. Rud', Phys. Status Solidi A **67**, 333 (1981).

Translated by Frank J. Crowne

Surface of *n*-type InP (100) passivated in sulfide solutions

V. N. Bessolov and M. V. Lebedev

A. F. Ioffe Physicotechnical Institute, Russian Academy of Sciences, 194021 St. Petersburg, Russia

D. R. T. Zahn

Institut für Physik, TU-Chemnitz, D-09107 Chemnitz, Germany

(Submitted October 1, 1998; accepted for publication October 5, 1998)
Fiz. Tekh. Poluprovodn. **33**, 429–434 (April 1999)

X-ray photoelectron spectroscopy, the Kelvin probe method, and Raman scattering are used to study the properties of the surface of *n*-type InP (100) passivated by ammonium sulfide dissolved in water or in *t*-butyl alcohol. Both treatments are found to cause a reduction in the depth of the depleted skin layer, a shift of the surface Fermi level toward the conduction band, and an enhancement of the electron work function and increase in the ionization energy of the semiconductor. The processing in the alcohol solution yields a stronger effect than processing in an aqueous solution. For sulfidization in an alcohol solution the surface Fermi level shifts by 0.2 eV, while the ionization energy increases by 0.53 eV. © *1999 American Institute of Physics.* [S1063-7826(99)01104-7]

1. INTRODUCTION

Because of its high mobility and relatively wide conduction band, indium phosphide is an important material for high-frequency field-effect transistors, solar cells, and optoelectronic integrated circuits. Passivation of InP surfaces by sulfur atoms modifies its electronic properties significantly;[1–4] in particular, it lowers the density of surface states at an InPa/insulator interface,[1,2] makes the height of a Schottky barrier depend on the work function of the metal,[3] raises the photoluminescence intensity,[4] and improves the characteristic of InGaAlP (Ref. 5) and InGaAsP (Ref. 6) laser diodes.

The modification of the electronic properties of surfaces has initiated studies of the chemical composition and the atomic and electronic structure of InP surfaces covered with sulfur atoms. It has been found that when InP is treated in sulfide solutions, the sulfur on the surface is bound only to indium atoms[7] and can be found in at least three valence states[8] corresponding to: (a) elementary sulfur, (b) sulfur bound to indium on the surface, and (c) sulfur occupying a phosphorus site in the skin layer of the semiconductor. It has been shown that the adsorption of sulfur on *p*-type InP, followed by annealing at temperatures in the range 200–300 °C, has led in several cases to a shift in the surface Fermi level toward the conduction band,[9,10] while on a sulfided *n*-type InP surface the Fermi level was shifted only slightly in the direction of the valence band and returned to its original location after annealing.[10]

Sulfiding of InP surfaces is mainly done from the gaseous phase[9] or from water solutions of sodium sulfide,[4] or ammonium sulfide[1–3,7,8,10] On the other hand, the properties of the sulfide solution have a major effect on the chemical composition and electronic structure of the sulfided surface. Thus, for example, it has been shown that using alcohols increases the efficiency of sulfur coating formation on GaAs surfaces[11] and this has made it possible to increase the photoluminescence intensity substantially[11] and reduce the skin layer band bending.[12] Passivation in alcohol sulfide solutions has been used to enhance the efficiency of InGaAs/AlGaAs[13] and InGaAsP/InP[14] laser diodes.

In this paper we use x-ray photoelectron spectroscopy, the Kelvin probe method, and Raman scattering to compare the chemical composition and electronic properties of *n*-type InP (100) surfaces that have been sulfided in water and alcohol solutions of ammonium sulfide.

2. EXPERIMENT

Wafers of *n*-InP (100) with an electron concentration $n \approx 10^{18}$ cm^{-3} were studied. Prior to sulfiding, the wafers were etched in HF for 1 min at room temperature.

Two different solutions were used for sulfiding: first, in a water solution of ammonium sulfide $(NH_4)_2S+H_2O$ (1:10) for 1.5 min and second, in a solution of ammonium sulfide in *t*-butyl alcohol $(NH_4)_2S+t\text{-}C_4H_9OH$ (1:100) for 30 s. In order to remove the sulfide solution from the surface at the end of the sulfiding process the sample was placed in a centrifuge and spun in air at a speed of 1000 rpm.

X-ray photoelectron spectra of the InP surface were taken on a Perkin- Elmer PHI 5400 spectrometer using Mg-K_α emission (energy $h\nu = 1253.6$ eV) at a power level of 300 W. The samples were placed in a vacuum chamber no later than 10 min after the sulfiding process was completed. The energies of the peaks were measured relative to the carbon C 1*s* (285.5 eV) peak.[15]

The electron work function of the semiconductor before and after sulfiding was determined by the Kelvin probe method using a dynamic capacitor for measuring the contact potential difference between the semiconductor and a 500-nm-thick gold film deposited on the SiO_2 substrate.[16] The metal probe had a diameter of 40 μm and its work

 © 1999 American Institute of Physics

TABLE I.

Surface	Thickness of sulfide layer, ML	Work function eV	δ, nm	V_b, eV
Unsulfided (etched in HF)	⋯	4.885	13.8	0.14
Sulfided in $(NH_4)_2S+H_2O$	3.9	5.063	11.2	0.09−0.14*
Sulfided in $(NH_4)_2S+t-C_4H_9OH$	1.5	5.210	9.2	−0.06**

Note: *The scatter is because of the different shifts of the In $3d_{5/2}$ and P $2p$ peaks.
**A negative barrier height means that the bands are bent downward.

function did not change by more than 15 meV in the course of the measurements. The work function of gold was assumed to be 5.4 eV.[17]

Raman spectra were measured in the range 150–800 cm^{-1} at room temperature on a Dilor XY spectrometer equipped with a multichannel detector and an optical microscope to ensure focussing of the laser beam to a spot diameter of 1 μm.[18] The excitation wavelength was the $\lambda=457.9$-nm line of an Ar^+-laser (the penetration depth of the radiation in InP is 54.7 nm)[19] and the laser power was 2.5 mW. According to the selection rules[20] only optical LO-phonons should be observed in the spectra. The spectra were measured in air.

3. EXPERIMENTAL RESULTS

3.1. Studies of sulfided *n*-type InP (100) surfaces by x-ray photoelectron spectroscopy and the Kelvin probe method

The reference x-ray photoelectron spectra of all the surfaces contain peaks of In, P, C, and O, while the spectra of the sulfided surfaces also contain S. The intensities of the oxygen and carbon peaks were largely unaffected by sulfiding in an aqueous solution, but they decreased noticeably when an alcohol solution was used. The thickness of the sulfide coating estimated by the method of Carpenter *et al.*[21] is given in Table I in units of monolayers. All of the surfaces were rich in indium. The highest In/P ratio (1.61) was observed on the surface treated in the $(NH_4)_2S+t-C_4H_9OH$ solution and the lowest (1.43) on the surface of the unsulfided semiconductor.

Figures 1 and 2 show x-ray spectra of P $2p$ and In $3d_{5/2}$. All the spectra are normalized to the maximum peak height. The spectrum of P $2p$ of unsulfided InP after etching in HF (Fig. 1a) contains a doublet associated with indium phosphide in the bulk semiconductor, for which the P $2p_{3/2}$ energy is 129.0 eV relative to the position of the Fermi level at the surface. Since the P $2p_{3/2}$ peak stands 127.8 eV from the boundary of the valence band of InP (Ref. 22), we estimate the initial band bending of the unsulfided semiconductor to be 0.14 eV. The In $3d_{5/2}$ spectrum of the unsulfided semiconductor (Fig. 2a) contains a peak associated with bulk InP (with an energy of 444.8 eV) and a small peak at about 445.5 eV associated with indium oxides. Note that the oxygen observed in the reference spectra is mainly in a physisorbed

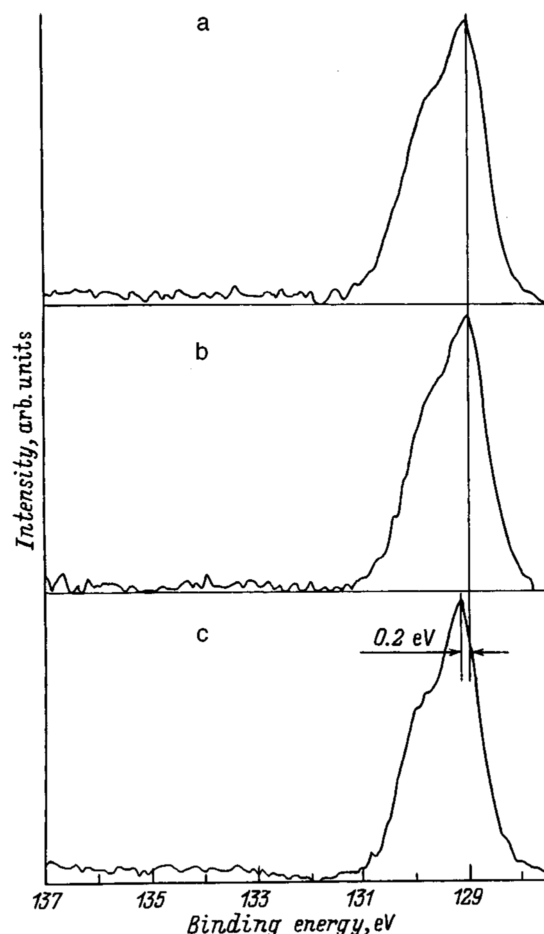

FIG. 1. P $2p$ photoelectron spectra of three different n-InP (100) surfaces initially etched in HF: (a) unsulfided surface, (b) sulfided in a water solution of ammonium sulfide $(NH_4)_2S+H_2O$, and (c) sulfided in an $(NH_4)_2S+t-CH_4H_9OH$ solution.

state, since the amount of it greatly exceeds the observed amount of indium oxides and no phosphorus oxides were observed at all.

With sulfiding in a water solution of ammonium sulfide, the P $2p$ spectrum was essentially unaffected (Fig. 1b), but in the In $3d_{5/2}$ spectrum the intensity of the 445.5 eV oxide peak decreased somewhat (Fig. 2b). Here a slight shift toward higher energies was observed. (The shift was <0.05 eV, i.e., less than the accuracy of the energy measurement.)

With sulfiding employing a solution of ammonium sulfide in *t*-butyl alcohol, the peaks of both P $2p$ (Fig. 1c) and In $3d_{5/2}$ (Fig. 2c) shifted by 0.2 eV toward higher binding energies relative to their positions for the unsulfided semiconductor. This indicates that the surface Fermi level has shifted into the conduction band. Given the magnitude of the band bending at the surface of the unsulfided semiconductor (0.14 eV), we may conclude that after sulfiding in a *t*- butyl alcohol solution of ammonium sulfide, the surface Fermi level lies above the conduction band.

The shape of the P $2p$ spectrum does not change when InP is sulfided in a solution of ammonium sulfide in *t*-butyl alcohol, and no distinctive features at high binding energies, due to the formation of oxides and sulfides of phosphorus, were observed. This suggests that compounds with P–S

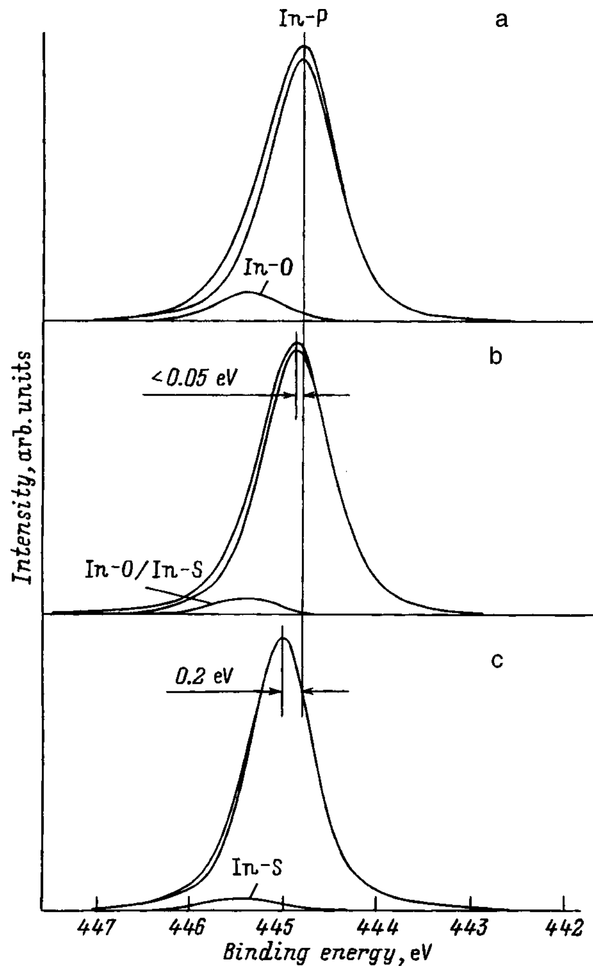

FIG. 2. In $3d_{5/2}$ photoelectron spectra of three different n-InP (100) surfaces initially etched in HF: (a) unsulfided surface, (b) sulfided in a water solution of ammonium sulfide $(NH_4)_2S+H_2O$, and (c) sulfided in an $(NH_4)_2S+t\text{-}CH_4H_9OH$ solution.

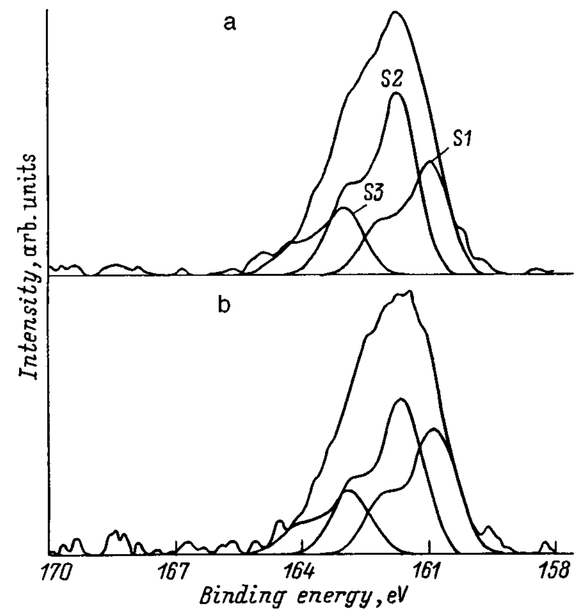

FIG. 3. S $2p$ photoelectron spectra of two different n-InP (100) surfaces initially etched in HF: (a) sulfided in a water solution of ammonium sulfide $(NH_4)_2S+H_2O$ and (b) sulfided in an $(NH_4)_2S+t\text{-}CH_4H_9OH$ solution.

bonds are as highly soluble in alcohol solutions as in water solutions.[23]

In the spectrum of In $3d_{5/2}$ (Fig. 2c) for InP sulfided in a solution of ammonium sulfide in t-butyl alcohol, the chemical shift between the two peaks decreases by 0.2 eV relative to the spectrum of unsulfided InP (Fig. 2a) or InP sulfided in a water solution of ammonium sulfide (Fig. 2b). The oxides and sulfides of indium are hard to distinguish by x-ray spectroscopy,[24] in contrast with those of gallium, where the positions of the corresponding peaks differ by $\sim 0.4-0.6$ eV (Ref. 25). Nevertheless, by analogy with gallium, the reduction in the chemical shift of the high-energy component of the In $3d_{5/2}$ spectrum indicates that this component originates mainly from indium sulfide. Note that a similar chemical shift has been observed for In–S bonds.[23]

Figure 3 shows S $2p$ spectra from InP sulfided in solutions of ammonium sulfide in water (Fig. 3a) and t-butyl alcohol (Fig. 3b). The spectra were resolved as in Ref. 8 using the following parameters: intensity ratio $2p_{3/2}:2p_{1/2}=2:1$, energy between $2p_{3/2}$ and $2p_{1/2}$ 1.08 eV, and half-width of the peaks 1.2 eV. Three different states of sulfur were resolved in the spectra, with $p_{3/2}$ peak energies relative to the top of the valence band of 160.90 eV (S1), 161.65 eV (S2), and 162.90 eV (3). The S1 state is associated with the sulfur bound to indium on the surface, S2 is associated with the sulfur occupying a phosphorus site in the skin layer of the semiconductor, and S3 is associated with the elementary sulfur on the surface adsorbed on the sulfide coating.[10]

The intensity of the S3 peak is the same for sulfiding in both solutions, while the ratio of the S1 and S2 peaks is different. For InP sulfided in a water solution of ammonium sulfide, the intensities are in the proportion S1 : S2 : S3 $=1.65:2.70:1$, and InP sulfided in a solution of ammonium sulfide in t-butyl alcohol, this proportion is 2.00:2.45:1.

The work function of n-InP (100) increases with sulfiding in a water solution and, to an even greater degree, with sulfiding in an alcohol solution of ammonium sulfide (Table I).

3.2. Raman scattering studies of the surface depletion region of sulfided *n*-type InP (100)

The depth of the surface region of the semiconductor was estimated by analyzing Raman scattering spectra.[26]

Given that the magnitude of the surface band bending is $V_{b0}=0.14$ eV for the unsulfided semiconductor, we estimate the depth δ of the depletion region using the formula

$$\delta=\sqrt{\frac{2\varepsilon_s\varepsilon_0 V_{b0}}{eN}},$$

where ε_0 is the dielectric constant, $\varepsilon_s=12.4$ is the static relative dielectric constant of InP, e is the electronic charge, and N is the donor concentration in InP. This calculation yields $\delta=13.8$ nm.

Since δ is less than the penetration depth of the laser light into the semiconductor, the Raman spectra should include both surface and volume scattering modes. In fact, two peaks can be seen clearly in the Raman spectra (Fig. 4). The peak L^- (303.7 cm^{-1}) is caused by scattering on a coupled

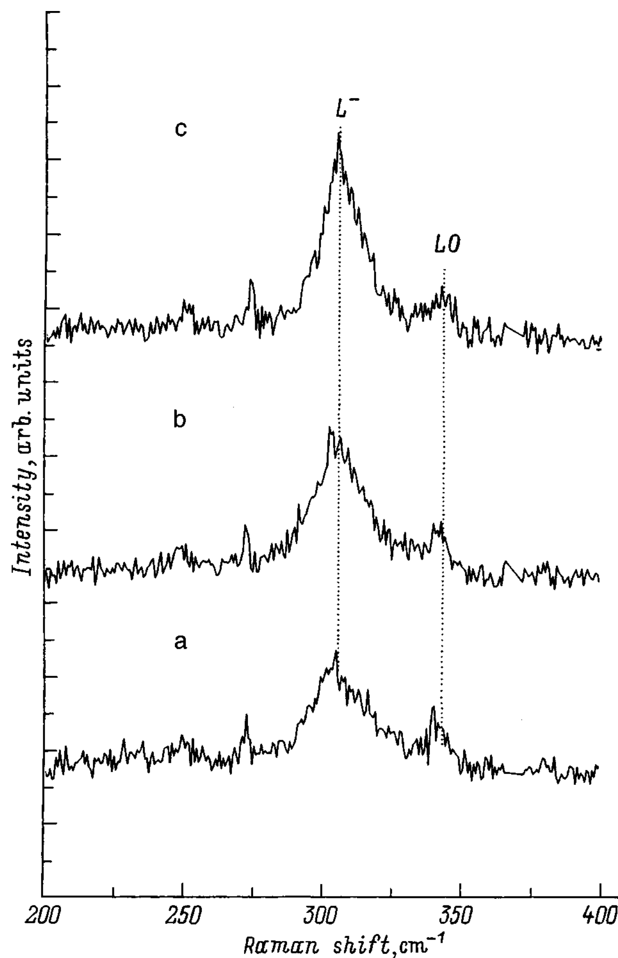

FIG. 4. Raman spectra of three different *n*-InP (100) surfaces initially etched in HF: (a) unsulfided surface, (b) sulfided in a water solution of ammonium sulfide $(NH_4)_2S+H_2O$, and (c) sulfided in an $(NH_4)_2S+t\text{-}CH_4H_9OH$ solution.

phonon-plasmon mode in the bulk of the semiconductor at free carriers. The peak LO (341.9 cm^{-1}) is associated with the depletion layer at the surface of the semiconductor. In unsulfided InP the intensity of the LO peak is half that of the L^- peak (Fig. 4a).

Sulfiding the semiconductor in the different solutions leads to a change in the relationship between the volume (L^-) and surface (LO) peaks. For sulfiding in an aqueous solution of ammonium sulfide, the L^- peak is three times higher than the LO peak (Fig. 4b) and for sulfiding in a *t*-butyl solution, it is 4.5 times higher. Thus, the sulfiding of InP causes a reduction in the depth of the depletion region of the semiconductor which is greater when the ammonium sulfide is dissolved in *t*-butyl alcohol.

The depth δ of the depletion layer was calculated[12,26] from the ratio $I(LO)/I(L^-)$ of the peak intensities. The results are shown in Table I. Also shown there are the surface band bending V_b obtained from the x-ray photoelectron spectroscopy data.

Thus, when an *n*-InP (100) surface is treated in a water solution of ammonium sulfide, the surface Fermi level E_{Fs} shifts slightly toward the conduction band; the depth of the depletion region of the semiconductor decreases slightly and the electron work function increases. Treating an *n*-InP (100) surface in a *t*-butyl alcohol solution of ammonium sulfide causes the surface Fermi layer to shift into the conduction band of the semiconductor, and leads to a larger reduction in the depth of the depletion layer and increase in the work function. Here the fraction of sulfur bound to indium atoms at the semiconductor surface is greater than the fraction that displaces phosphorus.

4. DISCUSSION OF RESULTS

The rate constant for formation of the sulfide coating was calculated from the x-ray photoelectron spectroscopy data as the ratio of the thickness of the sulfide layer to the concentration of sulfur in the solution and the duration of the sulfiding treatment. It turns out that the rate constant is roughly an order of magnitude higher when *n*-InP is sulfided with a *t*-butyl alcohol solution of ammonium sulfide than with a water solution. Similar results have been obtained for the sulfiding of GaAs in different solutions of ammonium sulfide.[27]

Decomposition of the S $2p$ spectra (Fig. 3) showed that as the rate of formation of the sulfide coating increases, the fraction of the S1 state increases compared to that of S2, i.e., just as in the case of annealing of a sulfided surface ,[12,14] there is an increase in the ratio of the sulfur bound to indium to the sulfur which displaces phosphorus vacancies in the surface layer of the semiconductor.

According to the Arrhenius equation, the rate constant for the sulfiding reaction characterizes the energy released during adsorption of atoms on the semiconductor surface. Since the rate constants for sulfiding from solutions of ammonium sulfide in *t*-butyl alcohol and water differ by roughly an order of magnitude, it is possible to estimate the difference in adsorption energies for sulfiding in these solutions. The energy released during adsorption of a sulfur atom from a *t*-butyl alcohol solution is roughly 0.06 eV higher than that from a water solution. Theoretical studies of InP (100) surfaces coated with S atoms[28] show that there are several possible atomic structures for these surfaces with different mutual positions of the sulfur and phosphorus atoms and a difference of less than 0.1 eV among the energies of the several structures. It was pointed out that the actual atomic structure of an InP (100)-S surface is a statistical sum of different structures with similar energies and special emphasis was placed on the importance of kinetic processes in establishing the surface structure. The decomposition of the S $2p$ spectra (Fig. 3) suggests that kinetic processes can have an important influence on the atomic structure of the surface.

On the other hand, increasing the reaction rate constant for formation of a sulfide surface reduces the depth of the depletion region and also shifts the surface Fermi level toward the conduction band. The latter is a consequence of a change in the electronic structure of the surface that can also serve as further indirect confirmation of changes in the atomic structure of sulfided InP (100) surfaces.

The Raman spectroscopy data make it clear that the reduction in the depth of the depletion region after passivation in a water solution should indicate a drop in the surface

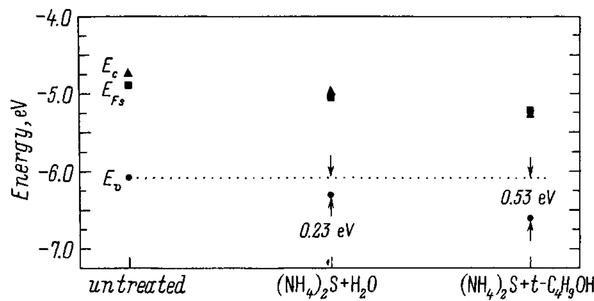

FIG. 5. Locations of the surface Fermi level (E_{Fs}) and the edges of the conduction (E_c) and valence (E_v) bands relative to the vacuum level for three different *n*-InP (100) surfaces– an unsulfided surface (etched in HF) and surfaces sulfided in $(NH_4)_2S+H_2O$ and in $(NH_4)_2S+t\text{-}CH_4H_9OH$.

barrier (by 0.05 eV). However, the x-ray photoelectron spectroscopy data do not confirm this result. This contradiction indicates that heightened doping level at the semiconductor surface must be taken into account when analyzing the Raman spectra, since the amount of sulfur occupying phosphorus vacancies (the S2 component) is quite high. The amount of sulfur associated with the S2 component is entirely sufficient to ensure a rise in the donor concentration by this amount at the semiconductor surface. Note that a rise in the donor concentration has been observed during sulfidizing of GaP in water solutions of ammonium sulfide.[29]

In the meantime, the change in depth of the depletion region due to sulfiding in a solution of ammonium sulfide in *t*-butyl alcohol still cannot be explained solely by the additional doping at the semiconductor surface, since the amount of sulfur on the surface and the amount of sulfur associated with the S2 component are less than the amount obtained with sulfiding in a water solution.

The combined x-ray photoelectron and Kelvin probe data show that sulfiding leads to a rise in the ionization energy of the semiconductor: by 0.23 eV in the water solution and by 0.53 eV in the alcohol solution (Fig. 5). The change in the ionization energy is caused by a change in the dipole moment at the surface.[30] Two facts– the greater change in the ionization energy and, therefore, in the magnitude of the dipole moment at an *n*-InP (100) surface sulfided in an alcohol solution compared to the case of sulfiding in a water solution, and the greater amount of sulfur bound to indium atoms (state S1)– indicate that the dipole moment is produced by sulfur atoms bound to indium atoms at the surface. On the other hand, the larger dipole moment may also be caused by the higher effective electronegativity of the sulfur ion in an alcohol solution.[31]

5. CONCLUSIONS

X-ray photoelectron spectroscopy, the Kelvin probe method, and Raman scattering have been used to show that when *n*-InP (100) is treated in a solution of ammonium sulfide in *t*-butyl alcohol, the surface Fermi level shifts toward the conduction band, but when it is treated in a water solution, the surface Fermi level is essentially unaffected. The reduction in the depth of the surface depletion layer during sulfiding may be caused either by an increase in the doping level at the surface due to the filling of phosphorus vacancies by sulfur or by a change in the surface barrier of the semiconductor. The increase in the ionization energy of the semiconductor is greater when the *n*-InP (100) is sulfided in an alcohol solution, rather than a water solution.

[1] H. Ishimura, K. Sasaki, and H. Tokuda, Inst. Phys. Conf. Ser. **106**, 405 (1990).
[2] R. Iyer and D. L. Lile, Appl. Phys. Lett. **59**, 437 (1991).
[3] H. Oigawa, J. Fan, Y. Nannichi, H. Sugahara, and M. Oshima, Jpn. J. Appl. Phys. **30**, L322 (1991).
[4] T. K. Paul and D. N. Bose, J. Appl. Phys. **70**, 7387 (1991).
[5] A. J. Howard, C. I. H. Ashby, J. A. Lott, R. P. Schneider, and R. F. Corless, J. Vac. Sci. Technol. A **12**, 1063 (1994).
[6] L. F. DeChiaro and C. J. Sandroff, IEEE Trans. Electron Devices **39**, 561 (1992).
[7] C. W. Wilmsen, K. M. Geib, J. Shin, R. Iyer, D. L. Lile, and J. J. Pouch, J. Vac. Sci. Technol. B **7**, 851 (1989).
[8] Y. Fukuda, Y. Suzuki, N. Sanada, S. Sasaki, and T. Ohsawa, J. Appl. Phys. **76**, 3059 (1994).
[9] R. W. M. Kwok and W. M. Lau, J. Vac. Sci. Technol. A **10**, 2515 (1992).
[10] T. Chassé, H. Peisert, P. Streubel, and R. Szargan, Surf. Sci. **331–333**, 434 (1995).
[11] V. N. Bessolov, E. V. Konenkova, and M. V. Lebedev, J. Vac. Sci. Technol. B **14**, 2761 (1996).
[12] V. N. Bessolov, M. V. Lebedev, and D. R. T. Zahn, J. Appl. Phys. **82**, 2640 (1997).
[13] V. N. Bessolov, M. V. Lebedev, Yu. M. Shernyakov, and B. V. Tsarenkov, Mater. Sci. Eng., B **44**, 380 (1997).
[14] R. Hakimi and M.-C. Amann, Semicond. Sci. Technol. **12**, 778 (1997).
[15] C. S. Sundararaman, S. Poulin, J. F. Currie, and R. Leonelli, Can. J. Phys. **69**, 329 (1991).
[16] R. Maeckel, H. Baumgaertner, and J. Ren, Rev. Sci. Instrum. **64**, 694 (1993).
[17] D. R. Lide, *CRC Handbook of Chemistry and Physics*, CRC Press, Boca Raton/ Ann Arbor/ London/ Tokyo (1995).
[18] G. Bauer and W. Richter, *Optical Characterization of Epitaxial Semiconductor Layers*, Springer, Berlin (1996).
[19] D. E. Aspnes and A. A. Studna, Phys. Rev. B **27**, 985 (1983).
[20] W. Haes and R. Loudon, *Scattering of Light by Crystals*, Wiley, N.Y. (1978).
[21] M. S. Carpenter, M. R. Melloch, B. A. Cowans, Z. Dardas, and W. N. Delgass, J. Vac. Sci. Technol. B **7**, 845 (1989).
[22] W .M. Lau, R. W. M. Kwok, and S. Ingrey, Surf. Sci. **271**, 579 (1992).
[23] Y. Tao, A. Yelon, E. Sacher, Z. H. Lu, and M. J. Graham, Appl. Phys. Lett. **60**, 2669 (1992).
[24] I. K. Han, E. K. Kim, J. I. Lee, S. H. Kim, K. N. Kang, Y. Kim, H. Lim, and H. L. Park, J. Appl. Phys. **81**, 6986 (1997).
[25] H. Sugahara, M. Oshima, H. Oigawa, H. Shigekawa, and Y. Nannichi, J. Appl. Phys. **69**, 4349 (1991).
[26] J. Geurts, Surf. Sci. Rep. **18**, 1 (1993).
[27] V. N. Bessolov, E. V. Konenkova, and M. V. Lebedev, Mater. Sci. Eng., B **44**, 376 (1997).
[28] Z. Tian, M. W. C. Dharma-wardana, Z. H. Lu, R. Cao, and L. J. Lewis, Phys. Rev. B **55**, 5376 (1997).
[29] L. Jedral, H. E. Ruda, R. Sodhi, H. Ma, and L. Mannik, Can. J. Phys. **70**, 1050 (1992).
[30] W. Mönch, J. Vac. Sci. Technol. B **7**, 1216 (1989).
[31] V. N. Bessolov, A. F. Ivankov, and M. V. Lebedev, J. Vac. Sci. Technol. B **13**, 1018 (1995).

Translated by D. H. McNeill

Electrical and photoelectric characteristics of an isotypic *n*-ZnO–*n*-Si structure

S. V. Slobodchikov, Kh. M. Salikhov, and E. V. Russu

A. F. Ioffe Physicotechnical Institute, Russian Academy of Sciences, 194021 St. Petersburg, Russia
(Submitted November 11, 1998; accepted for publication November 23, 1998)
Fiz. Tekh. Poluprovodn. **33**, 435–437 (April 1999)

Current-voltage and capacitance-voltage characteristics and the transverse and longitudinal photoelectric effects are measured for *n*-ZnO–*n*-Si heterostructures obtained by deposition from organometallic compounds. Some parameters of the interface, the mechanisms for current flow, and the photoelectric characteristics of these heterostructures, which are of interest for evaluating their practical applications, are determined. © *1999 American Institute of Physics.* [S1063-7826(99)01204-1]

Thin ZnO films have attracted the interest of researchers in connection with their possible attractive applications in optoelectronics. They have been used, in particular, in production technologies for gas sensors, varistors, color displays, and solar cells. For example, the conversion efficiency for sunlight in test samples of an anisotypic *n*-ZnO–*p*-Si heterostructure was 0.95%.[1] Pd-*n*-ZnO diode structures have been tested as hydrogen detectors.[2]

In this paper we present some results from a study of the electrical and photoelectric characteristics of isotypic *n*-ZnO–*n*-Si heterostructures with possible practical applications in mind.

We have used deposition from organometallic compounds to obtain conducting layers of *n*-ZnO. Zinc acetylacetonate $Zn(AcAc)_2$ was used as a source.

Processing was done in a vertical reactor on an Si substrate with a (100) orientation, held at a temperature of 300–350 °C. Deposition was from a mixture of Ar saturated with $Zn(AcAc)_2$ vapor and oxygen introduced into the reaction zone through a concentric injector. The *n*-type ZnO layers were deposited with a zinc acetylacetonate source temperature of 120 °C and in a 100 mL/min flow of argon and oxygen with a flux ratio $Ar/[Ar+O_2]=0.5$. It was noticed that as the substrate temperature increased, the rate of deposition of *n*-ZnO increased and that the morphological structure of the zinc oxide layer improved. The resulting conducting layers of *n*-ZnO have an electron concentration $(5-8)\times 10^{19}$ cm^{-3} and mobility ~ 50 cm^2/(V·s). The metallic contacts on the structures were Al on the *n*-Si and Pd on the *n*-ZnO.

Figure 1 shows current-voltage characteristics of a typical sample of isotypic Pd–*n*-ZnO–*n*-Si–Al heterostructure. A sublinear variation can be seen in both polarities. Note that the direction of easy flow of these structures corresponds to a negative potential on the *n*- Si. The detailed mechanism of current flow is complicated. If we include the existence of intermediate states on the interface, then current flow in the forward direction is associated with overcoming a lower boundary in the ⟨intermediate state⟩–*n*-Si system, and in the reverse direction, in the ⟨intermediate state⟩–*n*-ZnO system. To some extent, the process of current flow resembles one that has been examined[3] for *n*-Ge–*n*-Si heterostructures. In this case,

$$I \sim F_{1,2}\exp(-qV_{D1,2}/kT)(1-R_{1,2})f(\alpha_1,\alpha_2), \tag{1}$$

where $F_{1,2}$ are the emitted fluxes of carriers from the volume to barriers, $V_{D1,2}$ are the diffusion potentials at the interfaces, $R_{1,2}$ are the reflection coefficients for the carrier fluxes at the interfaces, $f(\alpha_1,\alpha_2)$ is a function of the transmission (by intermediate states) at the interface for the corresponding emitted fluxes, and the subscripts 1 and 2 denote parameter values for the two polarities of the applied bias. Figure 2 shows the forward and reverse currents as functions of temperature. According to Eq. (1), the barrier height obtained from curve *2* is $V_{D2}=0.25$ eV and corresponds to an *n*-Si–⟨interface⟩ barrier. The weak temperature dependence of the forward current (curve *1*) indicates that the tunnel current predominates in the *n*-ZnO–⟨interface⟩ segment.

Measurements of the capacitance as a function of the reverse bias (Fig. 3) yield a barrier height of 0.9 eV. The total capacitance of an isotypic heterostructure can be written in the form

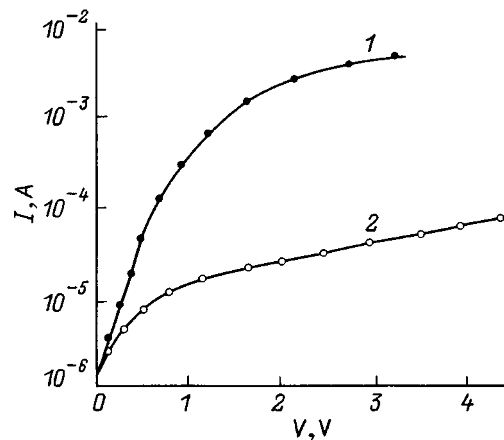

FIG. 1. Current-voltage characteristics of an isotypic *n*-ZnO–*n*-Si heterostructure: (*1*) forward branch (negative potential on the *n*-Si, (*2*) reverse branch.

 © 1999 American Institute of Physics

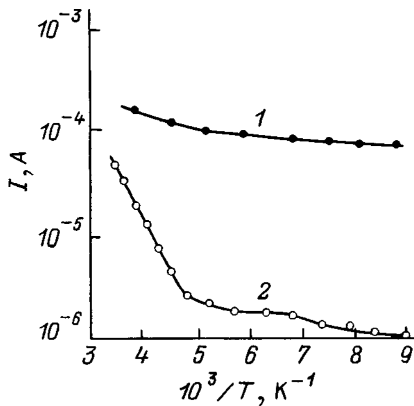

FIG. 2. The forward (*1*) and reverse (*2*) currents of an n-ZnO–n-Si structure as functions of temperature.

$$\frac{C_1C_2}{C_1+C_2}=C, \tag{2}$$

where C_1 is the capacitance determined by the intermediate states in the ⟨interface⟩–n-ZnO junction, and C_2 is the capacitance of the depleted layer in the n-Si. If $C_1 \ll C_2$, then the measured $C^{-2}=f(V)$ dependence probably gives the height of the n-ZnO–⟨interface⟩ barrier.

The measured maximum photosensitivity of the isotypic heterostructure corresponds to the spectral region where silicon is sensitive. A comparative estimate of the short-circuit current, observed by illuminating the isotypic heterostructure by monochromatic light at a wavelength of $\lambda=0.64$ μm, on one hand, and, for example, a silicon $p-n$ junction photodetector of average sensitivity, on the other, showed that the heterojunction had a photocurrent that was only a factor of 1.8 smaller than that of the photodetector. But the difference for illumination by white light was much greater because of the lower collection efficiency for the minority current carriers in the heterostructure.

Figure 4 shows a plot of the inversion characteristics for the longitudinal photoelectric effect in the heterostructure.

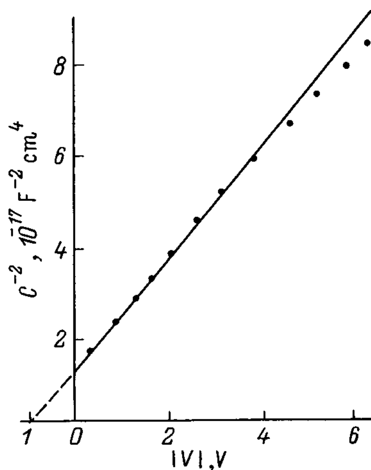

FIG. 3. The capacitance (per unit area) as a function of reverse bias voltage for an n-ZnO–n-Si structure.

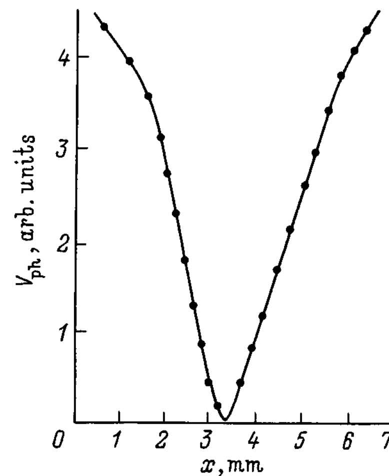

FIG. 4. Inversion characteristics for the longitudinal photoelectric effect in an n-ZnO–n-Si structure.

The characteristics are linear for a distance $l \simeq 5$ mm between the contacts. The linearity condition[4] has the form $\alpha l \to 0$, where

$$\alpha=\sqrt{g\left(\frac{\rho_{n1}}{w_{n1}}+\frac{\rho_{n2}}{w_{n2}}\right)}. \tag{3}$$

Here g is the perpendicular conductivity of the structure, ρ_{n1} and ρ_{n2} are the resistivities of the n-ZnO and n-Si layers, respectively; and w_{n1} and w_{n2} are their effective thicknesses.

Calculations[4] show that a rather wide range of linearity should be observed even for $\alpha l<1$. Here the condition for estimating the transverse conductivity of our structures, including the electrical and geometric characteristics of the n-ZnO ($w_{n1} \simeq 4\times 10^{-6}$ cm) and n-Si layers ($n=10^{16}$ cm^{-3}, $w_{n2}=0.5\times 10^{-4}$ cm) gives $g \leqslant 10^{-5}$ Ω^{-1}. The other parameters of a longitudinal photodetector include, in particular, the capacitance per unit area under reverse bias, C_d, and the time constant for the same bias, βl^2, where $\beta=C_d\rho_{n2}/w_{n2}$. In the structures that were measured, $C_d=9\times 10^{-9}$ F/cm^2 ($V=1$ V) and $\beta l^2=2\times 10^{-6}$ s.

It is clear that, in order to increase their prospects for practical application, n-ZnO–n-Si heterostructures must be optimized, both in terms of their engineering design and in terms of the choice of electrical and photoelectric characteristics of the n-ZnO and n-Si layers. They probably cannot be made into efficient converters of solar energy, but they can serve, in practice, as relatively fast photodetectors based on the transverse or longitudinal photoelectric effects.

[1] M. Shimizu, T. Horii, T. Shiosaki, and A. Kawabata, Thin Solid Films **96**, 149 (1982).
[2] K. Ito, Surf. Sci. **86**, 345 (1979).
[3] W. G. Oldham and A. G. Milnes, Solid-State Electron. **7**, 153 (1964).
[4] U. Nin, T. Matsuda, H. Sadamtzu, and M. Takai, J. Appl. Phys. **53**, 457 (1982).

Translated by D. H. McNeill

LOW-DIMENSIONAL SYSTEMS

Analysis of mechanisms for electron scattering in GaAs/Al$_x$Ga$_{1-x}$As superlattices with doped quantum wells for longitudinal resonant current flow in high electric fields and at low temperatures

S. I. Borisenko and G. F. Karavaev

V. D. Kuznetsov Siberian Physicotechnical Institute, 634050 Tomsk, Russia
(Submitted July 6, 1998; accepted for publication July 7, 1998)
Fiz. Tekh. Poluprovodn. **33**, 438–444 (April 1999)

Formulas are derived for, and a numerical analysis made of, the dependence of the transverse phase relaxation time on electron energy for resonant current flow through GaAs/Al$_x$Ga$_{1-x}$As superlattices with doped quantum wells. The parameters are chosen to be close to those of superlattices used for creating photodiodes for operation at $\lambda \simeq 10$ μm. The analysis is limited to the interactions of electrons with neutral atoms and impurity ions at low temperatures. Resonant current flow is ensured by an electric field that brings the ground state and the first excited state of the ''Stark ladder'' into resonance with neighboring, weakly interacting quantum wells. © *1999 American Institute of Physics.* [S1063-7826(99)01304-6]

Because of their possible use in infrared (IR) detectors[1–5] and ultrahigh frequency generators,[6–9] the kinetic properties of weakly interacting quantum-well superlattices of the type GaAs/Al$_x$Ga$_{1-x}$As in an electric field along the longitudinal axis of the superlattice are currently studied extensively, both experimentally and theoretically. The region of high electric fields, which cause ''Stark'' quantization of the subbands in the conduction band, is of greatest interest from the standpoint of increasing their photosensitivity.[1] In this case, the current-voltage characteristic is highly nonlinear and when the electron concentration in the quantum well is high enough, the current-voltage characteristic has distinct oscillatory structures.[10,11] The latter are related[10,12] to the presence of a high field at the anode domain wall. It has recently been shown[13–16] that current flow in these domains is determined, in general, by nonresonant transitions of electrons between neighboring quantum wells. If, however, a domain encompasses the entire superlattice as the applied field increases, then current flow through the domain can acquire a resonant character.[15] The condition for resonant current flow is that the lowest state and an excited state of the Stark ladder be brought into resonance with the neighboring quantum wells by the electric field.[17]

Until now, the theoretical analysis of the role of the different scattering mechanisms which affect the longitudinal current flow in a superlattice has mainly touched on the first miniband in the classical electric field region.[18–21] The effect of different scattering mechanisms on resonant and nonresonant current flow in a high-field superlattice domain has been given virtually no attention in the literature.

In this paper we carry out a numerical analysis of, and present formulas for, the transverse phase relaxation time[17] during passage of a longitudinal current in a GaAs/Al$_x$Ga$_{1-x}$As superlattice with a straight barrier band gap for the case in which the electric field corresponds to step-by-step resonant tunnelling of electrons between the ground state and the first excited state of the neighboring quantum wells. Based on the operating regimes for photodetectors using these superlattices,[1] the analysis is carried out for low temperatures including elastic scattering of electrons on impurity ions and neutral atoms. An analysis of experimental data for the dark current density in the resonant flow region yields an estimate for the matrix element which determines the tunnelling transition probability for electrons between neighboring quantum wells.

1. THE PHASE RELAXATION TIME

It is known that in a strong electric field and with periodic boundary conditions, the electron wave function is localized and this localization accounts for the Stark quantization. This effect is especially noticeable in the case of narrow bands, such as the subbands in the superlattices used for IR photodetectors. According to theory,[17] in this case the energy of an electron's motion along a field parallel to the superlattice axis is given in terms of two quantum numbers by

$$E_{in}=E_i-eFdn, \tag{1}$$

where i is the number of a state in the unit cell of the superlattice with quantum number n, $-e$ is the electronic charge, F is the field strength, and d is the superlattice period. The energy E_{in} corresponds to the wave function

$$\tilde{W}_{in}(z)=\sum_j C_{ij}(F)W_{jn}(z), \tag{2}$$

where

$$W_{in}(z)=\frac{1}{\sqrt{N}}\sum_q e^{-iqdn}\Psi_{iq}(z) \tag{3}$$

 © 1999 American Institute of Physics

is the Wannier function; Ψ_{iq} is the one-dimensional Bloch wave function corresponding to energy E_{iq} with band number i and wave number q; and N is the number of periods of the superlattice along its axis. The energy E_i and the coefficients C_{ij}, which depend on the field, are found by solving the equations

$$\sum_j [(I_{i0}-E)\delta_{ij}-eFZ_{ij}]C_{ji}=0, \tag{4}$$

where

$$I_{i0}=\frac{1}{N}\sum_q E_{iq} \tag{5}$$

is the average value of the energy in the miniband i,

$$Z_{ij}=\langle W_{i0}|z|W_{j0}\rangle\int_L W_{i0}^* z W_{j0}\,dz \tag{6}$$

is the matrix element of the position operators along the superlattice axis, and $L=Nd$ is the length of the superlattice along the symmetry axis.

For a superlattice consisting of weakly interacting quantum wells, the resonant electric current density j_r, which is attributable to electron transitions between the ground state and the first excited state of the neighboring quantum wells is given by[17]

$$j_r=en\langle\tau_\perp\rangle\,\tilde{d}\,|\tilde{\Omega}_{12'}|^2, \tag{7}$$

where

$$\tilde{d}=\langle\tilde{W}_{21}|z|\tilde{W}_{21}\rangle-\langle\tilde{W}_{10}|z|\tilde{W}_{10}\rangle \tag{8}$$

is a parameter close in magnitude to the superlattice period d;

$$\hbar\Omega_{12'}=\langle\tilde{W}_{10}|H_0-eFz|\tilde{W}_{21}\rangle =\sum_{ij} C_{i1}^* C_{j2}(I_{i1}\delta_{ij}-eF\langle W_{i0}|z|W_{j1}\rangle) \tag{9}$$

is the matrix element for a tunnelling transition, which determines the probability of a transition of this type between neighboring quantum wells; H_0 is the Hamiltonian of the superlattice in the absence of an electric field with eigenfunctions Ψ_{iq};

$$I_{i1}=\frac{1}{N}\sum_q e^{iqd}E_{iq}; \tag{10}$$

$$\langle\tau_\perp\rangle=\frac{1}{2\pi^2 dn}\int\frac{\tau_\perp(\mathbf{k})d\mathbf{k}}{\exp\{[\varepsilon(\mathbf{k})-\xi]/k_0T\}+1} \tag{11}$$

is the transverse phase relaxation time averaged over an equilibrium distribution;

$$n=\frac{m^* k_0T}{\pi\hbar^2 d}\ln[1+\exp(\xi/k_0T)] \tag{12}$$

is the electron concentration in the approximation of isolated quantum wells for $k_0T\ll E_2-E_1$; $\varepsilon(\mathbf{k})=\hbar^2\mathbf{k}^2/2m^*$ is the energy of transverse motion of an electron in the effective-mass approximation; $\mathbf{k}$ is the two-dimensional wave vector; and ξ is the Fermi level.

The transverse phase relaxation time is given as a function of $\mathbf{k}$ by[17]

$$\frac{1}{\tau_\perp}=\frac{\pi}{\hbar}\sum_{k'}\overline{|U_{kk'}^{1010}-U_{kk'}^{2121}|^2}\,\delta(\varepsilon(\mathbf{k})-\varepsilon(\mathbf{k}')), \tag{13}$$

where

$$U_{kk'}^{imjn}=\langle\Psi_{kim}|U(r)|\Psi_{k'jn}\rangle \tag{14}$$

is the matrix element of the scattering operator

$$U(r)=\sum_\alpha V(r-R_\alpha) \tag{15}$$

in the basis of wave functions

$$\Psi_{kim}=\frac{1}{\sqrt{S}}e^{ikr_\perp}\tilde{W}_{im}(z), \tag{16}$$

which describe the bound motion of the electrons along the superlattice axis and their free motion transverse to the axis. In Eqs. (15) and (16) $V(r-R_\alpha)$ is the interaction energy of an electron with an impurity center located at the point R_α and S is the cross-sectional area of the superlattice. The horizontal bar in Eq. (13) denotes averaging over the coordinates of the scattering centers. Equation (13) has been written disregarding the scattering between the ground state and the first excited state within a single well, which we shall ignore because of its smallness for elastic scattering.

Using Eqs. (2) and (3), we can write the matrix element of the scattering operator in the form

$$U_{kk'}^{imjn}=\frac{1}{N}\sum_{\alpha j'i'}\sum_{\beta qq'}C_{i'i}^* C_{j'j}\exp[i(\mathbf{k}_{\beta q}-\mathbf{k}_{q'})R_\alpha] \times\exp[id(mq'-nq)]C_{i'j'\beta}(q,q')V(\mathbf{k}_{q'}-\mathbf{k}_{\beta q}), \tag{17}$$

where

$$\mathbf{k}_q=(\mathbf{k},q),\quad \mathbf{k}_{\beta q}=(\mathbf{k},q+2\pi\beta/d),\quad -N/2\leqslant\beta\leqslant N/2,$$

and

$$C_{ij\beta}(q,q')=\frac{1}{d}\int_{-d/2}^{d/2}e^{i2\pi\beta z/d}u_{iq}^* u_{jq'}\,dz \tag{18}$$

is the Fourier component of the product of the parts of the Bloch wave functions which are periodic in the superlattice period, while

$$V(\mathbf{K})=\int e^{i\mathbf{Kr}}V(\mathbf{r})\,d\mathbf{r} \tag{19}$$

is the Fourier component in three-dimensional wave vector $\mathbf{K}$ space of the interaction energy of an electron with a scattering center at the point $R=0$.

For scattering at impurity ions in the approximation of an isotropic Coulomb screening potential, it is known that

$$V(\mathbf{K})=\frac{4\pi e^2}{\varepsilon_s(\mathbf{K}^2+\alpha^2)}, \tag{20}$$

where ε_s is the static dielectric constant, and α is the screening parameter. In the Debye approximation, with allowance for Eq. (12) for the concentration, we have

$$\alpha^2=\frac{4m^*e^2}{\varepsilon_s\hbar^2 d}[1+\exp(-\xi/k_0T)]^{-1}. \tag{21}$$

For scattering on neutral atoms at energies corresponding to elastic scattering, we use the approximate formula

$$V(\mathbf{K})=\left[\frac{30\pi r_B\hbar^4}{(m^*)^2|\mathbf{K}|}\right]^{1/2}, \tag{22}$$

where $r_B=(2m^*\varepsilon_D)^{1/2}/\hbar$ is the Bohr radius of the impurity ground state, and ε_D is the impurity ionization energy. In the case of a bulk semiconductor, this formula yields the well-known expression obtained by Erginsoy[22] for the cross section of scattering at the neutral hydrogen-like atoms.

A numerical analysis of the coefficients C_{ij} showed that, for calculating the elements of the scattering matrix in Eq. (13), the field dependence of the $\widetilde{W}_{in}$ can be ignored in the resonant current flow region, i.e., it can be assumed that $C_{ij}=\delta_{ij}$. In addition, since the superlattices under consideration here consist of weakly interacting quantum wells, we can use the approximation of infinitely deep, isolated quantum wells for the W_{in}. Given these approximations, after averaging over the uniformly distributed impurity centers within the quantum wells, according to Eqs. (13) and (17), we obtain the following expression for the transverse phase relaxation time (see *Appendix I*):

$$\tau_\perp(\mathbf{k})=\tau_\perp(\varepsilon)=\tau_0 G(\varepsilon)^{-1}, \tag{23}$$

where $G(\varepsilon)$ is a dimensionless function of the energy. For scattering at impurity ions, with allowance for Eq. (20), we obtain

$$\tau_0^{\text{ion}}=\frac{\varepsilon_s^2\hbar^3}{\pi^5 e^4 a^3 m^* N_{\text{ion}}}, \tag{24}$$

where a is the width of the quantum well, m^* is the effective mass, and N_{ion} is the concentration of the impurity ions in the quantum well;

$$G(\varepsilon)=\int_0^\infty \frac{(2x^2+\nu\varepsilon+2\gamma^2)g(x)dx}{(x^2+\gamma^2)^{3/2}(x^2+\nu\varepsilon+\gamma^2)^{3/2}}, \tag{25}$$

$$g(x)=\frac{\sin^2(x)}{\eta x^2}\left\{\frac{1}{(\pi^2-x^2)^2}+\frac{16}{(4\pi^2-x^2)^2}-\frac{8\cos(\eta x)}{(\pi^2-x^2)(4\pi^2-x^2)}\right\}, \tag{26}$$

where γ and η are dimensionless parameters, and ν has the dimensions of reciprocal energy:

$$\nu=2\frac{m^*a^2}{\hbar^2}, \quad \gamma=\frac{1}{2}\alpha a, \quad \eta=2\frac{d}{a}. \tag{27}$$

A similar calculation of the constant τ_0 and the function $G(\varepsilon)$, using Eq. (22) when the transverse relaxation time is limited to scattering on neutral hydrogen-like atoms, yields

$$\tau_0^{n.a.}=\frac{e^2 m^{*2}}{60\pi^3\varepsilon_s\hbar^3 N_{n.a.}}, \tag{28}$$

where $N_{n.a.}$ is the concentration of neutral impurity centers in the quantum well, and

$$G(\varepsilon)=\int_0^{\pi/2}d\varphi\int_0^\infty dx\frac{g(x)}{(x^2+\nu\varepsilon\sin^2\varphi)^{1/2}}. \tag{29}$$

The integrals in Eqs. (25) and (29) have no general analytic form and can only be calculated numerically.

2. NUMERICAL ANALYSIS OF THE TRANSVERSE PHASE RELAXATION TIME

Since there is no analytic expression for the dependence of the transverse phase relaxation time on the energy and on the superlattice parameters, these dependences were analyzed numerically for a $\text{GaAs/Al}_x\text{Ga}_{1-x}\text{As}$ type superlattice with parameters close to those employed for fabricating photodetectors. For the parameters in the formula for $\tau_\perp^{\text{ion}}(\varepsilon)$, we have used the following values: $m^*_{\text{GaAs}}=0.067m_0$ and $\varepsilon_s=13.13$. The ionization energy of the impurity atoms, ε_D was estimated from the hydrogen-like model.

According to Eqs. (23)–(27), the transverse phase relaxation time $\tau_\perp^{\text{ion}}$, which is restricted to scattering on impurity ions, depends on the electron concentration n, the quantum well width a, and the ratio d/a of the superlattice period to the quantum well width. Note that, in the approximation of electrical neutrality, the electron concentration determines the impurity ion concentration ($N_{\text{ion}}=n$) and, according to Eq. (21), through the Fermi level, the screening parameter α. Figure 1 shows the calculated energy dependence of $\tau_\perp^{\text{ion}}$ for different electron concentrations. It is clear from the figure that $\tau_\perp^{\text{ion}}$ is an increasing function of energy. This distinguishes it from the ordinary relaxation time τ^{ion} for the bulk semiconductor, since $\tau_\perp^{\text{ion}}(\varepsilon)$ approaches a finite value as the energy goes to zero, while $\tau^{\text{ion}}(\varepsilon)$ approaches infinity as $\varepsilon^{-1/2}$. As the electron concentration increases, the transverse relaxation time decreases as a result of the higher impurity concentration. Figure 2 shows plots of $\tau_\perp^{\text{ion}}(\varepsilon)$ for different values of the ratio d/a with $a=70$ Å. According to this figure, as the superlattice barrier thickness increases relative to the quantum well width, the transverse relaxation time decreases for these values of d/a. Figure 3 shows plots of $\tau_\perp^{\text{ion}}(\varepsilon)$ for different quantum well widths. This figure implies that the transverse relaxation time also decreases with increasing a for constant d/a. The reason for such a dependence of $\tau_\perp^{\text{ion}}$ on these parameters is related to the interference properties of the square of the modulus of the difference in the matrix elements of the scattering operator for neighboring quantum wells, which determines the transverse phase relaxation time through Eq. (13).

According to Eqs. (23) and (26)–(29), the transverse relaxation time $\tau_\perp^{n.a.}$, which is limited to scattering on neutral hydrogen-like atoms, depends parametrically on the neutral

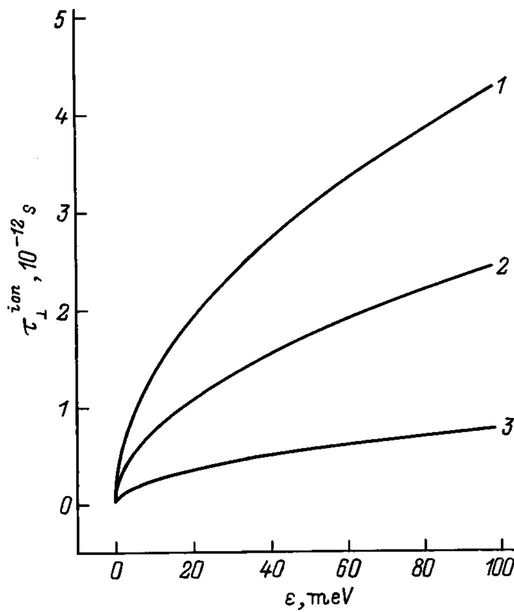

FIG. 1. The transverse relaxation time as a function of energy, $\tau_\perp^{\rm ion}(\varepsilon)$, for different electron concentrations ($a=70$ Å, $d=210$ Å). Concentrations n (cm^{-3}): *1* — 10^{15}, *2* — 2×10^{15}, and *3* — 10^{16}.

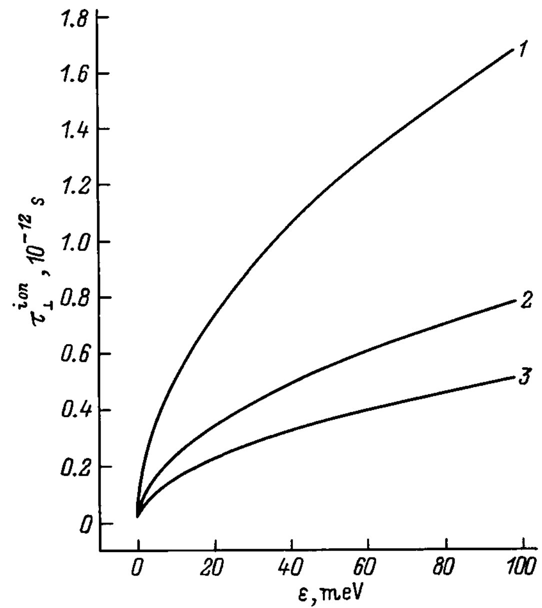

FIG. 3. The transverse relaxation time as a function of energy, $\tau_\perp^{\rm ion}(\varepsilon)$, for different widths of the superlattice quantum well, a, Å: *1* — 40, *2* — 70, and *3* — 100 ($d/a=3$, $n=10^{16}$ cm^{-3}).

atom concentration $N_{n.a.}$ in the quantum well, the quantum well width a, and the ratio d/a. Figures 4 and 5 show plots of $\tau_\perp^{n.a.}(\varepsilon)$ for different values of the parameters a and d/a. The calculations were done for $N_{n.a.}=10^{18}$ cm^{-3}. These figures imply that for these energies, $\tau_\perp^{n.a.}(\varepsilon)$ is an increasing function. This distinguishes it from the relaxation time $\tau^{n.a.}$ in the bulk material, which is independent of the energy at low energies $\varepsilon<\varepsilon_D/4$. As the parameter d/a increases with a constant, the transverse relaxation time $\tau_\perp^{n.a.}$ increases, in contrast with $\tau_\perp^{\rm ion}$. A rise in $\tau_\perp^{n.a.}$ with increasing a for constant d/a is also observed, in contrast with $\tau_\perp^{\rm ion}$.

3. CALCULATING THE TUNNELLING TRANSITION MATRIX ELEMENT

According to Eq. (7), if the resonant current density, carrier concentration, and the transverse phase relaxation time averaged over the energy are known, then in the approximation $\tilde{d}=d$ it is possible to estimate $|\hbar\tilde{\Omega}_{12'}|$, the matrix element which determines the tunnelling transition probability. An estimate of this sort was made for a GaAs/$Al_{0.36}Ga_{0.64}$As superlattice with a quantum well with of 70 Å and a barrier thickness of 140 Å ($d=210$ Å). An

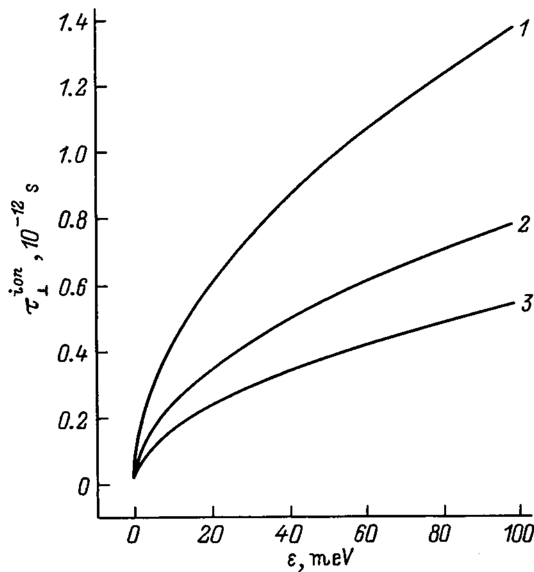

FIG. 2. The transverse relaxation time as a function of energy, $\tau_\perp^{\rm ion}(\varepsilon)$, for different ratios of the superlattice period to the quantum well width, d/a: *1* — 2, *2* — 3, and *3* — 4 ($a=70$ Å, $n=10^{16}$ cm^{-3}).

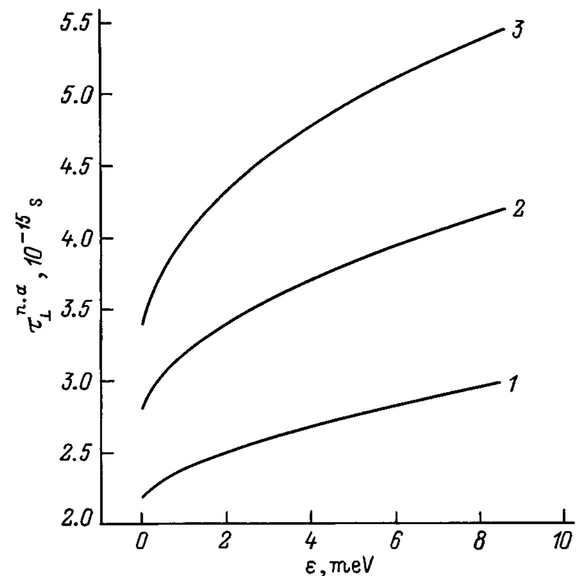

FIG. 4. The transverse relaxation time as a function of energy for the case of scattering on neutral atoms, $\tau_\perp^{n.a.}(\varepsilon)$, for different ratios of the superlattice period to the quantum well width, d/a: *1* — 2, *2* — 3, and *3* — 4 ($a=70$ Å, $N_{n.a}=10^{18}$ cm^{-3}, $\tilde{\varepsilon}_D=10.5$ meV).

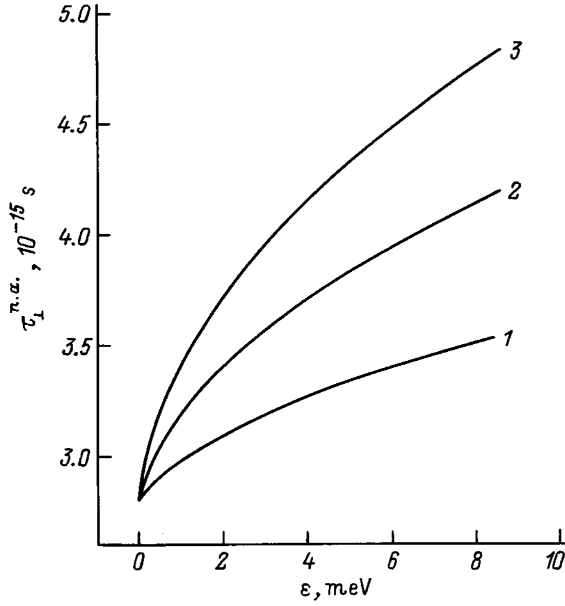

FIG. 5. The transverse relaxation time as a function of energy for the case of scattering on neutral atoms, $\tau_\perp^{n.a.}(\varepsilon)$, for different superlattice quantum well widths, a, Å: *1* — 40, *2* —70, and *3* — 100 ($d/a=3$ Å, $N_{n.a}=10^{18}$ cm^{-3}, $\tilde{\varepsilon}_D=10.5$ meV).

experiment[1] shows that at 15 K a superlattice with these parameters, doped quantum wells with a concentration $N_D=1.4\times10^{18}$ cm^{-3}, and 50 periods has resonant IR absorption at $\lambda=10.3$ μm ($\hbar\omega_{21}=120$ meV) and has a dark current (density) of $j_r\sim0.9$ A/cm^2 for a bias of 6V.

A calculation of the transverse relaxation time for this temperature and impurity concentration yielded $\langle\tau_\perp^{n.a.}\rangle=2.3\times10^{-15}$ s and $\langle\tau_\perp^{\text{ion}}\rangle=7.8\times10^{-13}$ s. In this calculation the electron density $n=1.3\times10^{15}$ cm^{-3} was calculated by solving the equation for the electrical neutrality condition (see *Appendix II*) with parameters taken from Mailhiot *et al.*:[23] $\varepsilon_0=12.5$ meV and $\Delta\varepsilon=0.11$ meV/Å. In calculating the Fourier component (22) of the electron-neutral impurity atom interaction, we have used the average value $\varepsilon_D=\tilde{\varepsilon}_D=10.5$ meV for the ionization energy.

The very small value of $\langle\tau_\perp^{n.a.}\rangle$ indicates that the interaction of the electrons with the neutral impurity atoms must be taken into account when calculating the electron energy spectrum and wave functions. In the zeroth approximation the motion of the electrons in the field of the neutral atoms can be treated as motion in a field with an average potential accompanied by weak scattering analogous to that in an alloy. With this approach to the problem, the main mechanism for scattering is scattering on impurity ions, which gives a value for $|\hbar\tilde{\Omega}_{12'}|$ of roughly 3.4×10^{-5} eV. This value is in good agreement with that calculated using Eq. (9), 4.0×10^{-5} eV. In the calculation the fit parameter for the given $\hbar\omega_{21}=120$ meV was the effective height of the potential barrier of the quantum well, which turned out to be roughly 218 meV.

The existing discrepancy may be related to the abovementioned weak scattering at neutral atoms and to phonon emission. It should also be noted that in calculating $\langle\tau_\perp^{\text{ion}}\rangle$ we have used a rather approximate Wannier function, in which the finite height and thickness of the potential barrier were ignored, along with an isotropic Coulomb potential for the impurity ion. Another factor which might affect the calculated value of $\langle\tau_\perp^{\text{ion}}\rangle$ is scattering which leads to transfer of electrons among neighboring quantum wells.

APPENDIX I

According to Eq. (13), the transverse relaxation time is

$$\frac{1}{\tau_\perp}=\frac{\pi}{\hbar}\sum_{k'}\{\overline{|U_{kk'}^{1010}|^2}+\overline{|U_{kk'}^{2121}|^2}-2\overline{\mathrm{Re}(U_{kk'}^{1010}U_{k'k}^{2121})}\}\times\delta(\varepsilon(\mathbf{k})-\varepsilon(\mathbf{k}')). \quad (\mathrm{A.I.1})$$

Ignoring the field dependence of the wave functions, we obtain the following expressions for the matrix elements of the scattering operator, taking Eq. (17) into account:

$$U_{kk'}^{2121}=\frac{1}{N}\sum_{\alpha}\sum_{\beta qq'}e^{i(\mathbf{k}_{\beta q}-\mathbf{k}_{q'})R_\alpha}e^{id(q'-q)}\times C_{22\beta}(q,q')V(\mathbf{k}_{q'}-\mathbf{k}_{\beta q}),$$

$$U_{kk'}^{1010}=\frac{1}{N}\sum_{\alpha}\sum_{\beta qq'}e^{i(\mathbf{k}_{\beta q}-\mathbf{k}_{q'})R_\alpha}\times C_{11\beta}(q,q')V(\mathbf{k}_{q'}-\mathbf{k}_{\beta q}). \quad (\mathrm{A.I.2})$$

In the approximation of isolated infinitely deep quantum wells, for the Wannier function we use the standard formulas

$$W_{10}=\begin{cases}(2/a)^{1/2}\cos(\pi z/a), & |z|\leqslant a/2,\\ 0, & |z|\geqslant a/2,\end{cases}$$

$$W_{20}=\begin{cases}(2/a)^{1/2}\sin(\pi z/a), & |z|\leqslant a/2,\\ 0, & |z|\geqslant a/2.\end{cases} \quad (\mathrm{A.I.3})$$

The coefficients $C_{ij\beta}$ are calculated using Eqs. (18) and (A.I.3):

$$C_{11\beta}(q',q)=C_1(Q)=\frac{\pi^2\sin(aQ/2)}{(aQ/2)[\pi^2-(aQ/2)^2]},$$

$$C_{22\beta}(q',q)=C_2(Q)=\frac{4\pi^2\sin(aQ/2)}{(aQ/2)[4\pi^2-(aQ/2)^2]}, \quad (\mathrm{A.I.4})$$

where $Q=2\pi\beta/d+q-q'$.

Using Eq. (A.I.4), Eq. (A.I.2) takes the form

$$U_{kk'}^{2121}=\frac{L}{2\pi}\sum_{\alpha}e^{i(\mathbf{k}'-\mathbf{k})R_{\alpha\perp}}\int_{-\infty}^{+\infty}e^{iq(R_{\alpha z}-d)}C_2(q)\times V(|\mathbf{k}'-\mathbf{k}|,|q|)\,dq,$$

$$U_{kk'}^{1010}=\frac{L}{2\pi}\sum_{\alpha}e^{i(\mathbf{k}'-\mathbf{k})R_{\alpha\perp}}\int_{-\infty}^{+\infty}e^{iqR_{\alpha z}}C_1(q)\times V(|\mathbf{k}'-\mathbf{k}|,|q|)\,dq. \quad (\mathrm{A.I.5})$$

Assuming independent scattering on individual impurity centers and considering a uniform impurity distribution within the quantum well, using Eq. (A.I.5) and integrating over the coordinates R_α, we obtain

$$\overline{|U_{kk'}^{1010}-U_{kk'}^{2121}|^2}=\frac{aN_vL}{2\pi d}\int_{\infty}^{+\infty}V^2(|\mathbf{k}'-\mathbf{k}|,|q|)\times[C_1^2(q)+C_2^2(q)-2\cos(qd)\,C_1(q)\,C_2(q)]dq, \quad (A.I.6)$$

where N_v is the concentration of impurity centers within a quantum well.

APPENDIX II

In the approximation of electrical neutrality the electron concentration n can be calculated using the formula

$$n=\frac{1}{L}\int_{-L/2}^{L/2}\frac{f(z)dz}{2\exp\{[\varepsilon_D(z)+\xi]/k_0T\}+1}, \quad (A.II,1)$$

where $L=Nd$ is the superlattice thickness, and $f(z)$ is the impurity distribution function (the number of centers per unit length at the point z). Assuming that the impurity distribution in the quantum well is uniform, and that the ionization energy function $\varepsilon_D(z)$ is periodic over the superlattice and symmetric with respect to the center of a quantum well, we transform Eq. (A.I.1) to the form

$$n=2\frac{N_D}{d}\int_0^{a/2}\frac{dz}{2\exp\{[\varepsilon_D(z)+\xi]/k_0T\}+1}, \quad (A.II.2)$$

where N_D is the concentration of the donor impurity inside a quantum well.

For the function $\varepsilon_D(z)$ we use the linear approximation

$$\varepsilon_D(z)=\varepsilon_0-\Delta\varepsilon z \quad (0\leqslant z\leqslant a/2), \quad (A.II.3)$$

where ε_0 is the ionization energy of an impurity atom located at the center of a quantum well. In this approximation the integral in Eq. (A.II.2) can be expressed analytically and the condition of electrical neutrality with Eq. (12) takes the form

$$\ln[1+\exp(\xi/k_0T)]=\frac{2\pi\hbar^2N_D}{m^*\Delta\varepsilon}\ln\left\{\frac{2\exp[(\varepsilon_0+\xi)/k_0T]+\exp(a\Delta\varepsilon/2k_0T)}{2\exp((\varepsilon_0+\xi)/k_0T)+1}\right\}. \quad (A.II.4)$$

For a nondegenerate electron gas at low temperatures ($k_0T\ll\varepsilon_0$), this equation for the reduced Fermi level ξ has the simple solution

$$\xi=\frac{k_0T}{2}\ln\left\{\frac{\pi\hbar^2N_D[\exp(a\Delta\varepsilon/2k_0T)-1]}{m^*\Delta\varepsilon\exp(\varepsilon_0/k_0T)}\right\}. \quad (A.II.5)$$

[1] K. K. Choi, B. F. Levine, C. G. Bethea, J. Walker, and R. J. Malik, Appl. Phys. Lett. **50**, 1814 (1987).
[2] B. F. Levine, A. Y. Cho, J. Walker, D. L. Sivco, and D. A. Kleinman, Appl. Phys. Lett. **52**, 1418 (1988).
[3] B. F. Levine, S. D. Gunapala, and R. F. Kopf, Appl. Phys. Lett. **58**, 1551 (1991).
[4] H. Lobentanzer, W. Konig, W. Stolz, K. Ploog, T. Elsaesser, and R. J. Bauerle, Appl. Phys. Lett. **53**, 572 (1988).
[5] X. Zhou, P. K. Bhattocharya, G. Hugo, S. C. Hong, and E. Gulari, Appl. Phys. Lett. **54**, 856 (1989).
[6] A. Sibille, J. F. Palmier, H. Wang, and F. Mollot, Phys. Rev. Lett. **64**, 52 (1990).
[7] C. Waschke, H. G. Roskos, and R. Schwedler, Phys. Rev. Lett. **70**, 3319 (1993).
[8] A. A. Ignatov, K. F. Renk, and E. P. Dodin, Appl. Phys. Rev. Lett. **70**, 1996 (1993).
[9] Yu. V. Kopaev and S. N. Molotkov, JETP Lett. **59**, 800 (1994).
[10] K. K. Choi, B. F. Levine, R. J. Malik, J. Walker, and C. G. Bethea, Phys. Rev. B **35**, 4172 (1987).
[11] H. H. Vuong, D. S. Tsui, and W. T. Tsang, J. Appl. Phys. **66**, 3688 (1989).
[12] H. T. Grahn, H. Schider, and K. Klitzing, Phys. Rev. B **41**, 2890 (1990).
[13] F. Prengel, A. Wacker, and E. Scholl, Phys. Rev. B **50**, 1705 (1994).
[14] S. H. Kwok, R. Merlin, H. T. Grahn, and K. Ploog, Phys. Rev. B **50**, 2007 (1994).
[15] S. H. Kwok, H. T. Grahn, M. Ramsteiner, K. Ploog, F. Prengel, A. Wacker, E. Scholl, S. Murugkar, and R. Merlin, Phys. Rev. B **51**, 9943 (1995).
[16] S. H. Kwok, T. B. Norris, L. L. Bonilla, J. Gallan, J. A. Cuesta, F. C. Martinez, and J. M. Molera, Phys. Rev. B **51**, 10171 (1995).
[17] R. F. Kazarinov and R. A. Suris, Fiz. Tekh. Poluprovodn. **6**, 148 (1972) [Sov. Phys. Semicond. **6**, 105 (1972)].
[18] A. Ya. Shik, Fiz. Tekh. Poluprovodn. **8**, 1841 (1972) [Sov. Phys. Semicond. **8**, 1642 (1974)].
[19] I. Dharssi and P. N. Butcher, J. Phys.: Condens. Matter **2**, 119 (1990).
[20] I. Dharssi and P. N. Butcher, J. Phys.: Condens. Matter **2**, 4629 (1990)
[21] N. J. M. Horing, X. L. Lei, and H. L. Cui, Izv. AN. Ser. fiz. **7**, 148 (1994).
[22] C. Erginsoy, Phys. Rev. **79**, 1013 (1950).
[23] C. Mailhiot, Y. C. Chang, and T. C. McGill, Phys. Rev. B **26**, 4449 (1982).

Translated by D. H. McNeill

Luminescence and electrical properties of InGaN/AlGaN/GaN light emitting diodes with multiple quantum wells

V. E. Kudryashov, A. N. Turkin, and A. É. Yunovich

M. V. Lomonosov Moscow State University, 119899 Moscow, Russia

A. N. Kovalev and F. I. Manyakhin

Moscow Institute of Steel and Alloys, 117936 Moscow, Russia

(Submitted July 25, 1998; accepted for publication July 28, 1998)
Fiz. Tekh. Poluprovodn. **33**, 445–450 (April 1999)

Luminescence spectra of light-emitting diodes based on InGaN/AlGaN/GaN heterostructures with multiple quantum wells are studied for currents in the range $J=0.15$ μA–150 mA. The comparatively high quantum efficiency for low J ($J_{max}=0.5-1$ mA) is a consequence of a low probability for the nonradiative tunnel current. The current-voltage characteristics $J(V)$ are studied for $J=10^{-12}-10^{-1}$ A; they are approximated by the function $V=\varphi_k+mkT\cdot[\ln(J/J_0)+(J/J_1)^{0.5}]+J\cdot R_s$. The portion of $V\propto(J/J_1)^{0.5}$ and measurements of the dynamic capacitance indicate that *i*-layers adjacent to the active layer play an important role. The spectra are described by a model with a two-dimensional density of states with exponential tails in multiple quantum wells. The rise in T with increasing J is determined from the short-wavelength decay of the spectrum of the blue diodes: $T=360-370$ K for $J=80-100$ mA. An emission band is observed at 2.7–2.8 eV from green diodes at high J; this band may be explained by phase separation with different amounts of In in the InGaN. © *1999 American Institute of Physics.* [S1063-7826(99)01404-0]

1. INTRODUCTION

The mechanisms for recombination in light emitting diodes (LEDs) based on complicated quantum well heterostructures such as InGaN/AlGaN/GaN are still not understood adequately, despite enormous progress in the fabrication of blue and green LEDs. Studies have been made[1–6] of the spontaneous luminescence spectra and electrical properties of LEDs with single InGaN quantum wells.[7,8] The spectra were fit well by a model which included the tails of the density of states attributable to fluctuations in the In concentration and to the boundaries of the two dimensional (2D) structures. High electric fields produce tunnelling effects in these structures.[3–5,9,10]

In discussions at the Second International Conference on Nitride Semiconductors[11] the possibility of phase separation in heterostructure layers that are enriched in In was demonstrated. We are unaware of any papers in which the luminescence spectra might have been analyzed in terms of a model which includes phase separation. In that discussion, as well as two other papers,[12,13] the possibility of piezoelectric effects in these heterostructures was pointed out.

In this paper we study the luminescence spectra and electrical properties of LEDs based on InGaN/AlGaN/GaN structures with multiple quantum wells,[14,15] which were sent to Moscow State University by Dr. M. Koike of the Toyoda Hosei Company. There was some interest in examining the feasibility of describing the spectra of the LED by a model which includes the tails of the density of states in 2D structures. It would be important to understand whether tunnel effects occur in these structures and to study the distribution of charges and electric fields in the structures and examine their influence on the luminescence.

2. EXPERIMENTAL PROCEDURE

We have studied samples of blue and green $In_xGa_{1-x}N/Al_yGa_{1-y}N/GaN$ LEDs.[14,15] The structures were grown by gaseous phase epitaxy from organometallic compounds on sapphire substrates with a buffer layer of AlN (30 nm). The *n*-GaN base layer (4-5 μm) was doped with Si and the active layer of $In_xGa_{1-x}N/GaN$ (5 periods of multiple quantum wells, period <8 nm) was grown on it. The layer of p-$Al_yGa_{1-y}N$ (50 nm) covering the multiple quantum wells and the upper layer of *p*-GaN (0.5 μm) were doped with Mg. The amount of In in the quantum wells was varied. The value of x determined the spectral region of the luminescence, as blue ($x\approx0.2$) or green ($x\approx0.4$).

It was possible to study the spectra at low currents ranging upward from $J=0.1$ μA in a dc mode (at room temperature). The spectra at high currents, up to $J=200$ mA, were studied in a pulsed regime (50 Hz, 5 μs).

3. EXPERIMENTAL RESULTS

3.1. LED luminescence spectra for dc currents

We studied the spectra of ten blue and ten green LEDs at room temperature. The spectral peaks for 10 mA lay in the interval $\hbar\omega_{max}=2.64-2.67$ eV ($\lambda_{max}=465-467$ nm) for the blue LEDs and in the range $\hbar\omega_{max}=2.35-2.37$ eV ($\lambda_{max}=465-467$ nm) for the green LEDs. The spectral width at half maximum was $\Delta(\hbar\omega)_{1/2}\approx0.21-0.23$ eV

 © 1999 American Institute of Physics

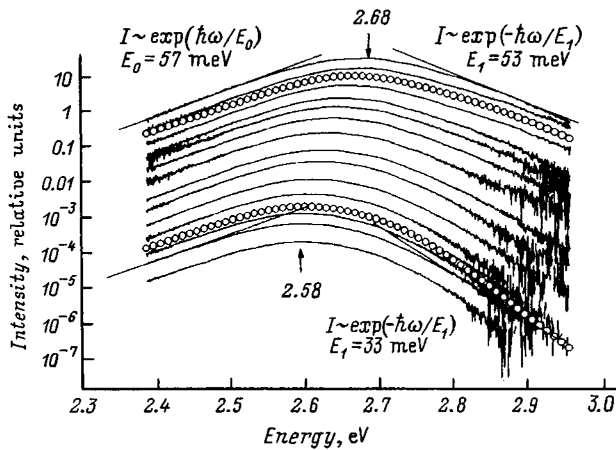

FIG. 1. Luminescence spectra of a blue LED at room temperature for currents of 0.5 μA (bottom curve) to 50 mA (top curve). The open circles represent approximations of the spectra for $J=5$ μA and 10 mA by Eq. (2).

$[\Delta(\lambda)_{1/2}=36-38$ nm]. The spectra of typical LEDs for a wide range of currents are shown in Figs. 1 and 2. Spectra from ≈ 0.15 μA are shown for the blue LED (Fig. 1) and from ≈ 0.5 μA, for the green (Fig. 2). Apparently, no spectra of GaN LEDs down to such low currents at room temperature have been published. The spectral peaks of the blue LEDs shift with current in the interval $\hbar\omega_{\max}=2.57-2.67$ eV, in contrast with the blue LEDs with single quantum wells, for which the peak of the fundamental band does not vary with J.[1–3] No separate band was observed in the yellow-green region, of the sort attributed to tunnel radiation in blue LEDs with single quantum wells.[3–6] The spectral peaks of the green LEDs shift in the interval $\hbar\omega_{\max}=2.2-2.45$ eV, which is wider than that for green single quantum well LEDs.[1–3] The long-wavelength portion of the spectra has an exponential decay, $I\propto\exp(\hbar\omega/E_0)$. In the exponent the parameter $E_0\approx 40-60$ meV for the blue and green LEDs, even when the current was varied over wide limits, in contrast with the case of LEDs with single quantum wells.[1–3] In the short wavelength portion of the spectrum, the intensity also falls exponentially, with $I\propto\exp(-\hbar\omega/E_1)$. The parameter $E_1=40-45$ meV for the blue LEDs and $E_1>50$ meV for the green; i.e., it differs substantially from kT. A band which appears as a shoulder on the short wavelength wing of the spectrum was observed at $\hbar\omega=2.7-2.8$ eV in the green LEDs (Fig. 2).

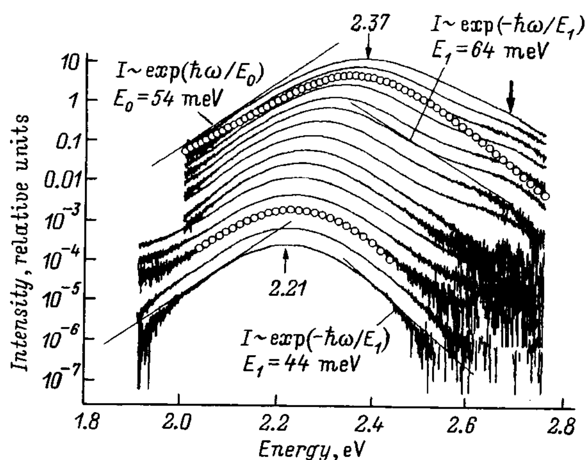

FIG. 2. Luminescence spectra of a green LED at room temperature for different currents from 1 μA (bottom curve) to 50 mA (top curve). The open circles represent approximations of the spectra for $J=5$ μA and 10 mA by Eq. (2).

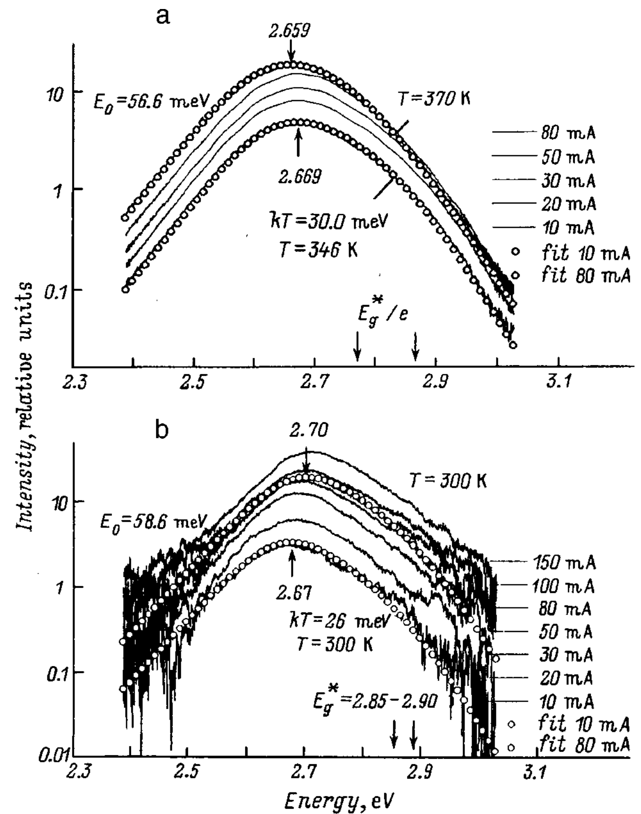

FIG. 3. Luminescence spectra of a blue LED at high currents: a — dc current; b — pulsed current (50 Hz, 5 μs). The hollow circles indicate an approximation of the spectra by Eq. (2) for $J=10$ and 80 mA. a — $J=10, 20, 30, 50, 80$ mA; b — $J=10, 20, 30, 50, 80, 100, 150$ mA.

3.2. Temperature dependence of the spectra

The parameter E_1 for the spectra of the blue LEDs was proportional to the temperature according to measurements in the range $T=220-300$ K: $E_1=m\cdot kT$, with $m=1.4-1.7$. Spectra of blue LEDs at high currents ($J=20-150$ mA) are shown in Fig. 3. The peaks of the spectra for dc currents began to shift to longer wavelengths when $J>40$ mA (Fig. 3a). The short-wavelength decay parameter E_1 increased during this shift of the peaks. The peaks of the spectra for pulsed currents (50 Hz, 5 μs) continued to shift with the current toward higher energies and E_1 did not vary (Fig. 3b). These facts must be explained by heating of the LED at high dc currents.

3.3. Spectral shift with rising voltage

The dependence of $\hbar\omega_{\max}$ on the energy eV (V is the voltage) is shown in Fig. 4. Over a fairly wide interval this dependence is linear, but the slope of the curve is much less than unity (in contrast with the peak in the tunnel emission band of single quantum-well diodes[3–6]). This shift can be

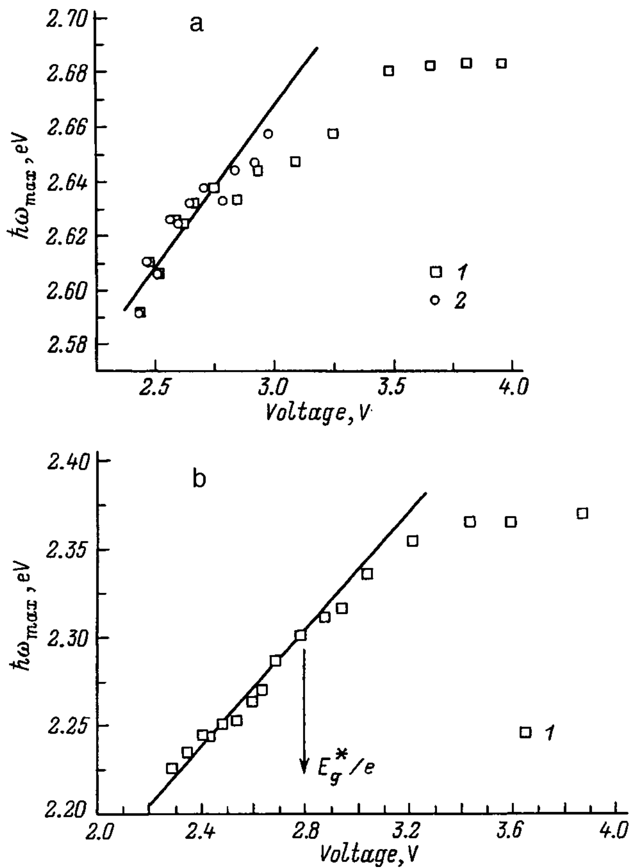

FIG. 4. The locations of the peaks in the emission spectra of blue (a) and green (b) LEDs as functions of the current and voltage on the diode (dc current). a: *1* — $\hbar\omega_{\max}$ $(V=U+JR_s)$, *2* — $\hbar\omega_{\max}$ (U); b: *1* — $\hbar\omega_{\max}$ $(V=U+JR_s)$; the smooth curves are a fit to $\hbar\omega_{\max}$ (U).

explained by filling of the tail in the density of states as a result of fluctuations in the potential and electric fields in an active layer with multiple quantum wells.

3.4. Current-voltage characteristics

Current-voltage characteristics $J(V)$ of blue and green LEDs are shown in Fig. 5. For low currents, $J<10^{-7}$ A, at 300 K the current rises exponentially with an energy $E_j\approx 150$ meV in the exponent. This part of the characteristic is explained by the tunnel component of the current. The tunnel component in these diodes is 3-4 orders of magnitude lower than in single quantum-well LEDs.[2–5] For voltages in the range $V=2.3-2.7$ V, a sharp exponential rise corresponding to injection into the active region is observed. For high currents, $J>20$ mA, the current increases almost linearly with voltage because of the series resistance R_s of the contact regions.

It was possible to approximate the characteristics with good accuracy when, besides the series resistance R_s, the formula for $J(V)$ was supplemented with a quadratic term $J\propto(V-V_1)^2$ corresponding to a double-injection model. The current-voltage characteristic for $J>10^{-4}$ A was approximated by the equation

$$V=\varphi_k+E_J[\ln(J/J_0)+(J/J_1)^{0.5}]+J\cdot R_s \quad (1)$$

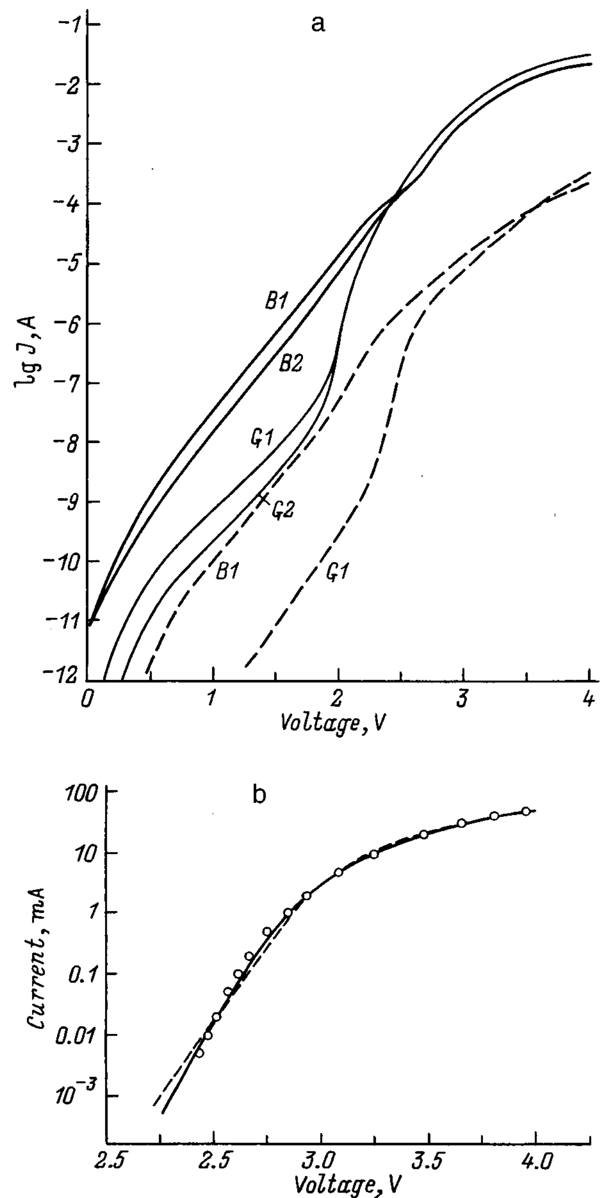

FIG. 5. a — Current-voltage characteristics of blue (B) and green (G) InGaN/AlGaN/GaN LEDs with single (*1*) and multiple (*2*) quantum wells at room temperature (smooth curves) and at 80 K (dashed curves); b — approximation of the current-voltage characteristic by Eq. (1): the dashed curve is $J(V)=J_0e^{\varphi k/E_J}e^{(V-JR_s)/E_J}$ and the smooth curve includes the $(V-V_1)^2$ term; the points are experimental data.

with the fit parameters φ_k (contact potential), E_J (the parameter in the injection exponent, $E_J=c\cdot kT$, $c=1-2$), J_0 (the saturation current), J_1, and R_s. The results of the fit are shown in Fig. 5. The part of the current-voltage characteristic of the form $V=E_J(J/J_1)^{0.5}$ plays an important role between injection growth and the linear portion of the characteristic, i.e., in the range $J=2-30$ mA corresponding to the operating current for these diodes. When T is reduced to 80 K, the current-voltage characteristics shift to higher voltages, while the slope of the tunnel exponent remains the same; the contribution of the quadratic term and R_s increase, so that the injection exponent does not show up as strongly as might be expected.

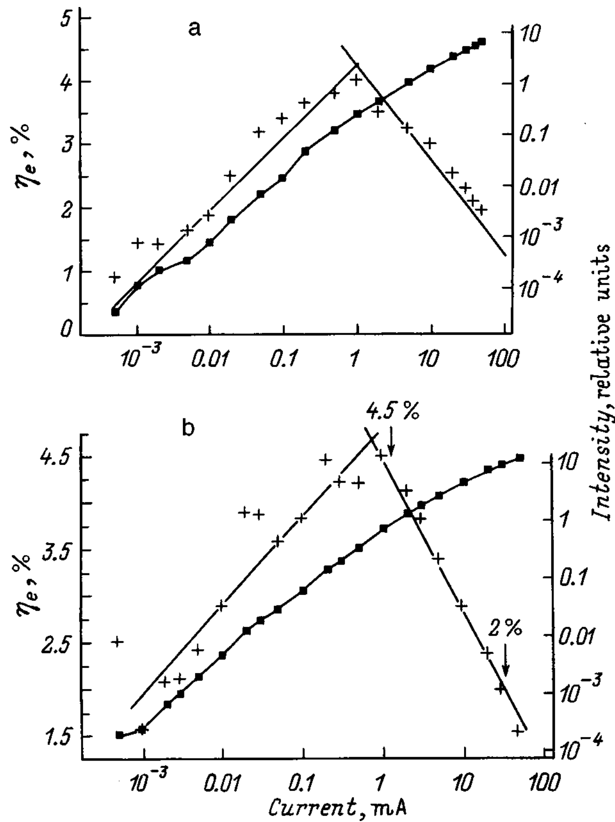

FIG. 6. The integrated emission intensity (squares) and external quantum efficiency (crosses) as functions of current for blue (a) and green (b) LEDs.

3.5. Luminescence quantum yield

Figure 6 shows the dependence of the integrated intensity Φ (photons/s) and external quantum efficiency $\eta_e = e\Phi/J$ on the current for typical green and blue diodes. The quantity η_e was measured by a method described elsewhere[16] and η_e reaches a maximum at a comparatively low J which corresponds to the onset of the injection portion of the current-voltage characteristic. The quantity η_e falls off logarithmically with increasing J for high currents (linearly with V).

3.6. Distribution of charge centers

The distribution of the concentration of charge centers in the p-region of these structures is shown in Fig. 7 (the method of measuring the dynamic capacitance is given elsewhere[17]). The charge distributions for LEDs with single and multiple quantum wells are compared in this figure. Diodes with single quantum wells[1–5] have a thinner space charge region and in both cases the space charge layer is thicker for green than blue LEDs. This is consistent with the weakness of tunnelling effects in multiple quantum-well diodes. Apparently, introducing high concentrations of In into the active region of these structures makes heavy Mg doping of the p-regions difficult and facilitates the formation of compensated regions adjacent to the active layer.

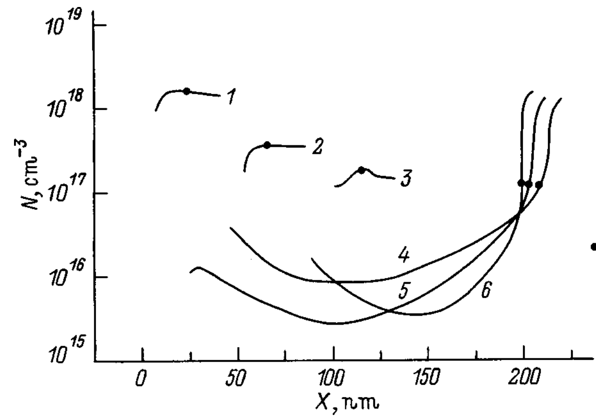

FIG. 7. Spatial distributions of the concentration of charged centers (the coordinate origin corresponds to the boundary of the n-region); the points are the values of N corresponding to zero external voltage on the diode. Blue (*1,3*) and green (*2,4–6*) LEDs with single (*1,2*)) and multiple (*3–6*) quantum wells.

4. DISCUSSION OF RESULTS

4.1. Approximation of the spectra

The spectra were described by a model that has been used for LEDs with single quantum wells.[1–6] In this model it is assumed that radiative recombination takes place between electrons and holes injected into the quantum wells; the voltage U on the active layer is close to the contact potential difference: $U \approx \varphi_k < V$.

Optical transitions take place between states $E_{(c)}$ and $E_{(v)}$ in the tails (of the density of states) produced by potential fluctuations in the 2D-structure. It is assumed that the density of states has the form

$$N^{2D}(\hbar\omega - E_g^{\text{eff}}) \sim [1 + \exp(-\hbar\omega - E_g^{\text{eff}})/E_0]^{-1}. \quad (2)$$

Here E_g^{eff} is the effective band gap, given by $E_g^{\text{eff}} = E_c^* - E_v^*$. The spectral intensity is proportional to the population function for the states near E_c^* and E_v^*; these functions depend on the Fermi quasi-levels F_n and F_p, where $F_n - F_p = eU$ (see Ref. 5):

$$I(\hbar\omega) \sim N^{2D}(\hbar\omega - E_g^{\text{eff}}) f_c(\hbar\omega, m, kT, F_n) \times (1 - f_v(\hbar\omega, m, kT, F_p));$$

$$1 < m < 2. \quad (3)$$

Figures 1 and 2 show how this function approximates the spectra and Table I lists the parameters for one blue LED. They demonstrate that the recombination mechanisms change when the current is varied over a wide range. In one range of J, the change in $\hbar\omega_{\max}$ can be attributed to a change in F_n, with E_g^{eff} and $E_1 = m \cdot kT$ fixed. This is evidence for the model of transitions in the tails of the density of state during random potential fluctuations.

The interval of J over which this description fits, however, is limited. These parameters for a series of LEDs and their dependence on the random and directed (in particular, piezoelectric) fields will be analyzed in more detail later. Here we note that the parameter $E_1 = m \cdot kT$ increases noticeably with J. This is caused by heating of the LED for

TABLE I. Approximation parameters for the spectra of a blue diode according to Eq. (3). The accuracy of the values is indicated by the number of places after the decimal point.

J, mA	U, V	$\hbar\omega_{max}$, meV	E_0, meV	m	ΔF_n, eV	E_g^{eff}, eV
50	3.108	2.683	65.07	1.375	−0.171	2.903
20	3.049	2.680	61.45	1.327	−0.196	2.920
10	2.982	2.657	60.42	1.321	−0.183	2.905
5	2.921	2.647	59.61	1.331	−0.167	2.870
2	2.841	2.644	58.74	1.342	−0.140	2.821
1	2.787	2.633	59.80	1.339	−0.140	2.809
0.5	2.712	2.637	58.41	1.368	−0.129	2.801
0.2	2.644	2.632	54.61	1.469	−0.152	2.846
0.1	2.602	2.624	45.75	1.576	−0.115	2.807
0.05	2.564	2.626	40.27	1.440	−0.112	2.781
0.02	2.512	2.606	36.97	1.384	−0.111	2.751
0.01	2.471	2.610	36.74	1.358	−0.112	2.743

$J > 10$ mA. The approximation is shown in Fig. 3. The shift in the spectra for the pulsed regime can be described without changing E_1 and that for dc currents, without changing m as T varies (Fig. 3a). The shift in $\hbar\omega_{max}$ for high J is consistent with Varshni's formula, $E_g^{eff}(T) = E(0) - \alpha T^2/(\beta + T)$ with parameters $E(0) = 3.07$ eV, $\alpha = 12.8 \times 10^{-4}$ eV/K, and $\beta = 1190$ K (Ref. 18).

4.2. A new spectral band

The short wavelength rolloff of the principal line changes with J in part because of the influence of another spectral line. That line shows up distinctly in the spectra of green LEDs and, close to the noise level, in blue LEDs (Figs. 1 and 2). It seems to be a consequence of large-scale inhomogeneities – phase separation with different amounts of In in $In_xGa_{1-x}N$. In Ref. 11, models of recombination in tails of the density of states and in ''quantum dots'' produced by the nonuniform distribution of In were considered as alternatives. Our data appear to show that both of these possibilities occur. This assumption must be verified by comparing the luminescence spectra with data on the structure of the multiple quantum wells obtained by electron microscopy and secondary ion spectroscopy.

4.3. The role of compensated regions and the maximum quantum efficiency

The question of the maximum η_e as a function of the current is important. It is related to the number of quantum wells and the features of the charge distribution in different heterostructures. The quantity η_e has a maximum, because tunnelling nonradiative recombination channels show up at low J. As J is increased, the electrons injected into the multiple quantum well layer fill it up; this is the region of exponential growth in J and the maximum of η_e. As J is increased further, the electrons partially flow over into the adjacent i-layer (such a model was proposed by Domen *et al.*[19]), having been drawn there by the electric field. This is indicated by the quadratic term in the current-voltage characteristic.

5. CONCLUSIONS

1. We have studied the electroluminescence spectra of multiple quantum well InGaN/AlGaN/GaN light-emitting diodes down to low currents on the order of 10^{-7} A. With increasing V, the spectral peaks of the blue diodes shift in the range 2.57–2.67 eV and those of the green diodes shift in the range 2.2–2.4 eV as the tail of the density of states in the multiple quantum wells is filled.

2. A model of radiative recombination in a 2D-structure with an exponential tail in the density of states provides a good fit to the spectrum with a small number of fitting parameters. The change in the parameters is evidence of variations in the recombination mechanism with current. At high currents a previously unobserved band is seen in the short-wavelength wing of the spectra. This band appears to be caused by the separation of phases with different amounts of In in the InGaN wells.

3. The tunnelling component of the current in the multiple quantum-well diodes is 3–4 orders of magnitude smaller than in analogous single quantum well diodes. The current-voltage characteristics of the LEDs have a segment corresponding to double injection into the i-layers adjacent to the multiple quantum wells. This is confirmed by the form of the distribution of charge centers in the structures.

4. The radiative quantum efficiency has a peak which depends on the current for low J ($J \approx 0.5 - 1 \times 10^{-3}$ A). The drop in η_e for $J > 1$ mA can be explained by overflow of electrons from the active layer and their being drawn by the electric field into the i-layers of the structure.

We are deeply indebted to Dr. M. Koike (Toyoda Hosei Company) for sending the diodes to Moscow State University. We thank S. S. Mamakin for help with the experiments.

A. É. Yunovich and V. E. Kudryashev thank the Soros Educational Program for financial support.

[1] K. G. Zolina, V. E. Kudryashov, A. N. Turkin, A. E. Yunovich, and S. Nakamura, MRS Int. J. of Nitride Semic. Res. 1/11; http://nsr.mij.mrs.org/1/11.

[2] K. G. Zolina, V. E. Kudryashov, A. N. Turkin, A. E. Yunovich, and S. Nakamura, Refer. Rep. J. of Eur. Ceram. Soc. 17, 2033 (1997).

[3] K. G. Zolina, V. E. Kudryashov, A. N. Turkin, and A. É. Yunovich, Fiz. Tekh. Poluprovodn. **31**, 1055 (1997) [Semiconductors **31**, 851 (1997)].

[4] A. E. Yunovich, A. N. Kovalev, V. E. Kudryashov, F. I. Manyachin, A. N. Turkin, and K. G. Zolina, MRS Symp. Proceedings **449**, 1167 (1997).

[5] V. E. Kudryashov, K. G. Zolina, A. N. Kovalev, F. I. Manyakhin, A. N. Turkin, and A. É. Yunovich, Fiz. Tekh. Poluprovodn. **31**, 1304 (1997) [Semiconductors **31**, 1103 (1997)].

[6] A. E. Yunovich, V. E. Kudryashov, A. N. Turkin, K. G. Zolina, A. N. Kovalev, and F. L. Manyakhin, in *Proceedings 2nd Symposium on III-V Nitride Materials and Processes*, 97–34, Electrochem. Soc., NJ, 83 (1998).

[7] S. Nakamura, M. Senoh, N. Iwasa, and S. Nagahama, Jpn. J. Appl. Phys. **34**, pt, 2, L797 (1995).

[8] S. Nakamura, M. Senoh, N. Iwasa, S. Nagahama, T. Yamada, and T. Mukai, Jpn. J. Appl. Phys. **34**, pt. 2, L1332 (1995).

[9] F. I. Manyakhin, A. N. Kovalev, V. E. Kudryashov, A. N. Turkin, and A. E. Yunovich, MRS Int. J. of Nitride Semic. Res. 2/11; http://nsr.mij.org/2/11.

[10] F. I. Manyakhin, A. N. Kovalev, V. E. Kudryashov, A. N. Turkin, and A. É. Yunovich, Fiz. Tekh. Poluprovodn. **32**, 63 (1998) [Semiconductors **32**, 54 (1998)].

[11] Second Int. Conf. on Nitride Semiconductors, Tokushima, Japan (1997).

[12] T. Takeuchi, S. Sota, M. Katsuragawa, M. Komari, H. Takeuchi, H. Amano, and I. Akasaki, Jpn. J. Appl. Phys. **36**, pt. 2, L382 (1997).
[13] A. Hangleiter, S. Heppel, J.S. Im, and H. Kollmer, J. Off. EGW-3, 1998, Abstr. 52-I.
[14] H. Sakai, T. Koide, H. Suzauki, M. Yamaguchi, S. Yamasaki, M. Koike, H. Amano, and I. Akasaki, Jpn. J. Appl. Phys. **34**, pt. 2, L1429 (1995).
[15] M. Koike, N. Koide, S. Asami, J. Umezaki, S. Nagai, S. Yamasaki, N. Shibata, H. Amano, and I. Akasaki, Proc. of SPIE-Int.Soc. Opt. Eng. 3002 (1997).
[16] A. N. Turkin and A. É. Yunovich, Pis'ma Zh. Tekh. Fiz. **22** (23), 82 (1996) [Tech. Phys. Lett. **22**, 989 (1996)].
[17] *Op. cit.*, Ref. 10.
[18] A. V. Dmitriev and A. I. Oruzheinikov, MRS Int. J. of Nitride Semic. Res. 1/46; http://nsr.mij.mrs.org/1/46.
[19] K. Domen, R. Soejima, A. Kuramata, and T. Tanahashi, MRS Int. J. of Nitride Semic. Res. 3/2; http://nsr.mij.mrs.org/3/2.

Translated by D. H. McNeill

Photoionization of deep impurity centers in quantum well structures

V. I. Belyavskiĭ and Yu. A. Pomerantsev

Voronezh State University, 394043 Voronezh, Russia
(Submitted May 25, 1998; accepted for publication August 25, 1998)
Fiz. Tekh. Poluprovodn. **33**, 451–455 (April 1999)

The absorption of light by photoionization of deep impurity centers in quantum well heterostructures is studied theoretically using a model with a maximally localized potential. Analytic expressions are found for the photoionization cross sections for light polarized perpendicular and parallel to the axis of the structure, disregarding the effect of the impurity potential on the continuum electronic states. The dependence of the frequency variation of the cross section on the charge state of the impurity after photoionization, as well as on the position of the impurity in the structure and the doping profile, is studied qualitatively near the absorption threshold. © *1999 American Institute of Physics.* [S1063-7826(99)01504-5]

1. Optical techniques for studying quantum-well heterostructures yield extensive information on the structure and quality of the interfaces and can be used to estimate the quantum-well width to within a monolayer.[1] A part of the visible spectrum, which corresponds to rather distinct exciton resonance lines, is used for these purposes, as well as for many device applications in optoelectronic equipment. The properties of quantum-well structures are determined, to a great extent, by the presence of certain impurities and point defects in them, which lead to the appearance of additional features in their optical absorption spectra due, in particular, to the photoionization of impurity centers. Substantial impurity concentrations are required in order to observe these features. Since the photoionization energy depends on the location of an impurity in a heterostructure, the impurity band spectra are spread out and this makes their resolution and interpretation more difficult. Despite these circumstances, the optical transitions associated with impurity centers are accessible to experimental study.[2–4] When impurities are introduced by δ-doping,[5] it is possible to determine the location of the impurities from the location of the edge of the absorption band. The high sensitivity of the binding energy between a carrier and an impurity to changes in an external electric field parallel to the axis of the heterostructure[6] makes it possible, in principle, to change the location of the impurity optical absorption edge.

Shallow (Coulomb) donor and acceptor impurities in quantum-well heterostructures have been studied in some detail.[7,8] The structure of deep impurities of the nontransition elements, which often play an important role in determining the properties of a heterostructure, are less well understood.[9] In this paper we examine impurity optical absorption in quantum well structures due to photoionization of deep impurity centers. It is assumed that a localized state is formed exclusively of states in the conduction band, and the impurity potential is assumed to be a maximally localized (singular) attractive potential. In fact, this involves an analog of the standard Lucovsky formula[10] and a modification of it to account for a Coulomb interaction excited in the conduction band between an electron and an impurity center.[11,12]

2. Let us consider the photoexcitation of an electron from a local level with energy E_i to one of the two-dimensional $(2D)$ subbands of the quantum-well system, whose dispersion relation we shall assume to be parabolic and isotropic, i.e.,

$$E_\lambda(k)=E_\lambda^{(0)}+\frac{\hbar^2k^2}{2m_\lambda}. \tag{1}$$

Here k is the $2D$ quasiwave vector, λ is the subband number, $E_\lambda^{(0)}$ is the energy of the subband edge (in the following, the energy reckoned from the bottom of the lowest subband, so that $E_1^{(0)}=0$), and m_λ is the effective mass. In the dipole approximation the total photoionization cross section can be written as

$$\sigma_\lambda=\frac{2m_\lambda S\alpha}{m_0^2\hbar\omega}\int d^2k|\langle\bar{\lambda}k|\xi\hat{p}|i\rangle|^2\delta(k^2-k_\omega^2), \tag{2}$$

where S is the normalizing area of the structure, $\alpha=e^2/\hbar c$, m_0 is the free electron mass, ξ is the polarization vector of the photon, $\hbar\omega$ is its energy, $\hat{p}$ is the electron momentum operator, and

$$k_\omega^2=\frac{2m_\lambda}{\hbar^2}[\hbar\omega-(E_\lambda^{(0)}+E_i^{(0)})]. \tag{3}$$

The refractive index and local field coefficient, which takes into account the difference in the amplitudes of the local and average macroscopic fields, have been left out of Eq. (2) and the binding energy of an electron at an impurity center, $E_i^{(0)}\equiv -E_i$, has been introduced. The matrix element $|\bar{\lambda}k\rangle$ of the momentum operator is calculated between electron states at the local level, $|i\rangle$, and in the $2D$ subband, λ. The symbol λ indicates that, when the Coulomb interaction of the excited electron with the ionized impurity atom is taken into account, the envelope of the continuum wave function must have the correct asymptotic behavior.[13] A function of this type for the $2D$ case can be found elsewhere.[14,15]

3. We assume that a deep localized state is formed by the $2D$ quantum-well subbands of the conduction band. For de-

 © 1999 American Institute of Physics

scribing the localized states we shall use the method of envelope functions in the effective-mass approximation.[7] The one-electron envelope functions for free motion with a definite transverse quasimomentum have the form

$$|\lambda k\rangle=\frac{1}{\sqrt{S}}e^{ik\rho}f_{\lambda k}(z). \tag{4}$$

Here the coordinate z is directed along the axis of the heterostructure, and ρ is the transverse $2D$ radius vector. Since the characteristic spatial scale of the localized state is, at least, considerably greater than the interatomic distance a, and that the main contribution to the expansion of the wave function $|i\rangle$ over the basis (4) is from states with $k\ll a^{-1}$, we shall disregard the dependence of the one-dimensional ($1D$) envelope of the wave function $f_{\lambda k}(z)$ on k, and write $f_{\lambda 0}(z)\equiv f_{\lambda}(z)$. In the model of a maximally localized potential, the Fourier transform of the envelope of the wave function, which corresponds to the contribution of the $2D$ subband λ to the localized state, has the form

$$\tilde{\Psi}_{\lambda}(k)=A\frac{f_{\lambda}^{*}(z_0)}{E_{\lambda}(k)-E_i}, \tag{5}$$

where z_0 is the coordinate of an impurity atom in the heterostructure, and A is a common normalizing factor. In the case of the dispersion relation (1) we have

$$\Psi_{\lambda}(\rho)=\frac{\kappa_{i\lambda}}{\sqrt{\pi}}K_0(\kappa_{i\lambda}\rho),\quad \kappa_{i\lambda}^2=\frac{2m_{\lambda}}{\hbar^2}(E_{\lambda}^{(0)}+E_i^{(0)}), \tag{6}$$

where $K_0(x)$ is a modified Bessel function of the third kind. The energy E_i of the localized state is found from the equation

$$\frac{U_0a^3}{(2\pi)^2}\sum_{\lambda}|f_{\lambda}(z_0)|^2\int\frac{d^2k}{E_{\lambda}(k)-E_i}=1, \tag{7}$$

where U_0 is a phenomenological parameter characterizing the magnitude of the impurity potential. The contribution of the $2D$ subband λ to the energy and the envelope function of the localized state is therefore determined by the values of the $1D$ envelopes at the site z_0 of the impurity atom. If we assume, for example, that the localized state is formed only by the lowest ($\lambda=1$) subband (this approximation is adequate if the separation between the edge of the lowest subband to the other subbands is much greater than the binding energy $E_i^{(0)}$), then the position of the impurity shows up in the envelope (5) only through the dependence of the binding energy on z_0. Including the other subbands changes the situation somewhat: the weight of the envelope (5) with a given number λ can be determined substantially by the value of the $1D$ envelopes of the corresponding subbands at the site of the impurity atom.

The Lifshitz method[16], which is used here for describing the deep electronic states, is semiphenomenological. Here the experimentally determined parameter is logically assumed to be the binding energy of an electron at an impurity center. When its value is known for some z_0, Eq. (7) can then be used to determine the parameter U_0, as when the zero-radius-potential method is used to describe deep impurity states in thin semiconducting films[17] and quantum-well structures.[18]

4. Specifying $|\bar{\lambda}k\rangle=f_{\lambda(z)}\varphi_{\lambda k}^{(-)}(\rho)$, where $\varphi_{\lambda k}^{(-)}(\rho)$ is the $2D$ continuum envelope,[15] the matrix element that determines the photoionization cross section can be written in the form

$$\langle\bar{\lambda}k|\xi p|i\rangle=\int d^2\rho\,\varphi_{\lambda k}^{(-)*}(\rho)\xi_{\rho}\hat{p}_{\rho}\Psi_{\lambda}(\rho)+\sum_{\lambda'}\left[\int d^2\rho\,\varphi_{\lambda k}^{(-)*}(\rho)\Psi_{\lambda'}(\rho)\right]\xi_z p_z^{\lambda\lambda'}, \tag{8}$$

where ξ_{ρ}, ξ_z, and $\hat{p}_{\rho}$, $\hat{p}_z$ are the perpendicular and parallel (relative to the heterostructure axis) components of the polarization vector and the momentum operator, respectively, and $p_z^{\lambda\lambda'}=\int dz f_{\lambda}^{*}(z)\hat{p}_z f_{\lambda'}(z)$.

Equation (8) implies that, when the localized state is formed by states only from the lowest ($\lambda=1$) subbands, impurity absorption of light polarized perpendicular to the heterostructure axis can only occur when an electron is excited from an impurity level into the $\lambda=1$ sublevel. On the other hand, when light polarized along the heterostructure axis is absorbed, then the transitions to the $\lambda=1$ subband are forbidden. In this case, only one term with $\lambda'=1$ and $p_z^{11}\equiv 0$ is left in the sum (8). Allowance for contributions from other subbands in the localized state cancels selection rules of this type, but, within sufficiently narrow quantum wells, where the distances between the edges of the quantum-well subbands are very large compared to the binding energy of an electron with an impurity center, the contribution from the lowest subband dominates in the photoionization cross section.

5. We now consider the simplest case of the photoexcitation of an electron from an impurity level into the lowest subband, assuming that the localized electronic state is formed exclusively by states from that subband. In addition, we shall ignore the interaction of the excited electron with the potential of the impurity center. In this case, the envelope function of the final state has the form (4), the matrix element (8) between envelope functions of the localized state and continuum states in the lowest subband is easily calculated, and for $\hbar\omega\geqslant E_i^{(0)}$ the photoionization cross section takes the form

$$\sigma_1=16\pi^2\alpha a_i^2\xi_{\rho}^2(E_i^{(0)})^2(\hbar\omega)^{-3}(\hbar\omega-E_i^{(0)}), \tag{9}$$

where $a_i^2=m_1\hbar^2/2m_0^2E_i^{(0)}$. Equation (9), the $2D$ analog of Lucovsky's formula,[10] describes the photoionization of a singly charged negative impurity ion in the ground state.

The plot of the function (9) has a peak corresponding to $\hbar\omega/E_i^{(0)}=3/2$ with magnitude

$$\sigma_1^{(m)}=\left(\frac{4}{3}\right)^3\pi^2\alpha a_i^2\xi_{\rho}^2. \tag{10}$$

Note that $\sigma_1^{(m)}\propto(E_i^{(0)})^{-1}$. For $E_i^{(0)}\sim 0.1$ eV, Eq. (10) gives $\sigma_1^{(m)}\sim 10^{-17}$ cm^2.

The photoionization cross section for transitions to a subband $\lambda \neq 1$, which are possible for light polarized parallel to the heterostructure axis, is given by

$$\sigma_\lambda = 16\pi^2 \alpha \tilde{a}_i^2 \xi_z^2 (E_i^{(0)})^3 (\hbar\omega)^{-1} \times \left(\hbar\omega - (E_\lambda^{(0)} + E_i^{(0)}) + \frac{m_1}{m_\lambda} E_i^{(0)} \right)^{-2}. \quad (11)$$

Here $\tilde{a}_i^2 = a_i^2 |p_z^{\lambda 1}|^2 / 2 m_\lambda E_i^{(0)} \propto (E_i^{(0)})^{-2}$, and $\hbar\omega \geqslant E_\lambda^{(0)} + E_i^{(0)}$. Equation (11) has a finite (and its highest) value at the photoionization threshold, $\hbar\omega = E_\lambda^{(0)} + E_i^{(0)}$:

$$\sigma_\lambda^m = 16\pi^2 \alpha \tilde{a}_i^2 \xi_z^2 \left(\frac{m_\lambda}{m_1} \right)^2 \frac{E_i^{(0)}}{E_\lambda^{(0)} + E_i^{(0)}} \propto \frac{1}{E_i^{(0)} (E_\lambda^{(0)} + E_i^{(0)})}. \quad (12)$$

When the inequality $E_\lambda^{(0)} \gg E_i^{(0)}$ is satisfied, the threshold value of the cross section (12) is much smaller as the number of the quantum-well subband increases.

6. If the impurity charge is nonzero after photoionization, then for $\varphi_{\lambda k}^{(-)}(\rho)$ it is necessary to use the correct continuum wave functions, which take into account the Coulomb interaction of the excited electron with the charged impurity center. Again restricting the analysis to a simple model for the impurity center, i.e., considering only the contribution of the lowest $2D$ subband and, therefore, when considering the absorption of light polarized perpendicular to the heterostructure axis, only the first term in Eq. (8), in $\varphi_{1k}^{(-)} \times (\rho)$ we can distinguish components that correspond to values $m = \pm 1$ for the projection of the angular momentum onto the heterostructure axis, which give a nonzero contribution to the matrix element (8). For the corresponding radial envelope function we have[14]

$$\varphi_{1k1}^{(-)} = \frac{1}{\sqrt{S}} C_Z(k) \rho \exp(-ik\rho) F\left(\frac{3}{2} + \frac{iZ}{ia^*}, 3; 2ik\rho \right), \quad (13)$$

where $F(\alpha, \beta; z)$ is the degenerate hypergeometric function, $a^* = \varepsilon \hbar^2 / m_1 e^2$ is the effective Bohr radius (ε is the dielectric constant), Z is the charge (in units of the elementary charge) of the impurities after photoionization, and

$$C_Z(k) = 2^{1/2} \left(\frac{1}{4} + \frac{Z^2}{k^2 a^{*2}} \right)^{1/2} \left[1 + \exp\left(-\frac{2\pi Z}{ka^*} \right) \right]^{-1/2} \quad (14)$$

is the Sommerfeld factor. $Z > 0$ corresponds to attraction of the electron to the ionized impurity and $Z < 0$ corresponds to repulsion.

No closed expression in the form of special functions is known for the matrix element (8) with the wave functions (13), but it is easy to determine its limits. In the limit $k \to 0$, for example, we have[19]

$$F\left(\frac{3}{2} + \frac{iZ}{ka^*}, 3; 2ik\rho \right) \Rightarrow J_0\left(2\sqrt{\frac{2\rho}{a^*}} \right), \quad (15)$$

and at the absorption edge the frequency dependence of the photoionization cross section is actually determined by the Sommerfeld factor. For $Z > 0$ the cross section has a finite threshold value of the same order of magnitude as given by Eq. (10). For $Z < 0$ the cross section at the photoionization threshold is exponentially small, $\sigma_1 \propto \exp(-2\pi Z / k_\omega a^*)$. When $\hbar\omega \gg E_i^{(0)}$, the frequency dependence of the cross section has a universal dependence for arbitrary Z, $\sigma_1 \propto \omega^{-2}$.

The absorption of light polarized along the heterostructure axis can be studied in a similar fashion. For $\hbar\omega \gg E_i^{(0)}$, for example, the frequency dependence of the cross section also has a universal dependence for arbitrary Z, $\sigma_\lambda \propto \omega^{-3}$. For $Z > 0$ the cross section, just as for $Z = 0$, has a finite threshold value, while for $Z < 0$ it is exponentially small.

7. Equations (9) and (11) for the photoionization cross section were obtained under the assumption that the atoms of the dopant impurity lie in a single monatomic layer of the heterostructure corresponding to a certain value of the binding energy $E_i^{(0)}(z_0)$. In real heterostructures the doping profile, which determines the distribution of the impurities with respect to the binding energy, may have a significant effect on the frequency dependence of the absorption. The attenuation of a light flux directed along the z axis coincident with the axis of the heterostructure is given by

$$\beta(\omega) = \int N_i(z_0) \sigma_1(z_0, \omega) dz_0, \quad (16)$$

where $N_i(z_0)$ is the volume concentration of the dopant impurity atoms (the dopant is assumed to be homogeneous in layers perpendicular to the heterostructure axis) and the integral is taken along the z coordinate of an impurity atom within the structure. The photoionization cross section depends on the position of the impurity atom through the binding energy $E_i^{(0)}(z_0)$.

In the case of deep impurities, it is easy to find the function $E_i^{(0)}(z_0)$, if, as before,we assume that the impurity state is formed exclusively from states in the lowest $2D$ subband. In this case, in accordance with Eq. (7), we have

$$E_i^{(0)}(z_0) \approx \frac{\pi^2 \hbar^2}{2 m_1 a^2} \exp\left(-\frac{1}{w(z_0)} \right), \quad (17)$$

where

$$w(z_0) = \frac{m_1 U_0 a^3}{2\pi\hbar^2} |f_1(z_0)|^2. \quad (18)$$

The function (17) has a rather sharp (in contrast with the Coulomb impurities[20]) maximum at some point z_{0m}, which is also the maximum point for the function of Eq. (18). Expanding the latter in a series in powers of $z_0 - z_{0m}$ while taking into account the equation for the $1D$ envelope $f_1(z)$, we can approximate Eq. (17) in the neighborhood of the point z_{0m} by

$$E_i^{(0)}(z_0) \approx E_i^{(m)} \exp\left(-\frac{(z_0 - z_{0m})^2}{\Delta^2} \right), \quad (19)$$

where $E_i^{(m)} \equiv E_i^{(0)}(z_{0m})$, and $\Delta^2 = \hbar^2 w(z_{0m}) / m_1 \tilde{E}_1^{(0)}$. Here $\tilde{E}_1^{(0)}$ is the energy of the edge of the lowest subband relative to the bottom of the quantum well. The parameter Δ, which determines the width of the peak of the function (17), is on

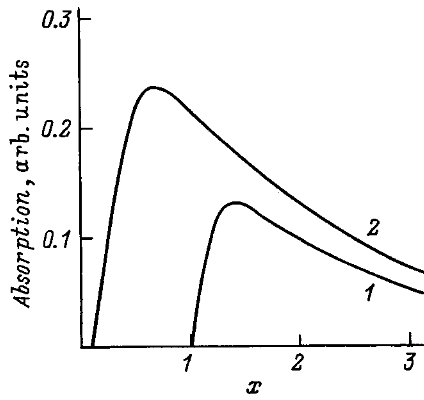

FIG. 1. Optical absorption by a quantum-well structure as a function of frequency (schematic) for (*1*) δ-doping of the layer at $z=z_{0m}$, Eq. (9), and (*2*) uniform doping within the confines of the quantum well, Eq. (20). The dimensionless variable is $x\equiv\hbar\omega/E_i^{(m)}$.

the order of a few times the interatomic distance for the typical $\widetilde{E}_i^{(0)}\approx 50$ meV and $U_0\approx 1$ eV and the characteristic width $\sim 10a$ of a quantum well. Thus, if the doping profile varies only slightly over distances $\sim\Delta$, then the dopant impurity concentration in Eq. (16) can be regarded as constant and equal to $N_i(z_{0m})$, and the limits of integration can be restricted to the dimensions of the doping region.

The quantity $\beta(\omega)$ corresponding to the cross section (9) can be calculated easily:

$$\beta(x)\propto\frac{1}{x^3}\left\{x[\Phi(\sqrt{\ln x_m^{-1}})-\Phi(\sqrt{\ln x^{-1}})\vartheta(1-x)]\right.$$
$$\left.-\frac{\sqrt{2}}{2}[\Phi(\sqrt{\ln x_m^{-2}})-\Phi(\sqrt{\ln x^{-2}})\vartheta(1-x)]\right\}. \tag{20}$$

Here $x\equiv\hbar\omega/E_i^{(m)}$, $x_m=\exp(-L^2/\Delta^2)$, $2L$ is the width of the doping profile inside the quantum well, $\Phi(\xi)$ is the probability integral, $\vartheta(\xi)$ is the Heaviside step function, and the factors which are unimportant in the frequency dependence have been omitted. Note that $\beta(x)$ has a maximum that is considerably shifted toward lower frequencies compared to the case of δ-doping for $z=z_{0m}$, as shown in Fig. 1.

8. A study of the energy spectrum and electron envelope functions in quantum-well structures with deep impurity centers using the Lifshitz method[16] yields physically understandable and quite intuitive results. The peculiarities of the band structure of ideal (without impurity atoms) quantum-well systems are already taken into account in the very statement of the problem in accordance with this method. When this method is actually applied, it is only necessary to include a finite (and small) number of quantum-well subbands and, in particular, the $3D$ continuum states above the barrier can be disregarded. With this approach, the domain of applicability of the Lifshitz method for studying localized states in quantum wells appears to be limited to structures in which the separation between the lowest $2D$ quantum-well subbands is very large compared to the binding energy of an electron to an impurity center.[20] Thus, there is considerable pedagogical interest in comparing the description of deep impurity states by the Lifshitz method (subject to the limitations mentioned above) to the solution of the effective mass equations for the electron envelope function in a rectangular quantum well in the presence of a singular attractive potential localized at the site of an impurity atom.[18] This solution, which is found in r-space and which accounts for the difference between the effective mass of the electron in the quantum well and barrier structures, is naturally fully equivalent to the solution (5) of the equation for the Fourier transform of the envelope function if the electronic states in all the quantum-well subbands in k-space are considered. In fact, the electron envelope functions in a system with a maximally localized potential are simply the Green's function taken for the appropriate allowed energies given by Eq. (7) or an equivalent equation found in Ref. 18. This approach to describing deep impurity states, including both the singular and long-range (Coulomb) impurity potentials, has been studied previously.[21*]

It is comparatively easy to establish that calculating the optical matrix elements for transitions between the electron envelope functions, found in Ref. 18, yields the selection rules pointed out in this paper (which naturally reflect the symmetry of the system), although the computational procedure itself is considerably more cumbersome and does not provide simple analytic expressions for the photoionization cross section such as Eqs. (9) or (11). A study of the frequency dependence of the cross section shows that, both for $\hbar\omega\ll E_i$ and the opposite limit, the dependences obtained in this paper have a universal character which appears to be entirely natural, since each term of a Gilbert-Schmidt expansion (over the quantum-well subbands) for the Green's function yields the correct asymptotic behavior in the limits $\omega\to 0$ and $\omega\to\infty$.

The most important restriction imposed on using the Lifshitz method for quantum-well structures with the simplifications mentioned here is the condition on the depth and width of the quantum wells: The method is fairly effective if $\widetilde{E}_i^{(0)}\propto\hbar^2/m_1d^2$, which is an estimate of the position of the first quantum-well level in an infinitely deep quantum well of width d, is much smaller than the magnitude ΔE_c of the gap in the conduction band of the heterostructure, which determines the depth of a real quantum well. In the opposite limiting case of relatively shallow and wide quantum wells, an adequate description of the dependence of the binding energy E_i on the location of an impurity in the structure can be found by direct solution of the effective mass equation obtained in Ref. 18.

*Ref. 21 is cited in the Russian original, but is not listed in the reference section.

[1] M. Herman, D. Bimberg, and J. Christen, J. Appl. Phys. **70** R1 (1991).
[2] R. C. Miller, A. C. Gossard, W. T. Tsang, and O. Munteanu, Phys. Rev. B **25**, 3871 (1982); Solid State Commun. **43** 519 (1982).
[3] D. Gammon, R. Merlin, W. T. Masselink, and H. Morkos, Phys. Rev. B **33**, 2916 (1986).
[4] G. C. Rune, P. O. Holtz, M. Sundaram, J. L. Merz, A. C. Gossard, and B. Monemar, Phys. Rev. B **44**, 4010 (1991).
[5] A. Ya. Shik, Fiz. Tekh. Poluprovodn. **26**, 1161 (1992) [Sov. Phys. Semicond. **26**, 649 (1992)].
[6] V. I. Belyavskiĭ, Yu. V. Kopaev, N. V. Kornyakov, and S. V. Shevtsov, JETP Lett. **61**, 56 (1995).

[7] G. Bastard, J. A. Brum, and R. Ferreira, Solid State Phys. **44**, 229 (1990).
[8] A. Pasquarello, L. C. Andreani, and R. Buczko, Phys. Rev. B **40**, 5602 (1989).
[9] C. E. M. Wood, in *Molecular Beam Epitaxy and Heterostructures*, L. Cheng and K. Ploog (Eds.), Mir, Moscow (1989), p. 127.
[10] G. Lucovsky, Solid State Commun. **3**, 299 (1965).
[11] A. S. Baltenkov and A. A. Grinberg, Fiz. Tekh. Poluprovodn. **10**, 1159 (1976) [Sov. Phys. Semicond. **10**, 688 (1976)].
[12] V. I. Belyavskiĭ and V. V. Shalimov, Fiz. Tekh. Poluprovodn. **11**, 1505 (1977) [Sov. Phys. Semicond. **11**, 1235 (1977)].
[13] L. D. Landau and E. M. Lifshitz, *Quantum Mechanics* [in Russian], Nauka, Moscow (1989).
[14] M. Shinada and S. Sugano, J. Phys. Soc. Jpn. **10**, 1936 (1966).
[15] A. V. Chaplik and M. V. Éntin, Zh. Éksp. Teor. Fiz. **61**, 2496 (1971) [Sov. Phys. JETP **34**, 1335 (1971)].
[16] A. M. Kosevich, *Theory of Crystal Lattices (The Physical Mechanics of Crystals)* [in Russian], Kharkov (1988).
[17] V. D. Krevchik and É. Z. Imamov, Fiz. Tekh. Poluprovodn. **17**, 1235 (1983) [Sov. Phys. Semicond. **17**, 780 (1983)].
[18] A. A. Pakhomov, I. V. Khalilov, and I. N. Yassievich, Fiz. Tekh. Poluprovodn. **30**, 1387 (1996) [Semiconductors **30**, 1379 (1996)].
[19] I. S. Gradshtein and I. M. Rizhik, *Tables of Integrals, Sums, Series, and Products* [in Russian], Nauka, Moscow (1971).
[20] V. I. Belyavskiĭ, M. V. Gol'dfarb, Yu. V. Kopaev, and S. V. Shevtsov, Fiz. Tekh. Poluprovodn. **31**, 302 (1997) [Semiconductors **31**, 246 (1997)]; V. I. Belyavskiĭ and V. V. Shalimov, Fiz. Tekh. Poluprovodn. **13**, 1364 (1979) [Sov. Phys. Semicond. **13**, 798 (1979)].

Translated by D. H. McNeill

Photovoltaic effect in the impurity absorption region of Si-structures with blocked impurity conductivity

B. A. Aronzon and V. V. Rylkov

Russian Scientific Center ''Kurchatov Institute,'' 123182 Moscow, Russia;
Scientific Research Center for Applied Problems in Electrodynamics, 127412 Moscow, Russia

L. Asadauskas and R. Brazis

Laboratoire de Physique de la Matiere Condense, Universite Paul Sabatier, 31062 Toulouse Cedex, France;
Semiconductor Physics Institute, 2600 Vilnius, Lithuania

D. Yu. Kovalev

Russian Scientific Center ''Kurchatov Institute,'' 123182 Moscow, Russia

J. Leotin

Laboratoire de Physique de la Matiere Condense, Universite Paul Sabatier, 31062 Toulouse Cedex, France
(Submitted September 8, 1998; accepted for publication September 15, 1998)
Fiz. Tekh. Poluprovodn. **33**, 456–463 (April 1999)

A study is made of the field dependence of the photoconductivity in two-layer Si:Sb- and Si:B-structures with blocked impurity-band conductivity and different thicknesses of the undoped (blocking) layer. The impurity concentration in the doped (active) layer was $\approx 10^{18}$ cm^{-3}. Measurements were made at temperatures $T=4-15$ K for high ($\Phi \sim 10^{16}$ photons/cm$^2\cdot$s) and low ($\Phi < 10^{14}$ photons/cm$^2\cdot$s) incident photon fluxes. A photovoltaic effect is observed in the Si:B structures with a thin (3 μm) blocking layer. It is found that a photovoltage develops for photons with energies exceeding the ionization energy of boron and its magnitude is independent of the photoexcitation intensity (for $\Phi > 10^{13}$ photons/cm$^2\cdot$s) and, in the limit of low temperatures, it is close to the activation energy ε_3 for jump conductivity in the active layer. The photovoltaic effect is explained by ballistic transit of the blocking layer by holes emitted from the contact which are then cooled in the active layer, as well as by the presence of a potential barrier $\approx \varepsilon_3$ between the active and blocking layers. These factors are taken into account in a model for describing the major features of the dependence of the photovoltage on temperature and on the photon intensity and energy. © *1999 American Institute of Physics.* [S1063-7826(99)01604-X]

1. INTRODUCTION

It is known that when inhomogeneously doped semiconductors equipped with ohmic contacts undergo monopolar photoexcitation, a stationary photovoltaic effect should not occur.[1] The case in which one of the contacts is a Schottky-type barrier and the energy of the incident photons exceeds the Schottky barrier height is an exception. The photovoltage which occurs then is caused by photoemission of charge carriers from the contact, because some of them absorb a photon and are drawn into the volume of the semiconductor by the field at the contact as their energy relaxes.[1]

In this paper we report the observation of a photovoltaic effect during impurity photoexcitation in silicon structures (referred to as BIB structures[2] below) with ohmic contacts consisting of two epitaxial layers: an active layer with a high doping level and a blocking layer with a low impurity content (Fig. 1, type A). These structures are of interest because of the possibility of creating miniature (in matrix form) infrared sensors with a detectivity close to the maximum possible determined by fluctuations in the cosmic radiation, $\Phi = 10^7 - 10^{12}$ photons/cm$^2\cdot$s (Ref. 2). The high sensitivity of BIB-structures is achieved through the use of a blocking layer, which greatly reduces the dark conductivity due to transport of carriers through the impurity band in the doped region. Here the free carriers produced by photoexcitation can move unimpeded under the influence of an external field in the direction of the front contact toward the blocking layer and thereby make a major contribution to the photocurrent.

Considerable attention has recently been devoted to research on BIB-structures with a rather high level of doping in the active layer, in which high electric fields cause a substantial shift of the photoconductivity threshold toward longer wavelengths than observed in conventional Si photoconductors.[3–5] Here, however, there is a pressing need to reduce the dark currents due to thermal generation of free carriers and their multiplication as a result of collisional ionization of impurities. In this regard, there is some interest in studying the mechanism of photoconductivity in BIB-structures for low bias voltages V_b. It is natural to expect that under these conditions a dominant role will be played by the field at the potential barrier at the interface between the

 © 1999 American Institute of Physics

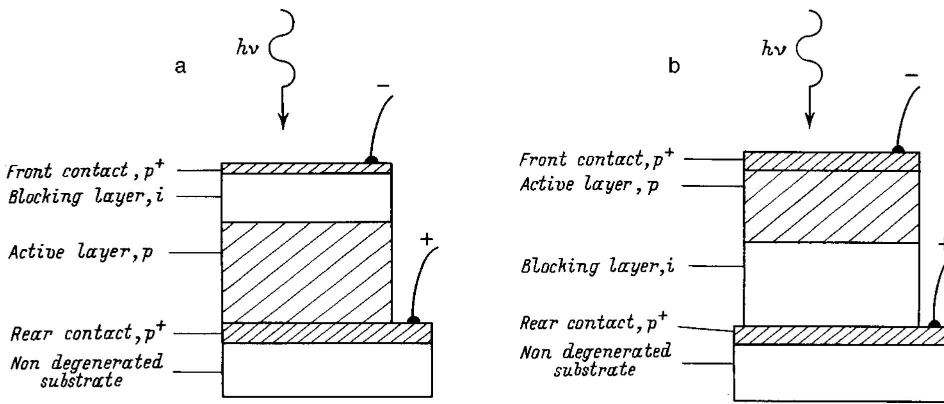

FIG. 1. Si:B structures with blocked conductivity across the impurity band. Type A: front contact, $p^+=10^{19}\,\mathrm{cm}^{-3}$ (thickness $d_+=0.1\,\mu$m); blocking layer, $N_B<5\times10^{13}\,\mathrm{cm}^{-3}$ ($d_a=3\,\mu$m); active region, $N_B=10^{18}\,\mathrm{cm}^{-3}$ ($d_a=6\,\mu$m); back contact, $p^+=10^{19}\,\mathrm{cm}^{-3}$ ($d_+=1.5\,\mu$m). Type B: p^+-$Ge_{0.12}Si_{0.88}$ alloy contact; 4.5-μm-thick active layer; the remaining parameters are as in type-A structures.

active and blocking layers due to the contact potential difference between materials with very different doping levels.[6] We shall show, however, that photoemission processes in the regions of the contacts can also play an important role in the photoresponse of BIB-structures when $V_b=0$. It is interesting that the photovoltage which arises in this case is independent of the photoexcitation intensity, and that its highest value V_{emf} is determined by the activation energy ε_3 for jump conductivity in the active layer.

2. SAMPLES AND TECHNIQUES

We have studied epitaxial Si:Sb and Si:B BIB-structures with similar doping levels in the active layer ($N_{\mathrm{B}}\cong N_{\mathrm{Sb}}\cong 1\times10^{18}\,\mathrm{cm}^{-3}$). The technology for fabricating the samples has been described in detail elsewhere.[4,5] There were two types of Si:B BIB-structures, A and B (Fig. 1), which differed in the contact materials at the active layer and in the sequence of depositing the epitaxial layers on the substrate. In the type A structures the contact with the active layer was degenerate Si:B, while in the type B structures it was a heavily boron-doped $Ge_{0.12}Si_{0.88}$ solid solution. In the first case, an active layer was first deposited on the substrate and then a blocking layer was grown on it. In the second case, the layers were deposited in the reverse order. The type of the Si:Sb structures was analogous to type A, but in them the blocking layer was considerably thicker ($d_b=10\,\mu$m) than in the Si:B BIB-structures ($d_b=3\,\mu$m). The thicknesses and impurity contents of the layers were determined through layer-by-layer etching of the structures in an electrolytic cell using the spread resistance method. Note that the distinctive feature of the objects being studied here was their rather low concentrations of compensating centers in the doped regions, as well as of majority impurities in the undoped Si layers ($<10^{14}\,\mathrm{cm}^{-3}$).[4,5]

The current-voltage characteristics were studied at temperatures $T=4-15$ K at both high ($\Phi\sim10^{16}$ photons/cm$^2\cdot$s) and low ($\Phi<10^{14}$ photons/cm$^2\cdot$s) incident photon fluxes. The photovoltage V_{emf} and the short-circuit current I_{sc} were determined in the standard way from the intersection of the current-voltage characteristics with the abscissa and ordinate, respectively.[1] The spectra of the short-circuit current, ΔI_{sc}, over wave numbers of 280–480 cm^{-1} were also studied for high levels of background illumination.

The photocurrents I_{ph} at high IR illumination levels were measured using an optical cryostat (Oxford Instruments) with an SR-580 low-noise preamplifier. Photoexcitation was produced by a room-temperature background incident on the sample through a cooled Si filter from the warm parts of the cryostat and spectrometer (Brucker IFS 113v).

The experiments with low photoexcitation intensities were done using a cryogenic cell mounted in a Dewar flask with liquid helium.[7] The photoexcitation source was a $Pb_{1-x}Sn_xSe$ semiconducting laser with an emission wavelength $\lambda=5.25\,\mu$m mounted in the cell. The output intensity of the laser was initially calibrated using a standard Si:Ga photoresistor. The photocurrent was measured with a current-voltage amplifier with a sensitivity of about 10^{-12} A. Because of the high resistance of the test objects, the contact potential on the active layer relative to the ground, φ_a, and the contact potential on the blocking layer, φ_b, were monitored independently. The contacts were connected to the input of the current-voltage amplifier and to the power supply, respectively. The bias voltage V_b on the structure was determined as the difference $V_b=(\varphi_b-\varphi_a)$. This method of recording V_b eliminated any influence on the current-voltage characteristics from the shunting effect of the voltage measurement device (an HP 3457A multimeter), as well as from parasitic photovoltages.

3. EXPERIMENTAL RESULTS

Current-voltage characteristics for the Si:B and Si:Sb BIB-structures taken at different temperatures with the same photon flux $\Phi\sim10^{14}$ photons/cm$^2\cdot$s are shown in Figs. 2–4. For the Si:Sb BIB-structures with a thick blocking layer, the photocurrent $I_{\mathrm{ph}}=0$ for $V_b=0$, which indicates the absence of a photovoltaic effect. The opposite situation is observed in the Si:B BIB-structures. In this case, the current-voltage characteristics do not pass through the coordinate origin and the photovoltages at the intersection of these curves with the abscissa are opposite in sign for the type A and B structures. In the type A structures the photovoltage corresponds to movement of holes from the blocking layer toward the active layer, while in the type B structures, the motion is in the opposite direction. (The resulting signs of the charge at the facets of the structure are indicated in Fig. 1.) The insets in Figs. 2 and 3 show the corresponding temperature depen-

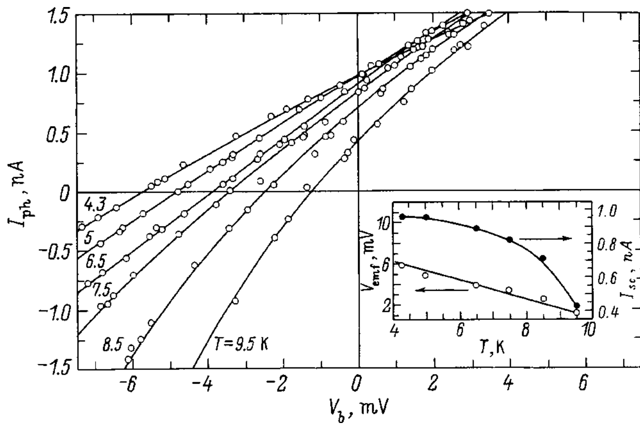

FIG. 2. Current-voltage characteristics of type-A Si:B BIB-structures at different temperatures obtained during illumination by a semiconductor IR laser ($\lambda = 5.25\ \mu$m, $\Phi \sim 10^{14}$ photons/cm$^2 \cdot$s). The inset shows the absolute magnitudes of the photovoltage V_{emf} and short-circuit current I_{sc} as functions of temperature.

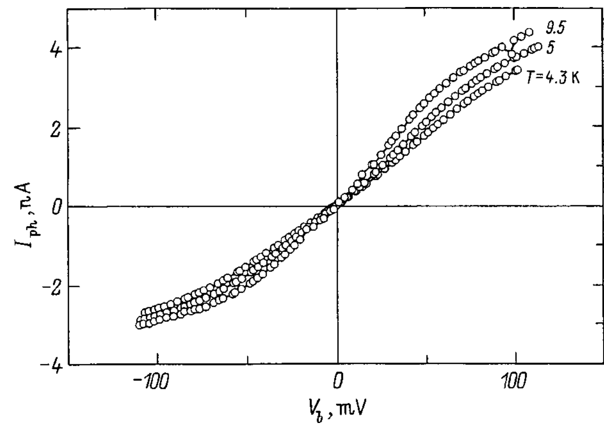

FIG. 4. Current-voltage characteristics of type-A Si:Sb BIB- structures with a thick blocking layer ($d_b = 10\ \mu$m) at different temperatures. The illumination conditions are the same as for the Si:B BIB-structures.

dences of the photovoltvoltage $V_{emf}(T)$ and short-circuit current $I_{sc}(T)$ for type A and B structures. It can be seen that in the type B structures V_{emf} and I_{sc} attain high values, with V_{emf} depending much less strongly on temperature. When T is increased from 4 to 10 K, the photovoltage in a type A structure decreases by a factor of 5 and in a type B structure, only by 20%. These structures shared, however, the absence of a dependence of V_{emf} on the intensity and the spectral features of the exciting radiation. To within the accuracy of the experiment, we were unable to observe, in either case, a change in the photovoltage when the intensity of the laser light was reduced by roughly an order of magnitude (Figs. 5a and 5b), although the short circuit photocurrent fell quite sharply ($I_{sc} \propto \Phi$). Figure 6 also shows plots of $I_{ph}(V_b)$ for a type A structure irradiated by room temperature background. The current-voltage characteristics give the same sign for the photovoltage as in the case of laser excitation. The values of V_{emf} at different temperatures also agree with good accuracy (see the data in the insets in Figs. 2 and 6).

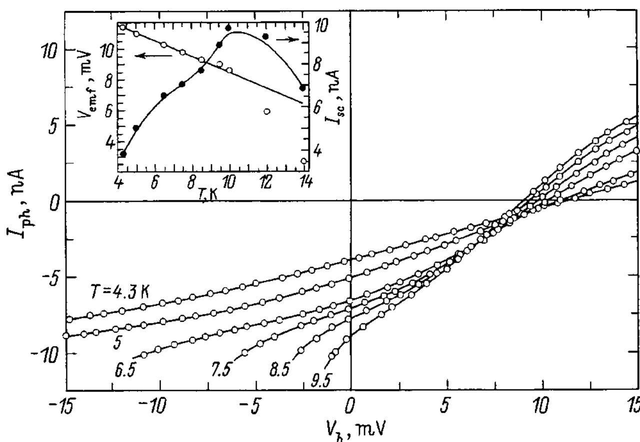

FIG. 3. Current-voltage characteristics of type-B Si:B BIB-structures at different temperatures. The illumination conditions are the same as for the type-A structures. The inset shows the absolute magnitudes of the photovoltage V_{emf} and short-circuit current I_{sc} as functions of temperature.

We now consider the spectral measurements of the short-circuit photocurrent (Figs. 7 and 8) obtained under conditions of room-temperature illumination. It is clear from Fig. 7 that in type A structures the photocurrent spectrum ΔI_{sc} contains a distinct threshold at 355 cm^{-1} (denoted by an arrow in Fig. 7), which corresponds to a photon energy of $h\nu = 44.0$ meV, essentially the same as the ionization energy for an isolated boron impurity, $E_B = 44.39$ meV.[8] In contrast, with type-B structures (Fig. 8) a ''long-wavelength tail'' shows up in the photocurrent spectrum beginning at

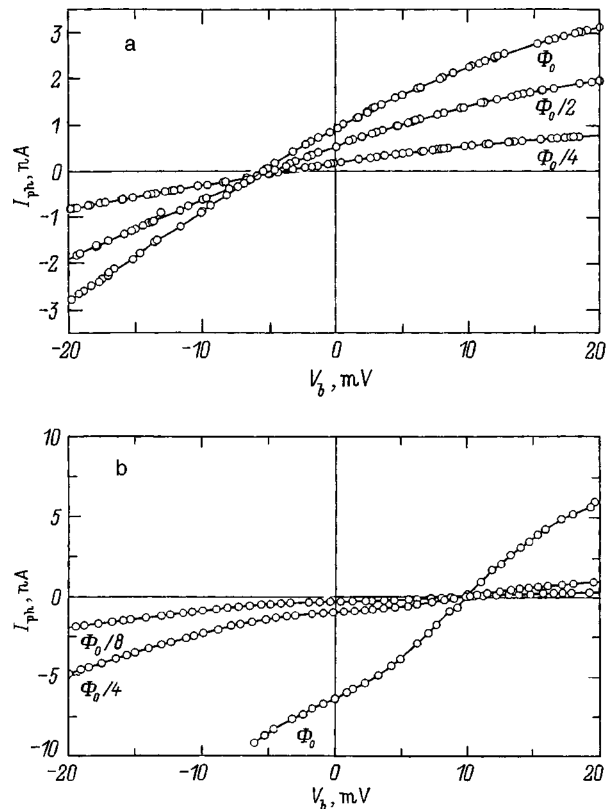

FIG. 5. Current-voltage characteristics of Si:B BIB-structures for different laser fluxes ($\Phi_0 \sim 10^{14}$ photons/cm$^2 \cdot$s): (a) for type-A structures, $T = 4.3$ K; (b) for type-B structures, $T = 6.5$ K.

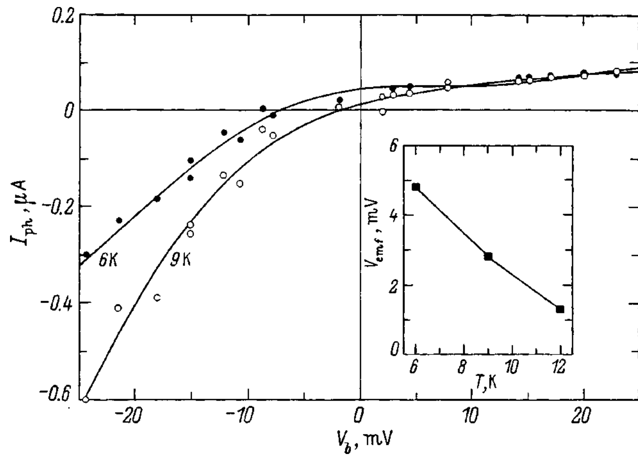

FIG. 6. Current-voltage characteristics of type-*A* Si:B BIB-structures for $T=6$ and 9 K, obtained with illumination by the room background. The inset shows the absolute magnitude of the photovoltage V_{emf} as a function of temperature.

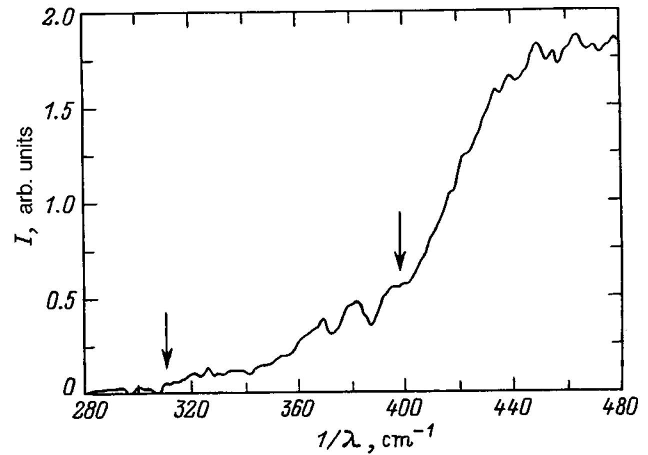

FIG. 8. The spectral variation in the short-circuit current for a type-*B* Si:B BIB-structure at $T=6$ K.

310 cm^{-1} ($h\nu=38.4$ meV) and a region where ΔI_{sc} rises rapidly (an additional threshold) is observed above 403 cm^{-1} ($h\nu=50.0$ meV), i.e., significantly shifted compared to the type-*A* structures. Note that our recent studies[5] of the photoconductivity spectra of Si:B BIB-structures at rather high reverse bias voltages $V_b>0$ (the photoresponse of BIB-structures is then determined entirely by the blocking layer) show that the major impurities in the blocking layers are isolated boron atoms. Given this fact, as well as the features of the spectral variation in the short-circuit current mentioned above, we conclude that in type-*A* structures the photovoltage is determined by junctions which exist near the interface between the blocking layer with p^+-Si (a p^+/i junction) and the active layer (an i/p junction). Here the absence of a photovoltaic effect in Si:Sb BIB-structures of type *A* with a thick blocking layer suggests that the photovoltage originates in photoemission. At the same time, in type *B* structures, as will be shown below, photoemission effects play an important role in the region of the interface between the p^+-$Ge_{0.12}Si_{0.88}$ heterocontact and the active layer (a p/p^+ junction), where boron impurities are no longer isolated.

4. DISCUSSION

We shall first examine the features of the band diagram of these structures, as these essentially provide a key to understanding the mechanism for the photovoltaic effect. Here we shall not consider the p/p^+ junction in type-*A* structures, since there is no photovoltaic in them when the blocking layer is thick.

Band diagram

The band diagram of these structures under equilibrium conditions is shown in Fig. 9. It is evident that the p^+/i junction is a potential barrier for holes, with a height ϕ_1 determined by the location μ_b of the Fermi level in the bulk (near the middle) of the blocking layer, i.e.,

$$\phi_1 \cong \mu_b = E_{\text{B}} - kT \ln[(N_{\text{B}}^* - N_D^*)/N_D^*], \tag{1}$$

where N_{B}^* and N_D^* are the concentrations of boron and compensating donor, respectively, in the blocking layer. On the other hand, the transition from the blocking layer to the active layer is accompanied by a drop in the potential energy of holes by

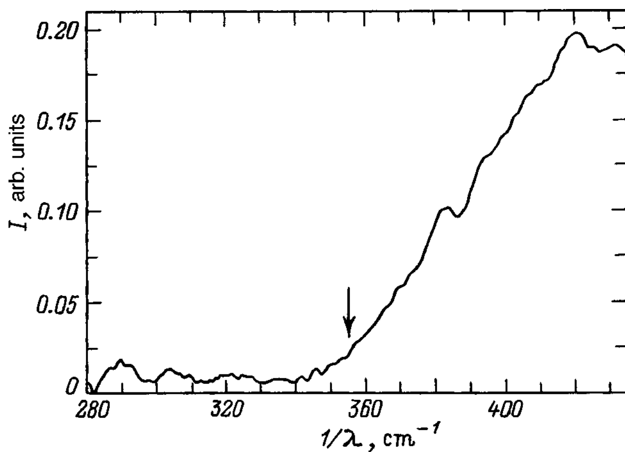

FIG. 7. The spectral variation in the short-circuit current for a type-*A* Si:B BIB-structure at $T=6$ K.

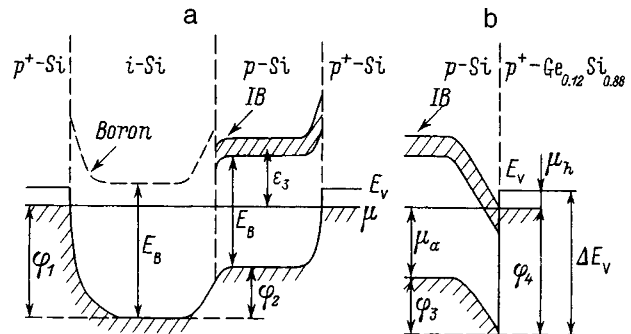

FIG. 9. Equilibrium band diagram: (a) for a type-*A* Si:B BIB-structure; (b) of a heterocontact for a type-*B* Si:B BIB-structure. *IB* impurity band, μ Fermi level, E_v ceiling of valence band, E_B ionization energy of impurity boron, ε_3 activation energy for jump conductivity.

$$\phi_2=(\mu_b-\mu_a)\approx\varepsilon_3-kT\ln[(N^*_{\rm B}-N^*_D)/N^*_D]. \qquad (2)$$

Here μ_a is the position of the Fermi layer in the active layer relative to the top of the valence band, and ε_3 is the activation energy for jump conductivity. Under jump conductivity conditions with a constant jump length, $\mu_a\approx(E_{\rm B}-\varepsilon_3)$ and is temperature independent.[6] According to Ref. 6,

$$\varepsilon_3=0.99e^2N_{\rm B}^{1/3}/\kappa, \qquad (3)$$

where e is the electronic charge, and κ is the dielectric constant. For sufficiently high doping levels approaching the critical value N_c, which corresponds to an insulator-metal transition [for boron in Si $N_c=(5-7)\times10^{18}$ cm^{-3} (Ref. 9), the experimentally measured value of ε_3 can be significantly lower than the value of ε_3 given by Eq. (3). One of the reasons is an increase in the width of the impurity band due to overlap of the wave functions of resonant states.[10] In estimating μ_a we shall proceed from the fact that the broadening is symmetric with respect to the positions of the unperturbed levels of the boron atoms and choose the theoretical value for ε_3. For $N_{\rm B}=1\times10^{18}$ cm^{-3} we have $\varepsilon_3\approx12$ meV, which corresponds to $\mu_a\approx32$ meV [the experimental value of $\varepsilon_3\approx6$ meV (Ref. 11)]. Note that Eqs. (1) and (2) assume the existence of an electrically neutral region in the blocking layer. This is valid provided the thickness of the blocking layer $d_b>(W_1+W_2)$, where W_1 and W_2 are the widths of the space charge regions at the left and right boundaries, respectively, of the blocking layer. In the approximation of a uniform distribution of the compensating donors, we have

$$W_{1,2}\cong(\kappa\phi_{1,2}/2\pi eN^*_D)^{1/2}. \qquad (4)$$

In fact, however, the donors are not distributed uniformly. In the bulk of the blocking layer $N^*_D<5\times10^{13}$ cm^{-3}, while in the active layer $N_D=2.5\times10^{14}$ cm^{-3} (Ref. 5), so that we can only speak of effective values of $W_{1,2}$. For $N^*_D\approx1\times10^{14}$ cm^{-3}, Eqs. (1), (2), and (4) imply that $W_{1,2}\approx0.8$ and 0.4 μm, respectively. In other words, the condition $d_b>(W_1+W_2)$ should, in principle, be satisfied.

The type-*B* structures have a different band diagram for the p/p^+ junction. At the Si/Ge$_x$Si$_{1-x}$ interface, it is known that there is always a discontinuity ΔE_v in the valence band, whose magnitude depends on x (the Ge content).[12] It is clear from Fig. 9 that when $(\Delta E_v-\mu_h)>\mu_a$ (μ_h is the Fermi energy in the heterocontact), a Ge$_x$Si$_{1-x}$ alloy doped to degeneracy forms a barrier contact with Si. The height of the Schottky barrier can then be written

$$\phi_3=(\Delta E_v-\mu_h)-\mu_a=\phi_4-\mu_a, \qquad (5)$$

where ϕ_4 is the internal work function for holes from the heterocontact into the active layer. For an estimate of $\phi_{3,4}$ we rely on the data of Ref. 12. For a doping level of 10^{19} cm^{-3} and $x\approx0.1$, the Fermi level $\mu_h\approx38$ meV. The calculations of the discontinuity in the valence band discussed in Ref. 12 give somewhat different values of ΔE_v: ΔE_v [eV]$=0.84x$ (Ref. 13) and ΔE_v [eV]$=0.75x$ (Refs. 14 and 15). Thus, for $x=0.12$ we obtain $\Delta E_v=90-101$ meV. Since $\mu_a\approx32$ meV, we have $\phi_3=20-31$ meV and $\phi_4=52-63$ meV. Note that the width of the Schottky barrier is

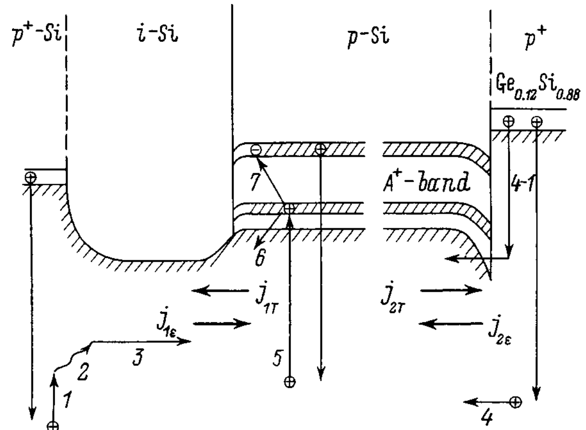

FIG. 10. Diagram of the major energy transitions to illustrate the mechanism of the photovoltaic effect in type-*A* and type-*B* Si:B BIB-structures.

determined by the concentration of the negatively ionized boron atoms (see Fig. 9) and is estimated to be no larger than the average distance between impurities (10 nm).

Therefore, an analysis of the experimental data and the band diagram for these structures shows that, in the case of the type-*A* structures, the threshold in the short-circuit current spectrum ΔI_{sc} is in good agreement with the internal work function (ϕ_1) for holes from the p^+-Si contact moving into the blocking layer. In addition, in the type *B* structures there is a certain correlation between the additional threshold in the ΔI_{sc} spectrum for $h\nu=50.0$ meV and the value $\phi_4=52-63$ meV, especially if we include the possibility of subbarrier tunnelling by holes in this case.

Mechanism for the photovoltaic effect

There are several important reasons for the photovoltaic effect in these samples. One is the rather long ballistic flight path of photoemission holes in the blocking layer, where their momentum collision time and energy relaxation time are controlled by acoustic phonons. It is also important that holes can be trapped inelastically in the active layer on neutral boron atoms with the emission of a single acoustic phonon,[16,17] so that the time for the photoholes to transfer their excess energy to thermal lattice vibrations in this layer may be considerably shorter than in the contact regions. The resulting fluxes of highly energetic holes are then directed from the contact regions toward the active layer, and in the steady state (open circuit conditions) they should be equilibrated with the fluxes of predominantly thermal holes that are thermally excited from the active layer. This circumstance is clarified with the aid of Fig. 10 which illustrates the main currents responsible for the photovoltage.

With laser photoexcitation the initial hole energy is determined by the photon energy $h\nu=236$ meV ($\lambda=5.25$ μm) and is significantly greater than the optical phonon energy[18] in Si [$\hbar\omega_{\rm opt}=63$ meV]. Thus, the initial, most rapid stage of energy relaxation is associated with the emission of optical phonons (Fig. 10, transition *1*). After three phonons have been emitted, the hole energy is 47 meV, i.e., it will still exceed the barrier height at the p^+/i junction. Note that this energy is sufficient for hole photoemission:

$h\nu_1 = 44$ meV, while the maximum of the photovoltaic effect occurs at $h\nu = 50$ meV (Fig. 7). The next energy relaxation step (transition *2*) is determined by the interaction with free holes and acoustic phonons, and those photoholes which diffuse into the blocking layer interact only with acoustic phonons. The carrier mean free path l_a then reaches a maximum, and if $l_a > (d_b - W_2)$ a hole can reach the active layer (transition *3*). Let us estimate l_a. It is known that l_a is independent of the carrier energy for scattering on acoustic phonons,[19] i.e.,

$$l_a = \frac{\pi\hbar^4 \rho s^2}{m^2 E_c kT} = l_0 \frac{2ms^2}{kT}, \tag{6}$$

where ρ is the density of the crystal, s is the speed of sound, m is the effective mass, E_c is the deformation potential constant, and l_0 is a constant with the dimensions of length. The values of l_0 and ms^2 required to estimate l_a are given in Ref. 19. At $T = 6$ K, $l_a = 2.8$ μm for holes in Si and 4.5 μm for electrons. The absence of a photovoltaic effect in Si:Sb BIB-structures thicker than $d_b = 10$ μm is not, therefore, surprising and nor is the large drop in the short-circuit current above 7.5 K in type-*A* Si:B BIB-structures with $d_b = 3$ μm (see the inset in Fig. 2). Consequently, in Si:B BIB-structures conditions are such that a flux $J_{1\varepsilon}$ of highly energetic holes develops from the p^+–Si junction toward the active layer.

In type-*B* structures there is an additional counterstreaming flux $J_{2\varepsilon}$ directed away from the p^+-$Ge_{0.12}Si_{0.88}$ heterocontact (Fig. 10). The magnitude of the flux $J_{2\varepsilon}$ can exceed $J_{1\varepsilon}$, since it includes holes with energies greater than that of an optical phonon (transition *4*), which is attributable to the narrowness of the potential barrier. Figure 10 also shows a two-step $4-1$ transition which includes subbarrier tunnelling of holes into states in the valence band. We attribute the threshold at $h\nu = 38.4$ meV in the spectral dependence of the short-circuit current for type *B* structures (Fig. 8) to the possibility of transitions of this kind. As Fig. 9 implies, subbarrier tunnelling can, in principle, occur for photon energies $h\nu > \mu_a$; we estimate that μ_a is ≈ 32 meV.

The mechanism by which photoholes are cooled in the active layer is different. Here the initial relaxation stage is also associated with the emission of optical phonons. However, when their energy is less than $\hbar\omega_{\rm opt}$, the next relaxation step may be entirely determined by inelastic capture of holes by neutral boron atoms with the emission of a single acoustic phonon (transition *5*).[16,17] The binding energy of a carrier with a neutral center is fairly low and, in the case of isolated impurities, is 0.05 times the ground state energy ($E_{\rm B}$). In our case, the concentration is relatively high and the states of the neutral boron atoms form an A^+-band.[20] Part of the trapped holes are thermally ejected back into the valence band (transition *6*) with energies determined by the lattice temperature and part undergo indirect recombination[20] at negatively charged acceptors (transition *7*). The cooling time for the holes in this case is determined by the time τ_0 for them to be captured at neutral boron centers,[21] which can reach $\tau_0 \approx 5\times10^{-12}$ s in weakly compensated Si:B samples with $N_{\rm B} \approx 10^{17}$ cm^{-3} (Ref. 20). Since $\tau_0 \propto 1/N_{\rm B}$, we might expect that, in our case, $\tau_0 \approx 5\times10^{-13}$ s, or certainly less than the energy relaxation time at acoustic phonons, $\tau_\varepsilon \sim 10^{-10}$ s at $T = 10$ K.[19]

In this situation the fluxes $J_{1\varepsilon}$ and $J_{2\varepsilon}$ of high-energy holes should neutralize the negatively charged acceptors and cause buildup of a positive charge in the active layer near the i/p- and p/p^+ junctions, respectively. Here the barriers ϕ_2 and ϕ_3 decrease (Fig. 9) for the thermal hole fluxes J_{1T} and J_{2T} directed from the active layer toward the contacts (Fig. 10). In the steady state ($I_{\rm ph} = 0$): $J_{1\varepsilon} = J_{1T}$ and $J_{2\varepsilon} = J_{2T}$. On the other hand,

$$J_{1,2T} \propto p_T \exp\left(-\frac{\phi_{2,3\Phi}}{kT}\right) = J_{1,2} \exp\left(-\frac{\phi_{2,3\Phi}}{kT}\right), \tag{7}$$

where p_T is the concentration of thermalized photoholes in the active layer, and $\phi_{2,3\Phi}$ are the values of the potential barriers $\phi_{2,3}$ with IR illumination. the potential difference that develops between the facets of the structures during photoexcitation is determined by the change in the barrier heights.[1] In type-*A* structures, Eq. (2) and the equality of the fluxes imply that

$$eV_A = -eV_{\rm emf} = -(\phi_2 - \phi_{2\Phi}) = -\left\{ \varepsilon_3 - kT \ln\left[\left(\frac{N_{\rm B}^* - N_D^*}{N_D^*}\right)\frac{J_1}{J_{1\varepsilon}}\right]\right\}. \tag{8}$$

Similarly, for a type-*B* structure,

$$eV_B = -(\phi_2 - \phi_{2\Phi}) + (\phi_3 - \phi_{3\Phi}) = \phi_3 - \varepsilon_3 + kT\left\{ \ln\left[\left(\frac{N_{\rm B}^* - N_D^*}{N_D^*}\right)\frac{J_1}{J_{1\varepsilon}}\right] - \ln\left(\frac{J_2}{J_{2\varepsilon}}\right)\right\}. \tag{9}$$

Equations (8) and (9) imply that V_A and V_B depend on the relationship among the currents $J_{1\varepsilon}$, $J_{2\varepsilon}$, J_1, and J_2 which are proportional to the concentrations of the high-energy p_ε and thermal p_T photoholes. In turn, p_ε and p_T are proportional to Φ. This implies that the photovoltage should not depend on the photoexcitation intensity, as is observed experimentally. Furthermore, according to Eqs. (8) and (9), a linear extrapolation of V_A and V_B to $T = 0$ can be used to estimate ε_3 and $(\phi_3 - \varepsilon_3)$, respectively. Using the data in the insets in Figs. 2 and 3, we obtain: $\varepsilon \approx 9.6$ meV and $(\phi_3 - \varepsilon_3) \approx 13.3$ meV, i.e., $\phi_3 \approx 22.9$ meV. These values are consistent with the earlier theoretical estimates $\varepsilon_3 \approx 12$ meV and $\phi_3 \approx 20-31$ meV. Note also that Eqs. (8) and (9) predict a weaker temperature variation for V_B than for V_A. This is essentially related to the different directions of the hole fluxes, both thermal J_{1T} and J_{2T}, and high energy $J_{1\varepsilon}$ and $J_{2\varepsilon}$. In other words, at sufficiently low temperatures, the differences in the shapes of the barriers at the left and right boundaries of the active layer in type-*B* structures do not affect the development of the photovoltaic effect. However, the photovoltages produced by these barriers are opposite in sign and this compensates for the temperature dependence of V_B to some extent. Note that for $T > 6$ K the ballistic flight path for the holes becomes shorter than the blocking layer thickness; this is accompanied by a reduction

in the flux of highly energetic holes from the p^+-Si contact and an increase in the short-circuit current (see the inset in Fig. 3). With further increases in the temperature, the flux of thermal holes begins to become comparable to the flux of highly energetic holes from the heterocontact. There is a gradual transition to a thermal diffusion Dembert photovoltage,[1] which is symmetric and goes to zero with rising temperature. Thus, as the temperature is increased, the rise in the short-circuit current is replaced by a fall (Fig. 3).

On the whole, therefore, our model provides a satisfactory description of the photovoltaic effect in these BIB-structures. The principal factors controlling the photovoltaic effect in these objects are the following: 1) the existence of a potential barrier between the active and blocking layers, as well as between the active layer and the heterocontact in type-B structures, 2) the possibility of ballistic flight by photocarriers across the blocking layer for sufficiently low temperatures, and 3) shorter energy relaxation times for photocarriers in the active layer than in the contact regions.

We wish to thank T. M. Livshits for his interest in this work and for some discussions.

This work was supported in part by the Russian Fund for Fundamental Research (Grant 96-02-18429-a, Grant PICS 98-02-22037) and the Interbranch Scientific-Technical Program on the ''Physics of Solid State Nanostructures'' (Grant 1-052).

[1] S. M. Ryvkin, *Photoelectric Effects in Semiconductors*, Consultants Bureau, N. Y. (1964).
[2] M. D. Petroff, M. G. Stapelbroek, and W. A. Kleinhans, Appl. Phys. Lett. **51**, 406 (1987).
[3] J. E. Huffman, A. G. Crouse, B. L. Halleck, T. V. Downes, and T. Herter, J. Appl. Phys. **72**, 273 (1992).
[4] S. Pasquier, G. Sirmain, C. Meny, A. Murray, M. Griffin, PAde L. Essaleh, J. Galibert, and J. Leotin, in *Proceedings of the 8th International Conference on Millimeter and Submillimeter Waves and Applications*, San Diego (1994), p. 35.
[5] S. Pasquier, C. Meny, L. Asadauskas, J. Leotin, B. A. Aronzon, V. V. Rylkov, V. Conedera, N. Fabre, S. Regolini, and C. Morin, J. Appl. Phys. **83**, 4222 (1998).
[6] B. I. Shklovskiĭ and A. L. Éfros, *Electronic Properties of Doped Semiconductors*, Nauka, Moscow (1979).
[7] A. G. Zhdan, A. M. Kozlov, S. N. Klemin, and V. V. Rylkov, PTÉ, No. 2, 189 (1994).
[8] D. V. Fischer and J. J. Rome, Phys. Rev. B **27**, 4826 (1983).
[9] J. A. Chroboczek, F. H. Pollak, and H. F. Staunton, Philos. Mag. B **50**, 113 (1984).
[10] B. I. Shklovskiĭ, Fiz. Tekh. Poluprovodn. **6**, 1197 (1972) [Sov. Phys. Semicond. **6**, 710 (1972)].
[11] D. I. Aladashvili, Z. A. Adamiya, K. G. Lavdovskiĭ, E. I. Levin, and B. I. Shklovskiĭ, Fiz. Tekh. Poluprovodn. **23**, 213 (1989) [Sov. Phys. Semicond. **23**, 132 (1989)].
[12] S. C. Jain, *Germanium-Silicon Strained Layers and Heterostructures*, Advances in Electronics and Electron Physics, Suppl. 24 (Academic Press, 1994).
[13] C. G. Van de Walle and R. M. Martin, Phys. Rev. B **34**, 5621 (1986).
[14] J. M. Bass and C. C. Matthai, Semicond. Sci. Technol. **5**, 707 (1990).
[15] L. Colombo, R. Resta, and S. Baroni, Phys. Rev. B **44**, 5572 (1991).
[16] E. B. Gol'dgur and R. I. Rabinovich, Zh. Éksp. Teor. Fiz. **84**, 1109 (1983) [Sov. Phys. JETP **57**, 643 (1983)].
[17] V. N. Abakumov, V. I. Perel, and I. N. Yassievich, *Nonradiative Recombination in Semiconductors*, North-Holland, Amsterdam, Oxford, N. Y., Tokyo (1991).
[18] S. Sze, *Physics of Semiconductor Devices*, Wiley, N. Y. (1973).
[19] V. N. Abakumov, V. I. Perel', and I. N. Yassievich, Fiz. Tekh. Poluprovodn. **12**, 3 (1978) [Sov. Phys. Semicond. **12**, 1 (1978)].
[20] L. A. Vorozhtsova, E. M. Gershenzon, Yu. A. Gurvich, F. M. Ismagilova, and A. P. Mel'nikov, Zh. Éksp. Teor. Fiz. **94**, 350 (1988) [Sov. Phys. JETP **67**, 416 (1988)].
[21] V. V. Rylkov, Fiz. Tekh. Poluprovodn. **22**, 1661 (1988) [Sov. Phys. Semicond. **22**, 1048 (1988)].

Translated by D. H. McNeill

AMORPHOUS, GLASSY AND POROUS SEMICONDUCTORS

Defects in *a*-Si:H films induced by Si ion implantation

O. A. Golikova

A. F. Ioffe Physicotechnical Institute, Russian Academy of Sciences, 194021 St. Petersburg, Russia
(Submitted July 20, 1998; accepted for publication July 28, 1998)
Fiz. Tekh. Poluprovodn. **33**, 464–468 (April 1999)

Undoped a-Si:H films implanted with silicon ions (dose $10^{12}-10^{14}\,\mathrm{cm}^{-2}$, mean energy $\varepsilon=60\,\mathrm{keV}$) at room temperature have been studied. The following results of the interaction of such films with ion beams have been established: formation of defects (dangling Si–Si bonds) in the neutral state (D^0), change in the charge state $D^0\rightarrow D^-$, the a-Si:H$\rightarrow$$a$-Si transition, and growth of inhomogeneity of the structure. It is shown that these effects depend on the initial structures and electronic characteristics of the films. © *1999 American Institute of Physics.* [S1063-7826(99)01704-4]

INTRODUCTION

In recent years interest has grown in studying films of amorphous hydrogenated silicon (a-Si:H) subjected to silicon ion (Si^+) implantation. From the practical point of view, they are important for determining the radiation hardness of solar cells working under space conditions; however, to date they have mainly been tested for the action of light particles—electrons and high-energy protons.[1] Some data on Si^+ implantation (ion energy 300 keV, dose $D=5\times10^{10}\,\mathrm{cm}^{-2}$), resulting in changes in the parameters of the "intrinsic" (i) layer of the photo-element: its dark resistance, illuminated resistance, and density defects were published in Ref. 1. However, the initial characteristics of the material used in Ref. 1 were not indicated.

Gallone *et al.*[2] investigated the dark conductivity (σ_d) of undoped a-Si:H as a function of the implanted silicon concentration ($N_{\mathrm{Si}}=10^{18}-10^{21}\,\mathrm{cm}^{-3}$). The ion energies were of the order of several tens of keV. The process was carried out at room temperature with subsequent annealing in vacuum at 200 °C for 1 h. On the whole, implantation was viewed[2] as a method for increasing the electrical activity of boron introduced into a-Si:H films.

a-Si:H films were also irradiated with Si ions with energies $\varepsilon=1$ and 3 MeV and dose $D=10^{15}\,\mathrm{cm}^{-2}$ at liquid-nitrogen temperature, followed by a series of thirty-minute anneals in the temperature range $85-400\,^\circ\mathrm{C}$ (Ref. 3). The aim of that study[3] was to examine thermal relaxation of a-Si:H in comparison with the thermal relaxation of a-Si (hydrogen-free amorphous Si) previously examined in Ref. 4. The fundamental differences in the relaxation processes established in the two indicated cases[3,4] are clear evidence of the influence of hydrogen on the structural changes associated with ion implantation. However, data on the hydrogen content C_{H} and the nature of the silicon–hydrogen bonds or even just the deposition temperature of the film T_s are not given in Ref. 3.

In Ref. 5, as in Ref. 2, a series of a-Si:H films were implanted with keV Si ions at room temperature ($D=10^{12}-10^{14}\,\mathrm{cm}^{-2}$) to determine changes in the structure and electronic parameters of a-Si:H in comparison with those observed during extended intense illumination (the Stabler–Wronski effect). It was found, in particular, that dangling Si–Si bonds are formed during implantation, and that the Fermi level (ε_F) in the mobility gap is shifted.

This study is a continuation and development of the studies reported in Ref. 5 with the aim of establishing the interrelationship between the effects of Si^+ implantation and the initial electronic and structural characteristics of the films. Primary attention is devoted to peculiarities of the defects induced by implantation.

EXPERIMENTAL PROCEDURE

Implantation of silicon ions was carried out at room temperature on a heavy-ion accelerator (High Voltage Engineering Europa B.V.) using an SO-70 ion source and the gaseous compound SiF_4. For a uniform distribution of the ions over the thickness of the film ($d\simeq0.3\,\mu\mathrm{m}$) a "three-step" implantation of each of the films was performed with ion energies $\varepsilon=30$, 60, and 120 keV with variations of the dose, providing the required total dose D (Ref. 5). Thus, the average concentration of the implanted silicon varies in the range $N_{\mathrm{Si}}\simeq3\times10^{16}-3\times10^{18}\,\mathrm{cm}^{-3}$. Implantation was followed by annealing in a $(3-4)\times10^{-5}$ Torr vacuum at 200 °C for 1 h.

Undoped a-Si:H films obtained by rf ($f=13.56\,\mathrm{MHz}$) decomposition of SiH_4 were subjected to ion implantation at deposition temperatures $T_s=220-300\,^\circ\mathrm{C}$. Their structural and electronic parameters before implantation are described in Refs. 6 and 7: their dark conductivity (σ_d) and its activation energy (ΔE) (σ_d was measured in the temperature interval 300–470 K), the photoconductivity (σ_{ph}) (at $T=300\,\mathrm{K}$, $h\nu=2\,\mathrm{eV}$, carrier generation rate $10^{19}\mathrm{cm}^{-3}\cdot\mathrm{s}^{-1}$), defect density ($N_D$), and Urbach parameter (E_U) (at $T=300$ K by the constant photocurrent method). In addition, the hydrogen content of the films (C_{H}) was determined by

 © 1999 American Institute of Physics

infrared spectroscopy with special attention to the intensity of the absorption band at $630\,cm^{-1}$ and the microstructure parameter $R=I_{2090}/I_{2000}+I_{2090}$, where I_{2000} and I_{2090} are the intensities of the absorption bands at 2000 and $2090\,cm^{-1}$ which provide information on the content of the SiH and SiH_2 bonds in the films. We have also obtained information about the presence of clustered hydrogen found at the boundaries of the voids or ''grains'' that form the friable amorphous structure, as indicated by the shift of the peak of the absorption band characteristic of SiH bonds to $2010\,cm^{-1}$ (Ref. 6). In our study we determined the indicated parameters after ion implantation as functions of the total dose D.

EXPERIMENTAL RESULTS AND DISCUSSION

In our previous work[5] we showed that silicon ion implantation in *a*-Si:H leads to shifts of the Fermi level to the point $(\varepsilon_C-\varepsilon_F)_{T=0}=0.85\,eV$ corresponding to ''intrinsic'' *a*-Si:H, where the density of the implantation-induced defects for the total implantation dose $D\leqslant 10^{14}\,cm^{-2}$ was on the order of $10^{17}\,cm^{-3}$. In this regard, the effect of silicon ion implantation is similar to the Stabler–Wronski effect, and also to the effect of irradiation of *a*-Si:H by electrons with energies of several tens of keV. Therefore, we have concluded that the defects formed after implantation—dangling Si–Si bonds in the neutral state D^0—arise as a result of breaking of ''weak'' Si–Si bonds, as occurs in the two cases indicated above. Figure 1, however, reveals a more complicated picture regarding the Fermi-level shifts induced by ion implantation. Figure 1 plots the dependence of ΔE on D for a series of films with different initial characteristics; the initial (pre-implantation) values of ΔE are indicated. First we have film *1* consisting of ''intrinsic'' *a*-Si:H with

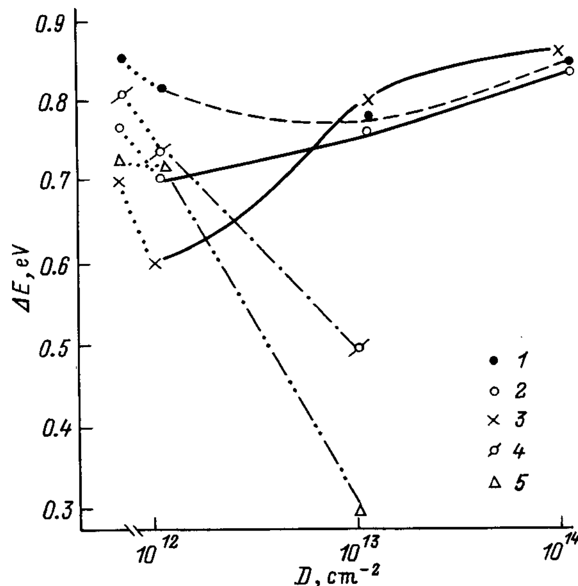

FIG. 1. Dependence of the activation energy of the dark conductivity, ΔE, of *a*-Si:H films on the Si ion implantation dose (films *1–5*). Figure also shows the initial ΔE for these films (before implantation). Remaining initial characteristics are given in text. The ΔE values have an accuracy of $\pm 0.02\,eV$.

$\Delta E=0.85\,eV$, $C_H=7$ at. %, $R=0$, $E_U=50\,MeV$, and $N_D\simeq 10^{16}\,cm^{-3}$, deposited at $T_s=300\,^\circ C$. Next, we have films *2* and *3*, also deposited at $T_s=300\,^\circ C$ and having respectively the parameter values $\Delta E=0.76$ and $0.70\,eV$, $C_H=8$ and 9 at. %, $R=0$ and 0.3, $E_U=55$ and 60 MeV, and $N_D\simeq 10^{16}\,cm^{-3}$ (Ref. 6).

It can be seen that with growth of D, ΔE does indeed reach 0.85 eV; however, the dependence of ΔE on D in all three cases is nonmonotonic. The most nonmonotonic dependence is that of curve *3*: for $D=10^{12}\,cm^{-3}$ the Fermi level is shifted toward the conduction band (ε_C) instead of the center of the mobility gap. Granted that it then turns around, and for $D=10^{14}\,cm^{-2}$ $\Delta E=0.85\,eV$. A consideration of the initial characteristics shows that before implantation film *3* exhibits the greatest inhomogeneity.

The shift of the Fermi level toward ε_C shows that at least some of the defects formed after implantation are found in the charged state D^- (Ref. 6). We therefore assume that the energy of the ion beam is expended not only in the formation of defects in the D^0 state, but also in changing their charged state: $D^0\rightarrow D^-$. As is well known, the correlation energy of the defect (dangling bond) in *a*-Si:H is positive ($\Delta=0.2-0.5\,eV$, Ref. 8). In an inhomogeneous film, fluctuations in Δ can be expected, and consequently an increase in the probability of $D^0\rightarrow D^-$ transitions. Indeed, for $D=10^{12}\,cm^{-2}$ the shift of ε_F toward ε_C is less for film *2*, which is more homogeneous before implantation. Film *1*, the most homogeneous film before implantation, reveals the largest shift of ε_F toward ε_C when, as a result of implantation, it becomes inhomogeneous (see below).

Let us consider the $\Delta E(D)$ curves for the two films deposited at lower temperatures, $T_s=220$ and $280\,^\circ C$ (films *4* and *5*). They have respectively the initial parameter values $\Delta E=0.81$ and $0.72\,eV$, $C_H=10$ and 16 at. %, $R=0.3$, $E_U=60\,MeV$, and $N_D=4\times 10^{16}\,cm^{-3}$. Clearly, the value of C_H for film *5* is higher than follows for the given T_s. However, what is most important is that they both contain clustered hydrogen: an SiH band with maximum at $2010\,cm^{-1}$ is observed for both these films in the IR absorption spectra. Their $\Delta E(D)$ curves have a completely different character in comparison with the curves for films *1–3* (Fig. 1).

As can be seen from Fig. 1, they fall monotonically with growth of the total implantation dose, at $D=10^{13}\,cm^{-2}$ attaining values of 0.5 and 0.3 eV, respectively. These ΔE values correspond to $T\geqslant 300\,K$. At lower temperatures, variable ΔE values are observed, as is characteristic for *a*-Si: In this case the defect density and hence the density of localized states in the mobility gap are so large that the conductivity mechanism with variable hopping length, known as the Mott mechanism, is realized (Fig. 2).

Indeed, the IR data show that films containing SiH clusters gradually ''lose'' hydrogen as the total implantation dose is increased. For $D=10^{13}\,cm^{-2}$ for example, their C_H values are equal to zero.[1)] According to estimates based on the Mott theory, the density of states at the Fermi level in this case $g(\varepsilon_F)\geqslant 10^{18}\,eV^{-1}\cdot cm^{-3}$ and, consequently, the defect density $N_D\gtrsim 10^{18}\,cm^{-3}$, i.e., it is at least an order of magnitude higher than the density of defects induced by ion implantation. The latter for different films is found in the

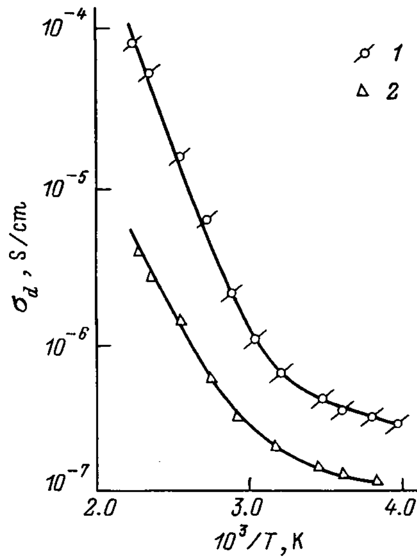

FIG. 2. Temperature dependence of the dark conductivity of films *4* and *5* (Fig. 1) after silicon ion implantation: $D=10^{13}\,\mathrm{cm}^{-2}$. Curves *1* and *2* correspond to films *4* and *5*, respectively.

limits $5\times10^{16}-3\times10^{17}\,\mathrm{cm}^{-3}$, growing in comparison with the initial (pre-implantation) value and reaching the indicated values at $D=10^{12}\,\mathrm{cm}^{-2}$ (Fig. 3).

Note that if the density of induced defects saturates as a function of D, the Urbach parameter, which characterize the degree of disorder of the structure, grows, especially steeply, beginning at $D=10^{13}\,\mathrm{cm}^{-2}$, and reaches values of 80 -90 MeV. As can be seen in Fig. 3, for $D>10^{13}\,\mathrm{cm}^{-2}$ the concentration of implanted silicon significantly exceeds the density of induced defects; i.e., the energy of the silicon ion beam is expended on the creation of disorder in the structure. It would seem in this case that if the density of weak Si–Si bonds grows, the density of dangling bonds should also grow; however, this is not observed (Fig. 3). The reason for this behavior is unclear; we can only refer to the analogy with the Stabler–Wronski effect. In that case the limiting densities of the light-induced defects of the same order of magnitude are observed.[5]

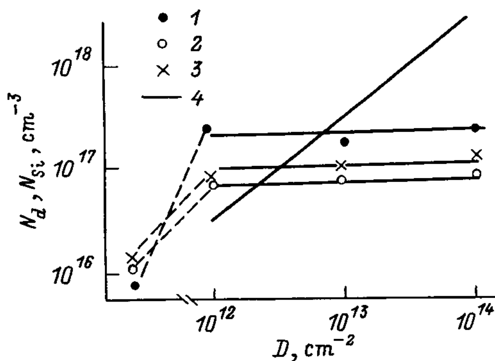

FIG. 3. Defect density, determined by the constant photocurrent method, in *a*-Si:H films, N_D, plotted versus the silicon ion implantation dose (films *1–3*). The figure also shows the initial values of N_D and the concentration of the silicon implanted in the film, N_{Si}, for different values of D (*4*).

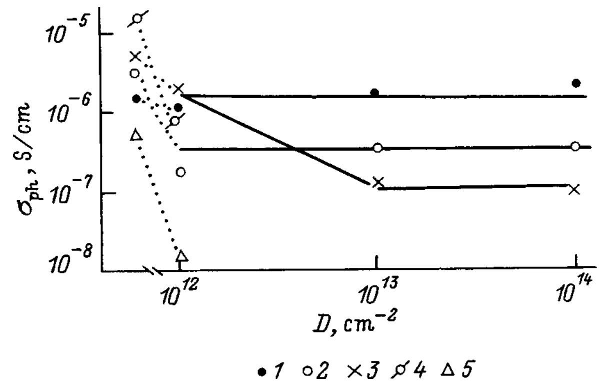

FIG. 4. Photoconductivity (σ_{ph}) of *a*-Si:H films plotted as a function of the silicon ion implantation dose (films *1–3*). The photoconductivity of films *4* and *5* could be determined only for $D=10^{12}\,\mathrm{cm}^{-2}$. The figure also shows the initial values of σ_{ph}.

As was noted earlier,[5] the highest values of E_U after implantation are observed for intrinsic *a*-Si:H; i.e., its structure becomes the most disordered.

Let us consider the dependence of the photoconductivity on the total implantation dose D (Fig. 4). Let us start with films *4* and *5*, which, as was shown above, ''transform'' as a result of implantation into films of hydrogen-free amorphous silicon (*a*-Si). In the initial state (before implantation) they have enhanced values of N_D in comparison with the values that should be expected for the given ΔE, which is typical of *a*-Si:H containing SiH clusters. Ion implantation leads to an abrupt drop in σ_{ph} with growth of D, such that for $D=10^{13}\,\mathrm{cm}^{-2}$ it cannot be measured, as is characteristic of *a*-Si.

The behavior of σ_{ph} for films *1–3* has several peculiarities.

First of all, the curve $\sigma_{\mathrm{ph}}(D)$ for film *3* stands out because of its nonmonotonicity. Recall that the same thing was noted about the $\Delta E(D)$ curve for this film (Fig. 1): It follows from Fig. 1 that the contribution of the defects in the D^{-1} state is especially large for $D=10^{12}\,\mathrm{cm}^{-2}$. Accordingly, for that dose σ_{ph} for film *3* is the highest in comparison with σ_{ph} for the other films. We know that since D^- does not capture electrons, σ_{ph} for undoped *a*-Si:H increases when ε_F shifts toward ε_C, when N_D increases, and when the value of the ratio N_{D^0}/N_{D^-} decreases (N_{D^0} and N_{D^-} are the defect densities in the D^0 and D^- states, respectively.[6]).

Second, at doses D at which N_D saturates, σ_{ph} does not depend on D for either film *1* or film *2* (Figs. 3 and 4), which seems reasonable if the defects do not change their charge state (D^0) during implantation. However, note that the largest σ_{ph} after implantation belongs to intrinsic *a*-Si:H, in which the density of induced defects is at a maximum.[2)] Note also that the change in σ_{ph} as a result of implantation for intrinsic *a*-Si:H is the lowest. These facts can be explained as follows. Although N_D of the defects induced by implantation in intrinsic *a*-Si:H grows in comparison with its initial value, implantation leads to the formation, along with defects in the D^0 state, of defects in the D^- state, which in turn is a consequence of the disordered state of the structure, also induced by implantation. We therefore obtain the paradoxical result

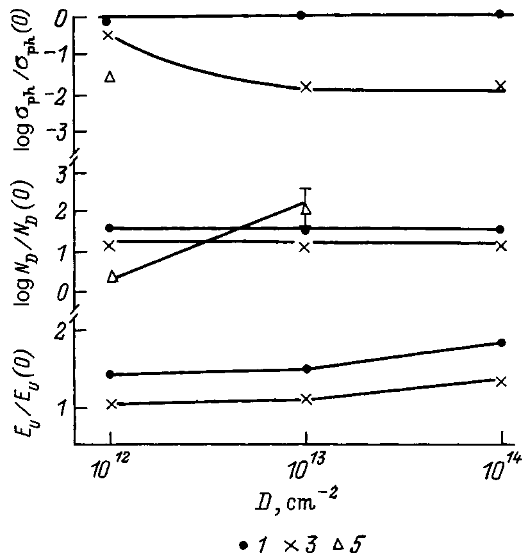

FIG. 5. Relative changes in the photoconductivity, Urbach parameter, and defect density of films *1*, *3*, and *5*, characterizing the stability of the electronic and structural parameters to implantation. The index (0) denotes the parameter before implantation. The estimate of $N_D/N_D(0)$ for film *5* for $D = 10^{13}\,\mathrm{cm}^{-2}$ assumes that $N_D \simeq 10^{18} - 10^{19}\,\mathrm{cm}^{-3}$.

that the changes in the structural parameters of intrinsic *a*-Si:H induced by implantation (N_D, E_U) are the largest, while the changes in σ_{ph} are the smallest. Thus, σ_{ph} of intrinsic *a*-Si:H is the most resistant to the action of silicon ion implantation under the above-indicated conditions of this process.

Relative changes of N_D, E_U, and σ_{ph} as a result of implantation for three typical *a*-Si:H films with different initial characteristics are plotted in Fig. 5.

CONCLUSIONS

Studies of the effects of implantation of silicon ions with energies of several tens of keV ($D = 10^{12} - 10^{14}\,\mathrm{cm}^{-2}$, $T = 300$ K) on films of amorphous hydrogenated silicon with different values of their initial characteristics—the Fermi level, defect density, Urbach parameter, photoconductivity, hydrogen content, Si–H bonds—have revealed the following results:

— Formation of defects in the D^0 state, accompanied by shifts of the Fermi level toward the center of the mobility gap; this is observed for all films not containing clustered hydrogen, regardless of C_H and R.

— Charge exchange of defects: $D^0 \rightarrow D^-$, accompanied by shifts of the Fermi level toward the edge of the conduction band facilitated by the inhomogeneity of the starting film or by the inhomogeneity induced by implantation.

— ''Loss'' of hydrogen by the films containing clustered hydrogen. As a result, *a*-Si:H converts to *a*-Si with growth of the implantation dose.

— A rapid growth of the Urbach parameter, which characterizes the inhomogeneity of the structure, especially for intrinsic *a*-Si:H, when the implanted silicon concentration is $N_{Si} > N_D$.

I am grateful to V. Kh. Kudoyarova, I. N. Petrov, and R. R. Yafaev for their collaboration in this work.

1)The IR spectroscopy was performed by V. Kh. Kudoyarova.

2)Recall that here we are not considering films that ''lose'' hydrogen as a result of implantation.

[1] G. Grabosh, D. Borchert, and W. R. Fahrer, *Abstracts of the Fourteenth European Photovoltaic Solar Energy Conference* (Barcelona, Spain, 1997), p. 8, A. 35.

[2] R. Gallone, Y. S. Tsuo, D. W. Baker, and F. Zignane, J. Non-Cryst. Solids **114**, 271 (1989).

[3] N. Nakata, S. Sherman, S. Wagner, P. A. Stolk, and J. M. Poate, MRS Symp. Proc. **377**, 173 (1995).

[4] S. Q. Gu, M. E. Raikh, and P. C. Taylor, Phys. Rev. Lett. **69**, 2697 (1992).

[5] O. A. Golikova, Kh. Yu. Mavlyanov, I. N. Petrov, and R. R. Yafaev, Fiz. Tekh. Poluprovodn. **29**, 577 (1995) [Semiconductors **29**, 299 (1995)].

[6] O. A. Golikova, V. Kh. Kudoyarova, Fiz. Tekh. Poluprovodn. **29**, 1128 (1995) [Semiconductors **29**, 584 (1995)].

[7] O. A. Golikova, M. M. Kazanin, O. I. Kon'kov, V. Kh. Kudoyarova, and E. I. Terukov, Fiz. Tekh. Poluprovodn. **30**, 405 (1996) [Semiconductors **30**, 226 (1996)].

[8] O. A. Golikova, Fiz. Tekh. Poluprovodn. **25**, 1517 (1991) [Sov. Phys. Semicond. **25**, 915 (1991)].

Translated by Paul F. Schippnick

Absorption and the optical gap of *a*-C:H films produced from acetylene plasmas

E. A. Konshina*

All-Russian Scientific Center "S. I. Vavilov State Optical Institute," 199034 St. Petersburg, Russia

(Submitted June 29, 1998; accepted for publication September 15, 1998)
Fiz. Tekh. Poluprovodn. **33**, 469–475 (April 1999)

Films of amorphous hydrogenized carbon (*a*-C:H) are prepared by chemical vapor deposition using a dc glow discharge. The absorption is studied over wavelengths of 400–2400 nm. Two Gaussian-like bands are identified with peaks at ~600 and ~800 nm. The ratio of the integrated intensities of these bands (I_{600}/I_{800}) is found to decrease as the voltage is raised. The changes in the ratio I_{600}/I_{800} are compared with the variation in the fundamental Raman scattering bands in order to clarify the nature of the visible absorption in the *a*-C:H films. Two simple schemes for transparent insulating films with $E_T \geqslant 1.5$ eV and for "black" conducting *a*-C:H films with $E_T \leqslant 1$ eV are proposed for explaining the relationship between the structure of the absorption edge and the width of the Tauc gap (E_T). © *1999 American Institute of Physics.* [S1063-7826(99)01804-9]

1. INTRODUCTION

The ability of amorphous carbon, including its hydrogenized form (*a*-C:H), to form various structural modifications has extended the range of optical and electronic properties and the range of applications of this material. Because of their low electron affinity and chemical inertness, *a*-C:H films are viewed as potential thin film materials for microcathodes in field emission displays.[1,2] Metal/*a*-C:H/metal sandwich-structures with a high-field conductivity may soon challenge the established position of *a*-Si devices as active matrix displays because *a*-C:H can be deposited on plastic substrates at room temperature.[3] A modification of *a*-C:H which absorbs in the visible has been used in liquid crystal matrix displays for contrast enhancement by depositing a "black" film of *a*-C:H on the interfaces between the elements of the matrix.[4]

The use of *a*-C:H films which absorb in the visible as light blocking layers for optically controlled modulators on reflective liquid crystals is a new technical solution of the problem of optically decoupling the write and read light signals. The efficiency of light blocking in semiconductor *a*-Si:H and *a*-Si:C:H layers with the aid of *a*-C:H films has been demonstrated.[5] It was found experimentally that the optimum light blocking layers are 1-μm-thick *a*-C:H with an absorption coefficient of 5×10^4 cm^{-1} at a wavelength of 632.8 nm, which attenuate the light flux that enters the semiconductor by a factor of 100. Although they were better absorbers, films with an absorption coefficient on the order of 1×10^5 cm^{-1} caused a deterioration of the image spatial resolution in this sort of structure because of space charge leakage. This indicates a significant correlation of the optical absorption with the width of the optical gap and the conductivity of *a*-C:H.

Previous experimental studies have shown that the optical gap in the various modifications of *a*-C:H depends on the conditions under which it was produced in a glow discharge plasma. The gap is made smaller when the energy delivered to the condensate is increased by raising the temperature of the carrier gas[6] or substrate[7,8], by raising the power of the rf discharge,[9] and by raising the voltage.[10–14] At the same time, the conductivity of *a*-C:H films is observed to rise.[13]

The main purpose of this paper is to establish the correlations among the optical absorption, optical gap width, and conductivity of *a*-C:H films. We have used visible and near-infrared (IR) absorption spectroscopy to determine the spectral dependence of the absorption coefficient. An analysis is made of the effect on the absorption of the conditions under which the *a*-C:H films are fabricated in a dc glow discharge. The changes in the intensities of the absorption bands of the *a*-C:H as the voltage is raised are compared with the previously observed changes in the resonance Raman scattering spectra and the nature of the visible absorption is discussed. The Tauc parameters are determined, along with their correlation with the parameters and structure of the absorption spectra of *a*- C:H films and their conductivity.

2. EXPERIMENTAL TECHNIQUES AND RESULTS

2.1 Technique for *a*-C:H film deposition

Chemical deposition of hydrocarbon vapor in plasmas is the most widespread contemporary technology for producing *a*- C:H films. Here we have used film deposition from a dc glow discharge plasma. The plasma was created using planar magnetrons with a flat cathode and annular anode.[15] The substrate holder was mounted a distance of 50 mm from the anode and held at a constant negative potential. The voltage between the anode and electrode-holder was varied in the range $U=600-1200$ V. The electrode system and the glass cylindrical insulator between them formed a quasiclosed volume into which the working gas was fed. Pure acetylene or a mixture of it with argon were used to make *a*-C:H. This kind of system ensures a higher degree of ionization of the gas and makes it possible to vary the pressure P in the vacuum chamber from 0.1 to 0.01 Pa and to change the rate of *a*-C:H

 © 1999 American Institute of Physics

TABLE I. Experimental parameters of the absorption spectrum $\alpha(\lambda)$, $E_{\max}$ and I_{600}/I_{800}, along with the Tauc parameters E_T and B derived from the dependence of $(\alpha E)^{1/2}$ on E for a-C:H films.

Samples of a-C:H	I_{600}/I_{800}	$E_{\max}$, eV	E_T, eV	B, 10^4 eV^{-1} $\cdot$cm^{-1}
a	2.7	2.07	2.09	2.3
b	0.33	1.65	1.65	5.0
c	0.4	1.65	1.09	7.9
d	4.5	2.07	1.14	5.6

film deposition in a wide range from 40 to 1 Å/s. Films were deposited on polished copper and quartz substrates at the ambient temperature.

2.2. Determining the width of the optical gap

The reflection and transmission spectra of the films were recorded from 200 to 1000 nm on a Hitachi spectrophotometer. In these measurements we used a-C:H films with a thickness of $\sim 0.2\ \mu$m deposited on quartz substrates. The film thickness was determined using an MII-4M microinterferometer. The relative error in the thickness measurements was 10%. The natural absorption coefficient (α) of the films was calculated using the Lambert–Beer law. The absorption edge of these a-C:H films, like that of other amorphous semiconductors, was adequately fit by the Tauc equation.[16] The Tauc optical gap (E_T) was determined by extrapolating a plot of $(\alpha E)^{1/2}$ as a function of energy E as described previously.[14] The resulting values of E_T and the slope (B) of the straight line drawn as a function of E for the a-C:H films are listed in Table I.

2.3. Absorption spectra of a-C:H films for wavelengths of 400–2400 nm

Absorption spectroscopy was used to obtain direct information on the structure of the optical absorption edge of the a-C:H films. The spectral variations in the absorption $\alpha(\lambda)$ at wavelengths in the range $\lambda = 400$–2400 nm were obtained from the reflection spectra of films with thicknesses of $\sim 0.3-0.5\ \mu$m deposited on mirror copper substrates. Figures 1a and 1b show $\alpha(\lambda)$ spectra of a-C:H films prepared from acetylene with $P = 0.1$ Pa and $U = 600$ and 1200 V, respectively. Figures 1c and 1d give $\alpha(\lambda)$ spectra for a-C:H films obtained with $P = 0.01$ Pa and $U = 900$ V from mixtures of acetylene with 50% and 70% argon. These spectra can be resolved into a series of Gaussian-type bands. In the wavelength interval from 400 to 1000 nm, two absorption bands were identified with peaks at 600 ± 5 nm (band 1) and 800 ± 40 nm (band 2). The ratio of the integrated intensities of these absorption bands (I_{600}/I_{800}) and the energies $E_{\max}$ of the peaks in the spectra of Fig. 1 are listed in Table I.

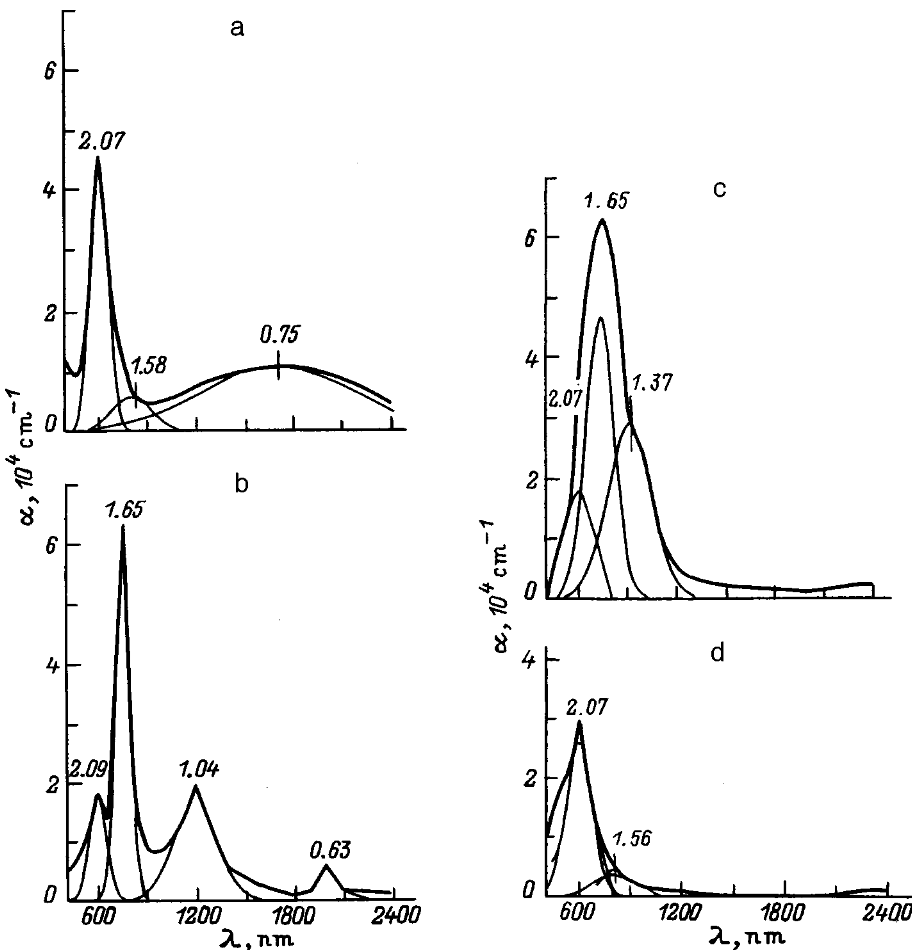

FIG. 1. Spectral dependences of $\alpha(\lambda)$ of a-C:H films obtained from acetylene at a constant pressure of 0.1 Pa with interelectrode voltages $U = 600$ (a) and 1200 V (b), as well as for a constant voltage $U = 900$ V and pressures of 0.01–0.03 Pa from a mixture of acetylene with 50 (c) and 70% (d) argon. The decompositions of the spectra into their components are shown with the peak energies (eV) indicated. The labels of spectra a–c correspond to the samples in Table I.

3. DISCUSSION OF RESULTS

3.1. Currrent theory of the atomic and electronic structure of *a*-C:H

The known forms of amorphous carbon, including the various modifications of *a*-C:H, consist of carbon atoms in the sp^3-state which form tetrahedral σ-bonds with four neighboring atoms, atoms in the sp^2-state which form σ-bonds with three neighboring atoms in a plane, a weak π-bond perpendicular to this plane, and, to a lesser extent, atoms in the sp^1-state. According to the cluster model for the structure of amorphous carbon developed by Robertson,[17–20] aromatic graphite π-bound atomic clusters consisting of sp^2-states, are distributed within an sp^3-bound matrix. Here the strong σ-bonds control the near ordering of the lattice, i.e., the bond lengths and angles of the skeleton, while the π-bonds cause clustering or a middle-range ordering within the structure. In the electronic structure of amorphous carbon, the σ- and σ^*-states form the deep valence and conduction states, while the π- and π^*-states, which lie inside the $\sigma-\sigma^*$-gaps, form the edge of the absorption band and control the width of the optical gap. The π-states form a filled valence band, while the π^*-states correspond to an empty conduction band in the optical gap near the Fermi level. In accordance with the cluster model, the width of the optical gap depends on the sizes of the π-clusters and decreases as the fraction of sp^2-states which form them rises,[20] while the sp^3-bound matrix determines the tunnel barrier between them.[18]

Increasing the hydrogen concentration in an amorphous carbon structure leads simultaneously to a reduction in its equilibrium density and to a substantial change in the character of the clustering. This has been shown by studies of the stability of *a*-C:H systems and of their atomic and electronic structure as functions of the mass density and concentration of hydrogen using the molecular-dynamic density method.[21,22] The extent of the clusters is reduced by the introduction of sp^2-segments inside the stressed sp^3 host. The distribution of the clusters and of the segments which bind them affects the energy gap of *a*-C:H. Jungnickel *et al.*[22] believe that the reduction in the gap is most likely a consequence of the splitting of the smallest π-bonded clusters and of the introduction of local π-electron systems into a stressed-bonded rigid lattice in which mixed bonds predominate. The very different assessment of the nature of the optical gap in *a*-C:H offered in Ref. 22 compared to that developed earlier by Robertson indicates that further study of the electronic structure of *a*-C:H is needed.

3.2. Results of a study of the medium-range order in the structure of *a*-C:H using resonant Raman scattering spectroscopy

The Raman scattering spectra of amorphous carbon in its different modifications consist of a broad band and can easily be resolved into two gaussian-type bands. The first has a peak in the interval 1530–1580 cm^{-1} and was initially attributed to an active 1585 cm^{-1} line of single-crystal graphite, while the second band near 1300–1400 cm^{-1}, with a line at 1355 cm^{-1}, corresponds to a disordered mode.[23] However, a high-frequency shift of the principal maximum observed in the Raman scattering spectra of various modifications of *a*-C:H when the excitation energy is raised has cast doubt on this interpretation.[24–27] It is the result of scattering from π-bond elements of the *a*-C:H structure which is enhanced resonantly at photon energies approaching the $\pi-\pi^*$-resonance. The bands near 1400 and 1530 cm^{-1} may be associated with scattering on large- and small-sized π-bond clusters, respectively.[25] At the same time, the relative intensity of the 1350-cm^{-1} band cannot be used to determine the dimensions of the graphite clusters.[26]

The absence of graphite clusters in the structure of fresh and thermally worked (at a temperature of 400 °C in vacuum) *a*-C:H films has been confirmed by comparing resonant Raman scattering spectra of *a*-C:H and graphite.[27,28] The observed features of the *a*-C:H Raman scattering spectra have led us to conclude that their structure includes a set of scattering centers characterized by different excitation energies of $\pi-\pi^*$ electronic transitions and vibrational energies. The different sizes of the π-bond elements of the structure, which lead to different values of the coupling parameter, and the strong disordered interaction among them cause the large spread in their electronic and vibrational spectra. Resonant excitation of the Raman spectra produces a selective enhancement in the scattering at the frequencies of those centers for which these conditions are optimal. The width and shape of the Raman scattering bands are determined by the dependences of the vibrational frequency and location of an absorption band on the length of the coupling chain and on the size distribution of the elements. In this case, the procedure of expanding the complicated Raman scattering band and absorption bands in the electronic spectra into Gaussian profiles is arbitrary.

The way the relative intensity of the Raman scattering bands of fresh and thermally processed *a*-C:H depends on the excitation wavelength shows that these bands correspond to different types of structural elements which are polyene chains of various lengths and polycyclic aromatic groups with different numbers of rings. The former predominate in the intensity of the band at $\sim$1540 cm^{-1} and the latter, to that of the band at $\sim$1340 cm^{-1}, which is extremely probable, since in the Raman scattering spectra of the corresponding molecular structures the most intense bands lie in the corresponding range of vibrational frequencies.[27]

The existence of olefin chains in the structure is confirmed by studies of *a*-C:H films by elastic neutron scattering[29] and by nuclear magnetic resonance and neutron diffraction.[30,31] Theoretical calculations of resonant Raman scattering spectra of amorphous carbon have shown that the band shapes are determined by a complex of sp^2-clusters with six or fewer rings. Polyene chains can contribute to the formation of the 1540-cm^{-1} band when the Raman scattering spectra are excited by visible light, while a lattice sp^3-structure has no direct effect on the resonant Raman scattering spectra.[32]

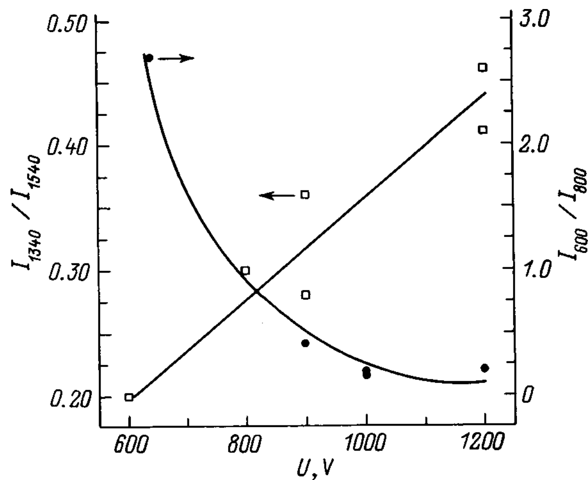

FIG. 2. The variation with interelectrode voltage (U) in the ratio I_{600}/I_{800} of the integrated intensities of the principal bands in the spectral dependence of the absorption coefficient $\alpha(\lambda)$ and in the ratio I_{1340}/I_{1540} of the fundamental bands in the resonance Raman scattering spectra of *a*-C:H films.

3.3. Comparison of Raman scattering and absorption spectra

Resonant Raman scattering spectroscopy is an extremely informative and highly sensitive method for investigating the characteristics of middle-range π-bond elements in *a*-C:H structures. Increasing the energy of the ions involved in the condensation of *a*-C:H in rf (Refs. 26 and 33) and dc (Ref. 34) glow discharge plasmas leads to a rise in the intensity ratio of the main bands at 1340 and 1540 cm^{-1} (I_{1340}/I_{1540}) in the Raman scattering spectrum. These changes can be explained by an increased amount of polycyclic aromatic groups compared to polyene chains in the *a*-C:H structure. A reduction in the amount of CH-groups in sp^3-states and a reduction in the optical gap were observed[14] at the same time as the rise in I_{1340}/I_{1540}. Since the Raman scattering spectra are caused by resonant scattering on π-bond elements of the structure, changes in these elements should correlate with changes in the electronic absorption spectra of *a*-C:H films.

Figure 2 shows plots of the band intensity ratio I_{600}/I_{800} in the absorption spectra $\alpha(\lambda)$ and of the ratio I_{1340}/I_{1540} of the principal bands in Raman scattering spectra of *a*-C:H films obtained previously in Refs. 20 and 32 as functions of the voltage. It can be seen that as the ratio I_{600}/I_{800} in the absorption spectrum decreases, the ratio I_{1340}/I_{1540} in the Raman scattering spectrum increases. This suggests that the peak near 600 nm in the absorption spectra probably reflects the distribution of isolated polyene-type linear chains in the structure (it is known that the limiting wavelength in the absorption spectra of the polyenes is 610 nm[35]), while the Gaussian-like band at 800±40 nm reflects the distribution of combined π-bond elements in the structure *a*-C:H. They can include polyene chains of various lengths, as well as polycyclic groups with a different number of aromatic rings. The many kinds of combinations of these π-bond structural elements with a single system for coupling of the multiple bonds, along with isolated polycyclic groups and polyene chains, are the most likely chromophores responsible for visible absorption in *a*-C:H films.

Taking this circumstance into account, we may assume that the absorption spectra of *a*- C:H films are formed by the superposition of absorption spectra corresponding to electronic $\pi-\pi^*$ transitions in isolated π-bond elements of the structure and they are quasicontinuous. The composition of the π-bond elements, their spatial distribution in the film structures, and the interaction probability of their π-electron systems determine the position of the peak, the intensity of the Gaussian-like bands which stand out in the spectrum, and the structure of the edge of the absorption band.

3.4. Analysis of the absorption spectra and the effect of the *a*-C:H film production conditions on them

The above discussion indicates that π-bond elements of the polyene chain type predominate in the structure of the *a*-C:H modification, whose spectrum includes the narrow band with a peak at 600 nm (Fig. 1a) and has a peak intensity ratio of $I_{600}/I_{800}=2.7$ (sample *a* in Table I). This kind of film was obtained from pure acetylene with a minimal voltage of $U=600$ V and a relatively high pressure (0.1 Pa). It is distinct in having the widest optical gap ($E_T=2.09$ eV) and highest resistivity (on the order of $10^{13}\ \Omega\cdot$cm).

When the discharge voltage was increased by a factor of 2 ($U_0=1200$ V), the spectrum of the resulting modification of *a*-C:H contained several isolated peaks (Fig. 1b). The maximum is at 750 nm and the ratio $I_{600}/I_{800}=0.33$. We conclude that the amount of polyene chains in the structure has decreased and the amount of more complex π-bond elements, including polycycles, has increased. When the voltage is varied from 600 to 1200 V, the peak at $\sim$800 nm can be shifted by $\pm$40 nm. This can be explained by the scatter of the polycyclic groups in the *a*-C:H structure with respect to the number of aromatic groups. Raising the discharge voltage also changes the Tauc parameters of the *a*-C:H films. E_T fell to 1.65 eV, while B increased; this indicates a rise in the density of states at the edge of the absorption band (sample *b* in Table I). This process was accompanied by a drop in the resistivity to $10^{10}\ \Omega\cdot$cm.

Dilution of the acetylene (C_2H_2) with argon (Ar) leads to a significant change in the spectra of the *a*-C:H films (Figs. 1c and 1d). The absorption at the peak of the spectrum exceeded 6×10^4 cm^{-1} (Fig. 1c) for films produced with a dc voltage $U=900$ V and 50% C_2H_2 and fell to $\sim3\times10^4$ cm^{-1} upon dilution to 30% C_2H_2 (Fig. 1d). At the same time, the peak in the spectrum of Fig. 1d was shifted to 600 nm, which led to a reduction in the integrated visible absorption. The low intensity of the absorption band and the large ratio $I_{600}/I_{800}=4.5$ (sample *d* of Table I) indicate that short polyene chains predominate in the structure of this film. E_T is smaller and B is greater by roughly a factor of 2 in sample *d* than in sample *a* of Table I. The observed differences in the Tauc parameters suggest that the distributions of the polyene chains in the sp^3-bound matrix are different. The drop in the resistivity of sample *d* to $10^7\ \Omega\cdot$cm is caused by the lowering of the tunnel barrier. The technological reason for this decrease is a reduction in the rate of *a*-C:H film deposition to $\sim$1 Å/s because of the lower C_2H_2 content.

The spectrum in Fig. 1c consists of a wide band which can be resolved arbitrarily into three Gaussian-type peaks in

the range 400–1200 nm. Besides bands at 600 and ~750 nm, which have an intensity ratio of $I_{600}/I_{800}=0.4$, a band can be distinguished at 920 nm. Most likely it corresponds to a distribution of large π-bound structures within the structure which are made up of several aromatic polycycles. The existence of a wide band spectrum for the *a*-C:H films is evidence of a substantial spread in the sizes of π-bound elements in the *a*-C:H structure. This sort of spectrum is typical of absorbing ''black'' *a*-C:H films.

3.5. Relationship of the Tauc parameters to the absorption spectra of *a*-C:H films

It has been shown[36,37] that there is no difference in the nature of the states below and above the edge of the optical absorption edge, and that the density of the π- and π^*-states close to the Fermi level can be described in terms of Gaussian-like π- and π^*-bands separated by an energy of 2 eV. Here the location and shape of the Gaussian curve correlate with the magnitude of E_T.

The width of the Tauc gap in the *a*-C:H films studied here varies from ~2 to ~1 eV. The constant B increases from 2.3×10^4 to 9.2×10^4 $\text{eV}^{-1}\cdot\text{cm}^{-1}$ (Table I), which indicates a rise in the density of states at the absorption edge of *a*-C:H with decreasing E_T. The nature of the $\pi-\pi^*$ transitions, which determine the optical gap width, is not clear from the plot of $(\alpha E)^{1/2}$ as a function of E. A comparison of the magnitudes of $E_{\max}$, which corresponds to the energy of the most probable $\pi-\pi^*$ transition, and E_T showed that the *a*-C:H films with several peaks in their spectra have $E_{\max}\simeq E_T$ (Table I, *a* and *b*), while the *a*-C:H films with a broad absorption spectrum (Figs. 1c and 1d) have $E_{\max}>E_T$ (samples *c* and *d* of Table I).

This implies that the optical gap in the *a*-C:H modification with $E_{\max}\simeq E_T$ is determined by the energy of the most probable electronic $\pi-\pi^*$ transition. It should be noted that when a photon with energy $E_{\max}$ is absorbed, there can be a transition of a valence π-electron localized on either isolated linear chains (Fig. 1a) or on complicated π-bound structural elements that include polycyles (Fig. 1b) to a corresponding free π^*-level in the conduction band. The spectra of these films contain weak discrete absorption bands which lie below the energy $E_{\max}$ with peaks at ~1, ~0.7, and ~0.6 eV (Figs. 1a and 1b). They correspond to localized states within a pseudogap whose distribution can also be described by a Gaussian curve.

Our data are a generalization of the schematic plots of the density of states (N) as a function of energy (E) shown in Fig. 3. The structure of the optical gap of an *a*-C:H modification with $E_T\geqslant1.5$ eV and a resistivity exceeding 10^{10} $\Omega\cdot\text{cm}$ can be illustrated by scheme *a* (Fig. 3). This modification of *a*-C:H is distinguished by a larger amount of bound hydrogen, as confirmed by IR spectroscopic studies of *a*-C:H films.[37] These films were highly durable mechanically and were identified as diamond-like. The atomic structure of the latter can be described as a stressed-bond rigid lattice, in which mixed bonds predominate with local π-electronic systems of π-bound atoms imbedded in it.[22] The presence of CH-groups in the sp^3-state in an *a*-C:H structure reduces the extent of the π-bond atoms[22], favors localization of their π-electrons, and raises the tunnel barrier between them.[18]

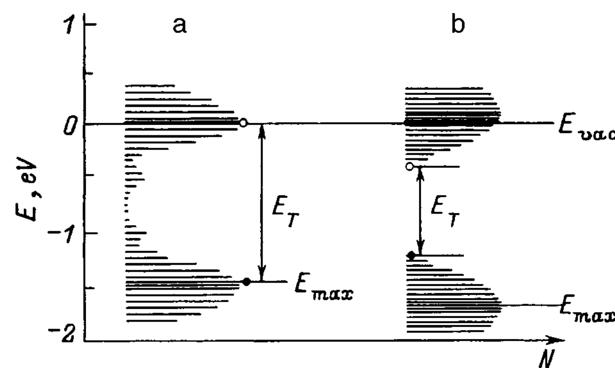

FIG. 3. Schematic diagrams of the electronic structure of the optical absorption edge and optical gap of transparent insulating (a) and ''black'' conducting (b) *a*-C:H films.

Scheme *b* of Fig. 3 describes the structure of the optical gap for *a*-C:H films with $E_{\max}>E_T$ (samples *c* and *d* in Table I). The discrete energy levels lying at the optical absorption edge below the level corresponding to the energy $E_{\max}$ form a dense quasicontinuous electron spectrum which can be described by a gaussian curve. There are essentially no states within the pseudogap for $E_T\leqslant1.0\pm0.1$ eV. The films are transparent in the IR. In this case E_T corresponds to the minimum transition energy of a valence π-electron to the corresponding empty π^*-level in the conduction band. This kind of electronic structure is typical of *a*-C:H films which absorb in the visible and have a resistivity of less than 10^9 $\Omega\cdot\text{cm}$. Raising the conductivity ensures a low content of sp^3-bound states in the films. In the proposed schemes of Fig. 3, the edge of the conduction band lies near the vacuum level E_{vac} (scheme *a*) or below it (scheme *b*), consistent with current ideas regarding the electronic structure of *a*- C:H.[20]

CONCLUSIONS

In this paper we have presented the results of an analysis of the spectral variation in the absorption of *a*-C:H films in the range 400–2400 nm and the effect on this variation due to the production conditions in a dc glow discharge plasma. A comparison of the variations in the ratio I_{600}/I_{800} of the integrated intensities of Gaussian-like bands resolved in the absorption spectra and the ratio of the fundamental bands observed in Raman scattering spectra has been used to explain the nature of absorption in the visible. Absorption in the range 400–600 nm is caused by $\pi-\pi^*$ transitions in polyene chains, while the absorption in the range 600–800 nm it is related to similar transitions in more complex π-bond combinations, including polycyclic aromatic groups.

Based on the relationship between their Tauc parameters and absorption spectra, the *a*-C:H film samples studied here could be divided arbitrarily into two groups. One group includes films with $E_{\max}\simeq E_T$, and the other, those with $E_{\max}>E_T$. They differ in the structure of their optical absorption edge, gap width, and conductivity. The *a*-C:H films with discrete narrow-band absorption spectra in the visible, for

which $E_{max} \simeq E_T \geqslant 1.5$ eV have insulating properties. Their optical gap is determined by the energy of the most probable electronic $\pi-\pi^*$ transition. Within the gap there are localized states which can serve as trapping centers for current carriers and this causes the lower conductivity in these films. The *a*-C:H films with wide-band absorption spectra in the visible, for which $E_{max} > E_T \leqslant 1$ eV are conductors. The width of the optical gap in this case is determined by the minimum energy of an electronic $\pi-\pi^*$ transition, and there are essentially no local levels within the gap. The proposed schemes for the absorption edge and optical gap of the *a*-C:H films are consistent with existing ideas regarding the electronic structure of amorphous carbon and provide a satisfactory explanation of the experimental data.

This paper is of practical importance for solving a specific problem: optimizing the properties of *a*-C:H light-blocking layers in light-controlled liquid-crystal modulators. Here the possibility of obtaining *a*-C:H films with different levels of optical absorption in the visible, ranging from transparent to opaque, has been demonstrated experimentally and a correlation has been established between the optical gap and conductivity of the films. These results will be useful in other applications employing *a*-C:H films in semiconductor devices.

I wish to thank M. V. Remizova for the spectral measurements, and J. Robertson and S. Matsunuma for kindly providing preprints of their latest papers.

*E-mail: konshina@soi.spb.su

[1] J. Robertson, Thin Solid Films **296**, 61 (1997).
[2] B. S. Satyanarayana, A. Hat, and W. I. Milne, J. Robertson, Appl. Phys. Lett. **71** (10), 1430 (1997).
[3] S. Egret, J. Robertson, W. I. Milne, and F. J. Clough, D & RM **6**, 879 (1997).
[4] B. Singh, S. McClelland, F. Tams III, B. Halon, O. Mesker, and D. Furst, Appl. Phys. Lett. **57**, 2288 (1990).
[5] E. A. Konshina and A. P. Onokhov, Zh. Tekh. Fiz. **69** (3) (1999) [*sic*].
[6] I. Wanatabe, S. Hasegawa, and Y. Kurata, Jpn. J. Appl. Phys. **22**, 856 (1982).
[7] D. I. Jones and A. D. Stewart, Philos. Mag. B **246**, 423 (1982).
[8] E. Pascual, C. Serra, J. Esteve, and E. Bertran, Surf. Coat. Technol. **247**, 263 (1991).
[9] Fangoing Zhang, Guanch Chen, Yafei Zhang, and Gong Yu, Phys. Status Solidi A **109**, K39 (1988).
[10] A. Bubenzer, B. Dischler, G. Branat, and P. Koidl, J. Appl. Phys. **54**, 4590 (1983).
[11] K. Yamamoto, Y. Ichikawa, T. Nakayama, and Y. Tawada, Jpn. J. Appl. Phys. **27**, 1415 (1988).
[12] C. Serra, E. Pascual, F. Maass, and J. Esteve, Surf. Coat. Technol. **247**, 87 (1991).
[13] K. Rohwer, P. Hammer, J.-U. Thiele, W. Gissler, P. Blaudeck, T. Frauenheim, and D. Meissner, J. Non-Cryst. Solids **137–138**, 843 (1991).
[14] E. A. Konshina, Fiz. Tverd. Tela **37**, 1120 (1995) [Phys. Solid State **37**, 610 (1995)].
[15] A. V. Balakov and E. A. Konshina, Zh. Tekh. Fiz. **52**, 808 (1982) [Sov. Phys. Tech. Phys. **27**, 520 (1982)].
[16] J. Tauc, R. Grigorovici, and A. Vancu, Phys. Status Solidi **15**, 627 (1966).
[17] J. Robertson, Adv. Phys. **35**, 317 (1986).
[18] J. Robertson and E. P. O'Reilly, Phys. Rev. B **35**, 2946 (1987).
[19] J. Robertson, Surf. Coat. Technol. **50**, 185 (1992).
[20] J. Robertson, D & RM **6**, 212 (1997).
[21] Th. Frainheim, P. Blaudeck, U. Stephan, and G. Jungnickel, Phys. Rev. B **48**, 4823 (1993).
[22] G. Jungnickel, Th. Frainheim, D. Porezag, P. Blaudeck, U. Stephan, and R. J. Newport, Phys. Rev. B **50**, 6709 (1994).
[23] R. O. Dillon, J. A. Woollam, and B. Katkanant, Phys. Rev. B **29**, 3482 (1984).
[24] M. Ramsteiner and J. Wagne, Appl. Phys. Lett. **51**, 1355 (1987).
[25] M. Yoshikawa, G. Katagiri, H. Ishida, A. Ishitani, and T. Akamatsu, Appl. Phys. Lett. **52**, 1639 (1988).
[26] M. A. Tamor, J. A. Haire, C. H. Wu, and K. C. Hass, Appl. Phys. Lett. **54**, 123 (1989).
[27] A. V. Baranov and E. A. Konshina, Opt. Spektrosk. **65**, 856 (1988).
[28] E. A. Konshina and A. V. Baranov, Poverkhnost', No. 4, p. 53 (1989).
[29] J. K. Walters, P. Honeybon, D. W. Huxley, and R. J. Newport, Phys. Rev. B **50**, 831 (1994).
[30] M. Jager, J. Gottward, H. W. Spiess, and R. J. Newport, Phys. Rev. B **50**, 848 (1994).
[31] J. R. Honeybone, R. J. Newport, J. K. Walters, W. S. Howells, and J. Tomkinson, Phys. Rev. B **50**, 839 (1994).
[32] Satoshi Matsunuma, Thin Solid Films **306**, 17 (1997).
[33] S. Xu, M. Hundhausen, J. Ristein, B. Xan, and L. Le, J. Non-Cryst. Solids **164–166**, 1127 (1993).
[34] E. A. Konshina, A. V. Baranov, and V. B. Yakovlev, Zh. Prikl. Spektrosk. **48**, 957 (1988).
[35] O. V. Sverdlova, in *Electronic Spectra in Organic Chemistry* [in Russian], Khimiya, Moscow (1985), p. 121.
[36] D. Dasgupta, F. Demichelis, C. F. Pirri, and A. Tagliaferro, Phys. Rev. B **43**, 2131 (1991).
[37] D. Dasgupta, C. De Martino, F. Demichelis, and A. Tagliaferro, J. Non-Cryst. Solids **164–166**, 1147 (1993).

Translated by D. H. McNeill

Conductivity relaxation in coated porous silicon after annealing

S. P. Zimin* and A. N. Bragin

Yaroslavl' (P. G. Demidov) State University, 150000 Yaroslavl', Russia
(Submitted July 21, 1998; accepted for publication October 1, 1998)
Fiz. Tekh. Poluprovodn. **33**, 476–480 (April 1999)

A study has been carried out of the effect of a brief anneal at 450–550 °C on the conductivity of porous silicon coated with a metallic film. Porous silicon, formed on *p*- and *n*-type substrates, had porosities of 16–40% and 5–10%, respectively. It has been shown that for anneals at 500 and 550 °C porous silicon on *p*-type Si is converted to the highly conducting state. The conductivity relaxation in coated porous silicon layers on *p*-Si after annealing is described. The results are analyzed from the point of view of a model of passivation of the impurity atoms by hydrogen. It is shown that after annealing an aluminum–⟨porous silicon⟩ junction possesses a rectifying property. The potential barrier parameters for Al–⟨porous silicon⟩ junctions on *p*- and *n*-type substrates are determined. © *1999 American Institute of Physics.* [S1063-7826(99)01904-3]

An important task in the fabrication of circuit elements of micro-, nano-, and optoelectronics based on porous silicon (PS) is that of forming porous layers with prescribed structural and electrical characteristics. While the technology of producing porous silicon with the necessary porosity and the required void morphology is well developed, many questions regarding the controlled modification of the electrical parameters of porous silicon are far from being resolved. At present, there are a number of hypotheses which consider the physical phenomena in a porous material that are responsible for the magnitude and nature of the conductivity in porous silicon (Refs. 1 and 2). Zimin and Komarov *et al.*[3] proposed another model, based on passivation of the impurity atoms by hydrogen. According to this model, during electrochemical anodic etching hydrogen is capable of penetrating from the electrolyte through the walls of the voids into the crystalline matrix of the porous silicon, which leads to electrical passivation of the impurity atoms and the creation of depleted regions around each void. In the presence of a developed system of voids, the depleted regions can propagate over the entire volume of the single-crystal matrix of the porous silicon. Zimin and Komarov[3] showed experimentally on uncoated layers of porous silicon prepared on *p*-Si substrates that a brief anneal in an inert medium at temperatures of 500–550 °C for 5–7 min leads to a radical decrease (by 4–5 orders of magnitude) in the resistivity of the porous layer, which is explained by destruction of complexes containing hydrogen and boron atoms. In the present work we have continued the study of the effect of a brief anneal on the electrical parameters of porous silicon. The objects of our study were porous-silicon layers with a metallic film deposited on their surface. Below we call them coated porous-silicon layers.

Porous layers were prepared by electrochemical anodic etching in electrolytes based on hydrofluoric acid under the same conditions as those in which porous silicon was prepared in Ref. 3. We investigated two groups of samples: in the first group, the porous silicon was deposited on KDB-0.03 substrates with orientation (111), and in the second group they were deposited on KEF-4.5 substrates with orientation (100). The porous silicon obtained on p^+-substrates had a high porosity $P=16-40\%$ and a developed network of finer voids. For the porous layer formed on *n*-Si, the porosity was 5–10% and the voids had a cylindrical shape with the direction of the axes of the cylinders corresponding to the direction of the electric field during anodic treatment. No efforts to separate the amorphous film from the porous material were attempted. An aluminum film of thickness 0.5–0.8 μm was deposited on the porous-silicon surface and on the back side of the silicon wafer by vacuum sputtering. This film was brazed in at 300 °C for 10 min. The aluminum–⟨single-crystal silicon (SCS)⟩ contacts were ohmic. Measurements were carried out on the metal–⟨porous silicon⟩–silicon–metal (Me–PS–SCS–Me) structure with dimensions 5×5 mm. The current–voltage characteristics (CVC's) of the structures were measured at 300 K ten hours after each heat treatment with a voltage step of 10–100 mV in the interval of bias voltages ±3 V in darkness.

Figure 1 shows a plot of typical current–voltage characteristics of Me–PS–SCS–Me structures based on p^+-Si in the initial state and after a brief anneal in an inert medium for 6–7 min at 450, 500, and 550 °C. Positive bias corresponded to application of a positive voltage to the silicon substrate. As can be seen from the curves shown in Fig. 1, at room temperature in the initial state the CVC (curve *1*) is characterized by weak rectification and has the form typical for such structures on *p*-type silicon substrates with an amorphous film on a porous-silicon surface.[4] The samples possess a relatively high resistance, and the currents on the forward and reverse branches do not exceed 15–600 μA for any of the investigated structures at a voltage of 3 V. Annealing at 450 °C led to an increase of the forward current and a decrease of the reverse current in the structure. The CVC of the structure acquired a pronounced diode character (curve *2*), and the rectification at a voltage of 1 V was at 10–60. Unusual behavior of the CVC was observed after annealing at

 © 1999 American Institute of Physics

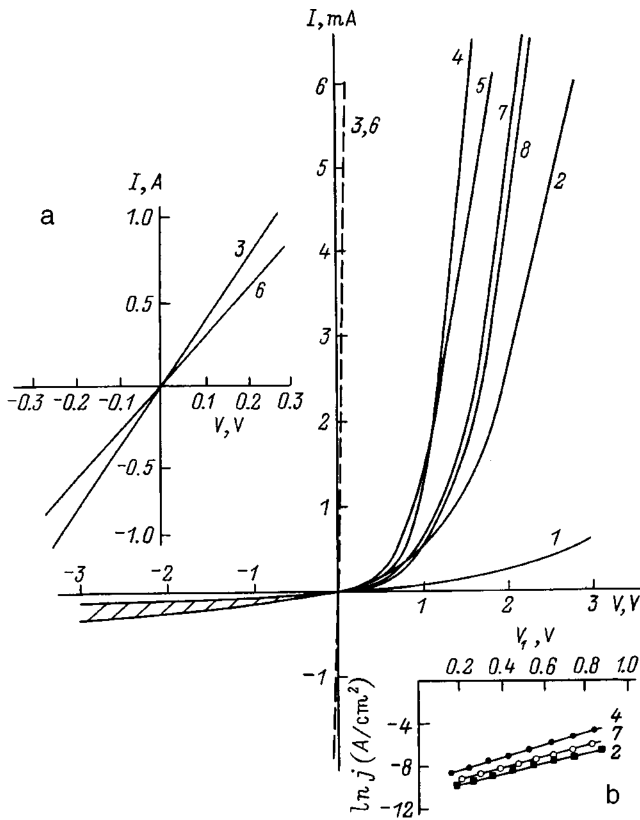

FIG. 1. Current–voltage characteristics of Al–⟨porous Si⟩–⟨single-crystal Si⟩–Al structures based on p-Si for 20% porosity for: *1* — the original sample, *2, 3 6* — after annealing, *4, 5, 7, 8* — after annealing and extended storage. Annealing temperature, °C: *2* — 450, *3–5* — 500, *6–8* — 550; storage time in days: *4, 7* — 10, *5, 8* — 20. The reverse branches of the CVC's for diode conductivity are subtended by the hatched region. Inset a: current–voltage characteristics of samples *3* and *6* in the region of small bias voltages; inset b: curves of the dependence $\ln j = f(V_1)$ for samples *2, 4*, and *7*.

500 and 550 °C (curves *3* and *6*). After such heat treatment, the Me–PS–SCS–Me structures transitioned into a low-resistance state with precisely linear symmetric CVC's (see inset a). These results are found to be in good agreement with the data[3] and are connected with the increase in the conductivity of the porous-silicon layer by several orders of magnitude during the anneals at 500 and 550 °C.

However, it is unexpected in comparison with the data on uncoated porous-silicon layers that the high-temperature anneal is followed by relaxation of the conductivity of the porous layer. It can be seen from Fig. 1 (curves *4, 7* and *5, 8*) that for several days after the anneal, dynamic changes in the CVC's are observed and the structure tends to return to its high-resistance state with recovery of the diode character of the CVC's. This indicates that with the passage of time the carrier concentration in the crystalline matrix decreases again and, as a result, barrier effects appear at the Me–Ps and/or PS-SCS boundaries. The relaxation was completely absent in the uncoated PS layers. Studies of structures with porous layers without a metallic film on their surface have shown that the low-resistance state of porous silicon is preserved even after one hour of storage under normal conditions. Therefore, our analysis of the reasons for the appearance of the relaxation effect in coated layers of porous silicon took into account those properties possessed by structures with a metallic film on a porous surface. If we stay with the model proposed in Ref. 3, which assumes passivation of the impurity atoms by hydrogen, then the observed phenomena can be explained as follows. It is known[5,6] that an intense discharge of hydrogen from porous silicon is observed during high-temperature anneals. The maximum intensity of this process is observed at certain temperatures which are included in the interval of annealing temperatures investigated here. Under these conditions, not only desorption of hydrogen from the void walls and the surface layer but also an outflow of hydrogen from the crystalline host can occur. Therefore, in the case of uncoated layers of porous material during anneals at 500−550 °C hydrogen not only breaks its bond with the impurity atom, but also appears capable of escaping the bounds of the material. In this case there is either no repeated passivation of the impurity atoms or it takes place to a lesser extent. In coated layers of porous silicon, escape of hydrogen from the porous material is hindered, the hydrogen remains within the bulk of the structure, and with the passage of time, because of the diffusion processes, again neutralizes the electrically active impurity atom, leading to the relaxation of the conductivity.

The measured CVC's were analyzed from the point of view of current-flow processes in the examined structures after annealing. It is known[7] that porous silicon deposited on p-Si under the given fabrication conditions manifests efficient n-type conductivity. Therefore, the initial structure can be represented as Me–PS(n)–SCS(p)–Me, which is usually well analyzed within the framework of the two-barrier model.[4] Determination of the type of conductivity after annealing at temperatures above 450 °C showed that porous silicon changes its conductivity type from n to p. This change is attributable to an increase in the concentration of holes due to a transition of the boron atoms from the passivated state to the electrically active state. In this case the structure has the form Me–PS(p)–SCS(p^+)–Me. For low porosity in the examined samples no change in the width of the band gap in the porous silicon in comparison with silicon occurs. Therefore, the PS–SCS boundary can be considered as a nonrectifying $p-p^+$ junction, and thus the experimental CVC's, on the basis of an analysis of the proposed polarity, are configured by the operation of one barrier at the metal–⟨porous silicon⟩ boundary. In this case, to calculate the electrical parameters of the structure, it is possible to use a classical equivalent circuit consisting of a Schottky barrier and a series resistance determined largely by the porous-silicon layer. Table I lists values of the resistance of the porous-silicon layer after various annealing regimes for the structures whose CVC's are plotted in Fig. 1. The data listed in the table make it possible to track the dynamics of the variation of the conductivity of porous silicon after an anneal and indicate that such changes are most pronounced during the first ten days after the anneal. Inset b in Fig. 1 plots the dependence of the current density j on the voltage on the Schottky barrier (V_1) in the coordinates $\ln j = f(V_1)$. The values V_1 were determined from the experimental CVC's, with allowance for the voltage drop in the series resistance of the

TABLE I. Parameters of Me–PS–SCS–Me structure after thermal anneal.

Substrate	Porosity by weight, P, %	Anneal conditions (T, °C) and storage time	Resistance of porous Si R, Ω	Barrier height U, eV
p^+-Si	20	Initial state	4580	···
		450	223	0.66
		500	0.25	···
		500, 10 da.	100	0.65
		500, 20 da.	127	0.65
		550	0.34	···
		550, 10 da.	120	0.64
		550, 20 da.	123	0.66
n-Si	8	Initial state	910	···
		450	30.7	0.64
		500	17.6	0.67
		500, 20 da.	16.7	0.64
		550	16.8	0.62
		550, 10 da.	19.9	0.63
		550, 20 da.	22.1	0.62

Note: In the initial state the amorphous film on the porous Si surface contributes the resistance. After annealing at temperatures above 450 °C the role of the film is not large (Ref. 3).

porous-silicon layer. In the coordinates $\ln j = f(V_1)$ the current–voltage characteristics are straightened out, which, on the one hand, confirms the operation of only one barrier (Me–PS) in the structure after an anneal and, on the other, makes it possible to determine the height of the barrier at the Al–PS boundary. The height of the Schottky barrier was calculated by the technique given in Ref. 8 for the Richardson constant $A^{**} = 30\,\mathrm{A/cm^2K^2}$ for p-type Si. The results of these calculations for the sample characterized in Fig. 1 are given in the table. The height of the potential barrier at the aluminum–⟨porous silicon⟩ contact for all the investigated structures on p^+-Si was $0.64-0.76$ eV. The ideality coefficient of the CVC's for the investigated Schottky barriers was equal to $1.3-9.0$, which is probably due to the presence of an intermediate layer at the metal–⟨porous silicon⟩ boundary.[9]

The variation of the current–voltage characteristics of Me–PS(n)–SCS(n)–Me structures prepared on n-type silicon after annealing at 450, 500, and 550 °C is shown in Fig. 2. The forward bias in this case corresponds to applying a positive voltage to the metal on the porous-silicon side. For the initial structures the CVC was nearly linear. This behavior is explained by the fact that due to the additional voltage drop on the amorphous surface layer the current flow through the Al–PS contact is small. As a result, the Al–PS junction does not possess rectifying properties since the voltage on the junction is near the zero point.[3] Annealing altered the properties of the surface layer, and as a result of annealing, the CVC's acquired a typical diode character. The transition to a high-resistance state with linear CVC's upon annealing at 500 and 550 °C was absent for the n-Si–based structures. To analyze the current–voltage characteristics it again proved to be possible to apply the model with a Schottky diode and series resistance. The resistance of the porous-silicon layer and the heights of the Al–PS potential barriers for the structures, whose CVC's are plotted in Fig. 2, are

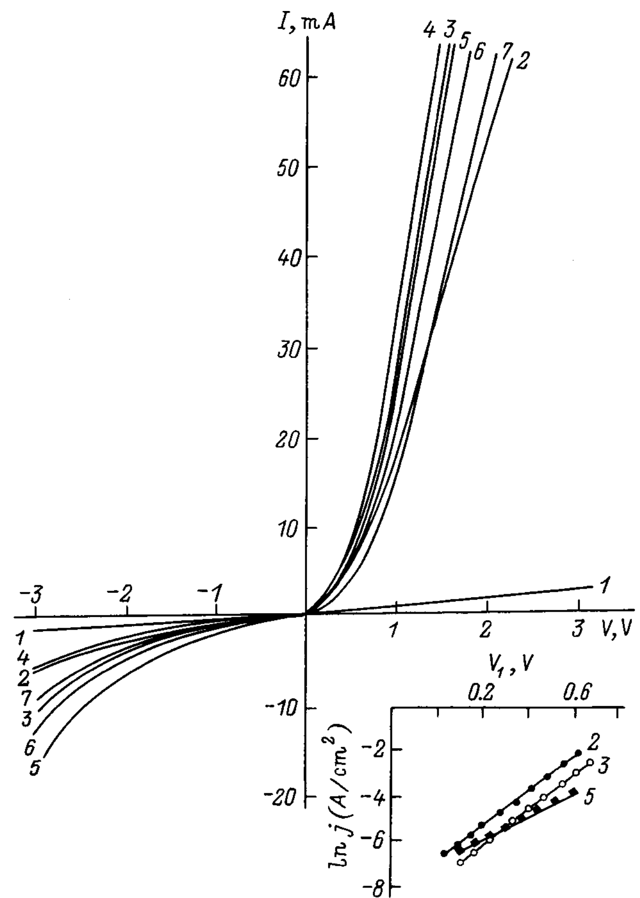

FIG. 2. Current–voltage characteristics of Al–⟨porous Si⟩–⟨single-crystal Si⟩–Al structures based on nSi for 8% porosity for: *1* — the original sample, *2, 3, 5* — after annealing, *4, 6, 7* — after annealing and extended storage. Annealing temperature, °C: *2* — 450, *3, 4* — 500, *5–7* — 550; storage time in days: *4, 7* — 20, *6* — 10. Inset shows typical curves of the dependence $\ln j = f(V_1)$ for Al–PS junctions.

given in the table. The height of the potential barrier at the aluminum–⟨porous silicon⟩ boundary on the n-type silicon substrates calculated for the Richardson constant $A^{**} = 120\,\mathrm{A/cm^{-2}K^2}$ was equal to $0.62-0.67$ eV. The ideality coefficient of the junctions was in the range 2.3–4.5. The conductivity of the porous-silicon layer varied hardly at all during annealing at temperatures above 500 °C with subsequent storage. This result agrees with the data of Ref. 3 and is linked, first of all, with the conductivity of the single-crystal porous-silicon host without noticeable participation of the depleted regions around each void and, secondly, with weak passivation of the donor impurity atoms by hydrogen.

In summary, the results of our study indicate that in porous-silicon layers on p^+-Si with porosity $16-40\%$ after a brief anneal at $500-550$ °C the porous silicon undergoes a transition to a low-resistance state. We observed a relaxation of conductivity in porous silicon coated with a metallic film. This relaxation may be linked with repeated passivation of impurity atoms by hydrogen in a closed system. We have shown that the results presented for porous silicon on p-Si cannot be transferred in full to the entire porous silicon. This, in particular, was demonstrated for porous silicon prepared on n-Si with low porosity. The role of hydrogen in the for-

mation of the electrical properties of the porous silicon depends on the porosity of the material, the morphology of the voids, and the type of dopant impurity in the original silicon substrate. The transition to the low-resistance state upon annealing is probably absent in porous silicon with high porosity, where the conductivity is determined not by carrier transport along the crystalline matrix, but by carrier transport from one isolated crystallite to another across a potential barrier. A change in the charge-carrier concentration in the crystallites, as before, can take place upon annealing; however, this no longer has a substantial effect on the character of the transport.

In conclusion, it should be noted that differences in relaxation processes in coated and uncoated structures after the porous silicon transitions to the low-resistance state can be used to control the electrical parameters of the porous layer. This makes it possible to fabricate multilayer structures for use in electronics, based on porous silicon in which the porous material has conducting, semiconductor, and insulating properties, and to vary the properties of Me–PS and PS–SCS contacts.

This work was carried out with the financial support of the State Committee for Higher Education of the Russian Federation on fundamental studies in chemical technology.

We are grateful to M. I. Makoviĭchuk and V. A. Rekshinskiĭ (IMRAN, Yaroslavl') for annealing the samples.

*E-mail: zimin@univ.uniyar.ac.ru; Fax: (0852) 225232

[1] V. Lehmann, F. Hofmann, F. Moller, and U. Gruning, Thin Solid Films **255**, 20 (1995).
[2] A. J. Read, R. J. Needs, K. J. Nash, L. T. Canham, P. D. J. Calcott, A. Qteish, Phys. Rev. Lett. **69**, 1232 (1992).
[3] S. P. Zimin and E. P. Komarov, Pis'ma Zh. Tekh. Fiz. **24**(6), 45 (1998) [Tech. Phys. Lett. **24**, 226 (1998)].
[4] S. P. Zimin, V. S. Kuznetsov, N. V. Perch, and A. V. Prokaznikov, Pis'ma Zh. Tekh. Fiz. **20**(22), 22 (1994) [Tech. Phys. Lett. **20**, 18 (1994)].
[5] K. N. El'tsov, V. A. Karavanskiĭ, and V. V. Martynov, JETP Lett. **63**, 119 (1996).
[6] P. Martin, F. Fernández, and C. Sánchez, *Materials of the International Conference "Porous Semiconductors: Science and Technology"*, (Mallorca, Spain, 1998), p. 243.
[7] A. L. Vinke, S. P. Zimin, and V. N. Palashov, Patent RF No. 2054746, priority date 13.01.93, registered 20.02.96.
[8] S. M. Sze, *Physics of Semiconductor Devices* (Wiley Interscience, New York, 1981).
[9] E. H. Rhoderick, *Metal-Semiconductor Contacts* (Oxford, Clarendon Press, 1978).

Translated by Paul F. Schippnick

THE PHYSICS OF SEMICONDUCTOR DEVICES

Photomemory in CdTe thin-film solar cells

É. N. Voronkov, A. E. Sharonov, and V. V. Kolobaev*

Moscow Energy Institute, 111250 Moscow, Russia
(Submitted July 6, 1998; accepted for publication July 28, 1998)
Fiz. Tekh. Poluprovodn. **33**, 481–483 (April 1999)

It is shown that a change in the chemisorption equilibrium on the crystallite boundaries in thin-film photoconverters based on polycrystalline CdTe occurs when they are subjected to radiation. This leads to the appearance of photomemory as a result of a change in the surface potential and a corresponding change in the surface recombination rate. This effect may be the reason for the instability of the parameters of polycrystalline solar cells and can lead to a degradation and to an enhancement of the photoconversion efficiency. An experimental technique, which allows one to determine the dominant type of surface state at the boundaries of the crystallites, is considered. © *1999 American Institute of Physics.* [S1063-7826(99)02004-9]

Thin-film solar cells based on CdTe have a promising future for wide application. We have therefore set out to investigate the stability of their parameters in time and to consider possible reasons for the appearance of instability. As our objects of study we chose solar cells with the structure glass–SiO_2–CdS–CdTe–metal and glass–SiO_2–CdTe–metal. Since the effects we observed are due mainly to processes in the high-resistance CdTe active layer, in what follows we will not distinguish these two types of structures.

As a parameter sensitive to changes in the active layer, we chose the reverse dark current I_0. Information about changes in I_0 were recorded by computer using an amplified and analog-to-digital converter. Illumination with an intensity of 5 mW/cm^2 was provided by a xenon lamp through a water filter.

Figure 1 plots curves of the variation of I_0 after three different exposures, measured on one of the samples. The relaxation of the forward dark current at small biases has a similar character.

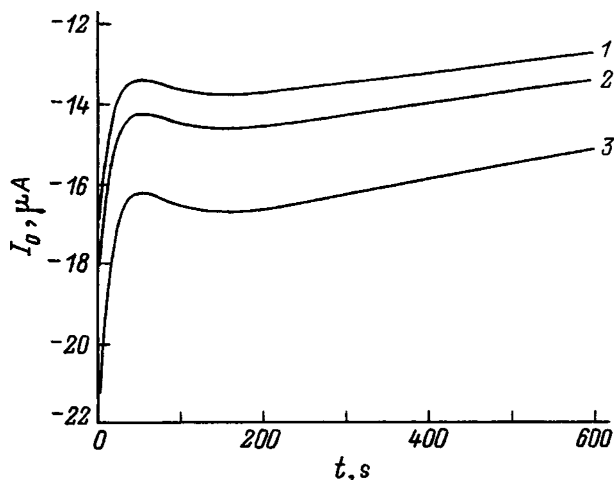

FIG. 1. Variation of the reverse dark current after preliminary exposure of the samples. Exposure time: *1* — 60 s, *2* — 120 s, *3* — 480 s.

The experimental data are described well by the dependence

$$I_0(t,t_f)=K_1(t_f)\exp(-t/\tau_1)+K_2(t_f)\exp(-t/\tau_2)-K_3(t_f)\exp(-t/\tau_3), \quad (1)$$

where t_f and t are, respectively, the exposure time and the time that has elapsed after cessation of exposure. The coefficients K_i are weak functions of the exposure F: $K_i \cong (C_i F)^n$, where $n \cong 0.2$. The solid curves in Fig. 1 plot the dependence calculated according to Eq. (1) for $\tau_1 = 20$ s, $\tau_2 = 2000$ s, and $\tau_3 = 50$ s.

To explain the observed effect, consider a simplified model of the active polycrystalline layer. We assume that the layer consists of crystallites of roughly identical shape with some average size d. The surface of the crystallites is depleted by the majority carriers in comparison with the bulk of the layer, and a potential barrier is formed on the boundaries between individual crystallites. The effective lifetime of the photo-injected charge carriers is determined by the bulk lifetime τ and the surface recombination rate on the intercrystallite boundary S:

$$\tau_{\text{eff}} = (1/\tau + S/gd)^{-1}, \quad (2)$$

where g is a coefficient characterizing the shape of the crystallite (for a sphere $g=0.75$). As a rule, the recombination rate on the intercrystallite boundary is higher than in the volume, and with accuracy adequate for practical estimates we can set

$$\tau_{\text{eff}} = gd/S. \quad (3)$$

The values of S and correspondingly τ_{eff} depend on the height of the potential barrier, i.e., on the value of the surface potential U_s at the boundary of the crystallites. Assuming that recombination takes place chiefly by way of trapping centers located in the middle of the band gap, we can write

$$S = S_0/\cosh(U_s/U_t), \quad (4)$$

where $U_t = kT/q$.

 © 1999 American Institute of Physics

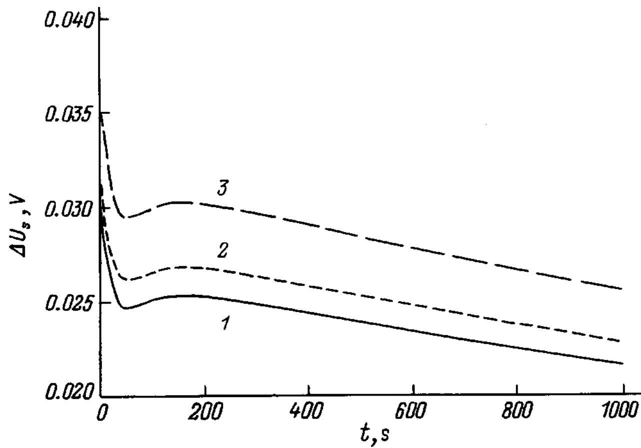

FIG. 2. Variation of the surface potential as a result of the appearance of photo-induced states at the crystallite boundaries. Exposure time: *1* — 60 s, *2* — 120 s, *3* — 480 s.

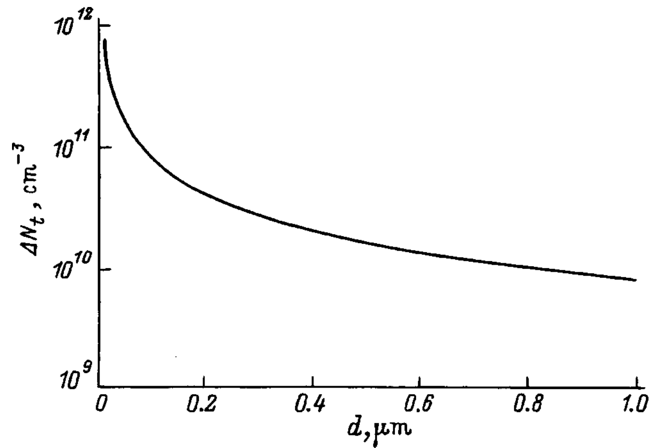

FIG. 3. Dependence of the density of photo-induced states on the size of the crystallites.

Since in the investigated solar cells the generation–recombination component dominates in I_0, we write for the relative variation of the dark current

$$I_0(t)/I_0 = S(t)/S(t_0) = \cosh[\Delta U_s(t)/U_t], \tag{5}$$

where we take as our reference point in time the instant the illumination is switched off, t_0, and I_0 is the steady-state value of the current $(t\to\infty)$. Since $U_s(t) \gg \Delta U_s(t)$

$$\Delta U_s(t) = U_t \ln[I_0(t)/I_0]. \tag{6}$$

The corresponding dependences $\Delta U_s(t)$, calculated from the experimental data, are plotted in Fig. 2. It is clear from the graphs that the change in the surface potential caused by illumination is insignificant and for crystallites of large dimensions it is possible that it would not even be noticeable.

It is of interest to estimate the change in the amount of charge in surface states and in the bulk of a crystallite. In the approximation of spherical crystallites, we obtain the following expression for the change in the density of the surface states:

$$\Delta N_t = \Delta Q/qS_c = [4\pi\varepsilon\varepsilon_0 \Delta U_s d)/(qS)] = [4\varepsilon\varepsilon_0 \Delta U_s)/(qd)], \tag{7}$$

where S_c is the total surface area of the crystallites. We can thus estimate the dependence of the density of photo-induced states on the boundaries of the crystallites (for given ΔU_s) on the size of the crystallites. The corresponding dependence is plotted in Fig. 3.

In our case, the mean diameter of the crystallites was on the order of 1 μm; therefore, the density of light-induced states at the intercrystallite boundaries was on the order of 10^{10} cm^{-2}, which is probably much smaller than the number of states created by defects at the boundary. Note that this quantity depends on the intensity of illumination and is essentially independent of its duration, which indicates that charge equilibrium is established rapidly upon illumination.

Let us consider the possible nature of the photo-induced states. They are characterized by a very short formation time and an extended relaxation time. It can be assumed, therefore, that these states are associated with atoms which are present in inactive form at the boundary and a change in their state occurs as a result of incidence of photoexcited electrons and holes on the surface. It seems most likely to us that illumination results in a change in the state of the molecules adsorbed on the surface, which is accompanied by a change in the form of the adsorption, e.g., a transition from a weak form of adsorption to a strong, chemical form of adsorption, where the reverse process is associated with overcoming a significant energy barrier,[1] which is manifested in the long relaxation times. Judging from the observed relaxation times, photo-injection in CdS films creates at least three sorts of slow centers, two of which are of acceptor type (it is assumed that the surface of the crystallites is depleted of electrons) and one is of donor type. It is most likely that these are water molecules, and that their fragments, which are in different charge states, can form both donor and acceptor centers.

CONCLUSIONS

We have shown that in thin-film photoconverters acted upon by radiation a change takes place in the chemisorption equilibrium at the boundaries of the crystallites, which leads to the appearance of photomemory as a result of a change in the surface potential and a corresponding change in the surface recombination rate.

This effect may be the reason for the instability of the parameters of polycrystalline solar cells and it can lead to a degradation and to an enhancement of the photoconversion efficiency.

We have considered an experimental technique which makes it possible to determine the type of dominant surface state at the boundaries of crystallites.

*E-mail: victor@lgtcm.ru; Fax: +7–095–2582167

[1] F. F. Vol'kenshteĭn, *Electronic Processes on Semiconductor Surfaces During Chemisorption* [in Russian], Nauka, Moscow, 1987.

Translated by Paul F. Schippnick

Polarization photosensitivity of $ZnO/CdS/Cu(In,Ga)Se_2$ solar cells

V. Yu. Rud'

St. Petersburg State Technical University, 195257 St. Petersburg, Russia

Yu. V. Rud'

A. F. Ioffe Physicotechnical Institute, Russian Academy of Sciences, 194021 St. Petersburg, Russia

H. W. Schock

Universität Stuttgart, Institut für Physikalische Elektronik, D-70569 Stuttgart, Germany

(Submitted July 20, 1998; accepted for publication July 28, 1998)
Fiz. Tekh. Poluprovodn. **33**, 484–487 (April 1999)

Results of the application of polarization spectroscopy of the photosensitivity of $ZnO/CdS/Cu(In,Ga)Se_2$ thin-film solar cells with different thicknesses of the CdS (50 and 100 nm) and ZnO (500 and 1000 nm) layers are considered. It is established that the induced photopleochroism coefficient is lowered while the quantum efficiency of photoconversion of the solar cells is raised by increasing the thickness of the front layer. The experimental conditions and spectral dependence of the induced photopleochroism are linked with the antireflection properties of the ZnO front layers. It is concluded that photosensitivity polarization spectroscopy can be used for rapid diagnostics of finished solar cells and to optimize their fabrication technology. © *1999 American Institute of Physics.* [S1063-7826(99)02104-3]

Ternary semiconductor compounds and their solid solutions with a chalcopyrite lattice are currently being studied more extensively as materials for photovoltaic systems.[1–5] The most efficient solar cells ($\sim 18\%$) are fabricated from $Cu(In,Ga)Se_2$ (CIGS) thin films.[2] For this reason, interest in the fundamental physical–technological studies of thin-film solar cells made from ternary compounds of this class has recently increased. In this paper we report the results of the application of polarization photoelectric spectroscopy to the study of solar cells containing CIGS layers in contact with CdS and ZnO wideband layers of several thicknesses.

1. As our substrates for deposition of CIGS layers we used molybdenum-coated glass plates of thickness up to 0.5 mm. CIGS films with thicknesses up to 2 μm were deposited in a system with high vacuum ($\sim 10^{-8}$ Torr) consisting of individual sources for each of the components in a combined process of evaporation onto substrates heated to temperatures of 600 °C. The composition of the films so obtained was monitored by x-ray spectroscopy (EDX) and the investigated structures contained Cu, In, Ga, and Se in the amounts of 23.58, 20.06, 6.62, and 49.74% by weight. A layer of CdS was deposited onto the CIGS surface by thermal evaporation; the front layer of ZnO was then deposited by magnetron sputtering of the target source. The thicknesses of the CdS and ZnO layers in the investigated structures are given in Table I. In addition to the ZnO/CdS/CIGS structures based on CIGS films, surface barrier structures were also created by vacuum thermal evaporation of indium.

The structures obtained by the method described above were mounted on an STF-1 Fedorov table, which made it possible to vary the angular coordinates of the front plane relative to the direction of the incident radiation with an accuracy no worse than 1°.

2. The main photoelectric parameters of the investigated structures are listed in Table I. It can be seen from them that variations in the thickness of the CdS (d_{CdS}) and ZnO (d_{ZnO}) layers do not have a strong effect on the no-load voltage U_{OC}, filling factor β, or quantum efficiency of photopleochroism η. We note that the obvious tendency of these parameters is to improve as a result of increasing the thickness of the front coating. This change can probably be attributed to an increase in the effect of clearing of the solar-cell surface. The spectral dependences η of a number of ZnO/CdS/CIGS structures, and also an In/CIGS surface-barrier structure fabricated on the basis of these CIGS films are plotted in Fig. 1. It follows from a comparison of the spectra η that the long-wavelength edge of the photosensitivity in all of these structures is identical. It obeys an exponential law and can be characterized by its slope $s=\delta(\ln\eta)/(\hbar\omega)$. It can be seen from the table that the high slope of the long-wavelength edge η for the obtained structures corresponds to direct optical transitions in the CIGS. The energy position of the slope change in the spectra η of the investigated structures, defined as the transition point from the exponential to the parabolic dependence, as follows from Fig. 1, varies in the limits 1.15–1.18 eV, which is close to the width of the band gap of the obtained composition of the CIGS solid solution. Therefore, the long-wavelength edge of η can be attributed to the edge of the direct interband transitions in the CIGS film. The observed fluctuations in the magnitude of s can then be attributed to the differences in the smearing of the edges of the free bands in the CIGS film by the electric fields of lattice defects of various origin.

 © 1999 American Institute of Physics

TABLE I. Photoelectric properties of thin-film structures based on $Cu(In,Ga)Se_2$ at $T=300$ K.

Type of structure Sample	d_{CdS}, nm	d_{ZnO}, nm	U_{OC} mV	β	η, %	s, eV^{-1}	$\delta_{1,2}$, eV	$\hbar\omega_m$, eV	P_I, %
In / CIGS MG-388	⋯	⋯	353.7	⋯	0.5	46	2.2	1.6	⋯
ZnO/CdS/CIGS MG-388-73	50	500	595.3	66	11.2	58	1.45	2.03	14
ZnO/CdS/CIGS MG-388-124	100	500	595.6	68	11.4	40	1.36	1.95	17
ZnO/CdS/CIGS MG-388-74	100	1000	619.7	79	12.2	46	1.34	1.64	11

As can be seen from Fig. 1, the quantum efficiency of photoconversion for comparable structures continues to increase in a wide range of photon energies $\hbar\omega > 1.2$ eV, which testifies to the adequacy of their degree of perfection relative to recombination of photogenerated carriers. Note that complicated oscillations are observed in the spectra η of the solar cells in the region $1.2-2.2$ eV. They are most distinctly manifested in the structures with $d_{ZnO} = 1000$ nm; however, due to their shallow depth of modulation a unique interpretation of their nature is still impossible.

It can be seen from Fig. 1 that the widest-band photosensitivity is realized on CIGS-based Schottky barriers. The full width of the spectra η at half-maximum (FWHM) $\delta_{1/2}$ in these barriers reaches 2.2 eV, whereas in the solar cells because of the influence of absorption it falls in the CdS layers (falloff at $\hbar\omega > 2.4$ eV) and in the ZnO layers (falloff at $\hbar\omega > 3.1$ eV) (see Table I).

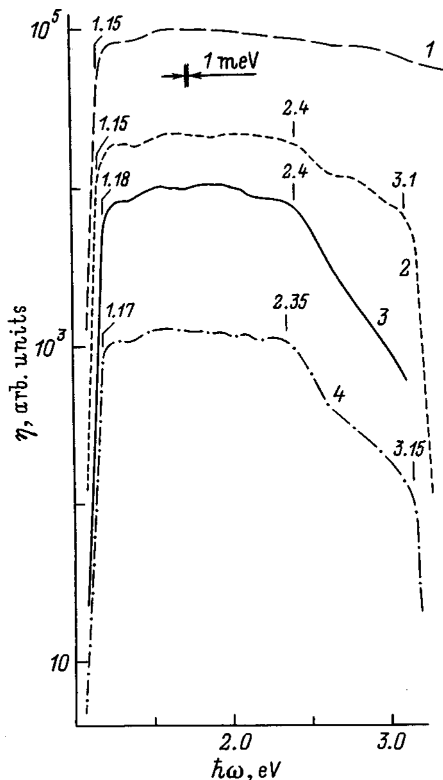

FIG. 1. Spectral dependence of the relative quantum efficiency of photoconversion of In/CIGS surface-barrier structures (*1* — sample MG-388) and a ZnO/CdS/CIGS solar cell at $T=300$ K in natural light (*2* — sample MG-388-73, *3* — MG-388-124, *4* — MG-388-74).

Note that the spectral contour η for the Schottky barriers and the solar cells has good reproducibility when scanning the surface of contiguous structures with surface area up to $7.5\,cm^2$ (diameter of the light probe 0.2 mm), and also in the fabrication of an array of 15 separate solar cells on a surface deposited in a combined production cycle of a CIGS film or solar cell. All this points to the high local homogeneity in the composition of the CIGS films, which is in line with the x-ray (EDX) data.

3. Studies of the photoelectric properties of solar cells in linearly polarized light (LPL) have made it possible to establish that polarization photosensitivity arises for oblique incidence on their front plane, as was reported in Ref. 5. For angles of incidence of the LPL $\Theta > 0°$ the short-circuit photocurrent as a function of the angle φ between the electric field vector of the light wave **E** and the plane of incidence of the radiation (PI) follows a periodic dependence—Malus's law.[6] In this case, the relation $i^P(\mathbf{E}\|\mathrm{PI}) > i^s(\mathbf{E}\perp\mathrm{PI})$ is satisfied over the entire spectral range of the photosensitivity of the solar cell. This relation reduces to the identity $i^p > i^s$ for $\Theta = 0°$, which has to do with the isotropic character of photoconductivity due to the polycrystalline components of thin-film solar cells.

Figures 2 and 3 show typical angular dependences of the short-circuit photocurrents and induced photopleochroism P_I for two solar cells. The character of the angular dependences i^p and i^s, as can be seen from Figs. 2 and 3, is identical. Indeed, for the p and s polarizations, as Θ grows, the photocurrents at first increase, pass through a maximum, and then begin to fall off. Such a nature of the angular dependence of the photocurrent i^p is attributed to an elimination of losses of the p wave upon reflection and agrees with an analysis of the passage of a light wave through the air–ZnO boundary based on the Fresnel relations.[7] However, noting that such an analysis for the s wave predicts a monotonic decay of i^s with growth of Θ, in the investigated solar cells we see that this analysis notwithstanding, the photocurrent i^s grows with increasing Θ for $\Theta > 0°$. This circumstance gives a basis, by analogy with $i^p(\Theta)$, to also link the growth of i^s with the elimination of losses of the s wave to reflection. The experimental data on $i^p(\Theta)$ and $i^s(\Theta)$ show that in solar cells with $d_{ZnO} < 1000$ nm the ratio of the maximum value of the photocurrent to the photocurrent at $\Theta = 0°$ I^S_m/I^S_0

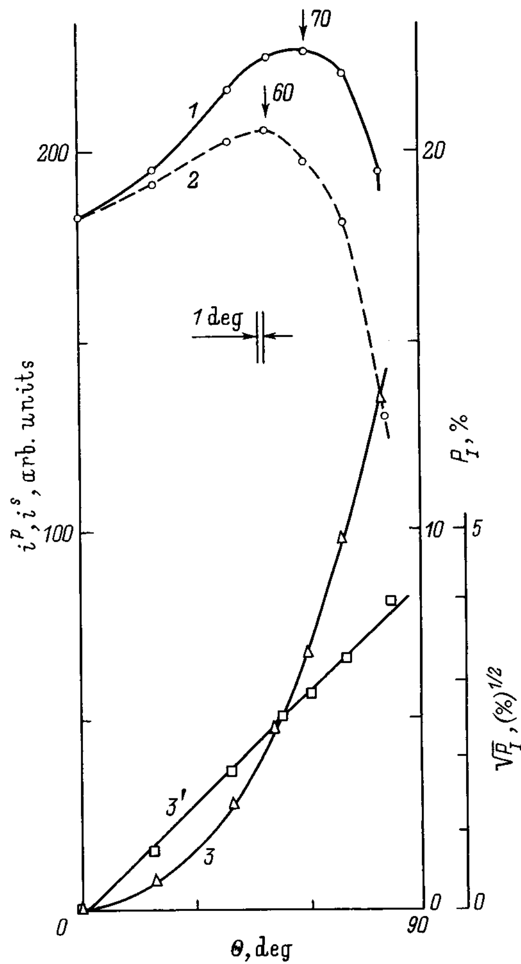

FIG. 2. Dependence of the short-circuit photocurrents (1 — i^p, 2 — i^s) and induced photopleochroism ($3, 3'$) on the angle of incidence of linearly polarized light on the ZnO plane of the ZnO/CdS/CIGS structure at $T=300$ K (sample MG-388-74, solar cell 2, $\lambda=0.50\ \mu$m.

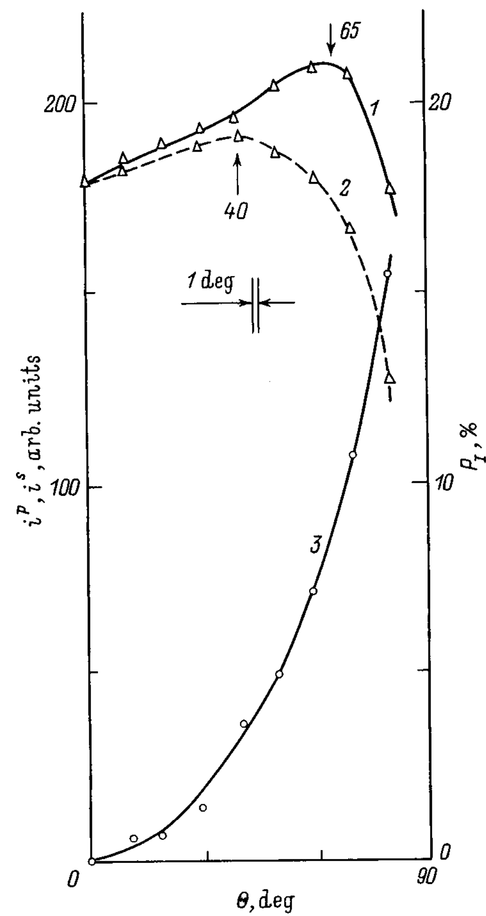

FIG. 3. Dependence of the short-circuit photocurrents (1 — i^p, 2 — i^s) and induced photopleochroism (3) on the angle of incidence of linearly polarized radiation on the ZnO plane of the ZnO/CdS/CIGS structure at $T=300$ K (sample MG-388-73, solar cell 3, $\lambda=0.60\ \mu$m.

falls in comparison with solar cells with $d_{\mathrm{ZnO}}<1000$ nm (Figs. 2 and 3, curves *2*). Therefore the ratios I_m^S/I_0^S and I_m^P/I_0^P can be taken as a measure of the clearing of the solar cell.

The induced photopleochroism in all of the solar cells, as can be seen from Figs. 2 and 3, obeys a parabolic law $P_I \sim \Theta^2$, in agreement with Ref. 8. For $\Theta=0°$, $P_I=0$ in all the solar cells, because of the masking of the natural optical anisotropy of the components of the heterostructures by the polycrystalline nature of the layers. Growth of Θ is accompanied by a monotonic increase in the photopleochroism, whose values differ for the investigated solar cells at $\Theta=75°$ and thus fill the range from 10 to 20% in the spectral region from 1 to 3 eV. If we take into account that in all the solar cells the role of the front layer is filled by the same material—ZnO, then, taking into account that P_I is directly related to the refractive index,[8] it should be expected that the photopleochroism induced by the oblique incidence of the LPL should be identical for all of the solar cells for $\Theta=\mathrm{const}$. An estimate of the refractive index from the experimental values of P_I, based on Ref. 8, gives $n=1.2-1.4$, which is lower than the known value for ZnO: $n=2$ (Ref. 9). The observed decrease in the experimental values of P_I relative to the values expected on the basis of Ref. 8, with allowance for the refractive index for ZnO, may be a consequence of interference of the incident LPL in the thin ZnO layer. The observed regularity was noted earlier for several systems.[9,10]

Figure 4 plots the spectral dependence of the induced photopleochroism of solar cells with various thicknesses of the wideband layers. We see that the sensitivity of photopleochroism to the geometrical parameters of the solar cells manifested in the angular dependences $P_I(\Theta)$ is preserved in a wide spectral range and remains lower than the theoretical value of P_I estimated from the refractive index for ZnO. The spread in the experimental values of P_I and their weak spectral dependence in the region $\hbar\omega>1.5$ eV may be due to the antireflection properties of the front layer of the solar cell. In this case the growth manifested in the P_I spectra for $\hbar\omega<1.5$ eV corresponds to departure from the clearing region. If we take the falloff of P_I as a measure of clearing, then it can be seen from Fig. 4 that the highest level of clearing is attained in the solar cell with $d_{\mathrm{ZnO}}=1000$ nm (curve *3*). The variations in P_I revealed by scanning the surface of the solar cell (Fig. 4, curves *3* and *4*) may be a reflection of local inhomogeneities of the optical parameters of the ZnO layers. It should still be emphasized that the

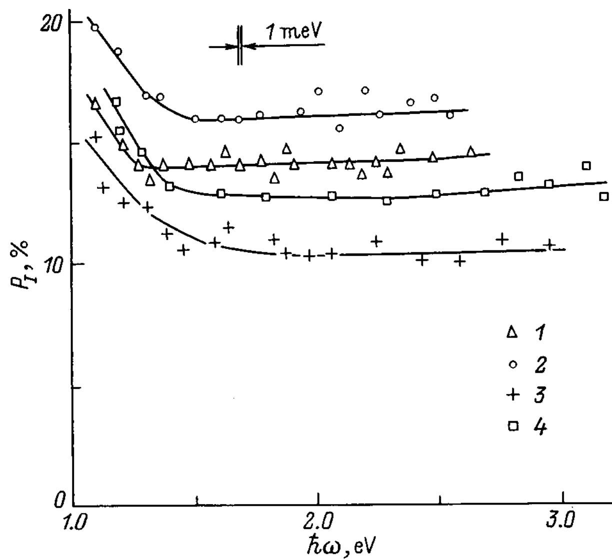

FIG. 4. Spectral dependence of the induced photopleochroism of ZnO/CdS/CIGS structures at $T=300$ K (*1* — MG-388-73, solar cell 2; *2* — MG-388-124, solar cell 1; *3* — MG-388-74, solar cell 1; *4* — MG-388-74, solar cell 3; $\Theta=75°$).

minimum in P_I and the corresponding maximum in the clearing and in the quantum efficiency of photopleochroism are reached for solar cells with $d_{\mathrm{ZnO}}=1000$ nm (see Table I). As the thickness of the front layer is reduced, the clearing effect estimated from the P_I values weakens and, accordingly, we see a decrease in η, whereas varying the thickness of the CdS layers in the investigated range does not have a substantial influence on the photoelectric parameters of solar cells of this type.

Consequently, polarization studies of the photosensitivity of CIGS-based thin-film solar cells can be used as diagnostics of finished solar cells and correspondingly for quality control of the production of photoconverters.

[1] A. M. Gabor, J. R. Tuttle, D. S. Albin, M. A. Contreras, R. Noufi, and A. M. Herman, Appl. Phys. Lett. **65**, 198 (1994).
[2] L. Stolt, J. Hedström, J. Kessler, M. Ruckh, K.-O. Velthaus, and H. W. Schock, Appl. Phys. Lett. **62**, 597 (1993).
[3] J. Hedström, H. Ohlsen, M. Bodegard, A. Kylner, L. Stolt, D. Harickos, M. Ruckh, H. W. Schock, in *Proceedings 23rd Photovoltaic Special. Conf.* (Louisville, 1993).
[4] M. Hornung, K. W. Benz, L. Margulis, D. Schmid, and H. W. Schock, J. Cryst. Growth **154**, 315 (1995).
[5] T. Val'ter, V. Yu. Rud', Yu. V. Rud', and H. W. Schock, Fiz. Tekh. Poluprovodn. **31**, 806 (1997) [Semiconductors **31**, 681 (1997)].
[6] Yu. V. Rud', Izv. Vuzov SSSR. Fizika **29**, 68 (1986).
[7] R. Azzam and M. Bashara, *Ellipsometry and Polarized Light* (North-Holland, Amsterdam, 1977).
[8] G. A. Medvedkin and Yu. V. Rud', Phys. Status Solidi A **67**, 333 (1981).
[9] V. Yu. Rud', Yu. V. Rud', T. Walter, and H. W. Schock, *Proc. STMS-11* (Salford, 1997) [Inst. Phys. Conf. Ser. **152**, 97 (1998)].
[10] V. M. Botnaryuk, A. V. Koval', V. Yu. Rud', Yu. V. Rud', A. V. Simashkevich, and D. A. Shcherban', Fiz. Tekh. Poluprovodn. **31**, 800 (1997) [Semiconductors **31**, 677 (1997)].

Translated by Paul F. Schippnick

Exciton waveguide and lasing in structures with superfine GaAs quantum wells and InAs submonolayer inclusions in an AlGaAs host

A. F. Tsatsul'nikov, B. V. Volovik, N. N. Ledentsov, M. V. Maksimov, A. Yu. Egorov, A. R. Kovsh, V. M. Ustinov, A. E. Zhukov, P. S. Kop'ev, and Zh. I. Alfërov

A. F. Ioffe Physicotechnical Institute, Russian Academy of Sciences, 194021 St. Petersburg, Russia

I. É. Kozin and M. V. Belousov

Institute of Physics, St. Petersburg State University, 198904 St. Petersburg, Russia

D. Bimberg

Institut für Festkörperphysik, Technische Universität Berlin, D-10623 Berlin, Germany

(Submitted September 8, 1998; accepted for publication September 15, 1998)
Fiz. Tekh. Poluprovodn. **33**, 488–491 (April 1999)

The optical properties of structures with InAs islands and narrow GaAs quantum wells in an AlGaAs host have been investigated. The InAs islands were formed by depositing a layer of InAs with an effective thickness less than one monolayer. The effect of an exciton waveguide and the onset of lasing due to optical pumping in the red spectral range are demonstrated in structures without external optical confinement by layers with a lower refractive index.
© *1999 American Institute of Physics.* [S1063-7826(99)02204-8]

The significant progress that has recently been made in the fabrication of quantum dots (QD) and the study of their properties can be attributed to the development of a method used to create such objects by spontaneously transforming a thin strained layer deposited on the surface of a material with a different lattice constant.[1–4] During deposition of thin submonolayer InAs coatings [with effective thickness ~0.5 monolayer (ML)] on a GaAs surface an array of islands of height 1 ML, which have an elongated shape (width ~40 Å and length ~200 Å), is formed.[5] Such structures possess unique optical properties: a significant increase in the exciton binding energy as a result of lateral quantization,[6] high efficiency of photoluminescence (PL), and a large oscillator strength of the exciton even when the effective thicknesses of the InAs layer are very small.[7] The large oscillator strength leads to the appearance of pronounced peaks in the exciton absorption. According to the Kramers–Kronig relations, this results in a modulation of the refractive index near the exciton absorption energy. If the photoluminescence peak is found on the long-wavelength edge of the absorption line (in the region of low self-absorption) and, at the same time, in the region of steep growth of the refractive index, then this could lead to the appearance of a waveguide effect without the use of external waveguide layers. The use of submonolayer coatings in the system CdSe/ZnMgSSe has made it possible to achieve lasing in structures without external optical confinement.[8,9]

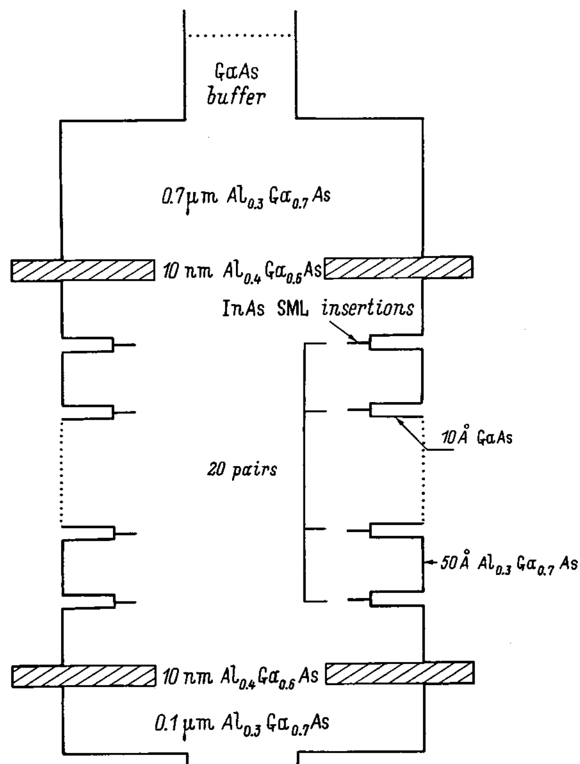

FIG. 1. Diagram of the investigated structures.

We used the concept of submonolayer coatings for the system InAs/AlGaAs. Our goal was to determine whether it is possible to create light-emitting devices based on the exciton waveguide effect, which operate in the red region of the spectrum. The application of this concept makes it possible to achieve a maximum shift of the laser wavelength toward shorter wavelengths and enhance the properties of injection lasers. We demonstrate the onset of lasing with optical pumping without external optical confinement at low excitation densities.

Samples were grown by molecular-beam epitaxy (MBE) on a semi-insulating GaAs (100) substrate on a RIBER 32P setup with a solid-state As source. Growth was carried out

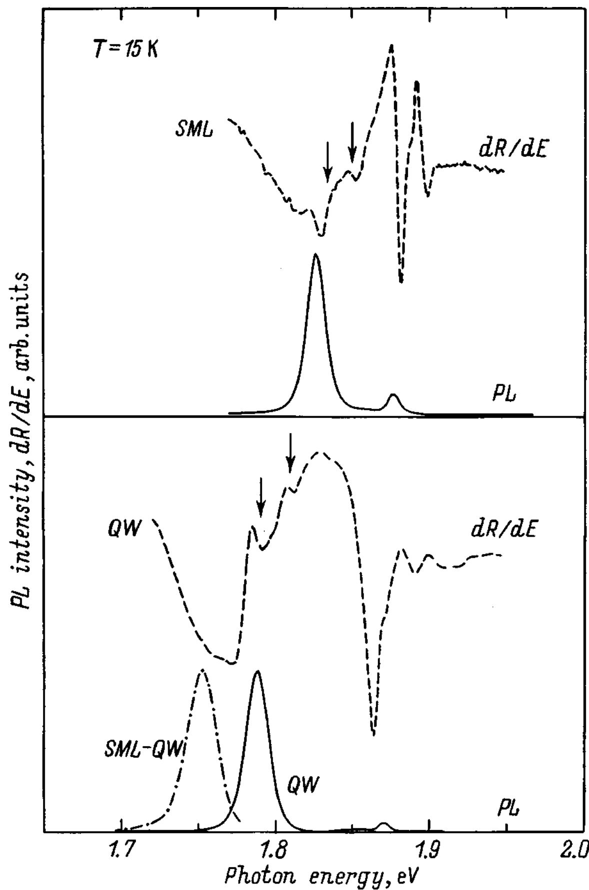

FIG. 2. Photoluminescence and reflection spectra of the investigated samples.

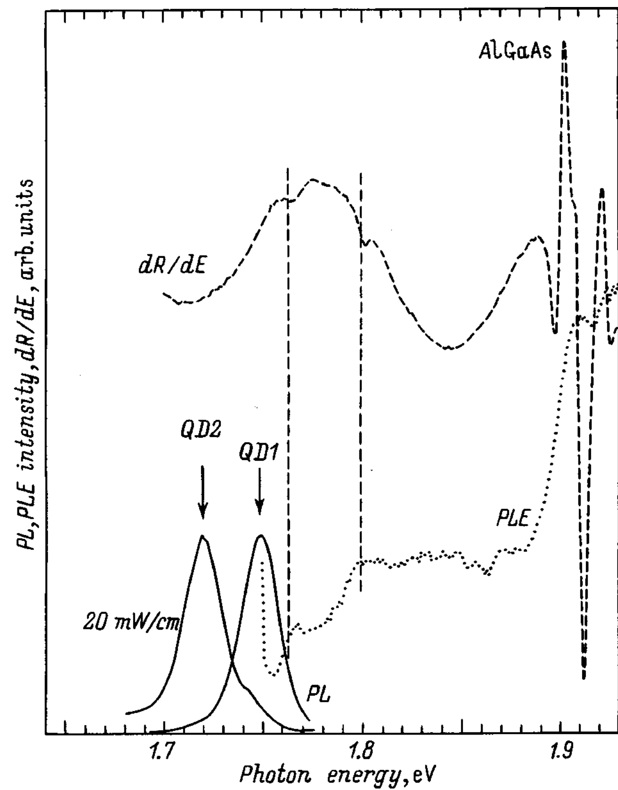

FIG. 3. Photoluminescence spectra, photoluminescence excitation spectrum, and reflection spectrum of sample SML–QW. $T=15$ K.

under arsenic-enrichment conditions that are standard for MBE. Figure 1 shows a diagram of the investigated structures. The thin (100 Å) $Al_{0.4}Ga_{0.6}As$ layers were imbedded to provide electron confinement of carriers. We examined samples with quantum wells (QW) without submonolayer inclusions (the QW samples) and also with InAs inclusions with an effective thickness of 0.5 monolayer deposited at the center of each GaAs quantum well (the SML–QW samples). We also examined the optical properties of a sample in which GaAs quantum wells were absent and the submonolayers were deposited directly on the $Al_{0.3}Ga_{0.7}As$ host (the SML samples). The growth temperature of the structure was 600 °C, and during growth of the active medium the temperature was lowered to 485 °C to avoid segregation and re-evaporation of In atoms from the surface.

Photoluminescence was excited either by an Ar^+ laser with pump density $\sim 300\,W/cm^2$ or by a pulsed N_2 laser with excitation density $100\,kW/cm^2$, or by an incandescent lamp with excitation density ~ 1 mW/cm^2, whose light was passed through a monochromator. Photoluminescence was recorded with the help of a cooled photomultiplier. Photoluminescence was investigated in a closed-cycle helium cryostat.

Figure 2 shows photoluminescence and reflection spectra of the investigated samples. Two features are observed in the reflection spectra. Theoretical estimates for the structure with GaAs quantum wells show that these features correspond to electron–heavy hole and electron–light hole transitions, respectively.[10] Similar estimates were not made for the samples containing InAs submonolayers since the properties of InAs quantum dots depend strongly on the conditions of growth (temperature, growth interruptions, etc.). Note that deposition of InAs in the center of the GaAs quantum wells leads to a shift of the photoluminescence line by ~ 35 meV toward lower photon energies. For all of the investigated structures we observed a long-wavelength shift of the photoluminescence line relative to the corresponding features in the reflection spectra. This is because recombination proceeds from localized states formed by fluctuations of the width of the quantum wells (for the QW samples) or size of the InAs quantum dots (for the SML and SML–QW structures). In the photoluminescence spectrum of a SML–QW structure the long-wavelength line *QD2* appears in the case of a weak intensity of excitation (Fig. 3). The existence of two peaks points to the formation of various groups of InAs quantum dots that differ either in shape or in size. The formation of vertically coupled quantum dots is also possible. An increase in the pump intensity leads to rapid saturation of the *QD2* band, which indicates that the density of the quantum dots that form the given line is low.

Figure 4 is a plot of the temperature dependence of the photoluminescence. Variation of the temperature in narrow limits 15–25 K leads to significant changes in the shape of the spectrum. The total photoluminescence intensity falls, and the intensity of the *QD2* line decreases relative to the intensity of the *QD1* band (inset) and its maximum shifts dramatically toward lower photon energies. The shift of the maximum of the *QD2* band toward longer wavelengths with

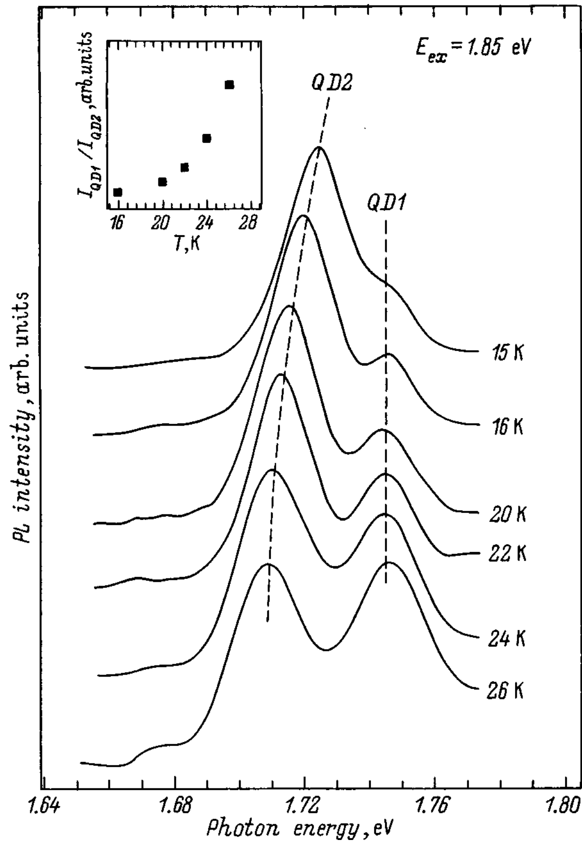

FIG. 4. Photoluminescence spectra of sample SML–QW at various temperatures. The inset shows the temperature dependence of the ratio of intensities of the *QD1* and *QD2* lines.

increasing temperature, which is significant in comparison with the change in the width of the band gap, is typical of recombination via quantum-dot states[11] and is due to growth of the probability for thermal ejection of carriers from the quantum-dot states which are associated with the short-wavelength side of the *QD2* maximum. At the same time, the small shift of the maximum of the *QD1* line corresponds to the temperature variation of the width of the band gap of AlGaAs.[12] Consequently, we can assume that the *QD1* band is associated with recombination of carriers via the approximately one-monolayer-thick quantum-dot array. In this case, the width of the photoluminescence line is due to the nonuniformity in the lateral dimensions of the islands, whose influence on the energy of the optical transition is significantly weaker than the influence of their nonuniformity in height. It follows from these results that despite the strong localization of the carriers in the quantum dots that form the *QD2* line, the photoluminescence intensity of this line decreases with temperature significantly faster than the intensity of the *QD1* band. This indicates that such a fall in the intensity of the *QD2* line is due to thermal ejection of carriers in the small quantum dots, which account for the *QD1* line, and not to the states of the continuum.

Thus, on the basis of the optical data we can make the following conclusions. Deposition of 0.5 monolayer of InAs in the center of narrow GaAs quantum wells leads to the formation of a dense quantum-dot array with a height of ~1

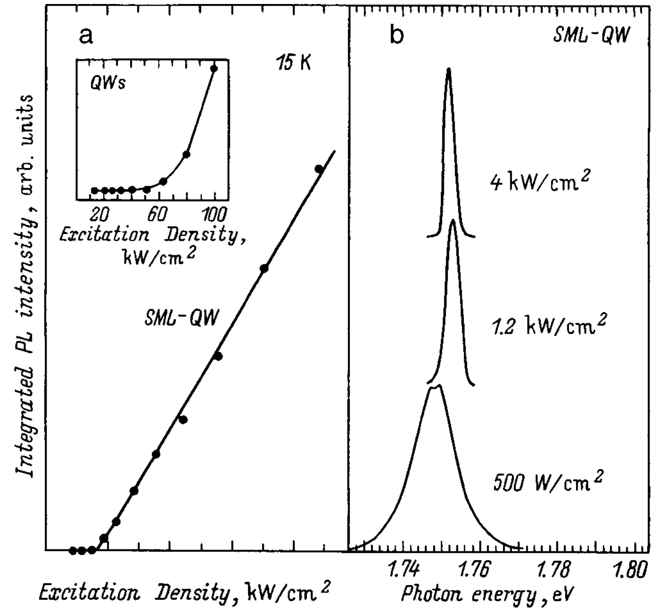

FIG. 5. Dependence of the total photoluminescence intensity of sample SML–QW (*QW* in the inset) on the pumping (a), and photoluminescence spectra for different excitation intensities (b).

monolayer, which corresponds to the photoluminescence band at ~1.75 eV. In addition, few quantum dots of larger size, which correspond to the photoluminescence line at ~1.73 eV, are formed.

Let us consider the particular features of lasing in the investigated structures. It should be noted that optical confinement is degraded by the fact that the refractive index of AlGaAs is less than that of GaAs, which leads to an expulsion of the light wave into the region of the GaAs buffer layer. On the other hand, the strong resonance absorption due to the quantum dots can lead to an exciton waveguide effect. Besides formation of an optical waveguide due to the exciton effect, optical confinement in the given structures can arise

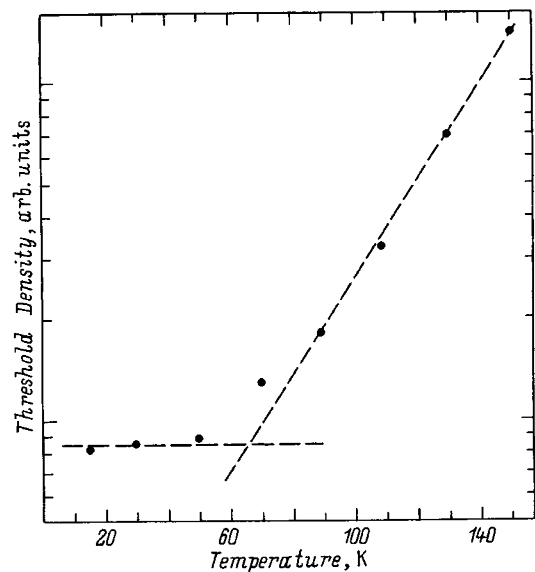

FIG. 6. Temperature dependence of the threshold excitation density for the structure SML–QW.

due to an effective change in the refractive index in the active region containing the GaAs and InAs layers that possess a large refractive index in comparison with the host material.

Figure 5a plots the dependence of the total photoluminescence intensity on the excitation density, and Fig. 5b shows photoluminescence spectra when observing from the end-face of SML–QW and QW structures (see inset) at $T = 15$ K, from which cavities of length $L = 1$ mm were cleaved. It can be seen from Fig. 5 that for a QW sample at an excitation density ~ 60 kW/cm^2 a steep rise in the photoluminescence intensity with pumping, which is indicative of the onset of stimulated emission, is observd. For the SLS–QW sample the threshold excitation intensity is significantly decreased and is equal to ~ 800 W/cm^2. Note that if rescaled to injection pumping the threshold density of 800 W/cm^2 corresponds to a threshold current ~ 200 A/cm^2, which, because the quantum yield for optical excitation is not known, is an upper limit of the threshold current. The observed decrease in the threshold may be attributable to the deposition of InAs quantum dots which leads to a decrease in the number of states that participate in lasing. Figure 6 plots the temperature dependence of the threshold density of excitation for the SML–QW structure. The growth of the threshold current density at temperatures above ~ 70 K can be described by the characteristic temperature $T_0 = 30$ K. Such behavior of the threshold density can be explained by thermal ejection of carriers from the quantum dots. Nevertheless, we observed lasing up to 170 K. The temperature stability of emission can be raised by increasing the localization energy by use of wider-band layers of the host material.

In summary, we have carried out an optical study of quantum dots formed by submonolayer deposition of InAs onto an $Al_{0.3}Ga_{0.7}As$ host. Optical transitions in such structures take place via localized states, whose energy is shifted relative to the exciton absorption energy toward lower photon energies, which makes it possible to realize an internal exciton waveguide. We have demonstrated lasing with optical pumping in the absence of external optical confinement. Lasing arises at low excitation densities, which makes such structures promising for the creation of low-threshold injection lasers in the visible spectral range.

This work was carried out with the partial support of the Russian Fund for Fundamental Research, the Volkswagen Foundation, and the scientific program ''Physics of Solid-State Nanostructures.''

[1] L. Goldstein, F. Glass, J. Y. Marzin, M. N. Charasse, and G. Le Roux, Appl. Phys. Lett. **47**, 1099 (1985).
[2] P. M. Petroff and S. P. Den Baars, Superlattices Microstruct. **15**, 15 (1994).
[3] M. Moison, F. Houzay, F. Barthe, L. Leprince, E. André, and O. Vatel, Appl. Phys. Lett. **64**, 196 (1994).
[4] P. M. Petroff and S. P. Den Baars, Superlattices Microstruct. **15**, 15 (1994).
[5] V. Bressler-Hill, A. Lorke, S. Varma, P. M. Petroff, K. Pond, and W. H. Weinberg, Phys. Rev. B **50**, 8479 (1994).
[6] P. D. Wang, N. N. Ledentsov, C. M. Sotomayor Torres, P. S. Kop'ev, and V. M. Ustinov, Appl. Phys. Lett. **64**, 1526 (1994).
[7] M. V. Belousov, N. N. Ledentsov, M. V. Maximov, P. D. Wang, I. N. Yasievich, N. N. Faleev, I. A. Kozin, V. M. Ustinov, P. S. Kop'ev, and C. M. Sotomayor Torres, Phys. Rev. B **51**, 14 346 (1995).
[8] N. N. Ledentsov, I. L. Krestnikov, M. V. Maximov, S. V. Ivanov, S. L. Sorokin, P. S. Kop'ev, Zh. I. Alferov, D. Bimberg, N. N. Ledentsov, and C. M. Sotomayor Torres, Appl. Phys. Lett. **69**, 1343 (1996).
[9] N. N. Ledentsov, I. L. Krestnikov, M. V. Maximov, S. V. Ivanov, S. L. Sorokin, P. S. Kop'ev, Zh. I. Alferov, D. Bimberg, N. N. Ledentsov, and C. M. Sotomayor Torres, Appl. Phys. Lett. **70**, 2766 (1997).
[10] M. P. C. M. Krijn, Semicond. Sci. Technol. **6**, 27 (1991).
[11] A. F. Tsatsul'nikov, N. N. Ledentsov, M. V. Maksimov, A. Yu. Egorov, A. E. Zhukov, S. S. Ruvimov, V. M. Ustinov, V. V. Komin, I. V. Kochnev, P. S. Kop'ev, Zh. I. Alfërov, and D. Bimberg, Fiz. Tekh. Poluprovodn. **30**, 1793 (1996) [Semiconductors **30**, 938 (1996)].
[12] P. S. Dobal, H. D. Bist, S. K. Mehta, and R. K. Jain, Appl. Phys. Lett. **65**, 2496 (1994).

Translated by Paul F. Schippnick

Influence of deep traps on current transport in Pd–$p(n)$–CdTe structures

S. V. Slobodchikov, Kh. M. Salikhov, and E. V. Russu

A. F. Ioffe Physicotechnical Institute, Russian Academy of Sciences, 194021 St. Petersburg, Russia
(Submitted September 10, 1998; accepted for publication September 15, 1998)
Fiz. Tekh. Poluprovodn. **33**, 492–493 (April 1999)

The current–voltage characteristics and photovoltage of Pd–$p(n)$–CdTe structures and changes in them produced by pulsed hydrogen treatment have been investigated. The current transport in Pd–n–CdTe structures $[I \sim \exp(\alpha V)]$ is found to be linked with double injection of carriers occurring as a result of their capture at trapping centers that are uniformly distributed over energy. The semiconductor regime of double injection with $I \sim V^2$ is important for Pd–p–CdTe structures. A series of deep trapping centers, including those in the interval 0.75–0.83 eV, is responsible for the extended relaxation of the photovoltage and dark current after a hydrogen pulse (H_2). © *1999 American Institute of Physics.*
[S1063-7826(99)02304-2]

Among II–IV semiconductor compounds, cadmium telluride occupies an important place as a material used in the production of a number of optoelectronic devices and, in particular, detectors of various types of radiation. A great deal of attention has been devoted to the study of the electrical, optical, and photoelectric properties of CdTe crystals and diode structures.[1] Many of these studies have revealed the large role of traps of various origin, which affect the lifetime of the majority and minority current carriers and which alter the characteristics of the sensitivity of such devices.

In this paper we report some results of an experimental study of the mechanism of current transport in diode structures with a palladium contact based on partially compensated p- and n-type CdTe.

CdTe crystals were grown by sublimation from presynthesized polycrystalline material. Growth took place in a two-zone furnace, in a quartz cell pumped down to 10^{-5} Torr, at a temperature of 850–900 °C; the cell moved at a speed of 0.5 mm/h. By varying the growth conditions we obtained partially compensated CdTe samples of both p- and n-type with resistivity $\rho = 10^4 - 10^6\ \Omega \cdot \text{cm}$. Palladium was deposited by vacuum sputtering and its thickness was 400 Å. Ohmic contacts were created on the backside of the substrate by indium sputtering.

We measured the current–voltage characteristics, the photovoltage, and the changes in them in response to pulsed hydrogen treatment and also the associated relaxation characteristics.

Figure 1 plots typical forward branches of the current–voltage characteristics for Pd–p–CdTe structures (curve *1*) and Pd–n–CdTe structures (curves *2* and *3*). Curves *1* and *2* were measured at $T = 300$ K, and curve *3*, at $T = 108$ K. In curve *1*, the ohmic segment is followed by a segment with $I \sim V^2$. The sample diode structures based on n-CdTe are characterized by an exponential dependence, both at $T = 300$ K and at $T = 108$ K (curves *2* and *3*)

$$I \sim \exp \alpha V. \tag{1}$$

Analysis shows that for both types of diode structures the current transport mechanism can be explained by double carrier injection into the $p(n)$-CdTe layers. The quadratic dependence on the voltage in structures based on p-CdTe more closely corresponds to the semiconductor regime of double injection, where

$$I \sim q(p_0 - n_0)\mu_n \mu_p \tau \frac{V^2}{L^3}. \tag{2}$$

[In relation (2) L is the thickness of the p-CdTe layer, and the remaining symbols have their usual meaning.] Evidence supporting this statement is provided by an estimate of the effective hole mobility μ_p^* in the insulator regime, where the quantity $q(p_0 - n_0)\mu_n \mu_p \tau$ transforms to μ_p^*. Using the experimental data, this estimate gives an unjustifiably high value $\mu_p^* > 10^3\ \text{cm}^2/(\text{V} \cdot \text{s})$.

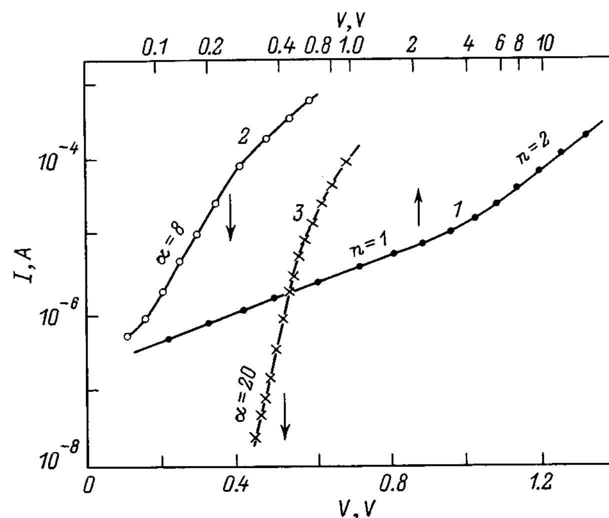

FIG. 1. Current–voltage characteristics of Pd–CdTe diode structures at the temperature T, K: *1, 2* — 300, *3* — 108. Conductivity type of CdTe: *1* — p, *2, 3* — n. Upper scale is for curve *1*.

 © 1999 American Institute of Physics

For the Pd–n–CdTe structures, in which the electron injection in the forward direction $I_n/I \gg I_p/I$, the capture of majority carriers should have a decisive effect on the form of the current–voltage characteristics. In this case, the energy distribution of the traps in the band gap is of substantial importance. The exponential dependence of the current on the voltage forces us to assume the existence in the band gap of a uniform distribution of the trapping centers with respect to energy. In this case we have[2]

$$I \sim \exp\left[\frac{2\varepsilon V}{N_t(E)kTL^2}\right], \tag{3}$$

where $N_t(E)$ is the trap density per unit energy. From the slope of the dependence $\log I = f(V)$ (curve *2*) we obtain

$$\alpha = \frac{2\varepsilon}{N_t(E)kTqL^2} = 8$$

and $N_t(E) \simeq 10^{12}\,\mathrm{cm}^{-3}\cdot\mathrm{eV}^{-1}$. At 108 K, according to relation (3), $\alpha = 22$. From the slope of curve *3* we obtain $\alpha = 20$, in good agreement with the expected value. Note that the order of magnitude of the found trap density corresponds to values known from a series of experimental studies on the electrical, optical, and photoelectric properties of CdTe.[3]

From the Fowler tail in the spectral photosensitivity data (at $T = 300$ K) we determined the height of the Schottky barrier in p-CdTe to be 0.95 eV, and in n-CdTe to be 1.1 eV.

Figure 2 plots relaxation curves of the photovoltage (*1*) and the forward current (*2*) after pulsed hydrogen treatment. They are characterized by an extended relaxation time reaching approximately 430 s for the photovoltage and roughly 240 s for the forward current. An analysis of the relaxation curves shows that in the time interval 200−430 s the current growth curve is fit by the dependence

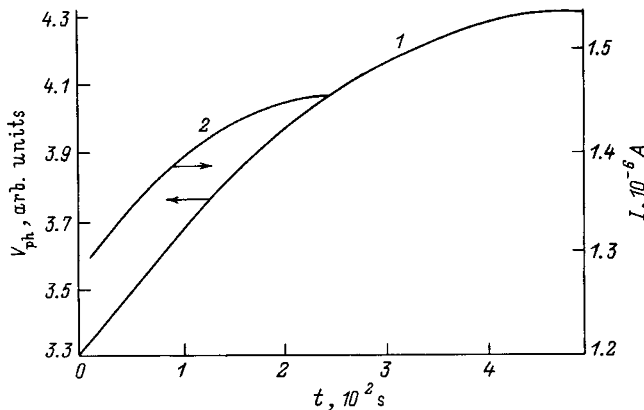

FIG. 2. Relaxation of the photovoltage (*1*) and forward dark current (*2*) for the structure Pd–n-CdTe at $T = 300$ K.

$$I = I_0\left[1 - \exp\left(-\frac{t}{\tau}\right)\right] \tag{4}$$

with $\tau = 80$ s. At $t < 200$ s the relaxation curve can be described by the sum

$$\sum_i I_i = \sum_i I_{0i}\left[1 - \exp\left(-\frac{t}{\tau_i}\right)\right]. \tag{5}$$

The relaxation curve of the forward current in the time interval 100−240 s follows dependence (4) with $\tau = 40$ s, and below 100 s it follows dependence (5). The energy position of the trap levels, if it is calculated from the thermal ejection time $\tau = \tau_0 \exp E_{ti}/kT$ with $\tau_0 \sim 10^{-13}$ s, turns out to be 0.81 eV for $\tau = 40$ s, and 0.83 eV for $\tau = 80$ s. For short times at the beginning of the relaxation curves we have $E_{ti} \geq 0.75$ eV.

The electron trap levels found in Ref. 4 fall in the the energy interval 0.75−0.83 eV. The drop in the photovoltage in a H_2 atmosphere is due, on the one hand, to a decrease in the height of the Schottky barrier, as was found to be the case, for example, in Ref. 5, and, on the other, to the trapping of minority hole (or electron) carriers as a result of charge exchange of the initial (background) traps and to ''temporary'' levels created by hydrogen absorbed at the Pd–CdTe boundary. The latter factor decreases the diffusion displacement length. For both reasons the change in the photovoltage was 20–30% in the first case, and 11–15% in the second. In connection with the decrease in the height of the Schottky barrier, one might expect a growth of the dark currents in a H_2 atmosphere. However, both the forward and the reverse current fall, in contrast to the data in Ref. 5. This is a consequence of capture of nonequilibrium electrons and holes to the background levels and to the above-mentioned ''temporary'' levels; this is the main reason for the change in the dark currents. Since $n(p)$-CdTe crystals are partially compensated, it can be assumed that acceptor centers in the lower half of the band gap are active trapping centers of holes and in the upper half they are electron traps. Hydrogen-initiated traps, which increase the capture of holes and electrons, fall in the energy interval 0.75−0.83 eV and also probably in the range of lower values.

[1] *Semiconductors and Semimetals* (Academic Press, New York, 1978), Vol. 13.
[2] M. Lampert and P. Mark, *Current Injection in Solids* (Academic Press, New York, 1970), Ch. 4.
[3] A. Castaldini, A. Cavallini, and B. Fraboni, J. Appl. Phys. **83**, 2121 (1997).
[4] T. Takebe, J. Saraie, and H. Matsunami, J. Appl. Phys. **53**(1), 457 (1982).
[5] G. G. Kovalevskaya, M. M. Meredov, E. V. Russu, Kh. M. Salikhov, and S. V. Slobodchikov, Zh. Tekh. Fiz. **63**(2), 185 (1993) [Tech. Phys. **38**, 149 (1993)].

Translated by Paul F. Schippnick

Determination of the parameters of deep levels from the relaxational delay of breakdown of a *p–n* junction

S. V. Bulyarskiĭ

Ul'yanovsk State University, 432700 Ul'yanovsk, Russia

Yu. N. Serëzhkin and V. K. Ionychev

Mordovian State University, 430000 Saransk, Russia

(Submitted July 25, 1998; accepted for publication October 1, 1998)
Fiz. Tekh. Poluprovodn. **33**, 494–498 (April 1999)

A technique for determining the deep-center parameters from the relaxational delay of avalanche breakdown of a $p-n$ junction is investigated. The method implemented does not impose any restrictions on the relation between the concentration of the deep centers and that of the dopant impurities and can be used in those cases when the current–voltage characteristic of the sample is poorly monitored or the equivalent circuit of the $p-n$ junction is complex. This may be a consequence of strongly compensated base regions, the presence of high-resistance layers, or imperfect ohmic contacts. Possibilities of the method are illustrated by the example of determining the parameters of the gold acceptor level in p^+-n-n^+ structures with high gold content ($N_{\mathrm{Au}}=0.9N_d$). © *1999 American Institute of Physics.* [S1063-7826(99)02404-7]

1. INTRODUCTION

It is known that avalanche breakdown of $p-n$ junctions is of a microplasma character. If the reverse bias on the $p-n$ junction is suddenly increased, the microplasmas exhibit a breakdown delay.[1] This delay is influenced by deep centers (DC) located in the space charge region (SCR) of the $p-n$ junction. If the concentration of the deep centers is small, then they can affect the static breakdown delay of the microplasmas. If the concentration of the deep centers is large, where the electric field intensity in the space charge region changes as a result of the charge exchange, the avalanche breakdown experiences a relaxational delay. Such a delay was first observed by Akimov *et al.*[2] and later efforts were made to use it in the deep-level transient spectroscopy (DLTS) of the microplasma channels.[3–5]

The most rigorous theoretical treatment of the relaxational delay of avalanche breakdown was first reported by the authors of Ref. 5, where the field dependence of the charge-carrier emission from the deep centers was taken into account in the approximation of the one-dimensional theory of Frenkel' and Poole. However, the they[5] were forced to restrict the analysis to the case of moderate concentration of the deep centers.

In all of the studies indicated above, the deep-level parameters were determined not from measurements of the breakdown delay, but from the temperature dependence of the avalanche breakdown field corresponding to a fixed duration of the breakdown delay.

In our study we have considered a technique for determining the deep-level parameters directly from the breakdown delay measured at different temperatures. This technique can also be used in the case of strong compensation, when the concentration of the deep centers is comparable in magnitude with the concentration of the dopant impurity in the base of the diode. In this case it is possible to utilize measurement regimes in which a charge exchange of the deep centers can occur in weak fields.

2. CALCULATIONAL FORMULAS

Let us consider an asymmetrical p^+-n junction whose n-base has acceptor-type deep centers with energy level E_t in the upper half of the band gap. Let the Fermi level in the n-base (F) at the measurement temperature be greater than E_t. The deep centers in the n-base will then be completely filled with electrons if $F-E_t$ is equal to several kT. Complete filling of the deep centers will also be observed in some part of the space charge region near the boundary with the n-base. The width of this region λ_0 is defined by the coordinate of the intersection point (in the space charge region) of the acceptor level E_t with the electron Fermi quasilevel and in the case of uniform doping is given by[6]

$$\lambda_0=\left[\frac{2\varepsilon(F-E_t)}{e^2(N_d-N_t)}\right]^{1/2}, \tag{1}$$

where N_d is the concentration of the donor impurity, and N_t is the concentration of the deep centers. In the remaining part of the space charge region the deep centers are almost completely destroyed. The concentration of deep centers holding trapped electrons is defined by the ratio between the electron (e_n) and hole (e_p) emission from the deep center[6]

$$N_\infty=\frac{e_p}{e_n+e_p}N_t. \tag{2}$$

Such filling of the deep centers will also occur for a reverse bias U if the $p-n$ junction persists until steady state is reached. In this case, the width of the edge region λ_0 does not depend on the magnitude of the applied voltage.

 © 1999 American Institute of Physics

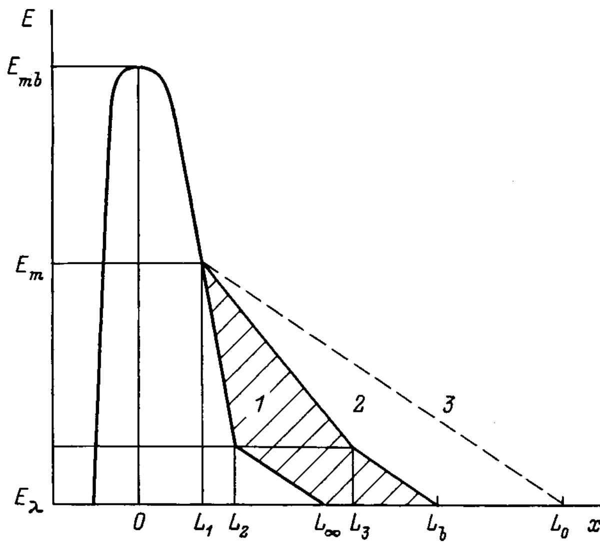

FIG. 1. Distribution of the electric field in a p^+-n junction with deep centers: *1* — before change in the charge state of the deep centers; *2* — at $t=t_b$, *3* — at $t_b=0$.

Let a reverse bias be applied to the $p-n$ junction equal to the lowest voltage at which a microplasma is formed in the junction, U_∞. We assume that an avalanche current does not yet flow at this voltage, but appears if it is increased by the slightest amount.

We decrease the bias voltage to U_m and then raise it back to $U>U_\infty$ at the $p-n$ junction. When we decrease the bias voltage, some of the deep centers previously found in the space charge region are rapidly filled with electrons, and when we raise it again, they begin to emit their trapped electrons. The concentration of deep centers, which are located in the relaxation region and which hold trapped electrons decreases in time in accordance with

$$N(t)=(N_t-N_\infty)\exp[-(e_n+e_p)t]+N_\infty, \tag{3}$$

and the space-charge density and the electric field increase. After some time t_b, the maximum field reaches its breakdown value and the condition for breakdown of the $p-n$ junction is satisfied. If the relaxation region, where the deep centers were occupied, does not touch the ionization region of the space charge region, then breakdown of the $p-n$ junction will take place at the same maximum field strength E_{mb} as it does for the bias voltage U_∞.

Figure 1 shows the distribution of the electric field in the space charge region at different times. The symbols along the x axis have the following meanings: L_∞ is the boundary of the space charge region at $U=U_\infty$, L_b is its boundary at the time $t=t_b$, and L_0 is its boundary at $t_b=0$:

$$L_1=L_m-\lambda_0,\ \ L_2=L_\infty-\lambda_0,\ \ L_3=L_b-\lambda_0.$$

Here L_m is the boundary of the space charge region at the voltage at which the deep centers are filled, which is equal to U_m. The area of the hatched region is the difference between the applied voltage U and the steady-state breakdown voltage U_∞. From simple geometrical arguments we obtain

$$U-U_\infty=\frac{a}{b\ \exp[(e_n+e_p)t_b]-1}, \tag{4}$$

where

$$a=\frac{1}{2}(E_m+E_\lambda)(L_\infty-L_m) \tag{5}$$

and

$$b=(N_d-N_\infty)/(N_t-N_\infty). \tag{6}$$

The voltage at which current avalanche or the first microplasma pulses appear (U_∞) can be easily determined experimentally. If N_d exceeds N_t by an order of magnitude or more, the subtracted term in the denominator in Eq. (4) can be disregarded and the relation between $U-U_\infty$ and the breakdown delay time t_b becomes a simple exponential. This at once allows us to determine the mean holding time of the trapped carriers in the deep centers

$$\tau=(e_n+e_p)^{-1}.$$

If N_t and N_d are similar in magnitude, then this same subtracted term can be ignored in the ''tail'' of the relaxation curve when $(e_n+e_p)t_b\approx 2$ to 3. Another way of determining τ is by fitting the dependence of $U-U_\infty)^{-1}$ on t_b, which, according to Eq. (4), is given by

$$(U-U_\infty)^{-1}=\frac{b}{a}\exp\left(\frac{t_b}{\tau}\right)-\frac{1}{a}. \tag{7}$$

By fitting this expression by the sum of an exponential and a constant, it is possible to determine all the parameters. By expressing E_m and E_λ in terms of the concentration of the deep centers and the geometrical parameters of the measured structure, it is possible to obtain the following relation defining the deep-center concentration (for the majority of the deep centers $N_\infty \ll N_t$):

$$\frac{a}{b}=\frac{e}{\varepsilon}(L_\infty-L_m)\left[\frac{N_d-N_t}{N_d}N_t\lambda_0+\frac{N_t}{2}(L_\infty-L_m)\right]. \tag{8}$$

Despite the relative cumbersomeness of this expression, the determination of N_t does not cause great difficulties: for example, by comparing the dependence $\lambda_0=f(N_t)$ found from Eq. (8) and the analogous dependence given by Eq. (1) if the energy position of the level E_t has already been found. The necessary values of L_n and L_∞ can be determined from the current–voltage characteristics.

It is of interest to consider relaxational delay in p^+-n-n^+ structures. If puncture of such a structure sets in at voltages U_p less than the steady-state breakdown voltage U_∞, then the situation simplifies significantly. In this case, the width of the edge space-charge region λ, in which the deep centers are completely filled, is less than λ_0. It can be easily shown that in a p^+-n-n^+ structure with puncture the following parametric dependence of λ on U holds:

$$\frac{\lambda}{\lambda_0}=\left\{1+\left[\frac{e\lambda_0E_0}{2(F-E_t)}\right]^2\right\}^{1/2}-\frac{e\lambda_0E_0}{2(F-E_t)},$$

$$U=lE_0+\frac{e}{2\varepsilon}[(N_d-N_\infty)l^2+(N_t-N_\infty)(\lambda-2l)\lambda],$$

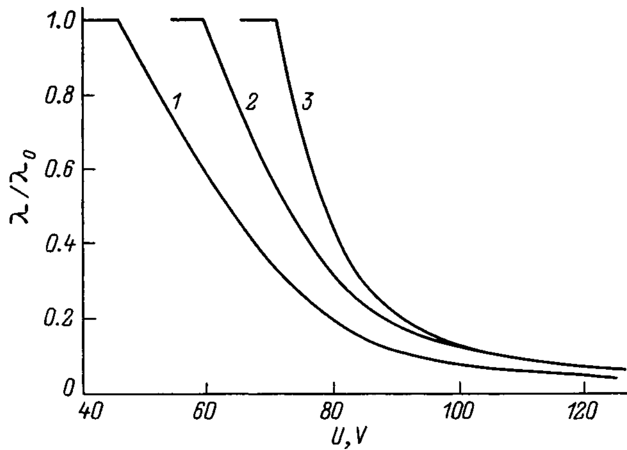

FIG. 2. Calculated curves of the dependence of the width of the edge region on the applied voltage for a p^+-n-n^+ structure; $N_d=4\times10^{15}\,\text{cm}^{-3}$, $l=5\,\mu$m, $N_\infty=0$. Values of the quantities $(F-E_t)$, eV and N_t, cm^{-3}: *1* — 0.5 and 3.6×10^{15}, *2* — 0.5 and 3×10^{15}, *3* — 0.25 and 2×10^{15}.

where the parameter E_0 is the discontinuity in the electric field at the $n-n^+$ boundary, and l is the width of the moderately doped region of the p^+-n-n^+ structure. Figure 2 plots such dependences for a silicon p^+-n-n^+ structure for assorted values of N_d, E_t, and N_t. For $E_0=0$ the applied voltage is $U=U_p$. It can be seen that for $U>U_p$ the ratio λ/λ_0 is substantially lower and the dependence on the voltage is weak. This implies that the width of the relaxation region remains essentially unchanged during the entire relaxation process.

The distribution of the electric field strength at different times assuming $\lambda=0$ for this case is shown in Fig. 3. Expressing the area of the hatched region in terms of the parameters of the deep centers and the p^+-n-n^+ structure, we obtain

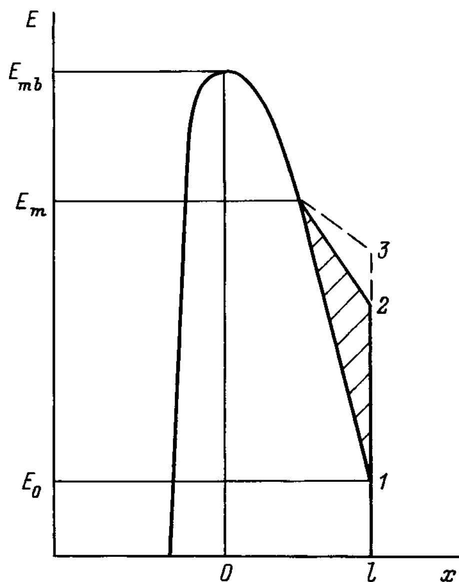

FIG. 3. Distribution of the electric field strength in a p^+-n-n^+ structure with deep centers: *1* — before change in the charge state of the deep centers; *2* — at $t=t_b$, *3* — at $t_b=0$.

$$U-U_\infty=\frac{e}{2\varepsilon}(l-L_m+\lambda_0)^2(N_t-N_\infty)\exp[-(e_n+e_p)t_b]. \quad (9)$$

Here it is assumed that when the deep centers are filled, the voltage U_m falls to values less than the puncture voltage U_p. This relation significantly simplifies the determination of the deep-center parameters. The deep-center concentration is found from the value of $U-U_\infty$ at $t_b=0$

$$U_0-U_\infty=\frac{e(N_t-N_\infty)}{2\varepsilon}(l-L_m+\lambda_0)^2. \quad (10)$$

The procedure for finding N_t is analogous to the procedure described above for a p^+-n junction.

3. MEASUREMENT PROCEDURE AND RESULTS

We measured the deep-center parameters of gold in n-type silicon in epitaxial planar p^+-n-n^+ structures. The samples were prepared by boron diffusion into an epitaxial n-type film with $\rho=1.2\,\Omega\cdot$cm grown on a substrate with $\rho=0.01\,\Omega\cdot$cm. The influence of curvature and surface breakdown were eliminated by creation of a dividing ring.[7] The depth of placement of the $p-n$ junction was 8.6 μm, and the thickness of the epitaxial film was 15.2 μm. Gold diffusion was carried out for 50 min at 1000 °C.

The concentration of the dopant impurity, determined from the current–voltage characteristics of the diodes not containing gold was $(4.1\pm0.2)\times10^{15}\,\text{cm}^{-3}$. The steady-state breakdown voltage U_∞ of the structure, for which the results given above were obtained, was 99.6 V at room temperature. The characteristic slope change of the capacitance–voltage characteristic is evidence that the structure is punctured at $U_p=74.5$ V.

To measure the breakdown delay at a constant bias voltage U_m, we imposed a voltage step with a leading edge of about 10 μs. Breakdown delay was measured with use of an S8-13 recording oscillograph which identified the onset of breakdown from the appearance of the avalanche current. No static breakdown delay was observed, which is explained by the high gold content in the investigated samples. Before applying the voltage step, the sample was held at the voltage U_m for 5 s. This was sufficient to set up steady-state filling of the deep centers in the space charge region in the investigated temperature range.

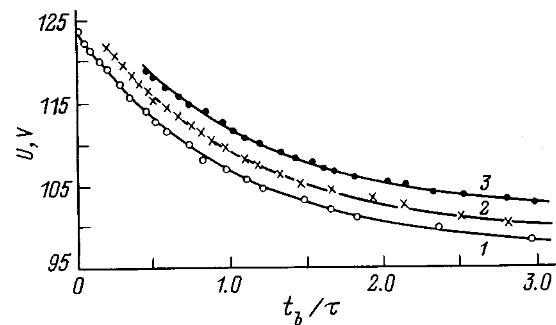

FIG. 4. Relation between the avalanche breakdown delay time and reverse bias for a p^+-n-n^+ structure. Temperature T, K: *1* — 255.8, *2* — 278.9, *3* — 302.8; time τ, ms: *1* — 16.92, *2* — 1.99, *3* — 0.27.

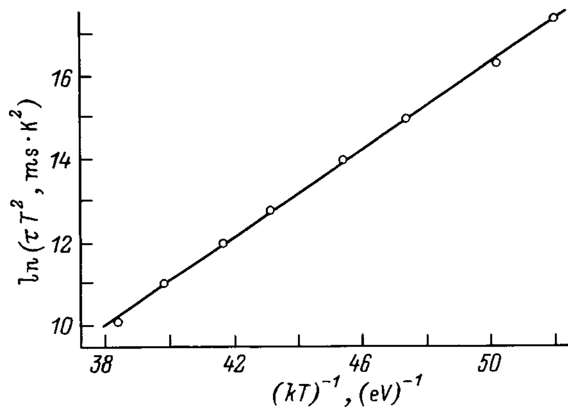

FIG. 5. Dependence of $\ln(\tau T^2)$ on the inverse temperature.

For all of the measurement regimes the relation between the applied voltage U and the breakdown delay time t_b is well described by the exponential dependence (9), which makes it easy to determine the time $\tau=(e_n+e_p)^{-1}$. Figure 4 illustrates the agreement between the theoretical and experimental curves for three temperatures. The plotted dependences were constructed using measured values of τ.

The temperature dependence of τ is plotted in Fig. 5. Assuming that the carrier capture cross section to the deep centers does not depend on temperature, we obtain for the depth of the energy level $E_c-E_t=0.521$ eV. This result is in good agreement with the energy position of the gold acceptor level in n-type silicon. The deep-center concentration is found from U_0-U_∞, which corresponds to zero time of the breakdown delay. At room temperature it is 25.4 V. The deep-center concentration N_t was determined with the help of relations (1) and (10). Initially we obtained a rough estimate, as described above, and then refined it numerically. The necessary values of the parameters L_m and l were determined from the current–voltage characteristics and were found to be $L_m=4.4\,\mu$m (for $U_m=25$ V) and $l=6.6\,\mu$m. The value of the deep-center concentration $N_t=3.7\times10^{15}\,\text{cm}^{-3}$ is about 91% of the concentration of the donor impurity N_d. Thus, the proposed technique enables one to determine the deep-level parameters in $p-n$ junctions with almost completely compensated base regions.

For such a high concentration of deep centers the electric field in the region of relaxation of the field varies considerably during the relaxation process. Estimates show that in the case in question for the filling voltage $U_m=25$ V the maximum electric field in the relaxation region during the relaxation process could grow from 1.8×10^5 V/cm to 2.2×10^5 V/cm. By varying the filling voltage (U_m) it is possible to vary the electric field strength in the relaxation region. The mean holding time of the trapped carriers in the deep centers (τ) was observed to increase with increasing filling voltage. However, the depth of the energy level varied very insignificantly. All this points to the influence of the electric field on the electron emission from the acceptor gold level in silicon. The obtained values of τ and E_t can probably be related to the mean value of the electric field in the relaxation region (roughly 10^5 V/cm). Inference of the field dependence of the emission of charge carriers from measured values of the relaxation delay of avalanche breakdown is an interesting question, but would require a special treatment.

4. CONCLUSIONS

The results discussed above show that relaxational delay of avalanche breakdown can be used for the spectroscopy of energy levels in semiconductors. It can be successfully applied in those cases where the equivalent circuit of the $p-n$ junction is complex. This may be a case of strong compensation of the base regions of the deep centers, the presence of high-resistance buffer layers near the space charge region or ohmic contact, and also a case of incomplete ionization of the dopant impurities in wide-band semiconductors.

[1] I. V. Grekhov and Yu. N. Serezhkin. *Avalanche Breakdowns of $p-n$ Junctions in Semiconductors* [in Russian], Énergiya, Leningrad, 1980.
[2] P. V. Akimov, I. V. Grekhov, and Yu. N. Serezhkin, Fiz. Tekh. Poluprovodn. **4**, 2099 (1970) [Sov. Phys. Semicond. **4**, 1802 (1970)].
[3] E. V. Astrova, V. M. Volle, V. B. Voronkov, V. A. Kozlov, and A. A. Lebedev, Fiz. Tekh. Poluprovodn. **20**, 2122 (1986) [Sov. Phys. Semicond. **20**, 1326 (1986)].
[4] Yu. V. Vyzhigin, B. N. Gresserov, and N. A. Sobolev, Fiz. Tekh. Poluprovodn. **22**, 536 (1988) [Sov. Phys. Semicond. **22**, 330 (1988)].
[5] A. S. Kyuregyan and P. N. Shlygin, Fiz. Tekh. Poluprovodn. **23**, 1164 (1989) [Sov. Phys. Semicond. **23**, 729 (1989)].
[6] S. V. Bulyarskiĭ and N. S. Grushko, *Generation–Recombination Processes in Active Elements* [in Russian], Moscow State Univ. Press, Moscow, 1995.
[7] A. Blikher, *Physics of Bipolar and Field-Effect Transistors* [in Russian], Énergoatomizdat, Leningrad, 1986.

Translated by Paul F. Schippnick

Effect of laser radiation on GaP epitaxial diode structures

V. V. Inyakov, E. N. Moos, and Yu. A. Shraĭner

Prof. P. A. Kostychev Ryazan' State Agriculture Academy, 390044 Ryazan', Russia
(Submitted June 9, 1998; accepted for publication October 5, 1998)
Fiz. Tekh. Poluprovodn. **33**, 499–500 (April 1999)

The effect of laser radiation on the current–voltage characteristics and intrinsic quantum yield of electroluminescence after irradiation is investigated. As a result of irradiation at supercritical radiant power flux levels (greater than 10^7 W/cm^2) an abrupt drop in the luminescence quantum yield and a steep growth of the leakage currents are observed in the current–voltage characteristics. It is assumed that by exciting the electronic subsystem of the impurity atoms the powerful optical radiation facilitates the occurrence of quasichemical reactions. © *1999 American Institute of Physics.* [S1063-7826(99)02504-1]

In studies of the mechanisms of degradation of the intrinsic quantum yield of light-emitting diodes and laser diodes it is of interest to examine the effect of self-generated as well as external radiation in the optical range on aging processes in diode structures. The degradation of AlGaAs double heterostructures occurring as a result of optical excitation of their active region was investigated in Ref. 1. Krypton laser radiation in the power density range $2\times10^4-5\times10^3$ W/cm^2 with photon energies near the width of the band gap of the given laser diodes leads to a considerable drop in the luminescence intensity after $2-3$ hours of irradiation at 150 °C. The reason given in Ref. 1 for this occurrence is the decrease in the intrinsic quantum yield of radiative recombination in the active region of the heterostructures as a result of amplification of nonradiative recombination channels. The effect of argon laser radiation in the optical range with a flux density of 10^3 W/cm^2 at 250 °C on epitaxial structures luminescing in the red, based on gallium phosphide doped with Zn and O (photon energy greater than the width of the band gap of gallium phosphide, $E_g=2.34$ eV), was determined in Ref. 2. A decrease in the intensity of the red emission band with simultaneous growth of the intensity of the infrared (IR) band due to transitions between distant O_P donors and Zn_{Ga} acceptors was observed. The reason for this behavior, in their view,[2] is the decay of Zn–O complexes upon excitation of the electronic subsystem of an actual crystal by optical light. Recombination-stimulated diffusion of Zn atoms from the p-layer[3] or the p^+-layer of the contact[4] into the space-charge region or the n-layer with formation there of nonradiative recombination centers can lead to a drop in the intensity of luminescence of green GaP:N light-emitting diode, in which Zn is the acceptor. Such an effect may account for the appearance of dark-line defects as a result of relaxation of the elastic stress that arises as the Zn concentration in the $p-n$ junction is increased.[5] Laser radiation generates shock waves in materials. Such shock waves have an effect on the properties of irradiated semiconductors, which can also lead to a drop in the luminescence intensity.[6] Irradiation of a semiconductor structure leads to a nonuniform density of point defects of vacancy–interstitial type, the generation of hypersonic waves, and nonuniform heating. Laser-stimulated diffusion of Zn atoms and displacement of the boundary of the $p-n$ junction by the action of neodymium laser light ($\lambda=0.53\,\mu$m) was observed in Ref. 7.

In this article we report the results of an experimental study of the effect of coherent laser radiation on the current–voltage characteristics and the intrinsic quantum yield of electroluminescence after irradiation of gallium-phosphide epitaxial diode structures, whose active region is doped with Zn and O. The aluminum–yttrium garnet laser with radiation wavelength $\lambda=1.06\,\mu$m and photon energy $h\nu=1.17$ eV is two times smaller than the width of the gallium-phosphide band gap. Using the same diode structures, we performed brief current tests lasting 12 h at a current density ~11 A/cm^2 and effective temperature of the $p-n$ junction $\sim115°$. The structures had contiguous ohmic contacts on both the p and n sides of the junction. Laser treatment was done at the end-faces of the crystals perpendicular to the plane of the $p-n$ junction. Optical action on the active region of the LED structures was effected by scanning a laser beam of diameter $\sim60\,\mu$m at a rate of ~4 cm/s over their end-face. The laser operated in the pulsed mode at a frequency of 10.2 kHz with a pulse length $\sim0.3\,\mu$s and power flux density in the pulse $\sim10^6$ W/cm^2. Scanning was realized in a single pass with a step of 10 μm.

For optical excitation at subcritical densities of the incident light energy (less than 10^6 W/cm^2) the current–voltage characteristics of the samples in the working current range remained stable while in the current range $10^{-8}-10^{-6}$ A the leakage currents grew slightly (see Fig. 1). No correlation between the variation of the current–voltage characteristics and the intrinsic quantum yield of the light-emitting diodes after irradiation was detected. Upon examining the supercritical regimes of laser action (power densities greater than 10^7 W/cm^2), we observed a partial destruction of the surface and a simultaneous steep growth of the leakage currents in the current–voltage characteristics with an abrupt decrease of the electroluminescence quantum yield. This phenomenon can be explained by avalanche growth of the absorption at high radiation power fluxes and significant surface heating accompanied by the liberation of phosphorus and enrichment

 © 1999 American Institute of Physics

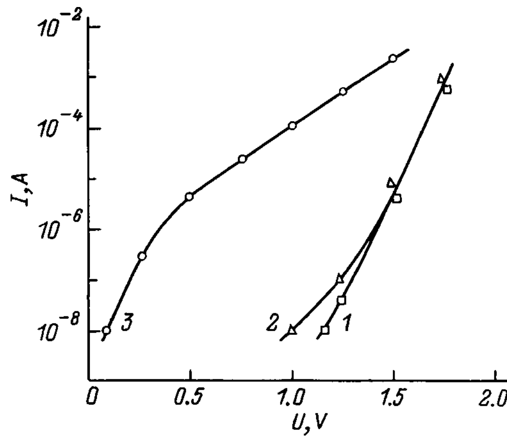

FIG. 1. Typical current–voltage characteristics of GaP : Zn, O structures before (*1*) and after laser treatment at a power density $\sim 10^6$ W/cm^2 (*2*) and $\sim 10^7$ W/cm^2 (*3*).

of the surface with metallic gallium. After optical irradiation of the diode structures at subcritical radiation power fluxes, the luminescence quantum yield was found to grow by 5–6%, on the average, although in the individual samples the radiation efficiency can vary from -20 to $+50\%$. The mean value of the electroluminescence quantum yield after 12 h of tests remained nearly constant and equal to the yield after optical treatment.

The results of our experiments can be explained by assuming that powerful optical radiation with photon energy $h\nu \sim E_g/2$ excites the electronic subsystem of the impurity atoms upon ionization of the deep levels, for which the condition $\tau_i \gg \tau_c$ (Ref. 8) is easily satisfied. Here τ_i is the lifetime of the ionized state of the atom and τ_d is the displacement time of an atom. These factors facilitate the process of quasichemical reactions with the participation of impurities and native lattice defects, including vacancies. A subthreshold mechanism of defect formation is probably realized when the photon momentum is insufficient for direct impact displacement of an atom. The changes in the quantum yield after irradiation may be a consequence of the simultaneous occurrence of reactions of the type $M + h\nu \rightarrow R$, $M + h\nu \rightarrow Q$, $R + h\nu \rightarrow Q$, and $Q + h\nu \rightarrow R$, where M is an inactive defect, R is a radiative center, and Q is a nonradiative center. Not ruled out here is the mechanism of thermal defect formation due to strong absorption at inclusions in the volume of the active region. The existence of defects is confirmed by the results of x-ray microanalysis and three-crystal diffractometry studies.

The data obtained here are evidence of the existence in the volume of the gallium-phosphide active region of defects with large photon capture cross sections at photon energies $h\nu \sim 1.17$ eV. Confirmation of the existence of such defects can clearly be obtained by examining the luminescence spectra of levels in the band gap near $E_g/2$. Charge carrier recombination via these levels is primarily of radiative type because of the satisfaction of the condition $E_g \gg h\omega_{\text{opt}}$ for gallium phosphide, where ω_{opt} is the angular frequency of the optical photons.

[1] Zh. I. Alfërov, V. G. Agafonov, V. M. Andreev *et al.*, Fiz. Tekh. Poluprovodn. **12**, 1054 (1978) [Sov. Phys. Semicond. **12**, 626 (1978)].

[2] P. D. Dapkus and C. H. Henry, Appl. Phys. **47**, 4061 (1976).

[3] B. Rheinlander, G. Oelgart, H. Halfner *et al.*, Phys. Status Solidi A **87**, 373 (1985).

[4] T. V. Torchinskaya, A. A. Shmatov, V. I. Strochkov, and M. K. Sheĭnkman, Fiz. Tekh. Poluprovodn. **20**, 701 (1986) [Sov. Phys. Semicond. **20**, 442 (1986)].

[5] T. V. Torchinskaya, T. G. Berdinskikh, and A. G. Korabaev, Zh. Tekh. Fiz. **59**(18), 134 (1989) [Sov. Phys. Tech. Phys. **34**, 1036 (1989)].

[6] V. S. Vavilov, A. E. Kiv, and O. R. Niyazova, *Mechanisms of Defect Formation and Migration in Semiconductors* [in Russian], Nauka, Moscow (1981), Ch. 8, p. 316.

[7] G. A. Sukach, Fiz. Tekh. Poluprovodn. **31**, 857 (1997) [Semiconductors **31**, 753 (1997)].

[8] A. A. Ptashchenko, Zh. Prikl. Spektrosk. **33**, 781 (1980).

Translated by Paul F. Schippnick

PERSONALIA

Vitaliĭ Ivanovich Stafeev (on his 70th birthday)

Fiz. Tekh. Poluprovodn. **33**, 501–502 (April 1999)
[S1063-7826(99)02604-6]

January 1, 1999 marked the 70th birthday and 45 years of scientific, pedagogical, and organizational activity of the well-known scientist, professor, doctor of physical and mathematical sciences, Distinguished Scientist and Engineer of the Russian Federation, Recipient of the State Prize of the USSR, and active member of the Academy of Engineering Sciences of the Russian Federation, Vitaliĭ Ivanovich Stafeev.

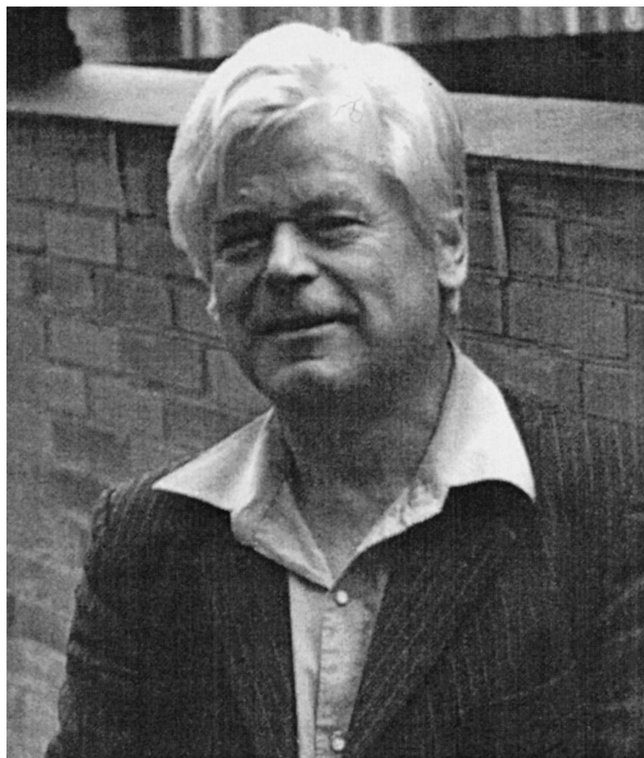

Stafeev was born on January 1, 1929. After completing the course of study of the physical–mathematical department of the University of Alma Ata in 1952 he was assigned to the A. F. Ioffe Physicotechnical Institute of the Academy of Sciences of the USSR, where he worked until 1964, simultaneously holding the position of professor in the department of semiconductor physics of the Leningrad Polytechnical Institute. In 1964 Stafeev was named director of the Scientific-Research Institute of Physical Problems of the Ministry of the Electronics Industry and for a long time was a department chairman in the Moscow Physicotechnical Institute. In 1969 he transferred to the Scientific-Research Institute of Applied Physics of the Ministry of Defense Industries, where he first directed a section, and then became head of a department. In 1961 he received the degree of doctor of physical and mathematical sciences, in 1964 he became a professor, and he was twice awarded the State Prize of the USSR (in 1982 and 1988). He was also awarded the Academician A. A. Lebedev Medal. At present, he is chief designer of photodetector arrays at the Scientific-Research Institute (now called State Scientific Center of the Russian Federation — the State Unitary Enterprise ''NPO Orion'') and professor at the Moscow Physicotechnical Institute.

Stafeev is a scientist with a great breadth of knowledge, a groundbreaker of new scientific and scientific-engineering directions. He suggested the principles of operation of a number of new semiconductor devices, functional logical circuits, and image detection, processing, and reproduction devices. He created highly efficient sensors possessing high sensitivity to magnetic fields, pressure, and electromagnetic radiation.

Under Stafeev's guidance, studies of the physical properties of a new promising semiconductor material, the solid solution CdHgTe, were carried out and its industrial production was organized. On the basis of this material infrared photodetectors and photodetector arrays, which are widely used in various branches of science and technology, were developed and are now produced.

Stafeev devoted a significant portion of his scientific activity to studies of physical processes in dielectric liquids and liquid crystals, studies of the properties of molecular films, and simulations of neurons and information processing in neural networks. He developed the principles of functional microelectronics utilizing injection-plasma space coupling in semiconductor structures and also new circuit and systems technologies. In 1958–1959 he made a significant contribution to the initial phase of the domestic realization of semiconductor-based solar energy technology.

Carried out under his guidance, the integrated studies of optical phenomena, occurring as a result of heating of the electron gas in semiconductors, led to the creation of injection-free semiconductor lasers in the far infrared and high-frequency modulators of infrared radiation.

The scientific activity of Stafeev is reflected in more than 500 scientific papers, 12 books, and 90 inventions. Many of the results of his studies have appeared in monographs published in Russia and abroad.

Stafeev is the head of a scientific school. Among his students number 20 doctors of science, more than 60 candidates of science, and recipients of the State Prize of the

 © 1999 American Institute of Physics

USSR. They work successfully in many cities of Russia and in other countries of the Former Soviet Union.

Stafeev is still active in scientific-organizational activity. He organized the publication of the scientific-technical collection *Micro-Electronics*, he was one of the participants in the organization of the publication of the journal *Micro-Electronics*, editor-in-chief of the 22nd series of VOT *Micro-Electronics*, member of the editorial board of the journals *Physics and Technology of Semiconductors* and *Radio Engineering and Electronics*, member of the Expert Committee of VAK, member of the Expert Committee of the Committee on Lenin and State Prizes of the USSR, vice-president of the section ''Narrowband semiconductors and photoelectronics,'' president of the section ''Physics and chemistry of semiconductors,'' and organizer and member of the organizing committees of many scientific conferences, symposia, and seminars.

We congratulate Vitaliĭ Ivanovich Stafeev on his jubilee and wish him health and many more years of productive scientific work.

Zh. I. Alferov, L. A. Bovina, V. I. Ivanov-Omskiĭ, and L. E. Vorob'ev

Translated by Paul F. Schippnick

Aleksandr Aleksandrovich Lebedev (on his 70th birthday)

Fiz. Tekh. Poluprovodn. **33**, 503 (April 1999)
[S1063-7826(99)02704-0]

January 25 marked the 70th birthday of the Chief Scientific Worker of the A. F. Ioffe Physicotechnical Institute of the Russian Academy of Sciences, steady contributor to and reviewer for our journal, doctor of physical and mathematical sciences, Aleksandr Aleksandrovich Lebedev.

Lebedev was born in Leningrad into the family of the famous physicist, Aleksandr Alekseevich Lebedev. After completing school, he entered the physics department of the university, and in 1951 began to work at the A. F. Ioffe Physicotechnical Institute, with which he has been associated his entire life. Pursuing the path from a senior laboratory assistant to chief scientific worker, Aleksandr Aleksandrovich embraced the best traditions of the institute, distinguishing himself among his colleagues by his erudition and excellent university training.

The start of Lebedev's scientific career coincided with the birth of semiconductor electronics, in the development of which he participated directly. His entire scientific activity was inseparably connected with the physics of semiconductors and to a significant degree defined its present level. He made a substantial contribution to the development of the domestic technology of growth of pure and doped germanium single crystals, and also to the study of the characteristics of devices based on this material. His most important scientific achievements were connected with the study of the properties of deep centers in semiconductors. Lebedev and his coworkers investigated the spectra of the impurity levels of more than 30 elements, and also the energy spectra of localized electron states of defects in silicon and gallium arsenide. In the review articles and monographs dealing with this topic many references to data obtained by him can be found. Lebedev is linked with the early development of the presently classical method of deep-level transient spectroscopy, which he successfully developed and put into practice. He published about 300 papers, and together with L. S. Berman authored a monograph. At present, another one of his books is to be published. Lebedev was recently in charge of work on light-emitting porous silicon and other porous semiconductors, and he contributed substantially to the understanding of the nature of this new phenomenon.

His pedagogical talent facilitated the growth and development of a large number of physicists who are engaged in scientific work at the A. F. Ioffe Physicotechnical Institute and in various institutes of the former Soviet Union. Lebedev is a talented experimental physicist who enjoys the respect of his colleagues and has earned the esteem of the world scientific community. Aleksandr Aleksandrovich is distinguished by a rare modesty, generosity of the soul, and a deep sense of order which draw people to him. Since his early years he correctly understood his proper purpose in life: to be involved in experimental work and avoid administrative duties. He belongs to the breed of eccentric scientists who have no need of degrees or titles and who pursue only the knowledge of the true nature of things.

We heartily congratulate Aleksandr Aleksandrovich on his jubilee and with all our hearts wish him health and more creative success.

Students and Colleagues

Translated by Paul F. Schippnick

 © 1999 American Institute of Physics